

**EXPERIMENTAL AND NUMERICAL  
EVALUATION OF THE BLAST-LIKE LOADING  
OF FIBER REINFORCED POLYMER  
COMPOSITES AND ALUMINUM CORRUGATED  
CORE COMPOSITE SANDWICHES THROUGH  
PROJECTILE IMPACT TESTING USING  
ALUMINUM CORRUGATED PROJECTILES**

**A Thesis Submitted to  
the Graduate School of Engineering and Sciences of  
İzmir Institute of Technology  
in Partial Fulfilment of the Requirements for the Degree of**

**DOCTOR OF PHYLLOSOPHY**

**in Mechanical Engineering**

**by  
İsmet Kutlay ODACI**

**September 2015  
İZMİR**

We approve the thesis of **İsmet Kutlay ODACI**

**Examining Committee Members:**

---

**Prof. Dr. Mustafa GÜDEN**

Department of Mechanical Engineering, İzmir Institute of Technology

---

**Prof. Dr. Bülent YARDIMOĞLU**

Department of Mechanical Engineering, İzmir Institute of Technology

---

**Prof. Dr. Rasim İPEK**

Department of Mechanical Engineering, Ege University

---

**Prof. Dr. Hasan YILDIZ**

Department of Mechanical Engineering, Ege University

---

**Assoc. Prof. Dr. Bülent Murat İÇTEN**

Department of Civil Engineering, Dokuz Eylül University

**29 September 2015**

---

**Prof. Dr. Mustafa GÜDEN**

Supervisor, Department of  
Mechanical Engineering  
İzmir Institute of Technology

---

**Assoc. Prof. Dr. Alper TAŞDEMİRCİ**

Co-Supervisor, Department of  
Mechanical Engineering  
İzmir Institute of Technology

---

**Prof. Dr. Metin TANOĞLU**

Head of the Department of  
Mechanical Engineering

---

**Prof. Dr. Bilge KARAÇALI**

Dean of the Graduate School of  
Engineering and Sciences

## ACKNOWLEDGEMENTS

I would like to gratefully thank to my supervisor Prof. Dr. Mustafa GÜDEN for his instructive comments, encouragement, guidance and support from the beginning to the final stage of my thesis study. Secondly, thank to my co-supervisor Assoc. Professor Alper TAŞDEMİRÇİ for his supports and brilliant ideas during my study. I also gratefully thank to my thesis progress juries Prof. Dr. Rasim İPEK and Prof. Dr. Bülent YARDIMOĞLU for their technical supports and contributions to my writing skills.

The authors also would like to thank The Scientific and Technological Research Council of Turkey (TUBITAK) and 2211-C doctoral research fellowship program. Thanks to all members of DTM Lab; Cenk KILIÇASLAN, Ali KARA, Ali Kıvanç TURAN, Selim ŞAHİN, Atacan YÜCESOY, Dođuş ZEREN for their endless support and association.

Furthermore, I would like to thank my wife Burcu ODACI whose love, patience and permanent confidence in me, has made the life easier during my study. I also wish to thank my family who deserve a special mention for their endless support and prayers. My father, Necmi ODACI, is the person who helped and directed me during my whole education life to be successful. My mother, Mine ODACI, is the one who sincerely raised me with her caring and gently love. Silay ODACI thanks for being supportive and caring sibling.

Finally, I would like to thank everyone who helped me during this thesis and I offer an apology that I could not mention personally one by one.

# **ABSTRACT**

## **EXPERIMENTAL AND NUMERICAL EVALUATION OF THE BLAST-LIKE LOADING OF FIBER REINFORCED POLYMER COMPOSITES AND ALUMINUM CORRUGATED CORE COMPOSITE SANDWICHES THROUGH PROJECTILE IMPACT TESTING USING ALUMINUM CORRUGATED PROJECTILES**

This thesis develops and validates a laboratory scale blast-like testing method that can simulate explosive blast tests in air and under water without using explosives. The study has mainly focused on the shock loading potential of 1050 H14 trapezoidal corrugated core aluminium sandwich structures on E-glass/polyester composite plates and corrugated core composite sandwich structures experimentally, numerically and analytically. The composite plates were modelled using MAT\_162 material model in LS-DYNA finite element code. Quasi-static and high strain rate tests were performed to determine the material model parameters of composite and corrugated structure. The resultant parameters were calibrated and validated by comparing the numerical results with the experimental results. The planar shock wave formation and propagation in corrugated core sandwich structures were shown experimentally using a direct impact Split Hopkinson Pressure Bar test set-up. Rigid-perfectly-plastic-locking material model and Hugoniot jump relations revealed the shock loading potential of the tested corrugated core sandwich structures. The shock loading response of composite plates and sandwich structures were investigated by firing the corrugated sandwich projectiles on the targets. These impact tests were also simulated numerically and an analytic model was used to predict the plate deflections. The experimentally, numerically and analytically determined back face deflections were compared with the deflections of the Conwep blast simulations in LS-DYNA. The results have shown that the corrugated core sandwich structures can generate shock loading as in the explosive blast tests and can be used to produce shock loads in laboratory scale experiments.

## ÖZET

### DALGALI ALÜMİNYUM PROJEKTÖRLER KULLANARAK PROJEKTÖR ÇARPIŞMA TESTİ İLE FİBER TAKVİYELİ POLİMER KOMPOZİT VE ALÜMİNYUM DALGALI ÇEKİRDEKLİ KOMPOZİT SANDVIÇLERİN PATLAMA BENZERİ YÜKLENMESİNİN DENEYSEL VE NÜMERİK DEĞERLENDİRİLMESİ

Bu tez havada ve su altında gerçekleştirilen patlama testlerinin patlayıcı kullanılmadan laboratuvar ölçekli patlama benzeri test metodlarıyla benzetilmesini geliştirir ve doğrular. Çalışma esas olarak 1050 H14 yamuk dalgalı çekirdekli alüminyum sandviç yapıların E-cam/polyester kompozit plakalar ve dalgalı çekirdekli kompozit sandviç yapılar üzerindeki şok yükleme potansiyeline deneysel, nümerik ve analitik olarak odaklanmıştır. Kompozit malzeme LS-DYNA sonlu elementler kodundaki MAT\_162 malzeme modeli modellenmiştir. Malzeme modelindeki parametrelerin belirlenmesi için yarı statik ve yüksek gerilme hızlarında testler gerçekleştirilmiştir. Elde edilen parametreler deneysel ve nümerik sonuçlar karşılaştırılarak kalibre edilmiş ve doğrulanmıştır. Dalgalı çekirdekli sandviç yapılarda düzlemsel şok dalgasının oluşumu ve ilerleyişi doğrudan çarpmalı Split Hopkinson Basınç Barı test düzeneği kullanılarak gösterilmiştir. Rijit-mükemmel-plastik malzeme modeli ve Hugoniot gerilim denklemleri test edilmiş dalgalı çekirdekli sandviç yapıların şok yükleme potansiyellerini göstermiştir. Kompozit plakaların ve sandviç yapıların şok yükleme tepkisi, hedeflere dalgalı sandviç yapılar fırlatılarak incelenmiştir. Bu çarpışma testleri nümerik olarak simüle edilmiş ve plaka sehimleri bir analitik model kullanılarak tahmin edilmiştir. Deneysel, nümerik ve analitik olarak bulunan arka yüzey sehimleri, LS-DYNA Conwep patlama simülasyonlarındaki sehimlerle karşılaştırılmıştır. Sonuçlar dalgalı çekirdekli sandviç yapıların patlayıcı kullanılan testlerdeki şok yükünü oluşturduğu ve laboratuvar ölçekli deneylerde şok yükü üretici olarak kullanılabileceğini göstermiştir.

# TABLE OF CONTENTS

LIST OF FIGURES.....	x
LIST OF TABLES .....	xxii
CHAPTER 1. INTRODUCTION .....	1
1.1. Introduction.....	1
1.2. Aim of the Study .....	3
1.3. Scope of the Study.....	4
CHAPTER 2. LITERATURE SURVEY .....	6
2.1. Polymer Composites.....	6
2.2. Mechanical Characterization of Composites .....	7
2.2.1. Quasi-Static Testing .....	7
2.2.2. High Strain Rate Testing.....	7
2.3. Finite Element Modeling .....	12
2.4. Sandwich Structures .....	23
2.4.1. Metal Foam Cores .....	23
2.4.2. Honeycomb Cores .....	24
2.4.3. Corrugated Cores.....	25
2.4.4. The Mechanical Responses of Corrugated Core Sandwiches.....	27
2.5. Blast and Blast-Like Loading of Plates and Sandwich Structures.....	35
2.5.1. Blast Loading of Plates and Sandwich Structures.....	36
2.5.2. Blast-Like Loading of Plates and Sandwich Structures .....	46
CHAPTER 3. EXPERIMENTAL.....	56
3.1. Introduction.....	56
3.2. E-Glass/Polyester Composite Processing .....	56
3.3. Mechanical Testing of E-Glass/Polyester Composite .....	59
3.3.1. In-Plane Tensile Tests.....	59
3.3.2. In-Plane Shear Test.....	60
3.3.3. Quasi-static Compression Tests .....	62

3.3.4. Flexural Tests .....	63
3.3.5. Curved Beam Tests.....	65
3.3.6. Laterally Constraint Compression Tests.....	65
3.3.7. Low Velocity Impact Tests .....	66
3.3.8. Split Hopkinson Pressure Bar Compression Tests .....	69
3.3.9. Projectile Impact Tests with Spherical Projectiles .....	70
3.4. Trapezoidal Corrugated Aluminum Fin Layers and Sandwich Structures .....	71
3.5. Mechanical Testing of 1050 H14 Aluminum Alloy and Corrugated Sandwich Structures .....	75
3.5.1. Mechanical Testing of 1050 H14 Aluminum Alloy.....	75
3.5.2. Quasi-static Compression Tests on Corrugated Sandwich Structures .....	77
3.5.3. Direct Impact SHPB Tests.....	78
3.5.4. Projectile Impact Tests with Corrugated Projectiles .....	80
3.5.5. Summary of The Experimental Study .....	81
 CHAPTER 4. NUMERICAL MODELS .....	 83
4.1. Introduction.....	83
4.2. Modeling Tools and Methodology.....	83
4.3. MAT_162 Composite Material Model.....	84
4.3.1. Failure Criteria .....	84
4.3.1.1. Tensile/Shear Failure Modes.....	85
4.3.1.2. Compression Failure Modes.....	85
4.3.1.3. Shear Failure Mode.....	86
4.3.1.4. Delamination Failure Mode.....	86
4.3.2. Damage Model .....	87
4.3.3. Strain Rate Effect .....	87
4.3.4. Delamination Factor .....	88
4.3.5. Element Erosion .....	89
4.4. Quasi-static Tension Test Numerical Modeling .....	89
4.5. Quasi-static Compression Test Numerical Modeling .....	90
4.6. Quasi-static Shear Test Numerical Modeling .....	91
4.7. Flexural Test Numerical Modeling .....	92

4.8. Low Velocity Impact Test Modeling .....	93
4.9. Projectile Impact Test Modeling .....	94
4.10. Trapezoidal Corrugated Fin Layers Geometric Modeling and Mesh Generation Studies .....	95
4.11. Material Models .....	97
4.11.1. Simplified Johnson-Cook (JC) Material Model .....	97
4.12. Numerical Models of Compression of Multi-layer Corrugated Sandwiches .....	97
4.13. Summary of The Numerical Study .....	107
 CHAPTER 5. ANALYTICAL SOLUTIONS .....	 110
5.1. Introduction .....	110
5.2. Rigid Perfectly Plastic Shock Theory .....	111
5.3. Application of Hugoniot Jump Equations to Corrugated Sandwiches .....	115
5.4. Analytical Model for Clamped Composite Plates .....	118
5.5. Analytical Model for Clamped Sandwich Structures .....	121
 CHAPTER 6. TESTING AND MODELLING OF E-GLASS COMPOSITE MATERIALS .....	 125
6.1. Introduction .....	125
6.2. The Experimental and Numerical Results of Composite Materials ...	125
6.2.1. Experimental Tension Test and Numerical Model Results .....	125
6.2.2. Experimental Compression Tests and Numerical Model Results	129
6.2.3. Experimental Flexural Tests and Numerical Model Results .....	136
6.2.4. Curved Beam Test Results .....	138
6.2.5. Laterally Constraint Compression Test Results .....	140
6.2.6. Experimental Shear Test and Numerical Model Results .....	142
6.2.7. Experimental Low Velocity Impact Test and Numerical Model Results .....	144
6.2.8. Experimental Projectile Impact Tests and Numerical Model Results .....	147

CHAPTER 7. TESTING AND MODELLING OF CORRUGATED STRUCTURES .....	153
7.1. Simplified Johnson Cook Material Model of 1050 Al .....	153
7.2. Compression of Corrugated Sandwiches .....	156
7.3. Mesh Sensitivity .....	158
7.4. Imperfection Sensitivity .....	160
 CHAPTER 8. SHOCK LOADING OF CORRUGATED STRUCTURES .....	 163
8.1. Direct Impact Testing .....	163
8.2. Direct Impact Test Simulations .....	166
8.3. Direct Impact with Backing Mass and Stationary Impact Simulations .....	 172
 CHAPTER 9. ANALYTIC MODELS OF IMPACT TESTS .....	 191
9.1. Rigid Perfectly Plastic Locking Shock Model .....	191
9.2. Effects of Number of Fin Layers .....	209
9.3. Hugoniot Jump Equations; tests with backing mass and stationary impact .....	 212
 CHAPTER 10. IMPACT TESTS ON CLAMPED COMPOSITE PLATES AND SANDWICH STRUCTURES .....	 218
10.1. Experimental, Numerical and Analytical Solutions of Blast-Like Loading of Composite Plates and Sandwich Structures .....	 218
10.2. Impact Tests Using Corrugated Core Sandwich as Projectile .....	218
10.3. Blast-Like Loading of Plates and Sandwich Structures .....	223
10.4. Analytical Studies of Blast-Like Loaded Plates and Sandwich Structures .....	 235
 CHAPTER 11. CONCLUSION .....	 239
 REFERENCES .....	 242

# LIST OF FIGURES

<b><u>Figure</u></b>	<b><u>Page</u></b>
Figure 1.1. Full scale blast test of a military vehicle [1]. .....	2
Figure 1.2. Non-explosive testing set-ups: (a) the McMillan blast testing device [8], (b) direct pressure pulse generator [2] and (c) shock tube [6]. .....	3
Figure 2.1. Schematic of SHPB compression test set-up [32]. .....	8
Figure 2.2. A typical record of compression SHPB test. ....	9
Figure 2.3. Particle velocities and incident, reflected and transmitted strains. ....	10
Figure 2.4. A fractured composite sample tested at $1100 \text{ s}^{-1}$ [36]. .....	12
Figure 2.5. Shear punch testing system and different SPR types [57]. .....	14
Figure 2.6. Shear punch test load-displacement curves for SPR=8 [57]. .....	15
Figure 2.7. Experimental and numerical load-displacement curves of shear punch test [57]. .....	15
Figure 2.8. Effect of mesh refinement on the structural response [58]. .....	16
Figure 2.9. Delamination shapes of three interfaces resulting from low velocity impact simulation [58]. .....	17
Figure 2.10. Delamination progression in three projectile sequential impact series: (a) experimental and (b) simulation at $S_d = 5$ [59]. .....	18
Figure 2.11. Simulated and experimental force versus time curves at (a) 50J and (b) 70J [60]. .....	19
Figure 2.12. Comparison of numerical results with experimental results with RCC at $v = 736 \text{ m/s}$ [60]. .....	19
Figure 2.13. Stress-strain curves of a unidirectional layer under axial tensile, transverse tensile and in-plane shear loads [61]. .....	20
Figure 2.14. (a) Laterally constraint test fixture and (b) fractured sample after the test [61]. .....	21
Figure 2.15. Experimental and numerical damage areas of composite materials [61]. ..	21
Figure 2.16. Stress-Strain curves of the composite in the (a) longitudinal, (b) transverse, and (c) through-thickness directions [62]. .....	22
Figure 2.17. Damage sequences of composites in transverse and through thickness directions [62]. .....	22
Figure 2.18. Schematic compressive stress-strain curve of a metal foam [64]. .....	24

Figure 2.19. Honeycombs cell configurations: (a) hexagonal core, (b) ox-core and (c) flex-core. ....	24
Figure 2.20. A typical compressive stress-strain curve of honeycomb cores [71]. ....	25
Figure 2.21. Core geometries: (a) hat-shaped, (b) triangular and (c) trapezoidal core [82].....	26
Figure 2.22. Compressive stress-strain curve of pyramidal core structures [83].....	26
Figure 2.23. Isometric and front views of corrugated core sandwich structure [84]. ....	27
Figure 2.24. (a) The out-plane compressive response and (b) longitudinal shear response of corrugated core sandwiches [84]. ....	28
Figure 2.25. Corrugated sandwiches and numerical models of (a) bonded $0^{\circ}/0^{\circ}$ , (b) brazed $0^{\circ}/0^{\circ}$ and (c) bonded $0^{\circ}/90^{\circ}$ [85].....	29
Figure 2.26. Simulation and experimental stress-strain curves multi-layer sandwiches tested at $40 \text{ s}^{-1}$ : (a) unconstrained, (b) constraint tests and (c) the experimental and simulation deformation pictures of bonded multi-layer samples [85].....	30
Figure 2.27. (a) Unit cell geometry of the corrugated-core sandwich panel (b) photo of an aluminum corrugation, (c) a GFRP corrugation and (d) a CFRP corrugation [86]. ....	31
Figure 2.28. Comparison of compression strength of the corrugated cores as function of equivalent core density [86].....	31
Figure 2.29. Warp structure of (a) integrated woven sandwich composite with ultra-thin sheets and wave cores, (b) sandwich panel with strengthened skins, and (c) finished sample [87].....	33
Figure 2.30. Failure modes and responses of IWWSC panel: (a) compression, (b) shear and (c) three point bending [87].....	33
Figure 2.31. Typical as-fabricated empty and aluminum foam-filled sandwich beams with corrugated cores. Long beam: (a) empty; and (b) filled and short beam: (c) empty; and (d) filled [88].....	34
Figure 2.32. Transverse bending behavior of empty and foam filled sandwich beams with loading spans of (a) 242 mm and (b) 112 mm [88].....	35
Figure 2.33. Pressure-time response of an explosive blast [89]. ....	36
Figure 2.34. Ballistic pendulum set-up and Dyneema test specimen [90]. ....	37
Figure 2.35. (a) Deformation modes of Dyneema and (b) comparison of permanent deflections [90]. ....	38

Figure 2.36. Debonded and petalled regions of (a) woven glass fiber FMLs and (b) unidirectional glass fiber FMLs [91]. .....	39
Figure 2.37. 2 mm and 3 mm thick deformed test plate profiles subjected to 10 g and 35 g charge masses [92]. .....	40
Figure 2.38. Comparison of deformed plate profiles obtained from the experiments and simulations for the 2 mm thick deformed test plates [92]. .....	40
Figure 2.39. The sandwich panel and equivalent monolithic plate midpoint (back face) displacement ratio $u_s / u_m$ for the various core materials with: (a) 0.6 mm face sheets and (b) 1.0 mm face sheets [93]. .....	41
Figure 2.40. Deformed core materials: (a) Alporas foam, (b) Cymat foam, (c) 13 mm honeycomb and (d) 29 mm honeycomb [93]. .....	42
Figure 2.41. Experimentally deformed (a) monolithic solid plate and (b) corrugated core sandwich structures [94]. .....	43
Figure 2.42. (a) numerical deformation of sandwich structures and (b) experimental and numerical deflections [94]. .....	43
Figure 2.43. The sand impulse test geometry and dimensions of the sandwich panels [95]. .....	45
Figure 2.44. The finite element model prior to detonation [95]. .....	45
Figure 2.45. Deformation of sandwich structures (a) experimental and (b) numerical [95]. .....	46
Figure 2.46. (a) Corrugated core sheet dimensions. (b) assembly procedure of corrugated steel core sandwich structures and (c) final sandwich panel side view [96]. .....	47
Figure 2.47. (a) Shock tube apparatus and (b) experimental pressure profile [96]. .....	47
Figure 2.48. (a) Fixture of the corrugated sandwich plate and (b) a schematic of shock tube tester [97]. .....	48
Figure 2.49. (a) Experimental and numerical damage and (b) mid-span deflections of face sheets [97]. .....	48
Figure 2.50. (a) Monolithic steel plate (b) bilayer plate with polyurea on the dish side and (c) bilayer plate with polyurea on the flat side [98]. .....	50
Figure 2.51. Average effective plastic strain history of a monolithic plate and bilayer plates of the indicated polyurea–steel interface bonding strengths [98]. ...	50

Figure 2.52. Shock loaded and deformed structures: (a) monolithic beams, (b) corrugated core sandwich beams, (c) foam core sandwich beams and (d) pyramidal core sandwich beams [99].	51
Figure 2.53. Comparison between experimental measurements and predictions of the mid-span deflections for the monolithic beams [99].	52
Figure 2.54. Piezoelectric force cell measurement of pressure history, impacts at 38.1 m/s [100].	53
Figure 2.55. Deformation of shock loaded (a) composite plates and (b) sandwich structures [100].	53
Figure 2.56. Projectile and components for impact [101].	54
Figure 2.57. Foam tipped tile blocks shown from left: 50.8 mm steel block F and 3.18 mm spacer; 6.35 mm aluminum, 1.59 mm spacer, and 44.5 mm steel blocks D, E; 12.7 mm aluminum and 38.1 mm steel block B, C; 25.4 mm aluminum and 25.4 mm steel block A [101].	55
Figure 2.58. Deformation of double honeycomb core sandwich structures: (a) non- explosive blast test and (b) explosive blast test [101].	55
Figure 3.1. (a) Metyx biaxial E-glass fiber and (b) Scott Bader Crystic 703 PA polyester.	57
Figure 3.2. Vacuum assisted resin transfer molding set-up.	58
Figure 3.3. E-glass/polyester composite principal coordinate system.	58
Figure 3.4. Tension test specimen with extensometer and strain gages.	59
Figure 3.5. ASTM 3039M tensile test specimen.	60
Figure 3.6. $[\pm 45^\circ]$ shear test specimen.	61
Figure 3.7. Shear test specimen dimensions according to ASTM D 3518.	62
Figure 3.8. Quasi-static compression test specimens; (a) ASTM D3410 and (b) cylindrical test samples.	62
Figure 3.9. Technical drawing of compression test samples according to ASTM D3410.	63
Figure 3.10. Flexural test set-up and flexural test specimen.	64
Figure 3.11. (a) Curved beam test set-up and (b) curved beam specimen.	65
Figure 3.12. Laterally constraint compression test set-up and cube composite samples.	66
Figure 3.13. (a) FRACTOVIS low velocity impact test equipment and (b) striker holder, weights and the impactor.	67

Figure 3.14. A typical load-energy-time curve for impact analyses [106].	68
Figure 3.15. Incident bar, transmitter bar and composite sample prior to impact.	69
Figure 3.16. (a) Projectile impact test set-up, (b) target frame and (c) laser barriers [107].	70
Figure 3.17. Hydraulic press used to form corrugated layers.	71
Figure 3.18. The pictures of (a) forming machine and (b) bottom die.	72
Figure 3.19. Picture and technical drawings of corrugated fin layers: (a) small fin corrugated layer and (b) big fin corrugated layer.	73
Figure 3.20. (a) Small fin corrugated core aluminum sandwich, (b) single layer big fin core composite sandwich and (c) three layers big fin corrugated core composite sandwich.	74
Figure 3.21. (a) Technical drawing and (b) picture of tensile test specimens [85, 109].	75
Figure 3.22. Furnace for heat treatment of 1050 H14 test samples.	77
Figure 3.23. Constraint compression test apparatus and compression samples.	78
Figure 3.24. Direct impact SHPB test set-up.	79
Figure 3.25. Projectile impact test set-up and high speed camera.	80
Figure 4.1. Steps in numerical model.	84
Figure 4.2. The numerical model of the composite tension test specimen.	90
Figure 4.3. The numerical model of the composite compression test specimen.	91
Figure 4.4. The numerical model of the composite shear test specimen.	92
Figure 4.5. Finite element model of quasi-static flexural test.	93
Figure 4.6. Low velocity impact model used in simulations.	94
Figure 4.7. Projectile impact test model used in simulations.	95
Figure 4.8. Mesh generation of a big fin corrugated core sheet; (a) CAD geometry, (b) meshing, (c) duplication in x-axis and (d) duplication in y-axis.	96
Figure 4.9. Mesh generation of a small fin corrugated core sheet; (a) CAD geometry, (b) meshing, (c) duplication in x-axis and (d) duplication in y-axis.	96
Figure 4.10. Imperfections in corrugated sandwich structures.	98
Figure 4.11. Fin wall bending type of imperfection in a unit fin.	98
Figure 4.12. Fin wall bulge imperfection in a unit fin.	99
Figure 4.13. Perfect numerical models of small fin corrugated sandwich structures: (a) with and (b) without face sheets.	100
Figure 4.14. Imperfect models: (a) fin wall bending in all layers, (b) mixed imperfection and (c) layers 6 and 12 fin wall bending.	100

Figure 4.15. Unit fin mesh size: (a) coarse mesh, (b) medium mesh and (c) fine mesh sizes. ....	101
Figure 4.16. The numerical model of quasi-static compression test set-up. ....	102
Figure 4.17. Direct SHPB impact test model with corrugated projectile. ....	103
Figure 4.18. Mass impact with SHPB: (a) moving projectile and (b) stationary projectile. ....	104
Figure 4.19. The numerical model of projectile impact on composite specimen. ....	105
Figure 4.20. Projectile impact on sandwich structures with; (a) single corrugated core and (b) 3 layered corrugated core. ....	106
Figure 5.1. Idealized material models: (a) elastic perfectly plastic, (b) elastic linear hardening and (c) rigid perfectly plastic [113]. ....	110
Figure 5.2. Sketch of corrugated sandwich corrugated projectile impacting on aluminum bar.....	113
Figure 5.3. Mass impact on a rigid perfectly plastic corrugated cylinder. ....	115
Figure 5.4. (a) Impact of mass attached corrugated sandwich on aluminum bar and (b) impact of mass on corrugated sandwich attached to the aluminum bar.....	116
Figure 5.5. Clamped composite plate loaded by corrugated projectile [119]. ....	119
Figure 5.6. Monolithic beam impulsive response analysis for Phase III; (a) velocity profile and (b) half beam free body diagram.....	120
Figure 5.7. Fully clamped sandwich structure under impulsive loading [119]. ....	121
Figure 5.8. Sandwich beam impulsive response analysis for Phase III; (a) velocity profile and (b) half beam free body diagram.....	124
Figure 6.1. In-plane tensile stress-strain curves of E-Glass/Polyester composite. ....	126
Figure 6.2. Damages in in-plane tensile tested specimen: (a) X- and (b) Y-directions.....	126
Figure 6.3. Tensile test models with different mesh sizes: (a) 1, (b) 2.5 and (c) 5 mm. ....	127
Figure 6.4. The stress-strain curves of experimentally and numerically tested composites. ....	128
Figure 6.5. The deformation modes of the tensile test samples with $m_1=m_2=4$ for different mesh sizes: (a) 1, (b) 2.5 and (c) 5 mm.....	128
Figure 6.6. Quasi-static and SHPB compression stress-strain curves of the composite: (a) X-, (b) Y- and (c) Z-direction.....	130

Figure 6.7. The failed quasi-static composite samples tested in (a) X-, (b) Y- and (c) Z-direction. ....	132
Figure 6.8. The deforming composite sample pictures in SHPB tested in (a) X-, (b)Y-and (c) Z-direction. ....	132
Figure 6.9. Determination of the strain rate sensitivity parameter of $C_{rate1}$ . ....	133
Figure 6.10. Determination of strain rate sensitivity parameters of $C_{rate2}$ and $C_{rate4}$ . ....	134
Figure 6.11. The experimental and numerical quasi-static ( $10^{-1} s^{-1}$ ) ASTM D3410 compression test sample stress-strain curves with $m_1=m_2=0.5$ values. ...	135
Figure 6.12. Quasi-static (a) experimentally and (b) numerical tested compression samples showing damage modes and locations. ....	135
Figure 6.13. Experimental and numerical simulation force-displacement responses of three point bending test. ....	136
Figure 6.14. Sequential deformation modes of three point bending test simulation. ....	137
Figure 6.15. The curved beam force-displacement responses of the composite samples. ....	139
Figure 6.16. Deformation types in curved beam strength test specimen. ....	140
Figure 6.17. Lateral constraint compression test results. ....	141
Figure 6.18. Lateral constraint test specimen failed with inclined shear plane. ....	141
Figure 6.19. Quasi-static shear test experimental and numerical simulation stress-strain responses. ....	142
Figure 6.20. Matrix mode damage patterns in quasi-static shear test numerical simulation. ....	143
Figure 6.21. Failed composite sample after quasi-static shear testing. ....	143
Figure 6.22. Force-time response of low velocity impact test and numerical studies at 4.21 m/s impact velocity. ....	145
Figure 6.23. Force-time response of low velocity impact test and numerical studies at 6.12 m/s impact velocity. ....	145
Figure 6.24. Experimental and numerical simulation displacement-time curves of rebound and perforation cases. ....	146
Figure 6.25. Displacement levels of rebound and perforation cases. ....	146
Figure 6.26. Experimental and numerical comparison of projectile residual velocity for 2 mm thick composite plates. ....	148
Figure 6.27. Experimental and numerical calculated ballistic limits for composite plates. ....	149

Figure 6.28. Displacement-time response of the projectile against composite plates...	149
Figure 6.29. Force-time response of the composite plates. ....	150
Figure 6.30. Finite element simulation damage progression of 5 mm thick composite.....	151
Figure 7.1. (a) Tensile true stress-true strain curves and (b) yield strength of as-received and heat-treated 1050 Al. ....	154
Figure 7.2. True stress-plastic true strain curves and JC parameters fitting of as-received and heat-treated 1050 Al.....	155
Figure 7.3. (a) The experimental compression and confinement stress-strain curves of corrugated sandwiches at $10^{-1} \text{ s}^{-1}$ . ....	157
Figure 7.4. The quasi-static confined test sample compressed until about 0.4 strain. ..	158
Figure 7.5. Mesh sensitivity analysis of perfect fin geometry at $10^{-1} \text{ s}^{-1}$ : (a) fine, (b) medium and (c) coarse mesh size. ....	159
Figure 7.6. The stress strain curves of the imperfect corrugated sandwiches (a) fin wall bending, (b) fin wall bending and bulging and fin wall bending in the layers of 6 and 12; (c) fine mesh and (d) coarse mesh.....	161
Figure 7.7. Quasi-static deformation of corrugated sandwich without face sheets at various strains: (a) experimental, (b) fin wall bending imperfection in the 6 <sup>th</sup> and 12 <sup>th</sup> layers, (c) fin wall bending in all layers and (d) mixed type of imperfection. ....	162
Figure 8.1. Direct impact pressure-time curves of the corrugated sandwich with face sheets tested at (a)105, (b) 140 and (c) 200 m/s. ....	164
Figure 8.2. Direct impact pressure-time curves of the corrugated sandwich without face sheets tested at (a)105, (b) 140 and (c) 200 m/s. ....	165
Figure 8.3. The pressure-time response of perfect and imperfect numerical models and experiment of corrugated projectiles without face sheet at 105 m/s.....	167
Figure 8.4. The experimental and numerical simulation pressure-time curves of the corrugated projectiles with face sheets tested at (a) 105 and (b) 200 m/s.....	168
Figure 8.5. The experimental and numerical simulation pressure-time curves of the corrugated projectiles without face sheets tested at (a) 140 and (b) 200 m/s.....	169
Figure 8.6. The deformation pictures of the high speed camera and numerical model of corrugated projectiles at 105 m/s: (a) with and (b) without face sheets.....	170

Figure 8.7. The simulation deformation pictures of corrugated projectile without face sheets at various impact time: (a) 50 and (b) 105 m/s.....	171
Figure 8.8. The simulation deformation pictures of corrugated projectile without face sheets (a) 1 m/s, (b) 10 m/s (final length= 47 mm), (c) 25 m/s (final length= 45 mm), (d) 50 m/s (final length= 38 mm) , (e) 75 m/s (final length= 30 mm), (f) 105 m/s (final length= 30 mm), (g) 140 m/s final length= 20 mm and (h) 200 m/s final length= 20 mm). .....	172
Figure 8.9. Pressure and velocity time profile of the projectile impacted (a) without and (b) with backing mass and (c) SHPB gage pressure-time profile and (d) proximal pressure-time profile of the projectile impacted with and without backing mass at 105 m/s. ....	174
Figure 8.10. Pressure and velocity time profile of the projectile impacted (a) without and (b) with backing mass and (c) the velocity time profile and SHPB gage pressure-time profile and (d) proximal pressure-time profile of the projectile impacted end with and without backing mass at 200 m/s.....	177
Figure 8.11. (a) SHPB gage and proximal end pressure-nominal strain and distal end pressures-strain curves: (b) above and (c) below the subcritical velocities and (d) distal end pressure-time curves of corrugated sandwich projectiles with backing mass. ....	180
Figure 8.12. The numerical simulation deformation sequence of corrugated projectile fired with a backing mass at (a) 105 and (b) 200 m/s. ....	184
Figure 8.13. The numerical simulation deformation sequence of corrugated projectile fired with a backing mass at (a) 10 and (b) 50 m/s. ....	185
Figure 8.14. (a) SHPB gage, proximal and distal end pressure and distal and proximal velocity-nominal strain curves of stationary impact, (b) proximal and distal end pressure, distal and proximal velocity-nominal strain curves of stationary and backing mass impact, (c) distal end pressure and (d) proximal end pressure nominal strain curves of stationary impact.....	187
Figure 8.15. The numerical simulation deformation sequence of corrugated projectile subjected to stationary impact at (a) 105 and (b) 200 m/s.....	189
Figure 8.16. The numerical simulation deformation sequence of corrugated projectile subjected to stationary impact at (a) 10 and (b) 50 m/s. ....	190

Figure 9.1. (a) experimental stress-strain and mean stress-strain curves and (b) energy efficiency-strain curves at $10^{-1} \text{ s}^{-1}$ .....	193
Figure 9.2. (a) velocity and (b) layer strain vs. time curves of direct impact test at 105 m/s.....	194
Figure 9.3. (a) velocity and (b) layer strain vs. time curves of direct impact test at 140 m/s.....	195
Figure 9.4. (a) velocity and (b) layer strain vs. time curves of direct impact test at 200 m/s.....	196
Figure 9.5. Layer strain vs. time curves of direct impact test at (a) 50 and (b) 75 m/s.....	198
Figure 9.6. Experimental, simulation and the r-p-p-l model predicted bar pressure-time curves. ....	199
Figure 9.7. The comparison of the numerically determined densification strain r-p-p-l model pressure-time curves with those of (a) experiment and (b) simulation.....	200
Figure 9.8. The comparison of the numerically and experimentally determined densification strain r-p-p-l model (a) velocity-time and (b) bar pressure-nominal strain curves with those of simulation. ....	201
Figure 9.9. The comparison of the numerically determined densification strain r-p-p-l model pressure-nominal strain curves with the simulation bar and proximal pressure-nominal strain curves at (a) 105, (b) 140 and (c) 200 m/s. ....	202
Figure 9.10. Bar pressure vs. time and mean pressure curves of numerical simulations (a) 25, (b) 75, (c) 140 and (d) 200 m/s and experiments of (e) 140 and (f) 200 m/s. ....	206
Figure 9.11. (a) Linear and power relation fit of numerical densification strain with velocity (b) simulation and experimental peak and mean pressure vs velocity and r-p-p-l model peak and mean pressure variation with velocity and (c) fitting simulation and peak pressures with r-p-p-l model of numerical densification strain. ....	207
Figure 9.12. (a) The experimental, numerical and r-p-p-l model arrest time and experimental and simulation final thickness of the corrugated projectile without face sheet and (b) experimental and simulation final thickness of the corrugated projectile with face sheet.....	208

Figure 9.13. Effect of number of fin layers on the pressure (a) 1 mm thick face sheets, (b) without face sheets and (c) the effect of face sheet thickness on the pressure.....	210
Figure 9.14. (a) Hugoniot shock speed vs. backing mass velocity and fitting and (b) variation of the densification strain with backing mass.....	213
Figure 9.15. (a) Hugoniot stress-backing mass velocity and (b) Hugoniot stress-strain plot and Rayleigh line for 140 m/s impact velocity. ....	215
Figure 9.16. Numeric and analytic pressure-time response impact with a backing mass at (a) 105, (b) 140 and (c) 200 m/s.....	216
Figure 9.17. Numeric and analytic residual velocities of corrugated projectiles with backing mass.....	217
Figure 10.1. High speed camera record of the monolithic composite plates loaded with corrugated projectiles; (a) 2, (b) 5 and (c) 8 mm-thick. ....	219
Figure 10.2. Projectile impact loading of sandwich structures with: (a) single layer corrugated core and (b) 3-layer corrugated cores. ....	221
Figure 10.3. The pictures of the sandwich structures after impact test: (a) single layer core, (b) 3-layer core and (c) single and 3-layer core together.....	222
Figure 10.4. Delamination zones: (a) 2 mm experimental, (b) 2 mm numerical, (c) 5 mm experimental, (d) 5 mm numerical, (e) 8 mm experimental and (f) 8 mm numerical.....	224
Figure 10.5. Delamination regions in: (a) front face, (b) back face of the sandwich structure and (c) crushed corrugated cores.....	226
Figure 10.6. Delamination regions in 3 layers core sandwich: (a) front face, (b) back face of the sandwich structure and (c) crushed corrugated cores.. ....	227
Figure 10.7. The numerical models of clamped: (a) composite plates, (b) single layer corrugated core sandwich and (c) 3-layer corrugated core sandwich structure. ....	229
Figure 10.8. Back face maximum displacement values of composite plates and sandwich structures loaded with corrugated structures having face sheets. ....	230
Figure 10.9. Back face maximum displacement values of composite plates and sandwich structures loaded with corrugated structures having no face sheets. ....	230
Figure 10.10. Projectile impact velocity vs. TNT mass. ....	232

Figure 10.11. Back face displacement of composite plates loaded by projectiles and Conwep blast loading. ....	233
Figure 10.12. Back face displacement of sandwich structures loaded by projectiles and Conwep blast loading. ....	233
Figure 10.13. Projectile impact velocity vs. corresponding TNT mass for sandwich structures. ....	234
Figure 10.14. Deformation of plates and sandwich structures loaded by projectiles at 100 m/s and its equivalent TNT blast simulations. ....	234
Figure 10.15. Analytical and numerical displacements of the composite plates loaded by projectiles with face sheets. ....	237
Figure 10.16. Analytical and numerical displacements of composite plates loaded by projectiles without face sheets. ....	237
Figure 10.17. Analytical and numerical displacements of sandwich structures loaded by projectiles with face sheets. ....	238
Figure 10.18. Analytical and numerical displacements of sandwich structures loaded by projectiles without face sheets. ....	238

# LIST OF TABLES

<b><u>Table</u></b>	<b><u>Page</u></b>
Table 3.1. Summary of experimental tests on composite samples. ....	81
Table 3.2. Summary of experimental tests on corrugated sandwich structures.....	82
Table 4.1. Summary of the numerical models on composite samples. ....	107
Table 4.2. Summary of the numerical models on composite samples. ....	108
Table 6.1. Calculated ballistic limits for 2 mm, 3 mm and 5 mm thick composite plates. ....	147
Table 6.2. Optimized MAT 162 material model parameters.....	152
Table 7.1. Determined simplified JC model parameters and failure strain of as-received and heat-treated 1050 Al alloys. ....	156
Table 8.1. Direct and stationary impact numerical simulation parameters. ....	173
Table 10.1. The parameters of the projectile (with face sheets) impact of composite plates. ....	220
Table 10.2. The parameters of the projectile (without face sheets) impact of composite plates. ....	220
Table 10.3. Numerical and experimental back face sheet displacements of the composite plates. ....	225
Table 10.4. Numerical and experimental back face sheet displacements of composite plates. ....	225
Table 10.5. Material properties of composite plates and sandwich structures. ....	236

# CHAPTER 1

## INTRODUCTION

### 1.1. Introduction

There have been more than 48000 terrorist attacks all over the world causing 107000 civilians and military personnel deaths for the last 14 years. In a single year of 2013, more than 10000 terrorist explosive incidents occurred resulting in 18000 deaths in 124 countries including Iraq, Afghanistan, Pakistan, Nigeria and Syria. The numbers clearly indicated that the terrorist attacks substantially increased at least by 180 percent over the last 14 years. In the last 30 years, the terrorist attacks ended up the loss of 35300 in Turkey. The terrorist attacks in Turkey and the wars in neighboring countries force the government to take precautions against these attacks to protect civilians and military personnel, particularly to the attacks with the use of explosives. As a result, the need for novel armors providing better protection level and lesser weight are requested as the number and intensity of the attacks increase by each year. In order to realize this, novel testing methods of armor materials and structures are of primary importance.

The common way of pre-testing real structures and military vehicle prototypes against blast is to expose them to a full-scale blast test (Figure 1.1). Although full-scale blast test gives a realistic response of a structure against blast, it requires the use of substantial amounts of explosives to reach high pressures in a short duration of loading on the structure. More importantly, blast testing requires reliable test facilities usually set far away from the residential areas. The severe testing conditions may also affect the sensors and equipment causing unusable data collections. During a blast test, the bright flash, dust cloud and debris make the visual inspection and camera recording of the tested structure difficult. It is also difficult to obtain the repetitive test results at the same conditions. Finally, the handling and transportation of the charges have to be performed carefully and the qualified labor and equipment are need for performing the blast test.



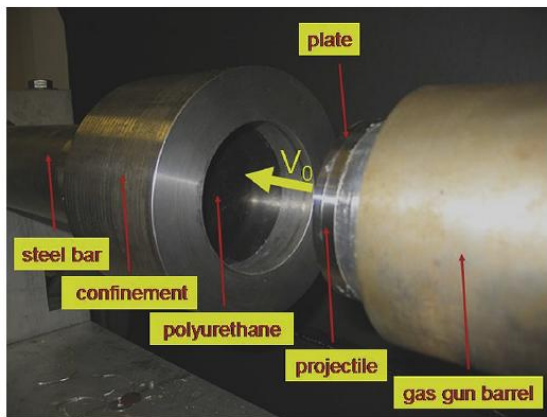
Figure 1.1. Full scale blast test of a military vehicle [1].

The safety regulations obstruct the explosive full scale blast test in university laboratories, while the blast test is a prerequisite to determine the damage caused by an explosion. Thus, non-explosive blast like test methods such as the McMillan blast test device (Figure 1.2(a)), direct pressure pulse generators (Figure 1.2(b)), shock tubes (Figure 1.2(c)), ballistic pendulums and gas gun test set-ups that fire crushable projectiles at high velocities are used to simulate the explosive blast events in laboratories [2-9]. All these tests provide repeatable and consistent pressure loading without flash and debris cloud that inhibits the high speed camera recording and heat generation and shock wave spreading out through the data collection equipment. The effective pressure can be altered by changing the impact velocities or actuating gas pressures, enabling faster testing and the rapid development and deployment of the structures to be tested. These non-explosive test systems do not require complicated data collection equipment and open test field as in the explosive blast tests. However, these tests must satisfy test pressures and impulse histories similar to those of the full-scale blast tests. The projectile must have an adiabatic compression modulus which increases with increasing compression strain to develop a stable shock front as it is observed in the stress-strain curve of a ductile foam material [10]. The pressure can be low with a long duration or high with a short duration determined by the characteristics of the chosen projectile material. Lastly, the testing method should be inexpensive, easy to conduct and time efficient to perform repetitive experimentation and enable to collect

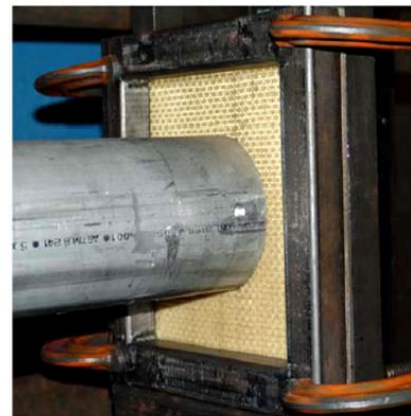
data to investigate the deflections, deformation and visual observation of the tested sample.



(a)



(b)



(c)

Figure 1.2. Non-explosive testing set-ups: (a) the McMullan blast testing device [8], (b) direct pressure pulse generator [2] and (c) shock tube [6].

## 1.2. Aim of the Study

The increasing demand for higher level of security against terrorist attacks is the major motivation for designing lightweight and high performance armors. However, the design stage of such protections involves intricate tests. Thus, novel blast-like laboratory scale tests eliminating the use of explosives can significantly reduce the time for initial design. These tests are applied prior to full-scale explosive blast tests. The focus of this thesis is to develop an adjustable, non-explosive blast-like test method using the indirect Split Hopkinson Pressure Bar (SHPB) test method. In this test, 1050 H14 aluminum trapezoidal zig-zag corrugated core sandwiches manufactured locally in a facility in İzmir were used as projectile to impose blast like pressure on the structures.

Following the determination of the pressure-time characteristics, the corrugated structure was impacted to E-glass/Polyester composite plates and corrugated core composite sandwiches. The indirect SHPB and projectile impact tests were simulated and the results were compared to validate the test results.

### **1.3. Scope of the Study**

The thesis is composed of eleven chapters. Chapter 1 is the introduction. The literature survey on polymer composites, sandwich structures, blast and shock loading of structures and simplified material models are given in Chapter 2. Chapter 2 also presents a literature survey of mechanical characterization and finite element modeling of composites and the mechanical behavior of sandwich structures with different core materials. The mechanical characterization testing programs for composites and 1050 H14 aluminum alloy are given in Chapter 3. These programs include both quasi-static and high strain rate loading to obtain material parameters for numerical modeling. The numerical model details of composite and corrugated structure are given in Chapter 4. The validation and calibration methods for MAT\_162 material model in LS-DYNA are also explained. The analytical solutions for 1D shock wave formation and propagation in corrugated structures, the Hugoniot Jump relations of the corrugated structures' shock responses, the analytical solutions of the impulsively loaded composite plates and sandwich structures using large deformations theorem are given in Chapter 5. Chapter 6 includes both testing and modeling of E-Glass composite materials. Testing and modeling of corrugated structures are given in Chapter 7. The shock loading characteristics of corrugated structures are given in Chapter 8. In Chapter 9, analytical models for impact test are given. The impact tests on clamped composite plates and sandwich structures are explained in Chapter 10. The conclusions are given in Chapter 11.

The scope of the thesis encompasses the following experimental, analytical and numerical studies

- Mechanical characterization of E-glass/Polyester composites according to the MAT\_162 material model in LS-DYNA and ASTM testing standards,
- Numerical validation of MAT\_162 material model,

- Mechanical characterization of 1050 H14 aluminum alloy according to MAT\_98 SIMPLIFIED\_JOHNSON\_COOK material model and ASTM test standard,
- Numerical validation of 1050 H14 material model parameters using quasi-static compression and Split Hopkinson Pressure Bar direct impact tests models,
- Experimental and numerical investigation of corrugated structures under confined and unconfined quasi-static deformation,
- Experimental and numerical investigation of shock formation and propagation in corrugated projectiles,
- Determination of proximal and distal end behaviors of corrugated structures under shock loading by using direct impact tests with and without backing mass and stationary impact test against mass numerical models,
- Numerical determination of effects of mesh sensitivity and imperfection sensitivity on the quasi-static and dynamic response of corrugated structures,
- Numerical determination of effects of impact velocity, face sheet thickness and the number of fin layers on the dynamic response of corrugated structures,
- Numerical determination of effects of micro inertia and shock in the compression response of corrugated structures,
- Application of rigid perfectly plastic locking material model analytical solutions to the corrugated structures,
- Verification of the shock response of corrugated structure by applying Hugoniot Jump analytic solutions and
- Numerical displacement and deformation comparison of composite plates and sandwich structures loaded by corrugated sandwich projectiles and Conwep blast function.

## CHAPTER 2

### LITERATURE SURVEY

#### 2.1. Polymer Composites

A fiber reinforced polymer composite (FRPC) is formed by the inclusion of high strength fibers in a polymer matrix [11-15]. The matrix surrounds and protects the fibers. The fiber-polymer matrix combination induces certain mechanical properties that cannot be reached by individual constituent materials. The composite form generally provides higher strength, stiffness and strength to weight ratio than the polymer matrix itself. The commonly used fibers include E-glass, S-glass, Kevlar, Twaron, and Carbon and the matrices are either thermosets such as epoxy, polyester and vinyl ester or thermoplastics such as polyetheretherketone (PEEK), polyphenylene sulfide (PPS), polyetherimide (PEI) and polypropylene (PP). The first three matrices are generally used for continuous FRPCs, while the PP resin is used in discontinuous FRPC due to its lower melting temperature [16].

The thermosets are in liquid state and cured at elevated temperatures or room temperature. The use of thermoset resins makes FRPC composite processing easy and advantageous because they are liquid at the start of the process, do not produce reactions during curing, lead to relatively low voids, pores and shrinkages and require relatively low heat and pressure [17]. Thermoset composite processing also requires relatively low cost of tooling. Thermoplastics are usually in solid form at room temperature and need to be melted to obtain the final shape. Thermoplastic composites are formed under heat and pressure and therefore the processing cycle is shorter than that of thermoset FRPCs as they do not require hardening and curing.

The mostly widely used processing methods of thermoset FRPCs are pre-preg lay-up, wet lay-up, spray-up, filament winding, pultrusion, resin transfer molding, vacuum assisted resin transfer molding, Seemann composite resin infusion molding, structural reaction injection molding, compression molding, roll wrapping process and injection molding. The processing methods of thermoplastic FRPCs include thermoplastic tape (filament) winding, thermoplastic pultrusion, compression molding

with glass mat, hot pressing, autoclave processing, diaphragm forming and injection molding [18, 19].

## **2.2. Mechanical Characterization of Composites**

As composites are nonhomogeneous and anisotropic, various types and combinations of the tests are employed to determine physical and mechanical properties. The particular mechanical properties are determined for the three different axes at quasi-static and high strain rates. The quasi-static tests including tension, compression and shear are carried at the strain rates between  $10^{-4}$  and  $10^{-1} \text{ s}^{-1}$ . In general, the strain rate levels higher than  $10^2 \text{ s}^{-1}$  are regarded as high strain rate and happen easily in impulsive loading. The high strain rate compression and tension behavior of composites can be conveniently determined using a compression or tension type SHPB test system.

### **2.2.1. Quasi-Static Testing**

The American Society of Testing and Materials (ASTM) published testing standards to characterize the composite laminates including tension (ASTM D 3039), compression (ASTM D 3410), shear (ASTM D3518), flexural (ASTM D 7264), off-axis tensile, through thickness tension and compression (ASTM D 7291) and curved beam (ASTM D 6415). The tensile and compressive strengths in in-plane and through thickness directions, the elastic modulus in in-plane and through thickness directions, Poisson's ratio in in-plane and through thickness directions and shear strength and shear modulus are determined at quasi-static strain rates using universal test machines; examples are found in refs. [20-30].

### **2.2.2. High Strain Rate Testing**

The dynamic properties of fiber-reinforced composites have been extensively investigated using SHPB. The SHPB testing of materials was originally developed by Kolsky in 1949 [31]. The schematic of a compression type SHPB test set-up is shown in Figure 2.1. The set-up consists of three parts as depicted in the same figure: loading

device, bar components, and data acquisition and recording system. Simply, the test starts with firing striker bar to the end of the incident bar by releasing the compressed gas in a gas gun. The velocity of the striker bar just prior to impact to the incident bar end is measured by a velocity measuring device mounted on the gas gun barrel. The striker bar velocity is changed by altering the gas pressure in the gas gun. The length of the striker bar determines the loading duration (incident time window) of the elastic stress wave developed on the incident bar. The bars are usually made from the same material with the same diameters. The bars are carefully aligned to the bar long axis in order to prevent stress wave dispersion and can be moved easily on the supports without any restriction to satisfy 1D wave propagation. The SHPB data reduction equations are based on 1D elastic wave propagation in long bars. The compressive wave imposed to the bars must be among the materials of high strength to avoid plastic deformation. The test specimen is sandwiched between the incident and transmitter bars. The data are collected from the strain gages installed on the surfaces of the bars. The signals from the strain gages are conditioned using Wheatstone Bridge and a signal conditioner amplifies the small voltage outputs of the Wheatstone Bridge. Then, the amplified voltage signals are recorded by an oscilloscope.

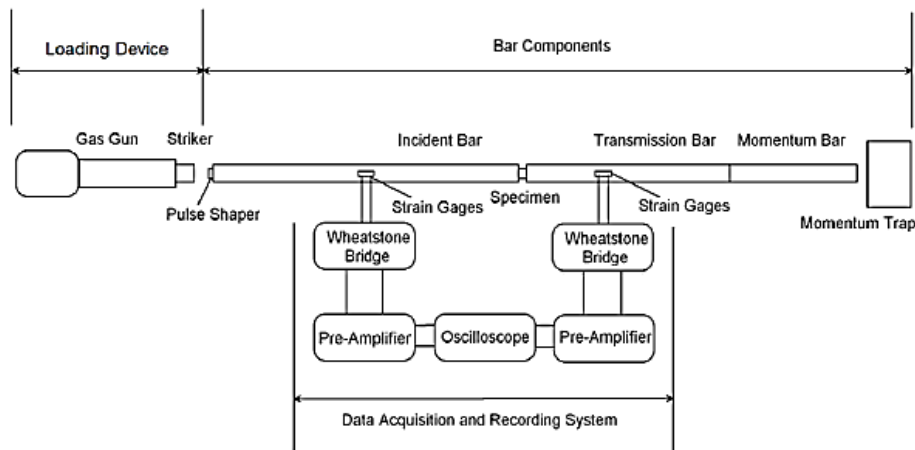


Figure 2.1. Schematic of SHPB compression test set-up [32].

The compressive wave created by the impact of the striker bar travels through the incident bar; upon reaching the specimen-incident bar interfaces, part of it is transmitted to the specimen as compression wave and the rest is reflected back to the incident bar as tension wave, unloading the compressive stress in the incident bar. The

compressive wave in the specimen is partly transmitted to the transmitter bar as compressive wave, while it is partly reflected back to specimen as tensile wave to unload the specimen at the specimen-transmitter bar interface. As the specimen used in the SHPB experiments is relatively thin, the stress equilibrium is reached quickly within few microseconds. A typical compression type SHPB recording of an E-glass/Polyester composite specimen is shown in Figure 2.2. The vertical axis in the same figure is the voltage read from the full-bridge strain gages, while the horizontal axis is the time. The incident compressive pulse and reflected tensile pulse are measured by the strain gages on the incident bar and the transmitted compressive pulse is measured by the strain gages on the transmitter bar. As the strain gages are mounted at equal distances from the specimen bar interfaces on the incident and transmitter bars, the voltage recordings of reflected and transmitted waves start from the same point in the time axis (the time elapsed by the propagation of wave along the length of the sample results in a short delay in transmitted wave).

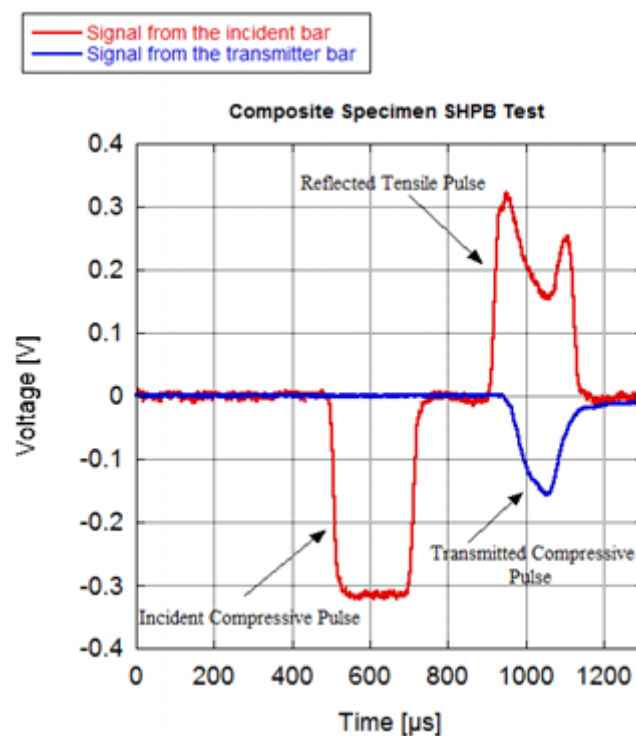


Figure 2.2. A typical record of compression SHPB test.

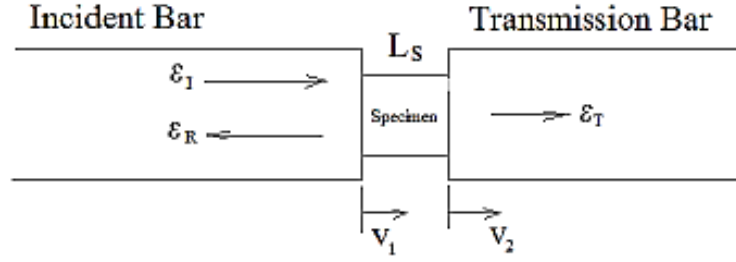


Figure 2.3. Particle velocities and incident, reflected and transmitted strains.

The particle velocities at both interfaces (Figure 2.3;  $V_1$  and  $V_2$ ), by assuming 1D stress wave propagates through the bars without any dispersion, are written as,

$$V_1 = C_0(\epsilon_I - \epsilon_R) \quad (2.1)$$

$$V_2 = C_0\epsilon_T \quad (2.2)$$

where  $I$ ,  $R$  and  $T$  represent the incident, reflected and transmitted waves, respectively.

The strain rate in terms of strains is

$$\frac{d\epsilon(t)}{dt} = \frac{C_0}{L} [\epsilon_I(t) - \epsilon_R(t) - \epsilon_T(t)] \quad (2.3)$$

where,  $C_0$  is the longitudinal wave velocity of the bar and  $L$  is the initial length of the specimen. The above equation is simplified using the  $\epsilon_I(t) + \epsilon_R(t) = \epsilon_T(t)$  equation as

$$\frac{d\epsilon}{dt} = -\frac{2C_0\epsilon_R}{L} \quad (2.4)$$

The integration of Eqn. 2.4 gives the specimen strain

$$\epsilon_S(t) = \frac{-2C_0}{L_S} \int \epsilon_R(t) dt \quad (2.5)$$

The stress on the specimen is calculated using the following equation

$$\sigma(t) = \frac{d_b^2}{d_s^2} \varepsilon_T(t) E_B \quad (2.6)$$

where,  $d_b$  and  $d_s$  are the bar and the specimen diameter, respectively and  $E_B$  is the elastic modulus of the bar. The SHPB test can be applied to any material that has a yield strength lower than that of the bar material. The fact that the SHPB test uses non-standard specimen sizes and geometries arises question about the validity of the tests.

Up till now, there have been significant number of experimental and numerical studies on the high strain rate behavior of FRPCs, which makes it impossible to cite every work in the literature. Therefore, the literature review was only given for the selected studies. The effects of length to diameter (L/D, aspect) ratio on the high strain rate response of a carbon/epoxy and graphite epoxy composite in in-plane and through thickness directions were investigated by Woldesenbet and Vinson [33] using cylindrical, square and rectangular samples. The strain rates varied between 300 and 1400 s<sup>-1</sup> and L/D ratios between 0.5 and 2. The major failure mode of the composite was longitudinal splitting with very little fiber buckling and kinking. It was also shown that square/rectangular samples showed the similar high strain rate responses with those of cylindrical samples. The effect of fiber orientation (0°-90°) on the dynamic stress-strain response of unidirectional glass/epoxy composite samples of the length and diameter sequentially varying between 12 and 35 mm and between 16 and 17 mm was investigated at the strain rate of 265 s<sup>-1</sup> by Kumar et al. [34]. The composite was found strain rate sensitive in all fiber orientations. The dynamic ultimate strength increased sequentially almost 100%, 80% and 45% for 0°, 10° and the other fiber orientations. The failure mode was tensile splitting in 0° orientation, shear fracture in 10°, 30° and 45° orientation and matrix fracture in 60° and 90° orientation. The tensile strain rate sensitivity of a IM7/977-2 Carbon/Epoxy composite of 10°, 45°, 90° and [±45°]<sub>s</sub> fiber orientations at the strain rates of 1 s<sup>-1</sup>, 400-600 s<sup>-1</sup> and 10<sup>-5</sup> s<sup>-1</sup> was investigated by Gilat et al. [35]. The increasing strain rates increased the stiffness. Although, a small increase in the maximum stress with increasing strain rate was found in 10° and 90° orientation, a significant effect of the strain rate on the maximum stress was determined for 45° and [±45°]<sub>s</sub> specimens. The strain rate sensitivity of S-2 glass/SC-15 epoxy composite through thickness direction was determined between 10<sup>-4</sup> and 1100 s<sup>-1</sup> by Güden et al. [36]. The elastic modulus and failure strength increased with increasing strain rate. The

matrix shear failure mode (Figure 2.4) remained the same at increasing strain rates in the through thickness direction. The other studies on the dynamic response of FRPCs including the refs. [36-54] also clearly indicate that the failure strengths of the FRPCs increase with increasing strain rate and the deformation modes change with loading directions and strain rate.

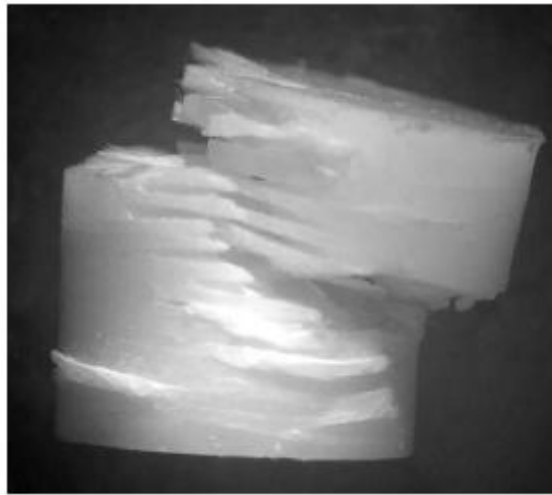


Figure 2.4. A fractured composite sample tested at  $1100 \text{ s}^{-1}$  [36].

### **2.3. Finite Element Modeling**

Finite element (FE) analysis is a method of solving complicated structural problems and geometries by subdividing the mathematical model into disjoint (non-overlapping) components of simple geometry called finite elements [37]. There are two types of solution methods: implicit and explicit. The implicit finite element method uses larger time steps since it is unconditionally stable. The equilibrium is satisfied by the iteration and involves the assembly and solution of a system of equations. The computational time per load step is relatively high. The implicit solutions are applied to linear, static and quasi-static loading conditions. ABAQUS, ANSYS and NASTRAN are among the mostly widely used commercial implicit finite element codes. The explicit finite element method however uses smaller time steps since it is conditionally stable; the time step for the solution has to be less than a certain critical time step and depends on the smallest element size and the material properties. There are no matrix solution and iterations in the explicit method; thus, the computational time per load step is relatively short. The explicit solution method are used in non-linear dynamic, impact

and blast problems. ABAQUS, LS-DYNA, PAM-CRASH and RADIOSS are among the most widely used explicit finite element codes.

The LS-DYNA material models of composites include MAT\_ENHANCED\_COMPOSITE\_DAMAGE (MAT\_054-055), MAT\_LAMINATED\_COMPOSITE\_FABRIC and COMPOSITE\_FAILURE (MAT\_058-059) and MAT\_COMPOSITE\_MSC (MAT\_162). The MAT\_054-055 material model is developed for the damage simulations in large structural orthotropic materials including unidirectional tape composite laminates. It requires minimum number of input parameters. MAT\_054 uses the Chang-Chang [38] failure criterion to determine the individual ply failure beyond the elastic region [39-48]. The MAT\_058-059 material model is developed for the plane and shell problems. The material model can also be used to model the unidirectional, laminate and woven fabric composites. The damage model is based on the Matzenmiller's damage mechanics [49] which model the damage independently in the principle directions. The details of MAT\_058 composite material model can be found in refs. [50-55]. The MAT\_162 material model is capable of modelling the progressive failure in unidirectional and woven fabric composites. The failure is based on the Hashin's failure criteria [56], five failure modes in unidirectional and seven failure modes in plain weave composites including matrix cracking, delamination, fiber tension, fiber shear, fiber compression and composite crush. The material model also determines the post damage softening behavior using continuum mechanics [49]. The strain rate sensitivity is included in the model. Both solid elements and 3D models are incorporated into the model and the model requires 32 inputs in order to fully model the damage in composite laminates.

The damage formation in plain weave S-2 glass/SC-15 epoxy composites, processed via VARTM in 1, 2, 4, 6, 11 and 22 S2 glass fabric layers, in punch shear tests at a speed of 2.54 mm/min was investigated both experimentally (Figure 2.5) and numerically using LS-DYNA MAT\_162 composite material model by Xiao et al. [57]. The initial slope of the punch shear test load-displacement curves shown in Figure 2.6 represents the initial stiffness of the specimen and the loading up to the maximum load exhibits non-linear softening, corresponding to progressive matrix cracking and crack propagation in the laminate. The plateau level of load in the same figure corresponds to the frictional sliding of the punch through the laminate and the local shear and fiber crushing accompanied by fiber bending and the progressive drop in load in the punch-shear zone represents the tensile fracture during complete punch-shear process. In order

to model the punch shear successfully, fiber tensile/shear failure modes, fiber compressive failure modes, fiber crush failure mode, fiber in-plane shear failure mode, delamination failure mode, damage progressive criterion and element erosion parameters must be defined in LS-DYNA MAT 162 material model. The properties to be calibrated are out-of-plane fiber and matrix shear strengths, SCT, SAB, SBC, and SCA, crush strength SFC, and damage parameters m. These parameters were obtained by a parametric study. It was reported that the optimized material model parameters resulted in well agreements with tests (Figure 2.7).

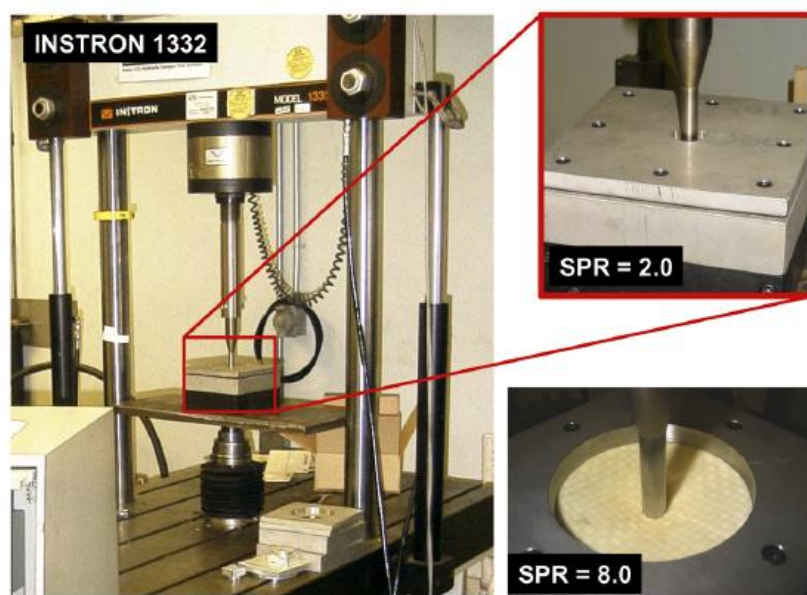


Figure 2.5. Shear punch testing system and different SPR types [57].

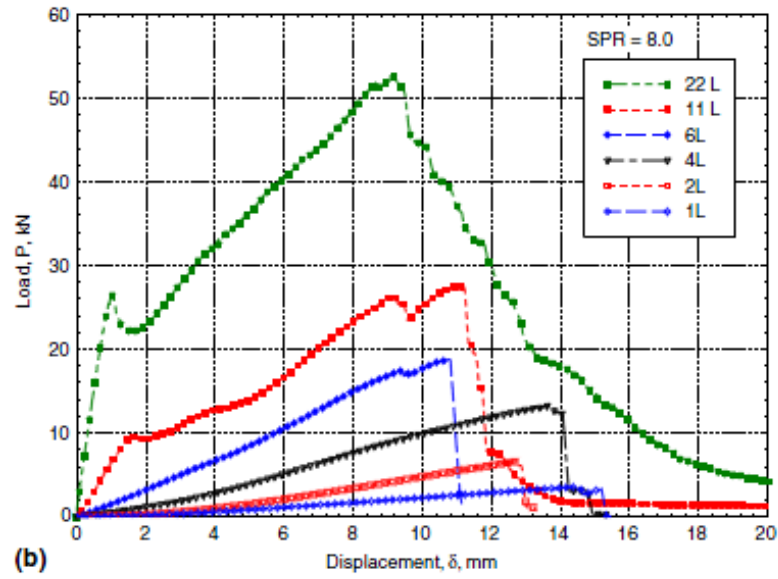


Figure 2.6. Shear punch test load-displacement curves for SPR=8 [57].

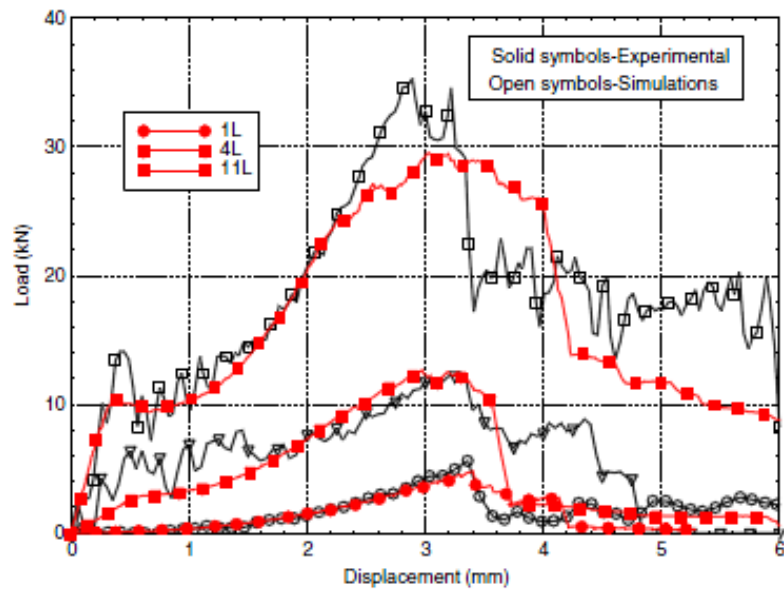


Figure 2.7. Experimental and numerical load-displacement curves of shear punch test [57].

The low velocity impact delamination damages of carbon fiber/epoxy and unidirectional graphite/epoxy prepreg composite plates were investigated using the MAT\_162 material model in LS-DYNA by Maio et al. [58]. Mesh sensitivity analysis was performed on the tensile test coupons of 20 x 10 x 2 mm. The post-peak force was found independent of the number of elements; the structural responses were almost

identical ensuring the energy dissipation regardless of mesh refinement and element topology. It was concluded that the dissipated energy in crack formation was mesh insensitive (Figure 2.8). In the simulations, a spherical impactor of 6.2 mm in radius was fired at 6.7 m/s to the clamped rectangular plates. The low values of damage parameters resulted in more ductile, while higher values more brittle material response. The high values of damage parameters extended the delamination areas. The shear strength in the through thickness and fiber plane governed the delamination extension along the major axis. The increase in the Coulomb's friction angle produced a damage reduction in the central area of the panel because it enhanced the shear resistances of the main cause of delamination onset. It was stated that it was possible to predict the delamination zone precisely with the selection of damage parameters, shear strengths and friction angles (Figure 2.9).

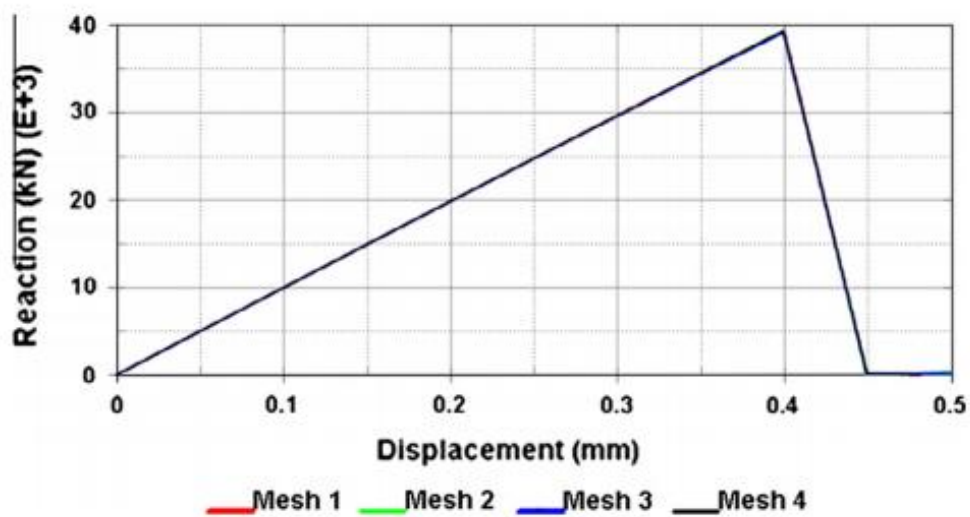


Figure 2.8. Effect of mesh refinement on the structural response [58].

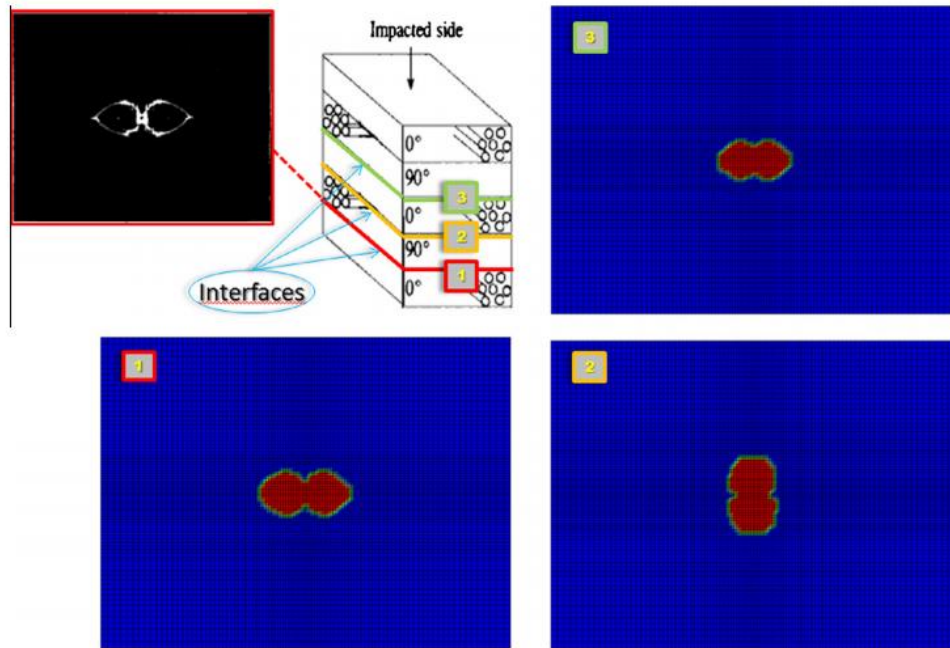


Figure 2.9. Delamination shapes of three interfaces resulting from low velocity impact simulation [58].

The high velocity multi-site impact response of laminated S2-glass/SC-15 epoxy composites was investigated both experimentally and numerically by Deka et al. [59]. A single stage gas gun was used for single, double and triple impacts at 200 m/s. The composite plates were modeled using MAT\_162 material model with the strain softening parameters of AM 1 and AM 2=0.6, AM 3=0.5 and AM 4= 0.2 after some iteration to provide the best correlation to predict energy absorption. The new surface creation was higher in the sequential impact than the simultaneously impacted composite samples (Figure 2.10). As the projectiles re-impacted the damaged regions, the progressive decrease in contact stiffness reduced the ability of the laminate to absorb energy, which resulted in an increase in exit velocity. This was noted for both sequential and simultaneous impact scenarios. The delamination constant and the damage parameters affected the delamination zones significantly.

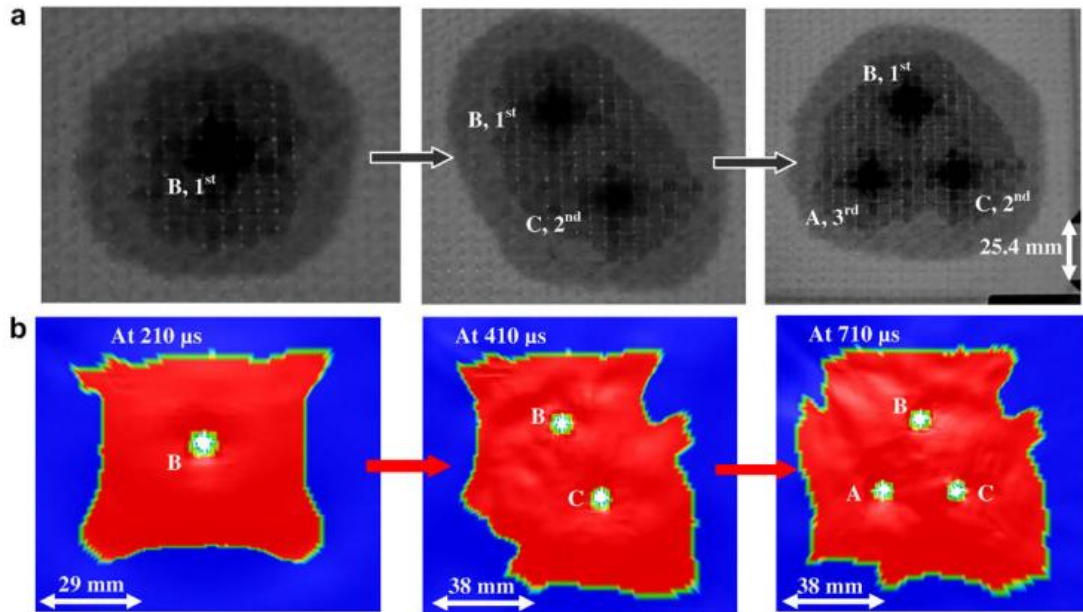


Figure 2.10. Delamination progression in three projectile sequential impact series: (a) experimental and (b) simulation at  $S_d = 5$  [59].

The MAT\_162 material model parameters of an E-glass/phenolic composite was determined by Jordan et al.[60] through parametric simulations of low velocity impact (LVI), depth of penetration (DOP), and ballistic impact tests. The modulus reduction parameter OMGMX was determined by simulating LVI tests and varying OMGMX values to find the best agreement with LVI experimental data. The limits of compressive volume strain for element eroding and the element eroding axial strain E\_LIMIT and EEXPAN were found by simulating DOP experiments and ballistic impact tests, respectively. SFS and SFC parameters were determined 160 MPa and 852 MPa, respectively. The modulus relation parameter OMGMX was determined in drop weight tests at 50 and 70 J energy levels on 4 mm-thick specimens. The simulations with OMGMX=0.994 showed the closest match to experimental results (Figures 2.11 (a-b)). The penetration erosion parameter ECRSH was determined by simulating penetration experiments. The value of ECRSH varied between 0.45 and 0.60 and excellent correlation with the experimental data was found when ECRSH value was equal to 0.55 (Figure 2.12). The penetration erosion parameters E\_LIMIT and EEXPAN were determined by simulating ballistic impact experiments in which the value of E\_LIMIT = EEXPAN ranged 3.5 to 4.5. At lower velocities, when EEXPAN = E\_LIMIT = 4.0, the simulations predicted well the experimental data and an optimized value of EEXPAN = E\_LIMIT = 4.0 was selected.

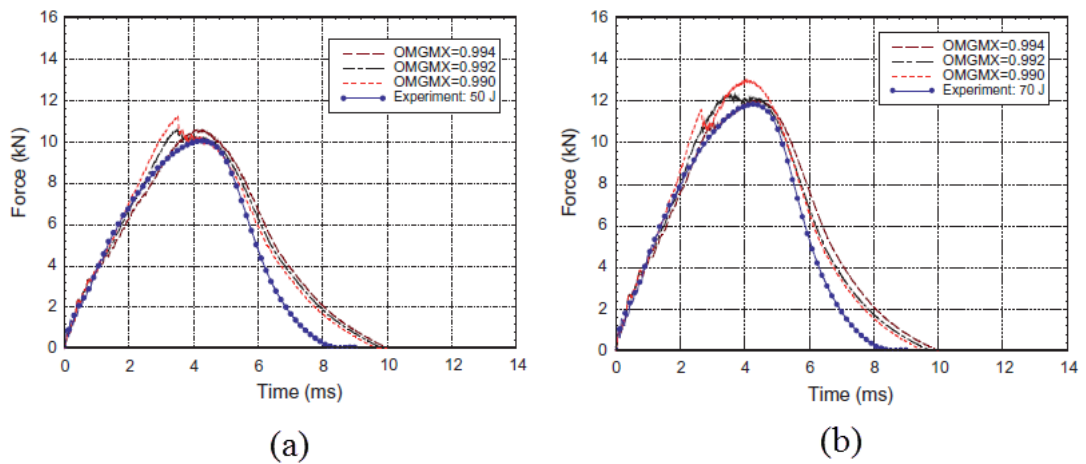


Figure 2.11. Simulated and experimental force versus time curves at (a) 50J and (b) 70J [60].

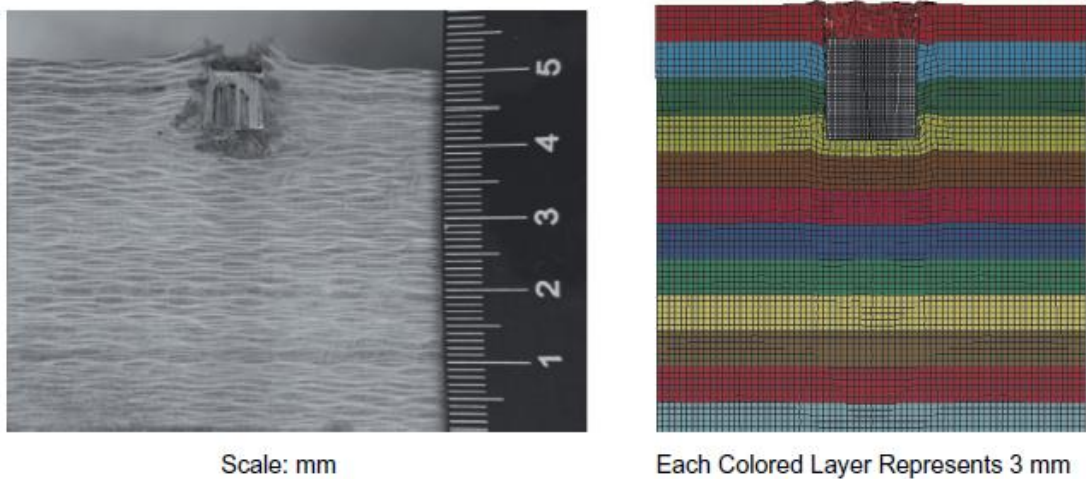


Figure 2.12. Comparison of numerical results with experimental results with RCC at  $v = 736$  m/s [60].

A ply-level material constitutive model of plain-weave composite laminates subjected to impact was developed by Yen [61]. The material model was established by generalizing the Hashin's failure criteria and the material model parameters were determined by axial tensile, transverse tensile and in-plane shear tests. The energy absorption capacity in the axial fiber direction was found significantly higher than those associated with the matrix fracture of the transverse tensile and in-plane shear loadings (Figure 2.13). The laterally constrained compression test (Figure 2.14(a)) was conducted to determine the shear strength in both unidirectional and plain weave

laminates. In this laterally constraint compression test, the fiber shear failure is resulted from transverse compressive load. A failure surface cutting through the fibers with an inclined angle in the compressive loading direction typically results from such a compression test. By loading the specimen in the through-thickness direction and constraining laterally in one direction, failure occurs on certain preferred planes which cut the fibers. By this testing method, the failure angle, punch shear strength and crush strength can be determined. The failure angle is determined after the test from the fractured sample as shown in Figure 2.14(b). Ballistic tests were performed on S2-Glass/Epoxy composite plates using 0.3 and 0.5 caliber FSP at 342 m/s velocity. The experimental and numerical damage areas showed well agreements with each other (Figure 2.15).

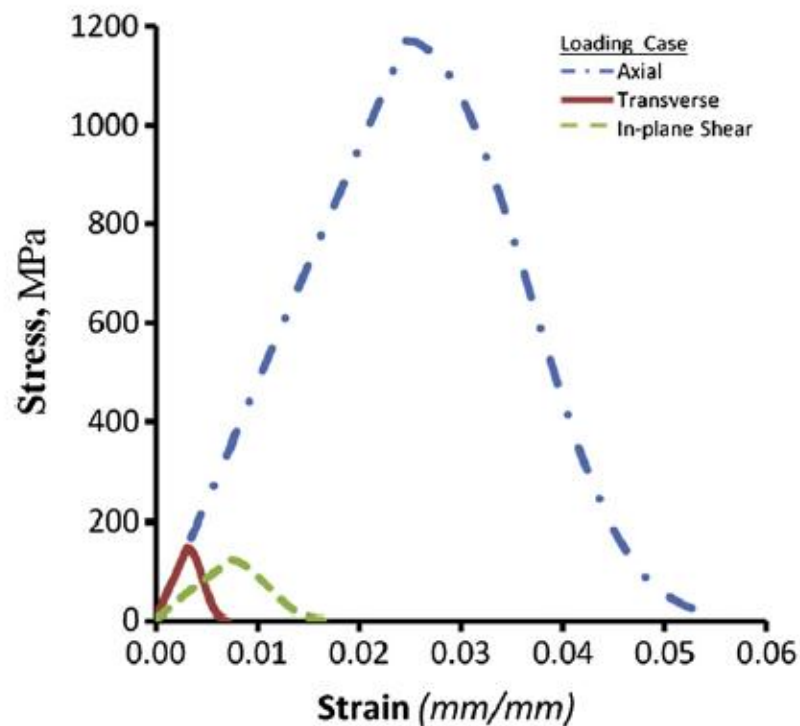


Figure 2.13. Stress-strain curves of a unidirectional layer under axial tensile, transverse tensile and in-plane shear loads [61].

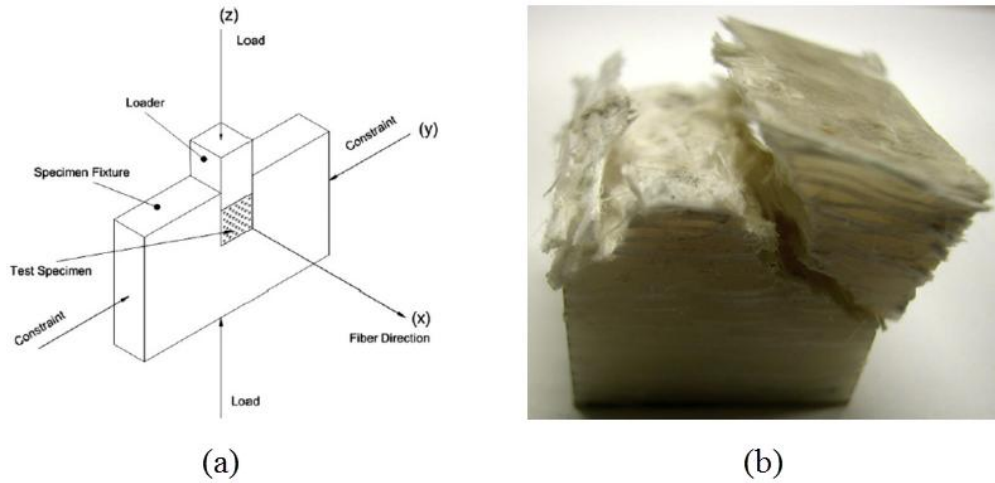


Figure 2.14. (a) Laterally constraint test fixture and (b) fractured sample after the test [61].

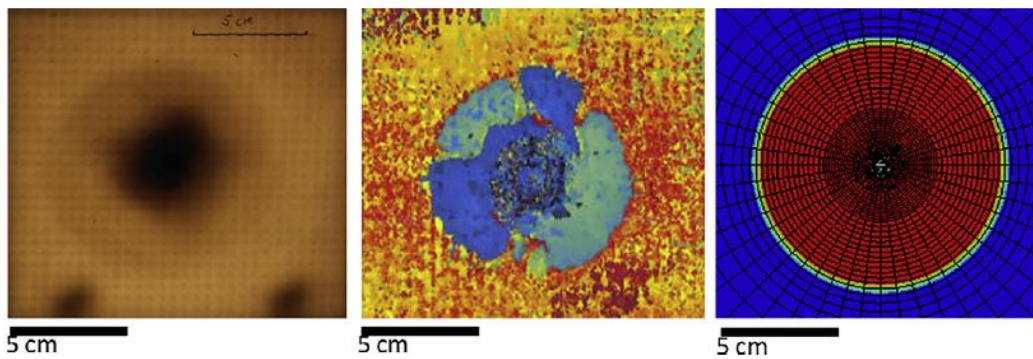


Figure 2.15. Experimental and numerical damage areas of composite materials [61].

The quasi-static and high strain rate compression behavior of an E-Glass/Polyester woven composite was investigated both experimentally and numerically by Taşdemirci et al. [62]. The quasi-static tests were conducted at  $10^{-3}$  and  $10^{-1} \text{ s}^{-1}$ , while the high strain rate tests were conducted using a CPM Rex76™ SHPB at  $\sim 900 \text{ s}^{-1}$  in all principle directions. The quasi-static elastic moduli of the composite were fitted to the strain rate dependency functions of the material model, CERATE's. MAT\_162 material model was used to model the behavior of composites in in-plane and through thickness directions. The elastic modulus and the failure strength of the composites increased at increasing strain rates (Figure 2.16). Higher strain rate sensitivity for elastic modulus was detected in the transverse direction. Excellent agreements were found

between high speed camera and simulation images of the deforming samples (Figure 2.17).

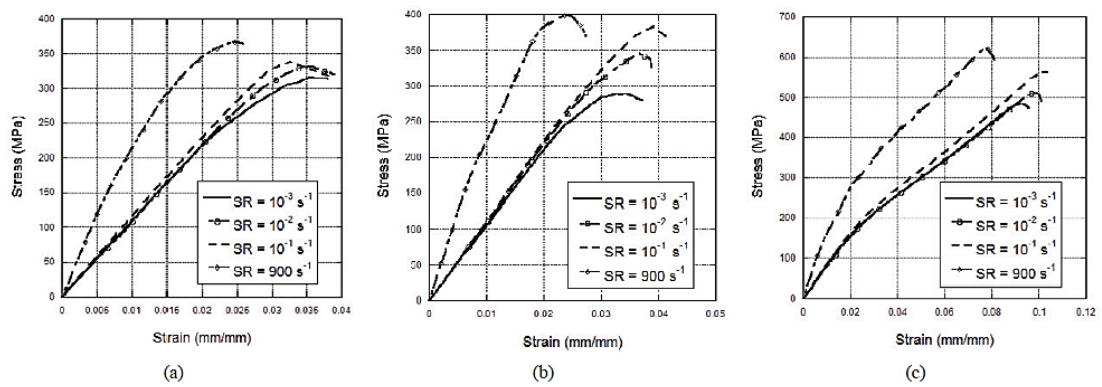


Figure 2.16. Stress-Strain curves of the composite in the (a) longitudinal, (b) transverse, and (c) through-thickness directions [62].

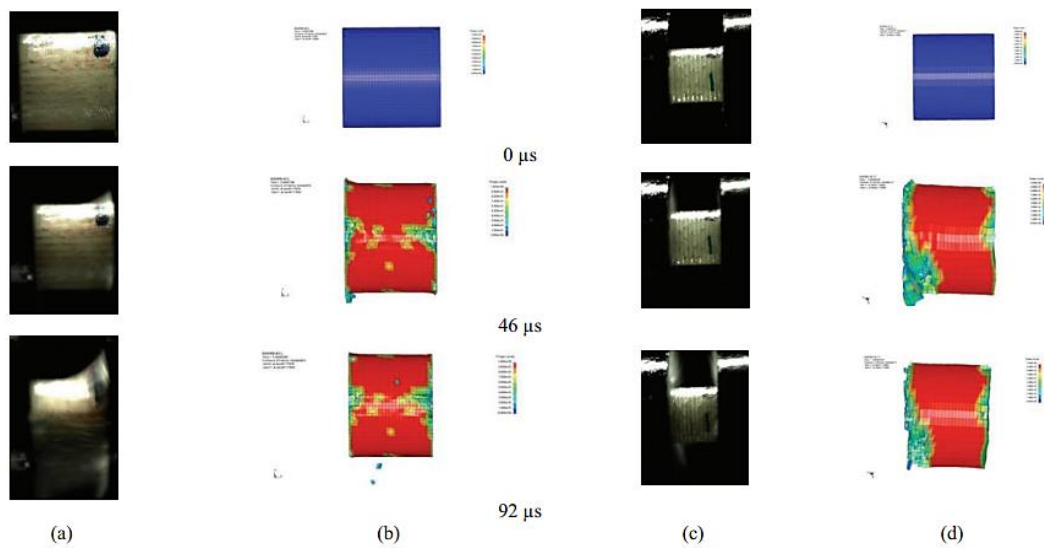


Figure 2.17. Damage sequences of composites in transverse and through thickness directions [62].

## **2.4. Sandwich Structures**

The sandwich structures consist of a pair of thin face sheet that distributes the actuating load, a thick and light weight core material that carries the load and an adhesive that transmits the shear and axial loads from face sheets to the core or from core to the face sheets. The face sheets must be thick enough to withstand the tensile and compressive loads. The core must be thick enough and have a high shear modulus to prevent overall buckling; must have enough shear strength to ensure that when bending is applied to the sandwich the faces do not slide and must have high enough modulus and compressive strength in order to prevent the local face wrinkling under compressive load. The cell size of the core must be small enough to prevent dimpling in the face sheets. The commonly used face sheets include aluminum alloys, fiber reinforced composites and steel alloys and cores aluminum foams, honeycombs and corrugated structures.

### **2.4.1. Metal Foam Cores**

The mechanical properties of metal foams depend on the base metal alloy, relative density and cell topology. The compressive stress-strain curves of metal foams compose of three consecutive regions: 1) linear elastic, 2) collapse and 3) densification (Figure 2.18). In the linear elastic region, the cell walls are subjected to bending and stretching loads. In the plateau region, the cell walls collapse plastically and experiences large amount of deformation energy absorption through cell wall buckling, crushing and tearing. Lastly, the cell walls are completely compressed at the densification strain and the stress increases sharply in the densification region [63-67].

Various techniques are implemented in the manufacturing of metal foam core sandwich structures. The metal face sheets bonding methods to core include adhesive bonding, brazing, diffusion bonding and in-situ bonding. In-situ bonding technique prevents the formation thick outer surfaces in the metal foams and is less heat sensitive than an adhesive. It can be used to manufacture heat resistant non-inflammable structures. Adhesive bonding is usually used in polymer composite face sheet sandwich structures.

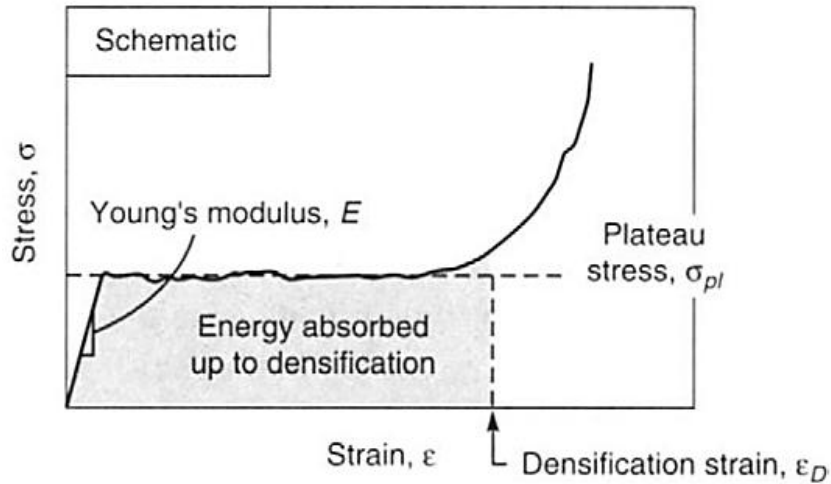


Figure 2.18. Schematic compressive stress-strain curve of a metal foam [64].

## 2.4.2. Honeycomb Cores

The light weight and high energy absorbing capacities of honeycomb cellular structures make them attractive as core materials in sandwich structures [68]. The standard honeycomb core has a uniform hexagonal structure, cell size, cell wall thickness and bulk density. The typical honeycomb cellular core materials are made of aluminum, fiberglass, aramid (NOMEX, KEVLAR, and KOREX), carbon and thermoplastic polyurethane. However, aluminum and aramid (NOMEX) are among the mostly widely used honeycomb materials in engineering applications. There are also various cell geometries; these are hexagonal, ox-core, reinforced hexagonal core, flex-core, and double flex-core and tube core (Figure 2.19). The honeycombs have anisotropic mechanical properties in three principal directions of longitudinal or ribbon (L), width or transverse to ribbon (W) and transverse or thickness (T) [69].

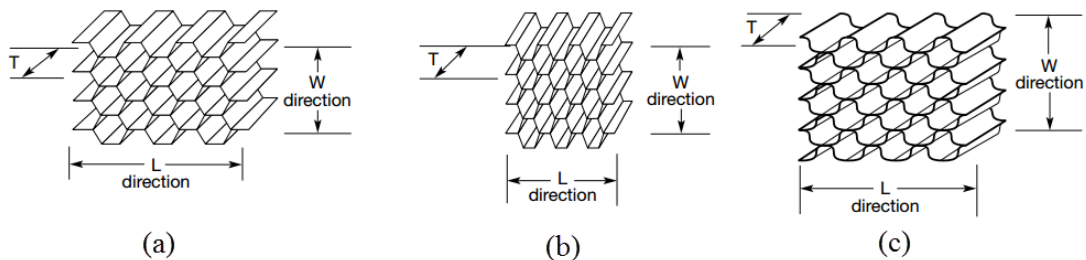


Figure 2.19. Honeycombs cell configurations: (a) hexagonal core, (b) ox-core and (c) flex-core.

The mechanical properties of the honeycombs depend on the loading direction, base material properties and cell dimensions. The mechanical response may be considered in two principle directions: through thickness and in-plane directions. In the through thickness direction, honeycombs behave very much similar to metal foams in that the uniaxial stress-strain curve is composed of three distinct deformation regions; the linear elastic, plastic buckling and densification. In aramid type honeycombs, elastic and plastic buckling of cell walls occur earlier and followed by debonding at cell interfaces and resin fracture (Figure 2.20) [70].

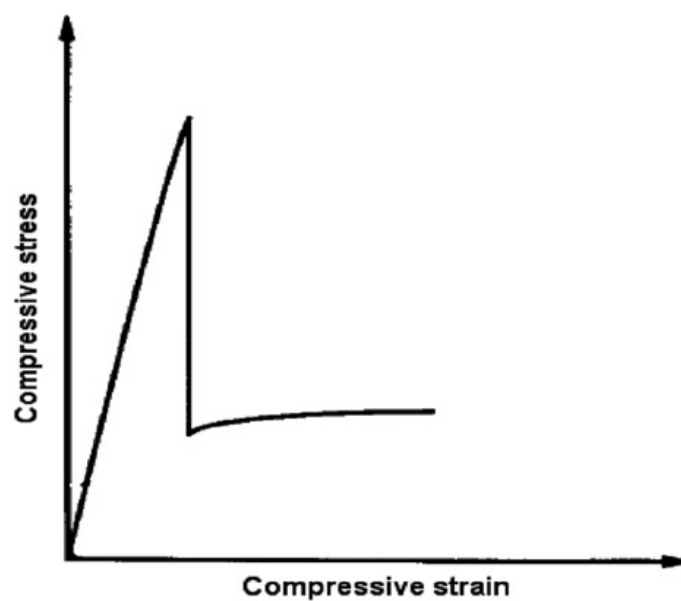


Figure 2.20. A typical compressive stress-strain curve of honeycomb cores [71].

### 2.4.3. Corrugated Cores

The corrugated cores (Figure 2.21) have been increasingly used in sandwich structures because of their easy and fast manufacturing routes. The most widely used corrugated core geometries include sinusoidal [72], trapezoidal [73, 74], triangular [75-77] and y-frame [78, 79]. The corrugated cores are manufactured from aluminum and steel alloys and fiber reinforced composites [80, 81].

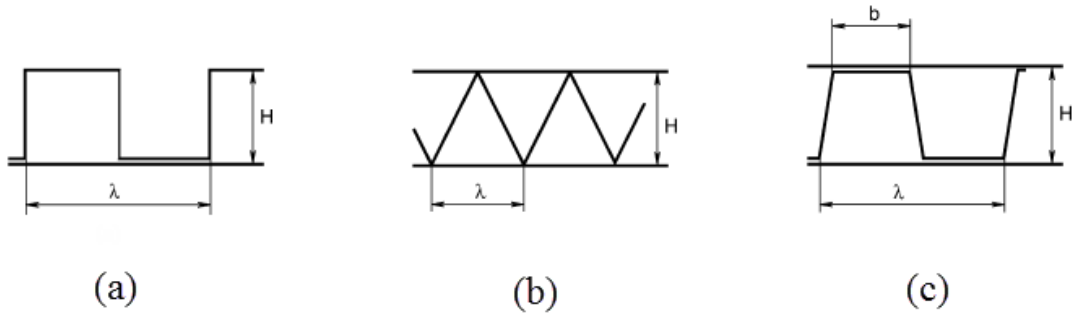


Figure 2.21. Core geometries: (a) hat-shaped, (b) triangular and (c) trapezoidal core [82].

The compression deformation of corrugated structures starts with elastic buckling of cores until about the peak stress is reached (Figure 2.22). The peak stress decreases with the partial bending of the cell walls which reduces overall bending. The deformation then continues with buckling of the walls and the loading stress decreases with the plastic hinge formation, if the corrugated structure is multi-layered. This bending and buckling deformation take place until all layers crush. Finally, the densification takes place and the loading stress increases sharply.

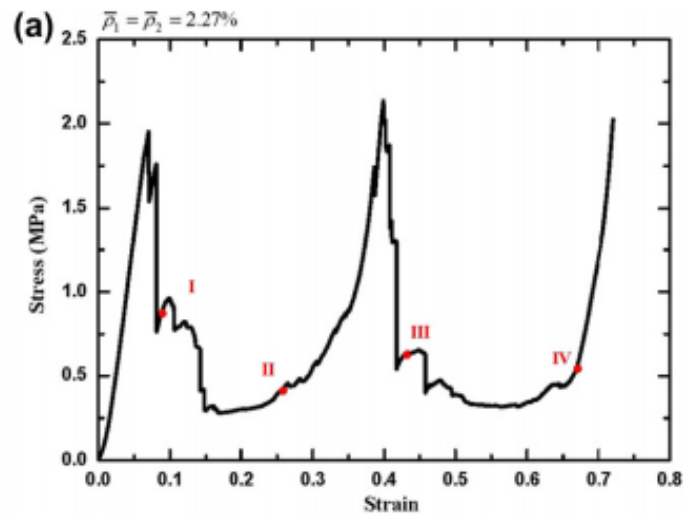


Figure 2.22. Compressive stress-strain curve of pyramidal core structures [83].

## 2.4.4. The Mechanical Responses of Corrugated Core Sandwiches

Cote et al. [84] investigated the compression and the out-of-plane and transverse and longitudinal shear responses of 304 stainless steel corrugated and diamond lattice structures of three different relative densities (0.036, 0.05 and 0.1) at the strain rate of  $10^{-4} \text{ s}^{-1}$  experimentally, numerically and analytically. The corrugated core sandwich structure had a width of 60 mm, an L/H ratio of 12 and a corrugation angle ( $\omega$ ) of  $\pi/4$  (Figure 2.23). The numerical models of the corrugated core were implemented in ABAQUS using 3D linear shell elements. The motion of the cross-head was applied uniformly to the nodes at the apex of the unit cells to simulate the compression and shear. Euler elastic buckling and Shanley plastic bifurcation stresses were simplified as ideally plastic material model in analytic models. The imperfections in the numerical models were shown to have significant effect on the compressive and shear responses of the corrugated core sandwich. When the imperfection constant was set to 0.25, the nominal and shear stresses of numerical model agreed well with those of the experiments (Figure 2.24). It was also shown in the same study that square honeycombs and pyramidal cores had higher out-of-plane compressive strengths than the corrugated and diamond core.

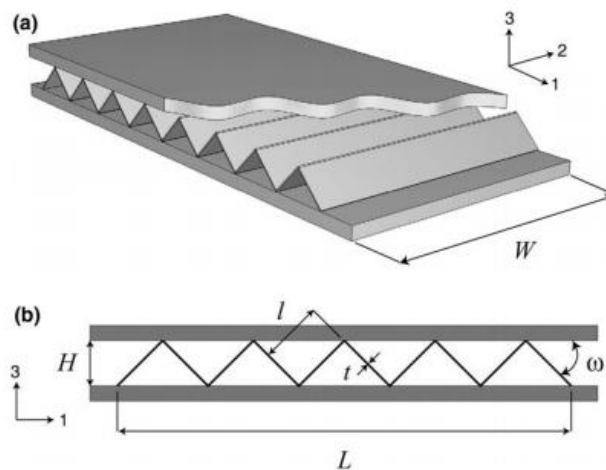


Figure 2.23. Isometric and front views of corrugated core sandwich structure [84].

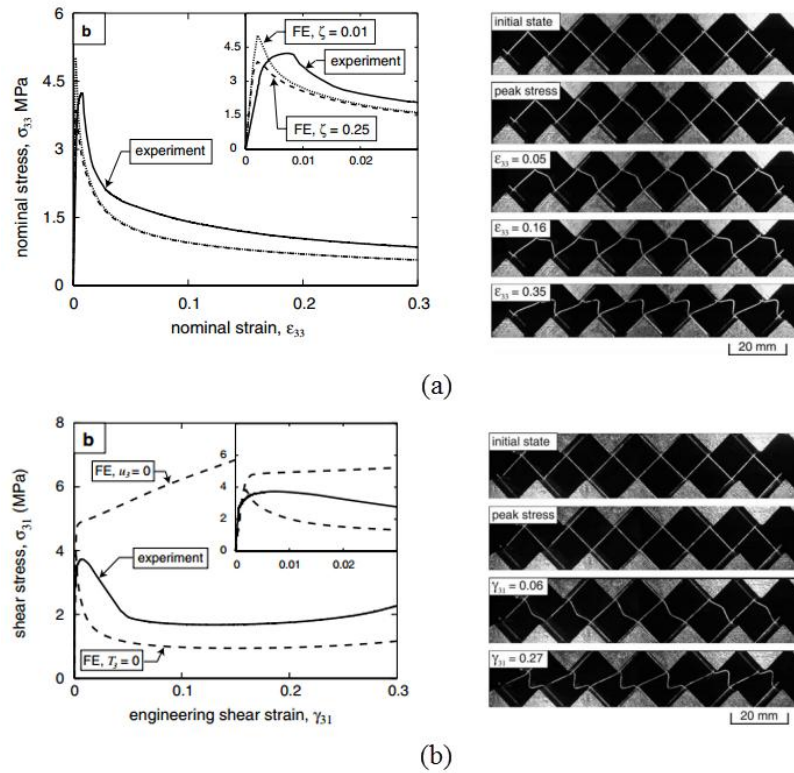


Figure 2.24. (a) The out-plane compressive response and (b) longitudinal shear response of corrugated core sandwiches [84].

Kılıçaslan et al. [85] investigated, both experimentally and numerically, the quasi-static and dynamic axial crushing responses of bonded and brazed multilayer 1050 H14 trapezoidal aluminum corrugated core sandwiches with and without interlayer sheets in  $0^\circ/0^\circ$  and  $0^\circ/90^\circ$  core orientations (Figure 2.25). The quasi-static compression tests were performed on rectangular sandwich specimens at  $10^{-3}$  and  $10^{-1} \text{ s}^{-1}$  while the dynamic compression tests at  $40 \text{ s}^{-1}$  using a drop weight tower. LS-DYNA explicit finite element code was used to simulate the quasi-static and dynamic tests. The multi-layering decreased the buckling stress and increased the densification strain. Although the deformation mechanisms of the sandwiches were shown to be similar, the bonded samples showed higher crushing stresses. The simulation and experimental results agreed well and revealed the progressive fin folding of the corrugated core layers and shearing the interlayer sheets as the main deformation modes (Figure 2.26). Furthermore, the increased buckling stress of  $0^\circ/0^\circ$  oriented core sandwiches was attributed to the micro-inertial effects which led to increased bending forces at increasing impact velocities.

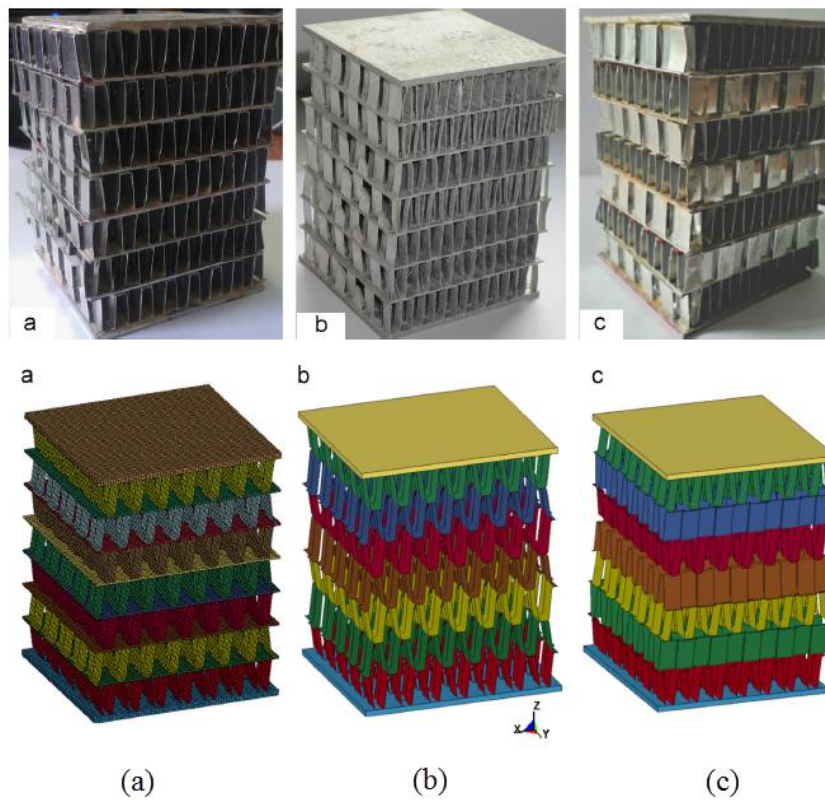


Figure 2.25. Corrugated sandwiches and numerical models of (a) bonded  $0^\circ/0^\circ$ , (b) brazed  $0^\circ/0^\circ$  and (c) bonded  $0^\circ/90^\circ$  [85].

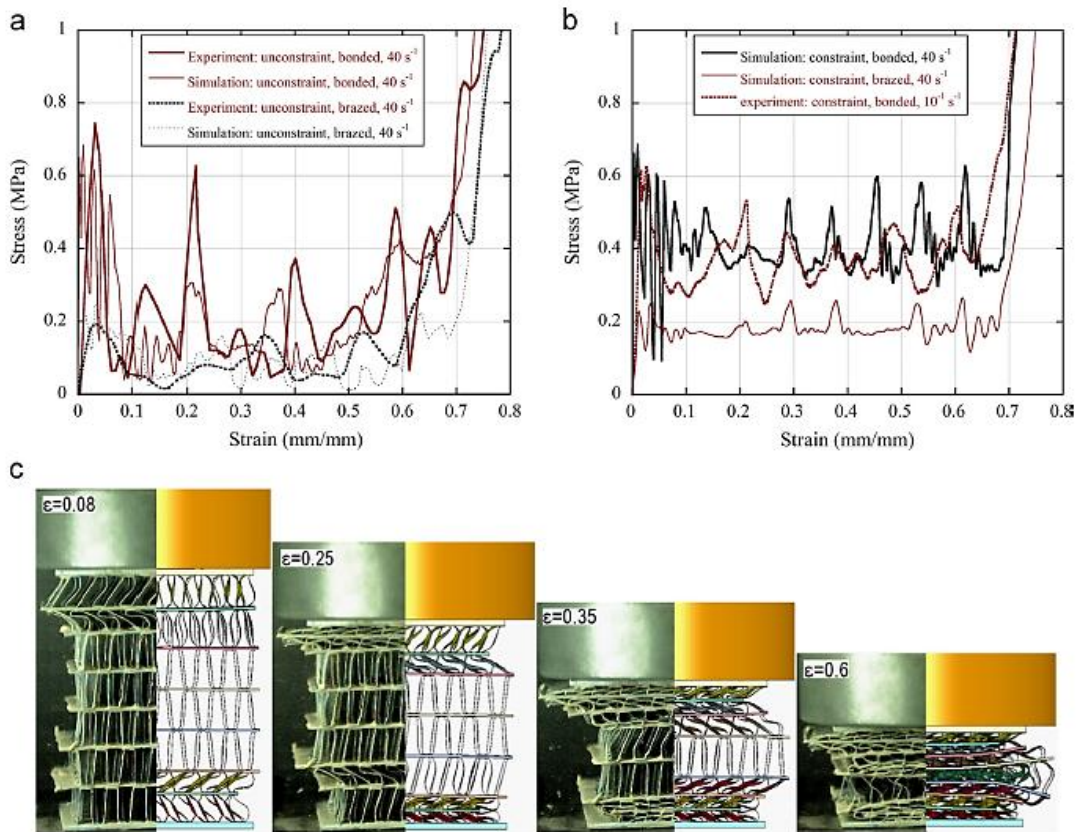


Figure 2.26. Simulation and experimental stress-strain curves multi-layer sandwiches tested at  $40 \text{ s}^{-1}$ : (a) unconstrained, (b) constraint tests and (c) the experimental and simulation deformation pictures of bonded multi-layer samples [85].

Rejab et al. [86] investigated experimentally and numerically the compression deformation of aluminum and glass and carbon fiber reinforced plastic triangular corrugated core sandwich panels (Figure 2.27). The aluminum core was modelled using hardening model and the composite Hashin's damage model. An imperfection constant varying between 0 and 0.5 was applied based on the shape of initial buckling mode using IMPERFECTION function in ABAQUS. The initial failure was dominated by the instabilities as the cell wall began to buckle. In the aluminum core, the cells deformed plastically after buckling and resulted in plastic hinge formation. In composite core, the failure occurred by fiber fracture, delamination and debonding. The numerical models showed reasonably good agreements with the experiments. The specific compressive strength of various types of corrugations and core materials were compared and it was found that thick carbon fiber reinforced plastic core offered the similar properties as the aluminum honeycombs. The composite cores outperformed conventional cores at the same densities (Figure 2.28).

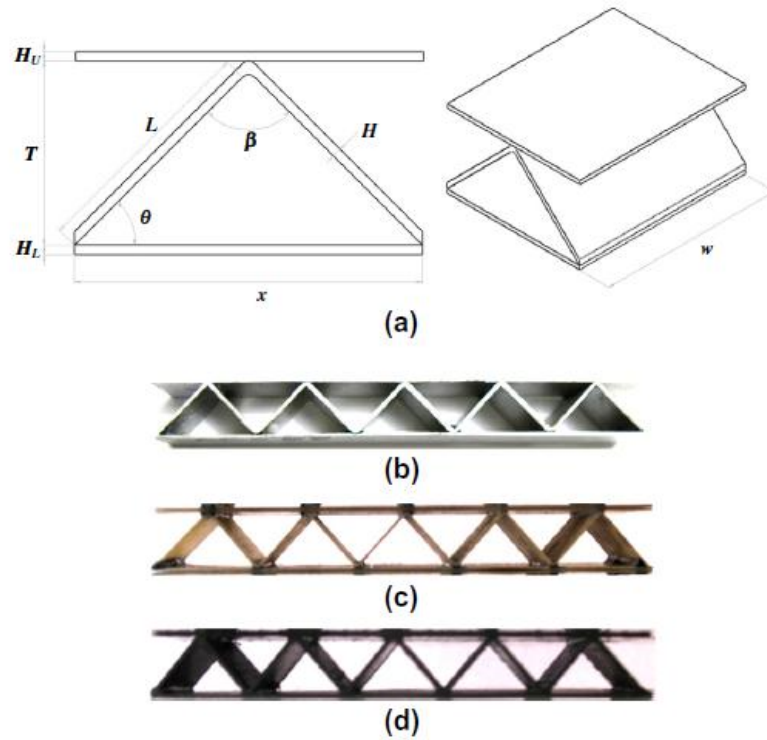


Figure 2.27. (a) Unit cell geometry of the corrugated-core sandwich panel (b) photo of an aluminum corrugation, (c) a GFRP corrugation and (d) a CFRP corrugation [86].

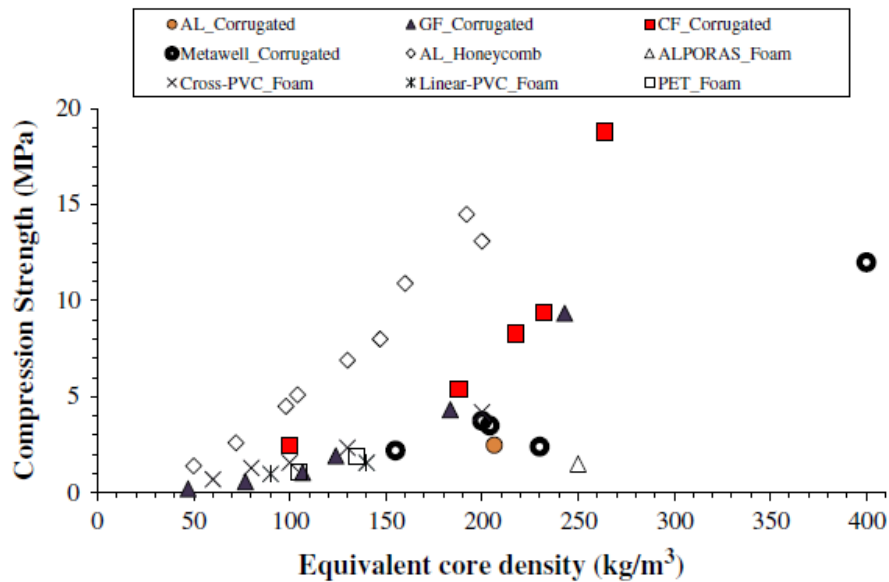


Figure 2.28. Comparison of compression strength of the corrugated cores as function of equivalent core density [86].

Jin et al. [87] studied the skin-core debonding of a woven corrugated sandwich composite in quasi-static compression, shear and three point bending tests. The skins of the sandwich were woven by two body warp and side weft yarns and the corrugated core was woven by two warp and weft yarns (Figure 2.29). Compression tests on sandwich panels were performed in out-of and in-plane directions at 0.2 mm/min. Double shear experiments in warp and weft directions were conducted in order to explore the anisotropic anti-shearing properties of the corrugated core at the same loading rate. The three point bending tests were applied to the beams of 120 mm span both in warp and weft directions and 100 mm width at 1 mm/min. The sandwich structure failed dominantly in bending mode. The gradual damage and contact behavior enabled stable plateau deformation and ductile failure mode. The shear response in warp direction was ductile and few core walls were compressed and the others were stretched due to tension. The buckling of compressed core walls decreased shear resistance of the sandwich panels. In the weft direction, the failure mode was brittle in the form of core shearing, interface debonding and inner skin delamination. The bending test in the warp direction resulted in elastic deflection, core shear failure and skin fracture. In the sheared part of the beam, thinning was observed while the rest of the core was stationary. The deflection of the bent beam was dominated by the shear failure. In the weft direction, the same failure sequence as in the warp direction was detected. However, the shear strength of the core was strong enough and indentation of the core was dominant due to the low compressive strength of the woven core in weft direction (Figure 2.30).

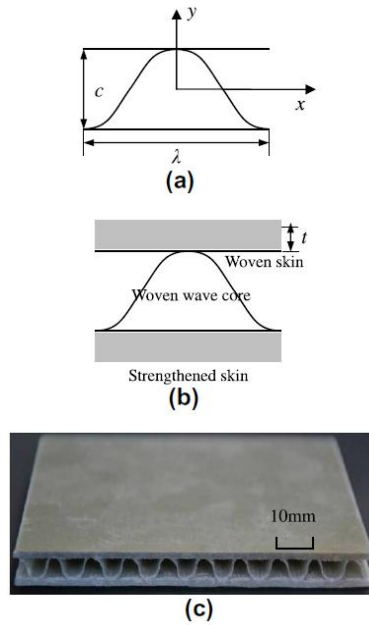


Figure 2.29. Warp structure of (a) integrated woven sandwich composite with ultra-thin sheets and wave cores, (b) sandwich panel with strengthened skins, and (c) finished sample [87].

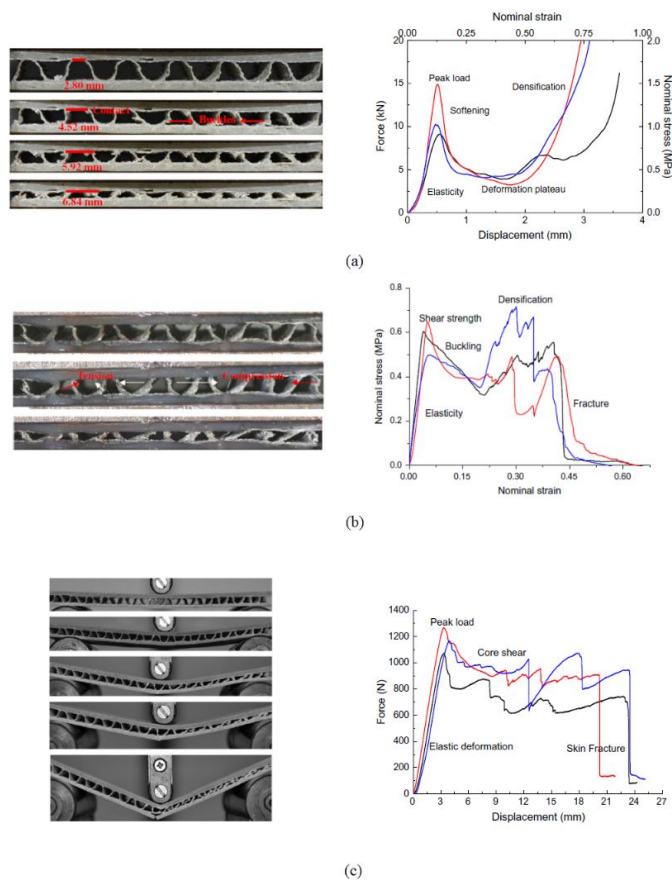


Figure 2.30. Failure modes and responses of IWWSC panel: (a) compression, (b) shear and (c) three point bending [87].

Yan et al. [88] explored the specific stiffness/strength and specific energy absorption capacity of empty triangular corrugated sandwich structures made of 304 stainless steel and closed cell aluminum foam filled triangular steel corrugated sandwich structures under three point bending tests (Figure 2.31). The quasi-static three point bending tests were performed at 0.5 mm/min in accord with ASTM C393 and ASTM D 7249 for long and short beam tests, respectively. The aluminum foam core inserts enhanced the load bearing capacity significantly. In the case of empty sandwich, the force increased linearly in the elastic region and then dropped immediately due to the face sheet wrinkling. In contrast, the foam filled sandwich exhibited both linear and non-linear deformation up to the wrinkling of the top face sheet due to local debonding which caused rapid decrease of the loading force. Furthermore, the inclusion of aluminum foam increased the loading capacity of the sandwich beam after debonding. The foam filling not only enhanced the bending stiffness and peak loading force but also changed the failure mode from elastic to plastic face wrinkling. The similar enhancements were observed for the foam filled short corrugated beams. The peak force and the plateau force increased with the stabilizing effect of the foam (Figure 2.32). Finally, the foam filling also increased the specific absorbed energy with respect to the empty corrugated beams at the same relative densities also the compressive strength and the specific energy absorption of the aluminum foam-filled corrugated core were considerably more competitive than empty corrugated, diamond and pyramidal truss cores, and comparable with the square-honeycomb core.

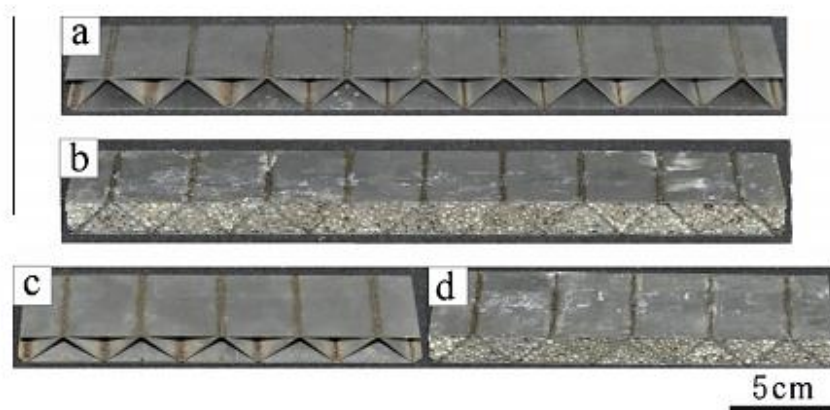


Figure 2.31. Typical as-fabricated empty and aluminum foam-filled sandwich beams with corrugated cores. Long beam: (a) empty; and (b) filled and short beam: (c) empty; and (d) filled [88].

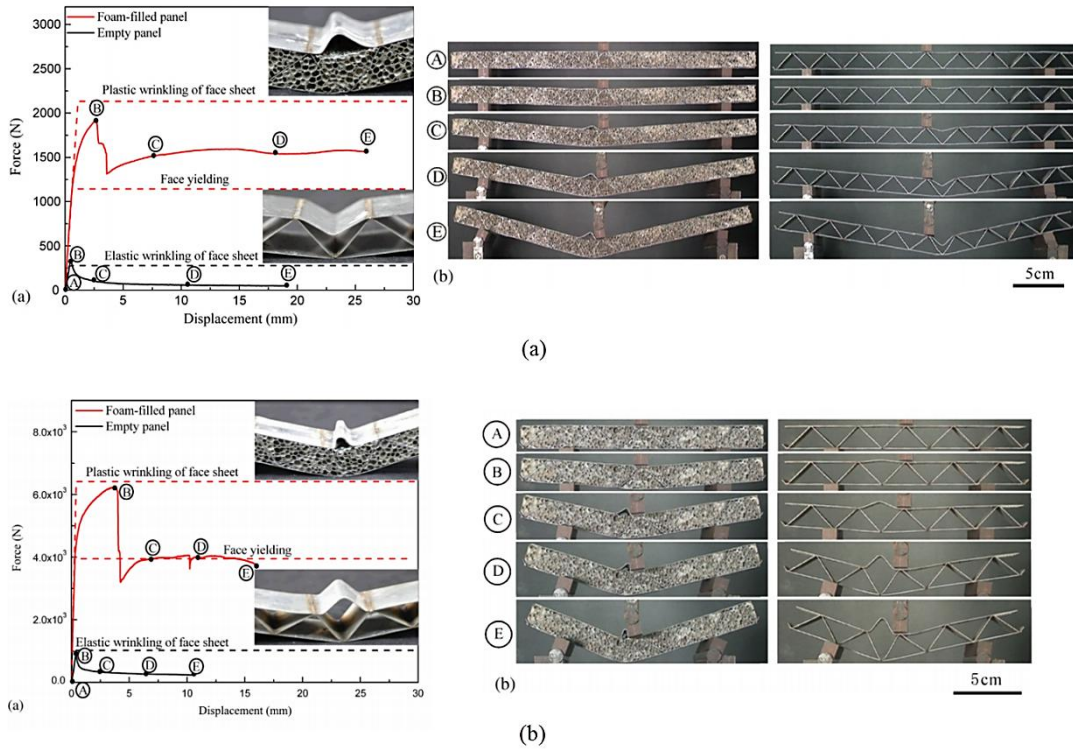


Figure 2.32. Transverse bending behavior of empty and foam filled sandwich beams with loading spans of (a) 242 mm and (b) 112 mm [88].

## 2.5. Blast and Blast-Like Loading of Plates and Sandwich Structures

Explosive blast can be defined as the rapid and sudden release of energy upon explosion. The explosive blast events can be categorized as physical, nuclear and chemical depending on the source of energy. Explosives are classified as primary or secondary based on their sensitivity to ignition. Primary explosives can easily be ignited by small distortions such as mercury fulminate and lead azide. Secondary explosives can cause more severe damage by creating shock waves on the surrounding objects such as TNT and ANFO. In explosive blast, the pressures can reach up to 300 kPa and the temperatures up to 3000-4000°C. In a typical pressure-time response of an explosive blast shown in Figure 2.33,  $t_A$  represents the arrival time of the shock wave to the structure after detonation and depends on the amount of explosive used and stand-off distance. Upon the shock wave arrives, the pressure suddenly rises to a peak pressure of  $P_{SO}$  over the ambient pressure of  $P_0$ . Then, the pressure drops from the peak to  $P_0$  in a short time, called positive phase duration,  $t_d^+$ , then to a negative pressure,  $P_{SO}^-$ , creating a vacuum for a negative phase duration,  $t_d^-$ . LS-DYNA, ABAQUS, AUTO-DYN, AIR

3D, CONWEP, ALE 3D and SHARC are the most widely used FE software in blast simulations. The fluid structure interaction and structural response are combined in the numerical analysis. In recent years, there has been a trend of creating blast-like loading experiments in the laboratories without using explosives in a safer, cheaper and more repetitive manner. The experiments are based on either launching a projectile or imposing gas pressures to the structure to satisfy the same impulse response of explosives at a lower pressure but with a higher loading duration.

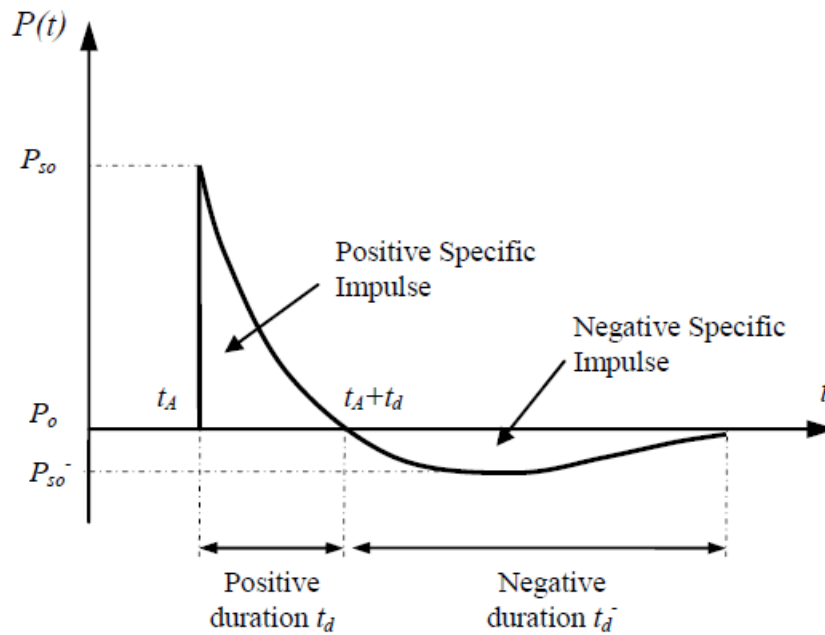


Figure 2.33. Pressure-time response of an explosive blast [89].

### 2.5.1. Blast Loading of Plates and Sandwich Structures

Fallah et al. [90] analyzed the response of ultra-high molecular weight polyethylene (UHMvPE) fiber (Dyneema) composites subjected to localized air blast experimentally and numerically. Air blast loading was generated by detonating small cylindrical charges of plastic explosive PE4 of TNT equivalence factor 1.3 in close proximity to the Dyneema test specimens. The mass of charge varied between 12 and 60 g with a constant stand-off distance of 50 mm on 300x300 mm Dyneema blast tests panels. The experiments were conducted by using a ballistic pendulum (Figure 2.34). ABAQUS finite element program was used to determine the deflections, while AUTODYN loading distribution and profile of the panels. In order to compare with Dyneema, mild armor steel and ArmoX 370T were numerically tested under the same

loading conditions with equivalent and areal masses. Dyneema panels exhibited large permanent deformation accompanied by multiple failures including delamination, shear, buckling, pulling-in and melting and fiber rupture in the front face (Figure 2.35(a)). At increasing charge masses, the buckling along the edges and inter-ply cracking due to shear movement were detected. It was shown numerically that the permanent displacement increased with increasing impulse up to rupture. The numerical simulations predicted that the mild steel had the largest plastic deformation. However, Dyneema improved the resistance to localized blast loading more than 30% and the armor steel reduced the permanent displacement around 50%. Furthermore, armor steel showed the most mass efficient solution by applying non-dimensional parameters (Figure 2.35(b)).

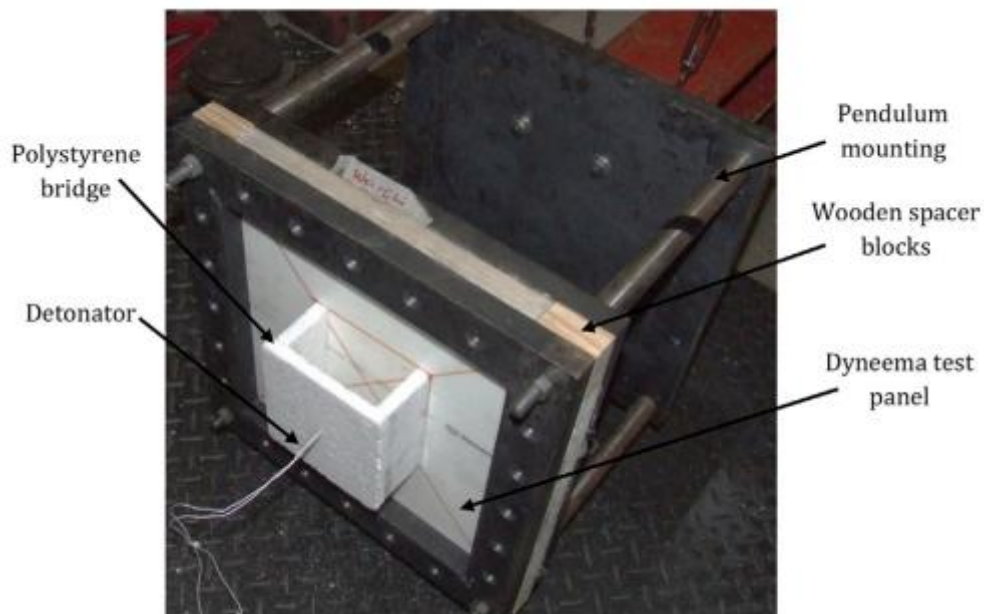


Figure 2.34. Ballistic pendulum set-up and Dyneema test specimen [90].

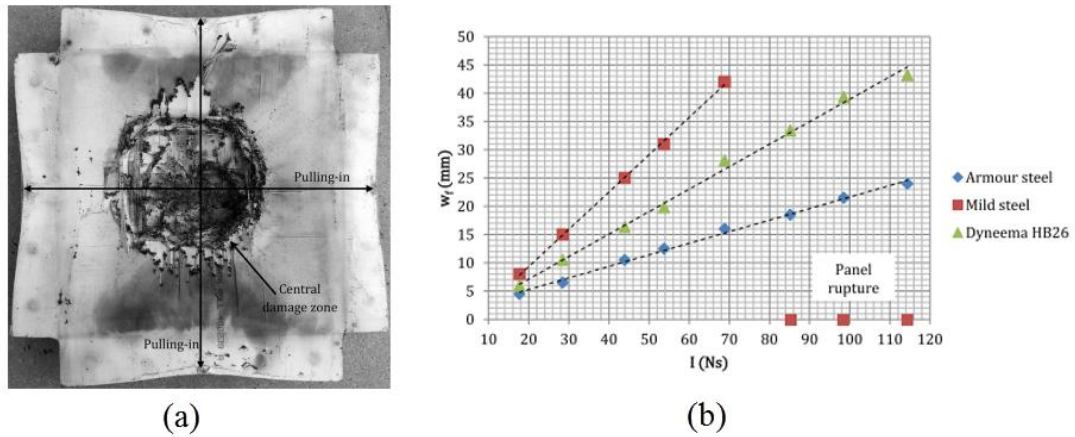


Figure 2.35. (a) Deformation modes of Dyneema and (b) comparison of permanent deflections [90].

Langdon et al. [91] investigated the blast response of fiber reinforced composite-metal laminates (FML) composing of E-glass/polypropylene composites and 2024 T3 plain aluminum alloy plates. The blast tests were conducted on 220x220 mm FML and aluminum plates using a ballistic pendulum. The blast loading was generated using a circular disk of PE4 positioned at the center of the plate on the top of polystyrene foam pad to attenuate the blast. In few tests, an explosive leader was used to produce concentrated blast loads. The permanent displacement generally increased with increasing impulse, except the aluminum-unidirectional composite-aluminum test samples. Increasing the stand-off distance decreased the permanent displacement and damaged area at the center of the panel. The woven fiber panels had symmetric centrally damaged regions of diamond shape and debonding and petalling were observed in the damaged region. In contrast, there was no symmetrical response in unidirectional fibers and petalling was observed when the  $0^\circ$  fibers fractured (Figure 2.36). It was found that the unidirectional and plain aluminum showed less permanent deflections than the woven hybrid plates.

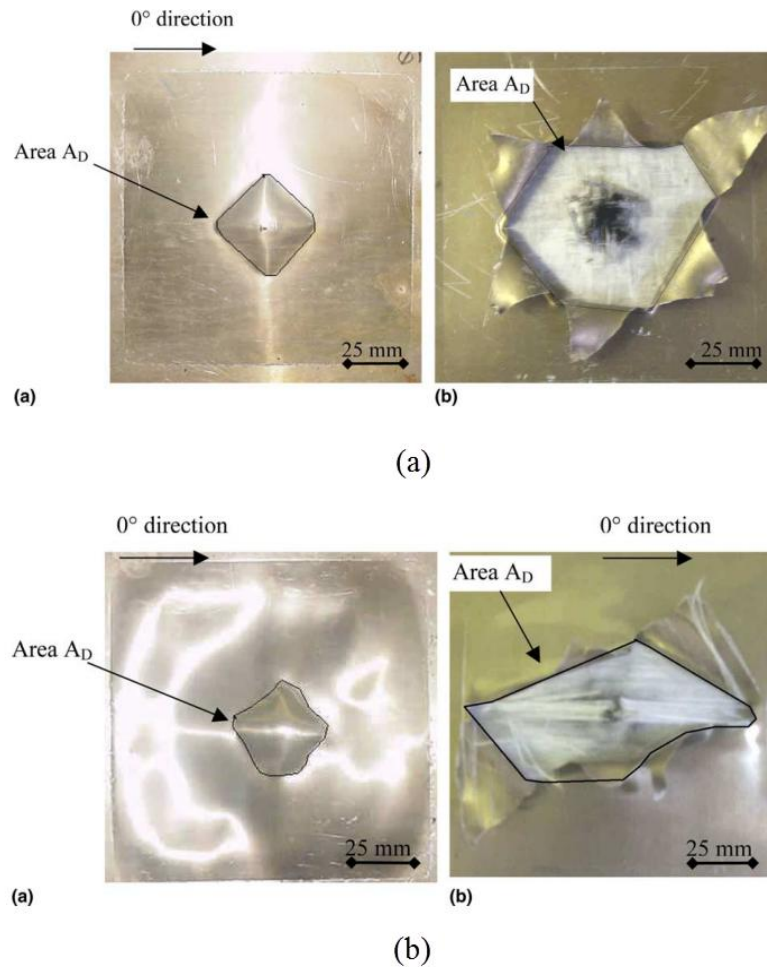


Figure 2.36. Debonded and petalled regions of (a) woven glass fiber FMLs and (b) unidirectional glass fiber FMLs [91].

Henchie et al. [92] investigated the blast response of circular Domex-700 MC steel plates subjected to uniform blast loads up to five times repeated loading experimentally and numerically. The specimen consisted of 2 mm or 3 mm thick circular plates with an exposed circular area of diameter 106 mm. In the experiments, PE4 plastic explosive with a mass range of 5 to 40 g was detonated at a constant stand-off distance of a 150 mm on the ballistic pendulum test set-up. For repeated loading, the already blast loaded plate was left in the test rig and reloaded with the same mass of explosive detonated in the same location. In the numerical simulations, the blast function code Conwep in ABAQUS finite element software was used. The numerical model consisted of the target plate and the clamps. The target plate was modeled with S4R shell elements that were 4 nodes doubly curved thin shell elements. Johnson-Cook material model without failure was used to model the target plate. The repeated blast load was indicated to start a desired time within an ABAQUS time step. This allowed

for all the repeated blasts to be loaded in a single step. It was concluded that the plate deformation was characterized by a large plastic dome. Thinning and tearing at the clamp boundaries were observed for repeated blast loadings. Furthermore, the midpoint deflection increased with increasing the number of blast loads and the charge mass. However, the difference in midpoint deflection between two blasts decreased with an increasing number of blasts due to work hardening at each step (Figure 2.37). The numerical solutions also showed good correlations with the experiments for impulse midpoint deflection and deformation profiles (Figure 2.38). Finally, the residual stresses occurred in the test plate due to blast loading inhibited the midpoint deflection of the test plate.

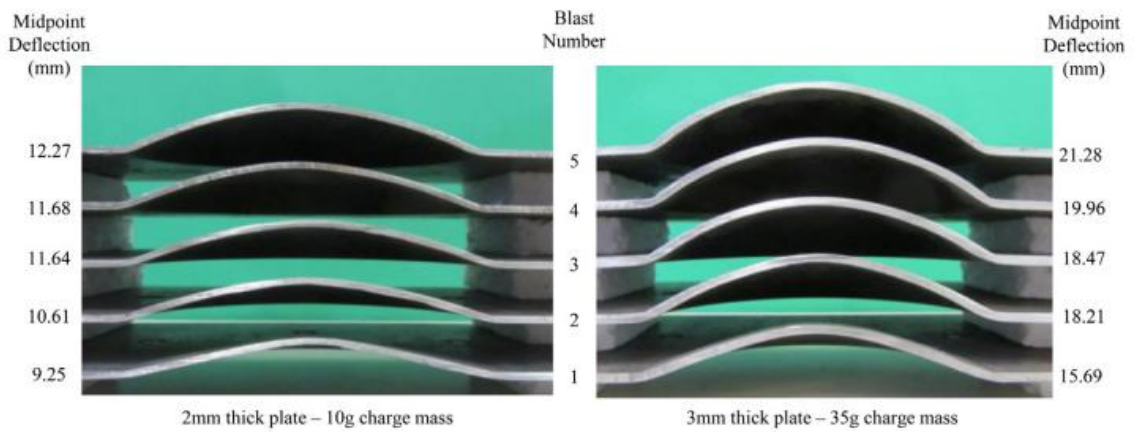


Figure 2.37. 2 mm and 3 mm thick deformed test plate profiles subjected to 10 g and 35 g charge masses [92].

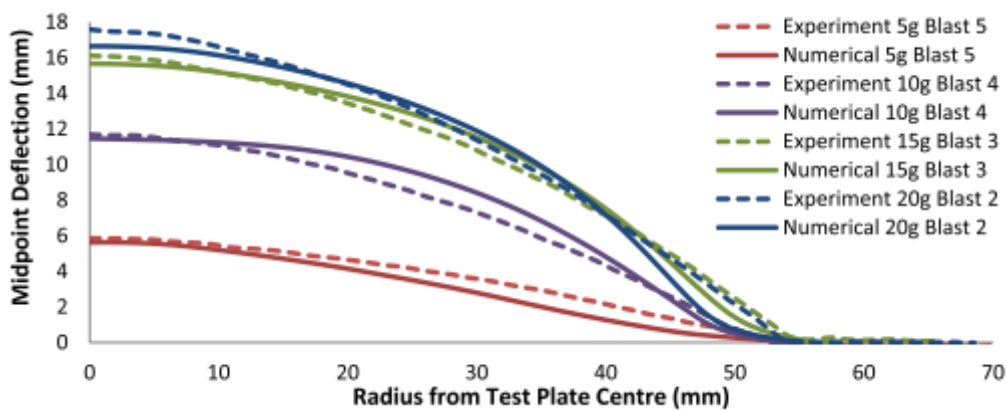


Figure 2.38. Comparison of deformed plate profiles obtained from the experiments and simulations for the 2 mm thick deformed test plates [92].

Theobald et al. [93] investigated the air-blast response of sandwich panels constructed from mild steel metallic face sheets (0.6 and 1 mm thick) and unbounded Alporas (235 kg/m<sup>3</sup>) and Cymat (440 kg/m<sup>3</sup>) aluminum foams and hexagonal honeycomb (103 and 91 kg/m<sup>3</sup>) cores. The face sheets were modelled using the Johnson-Cook material model. Fully clamped 250x250 mm sandwich panels and monolithic plates were subjected to PE4 charge masses ranging from 6 to 30 g using ballistic pendulum. The performance of Alporas foam cores showed significant improvement compared to Cymat aluminum foam core panels for 0.6 mm face sheet panels. Alporas foam core had the best performance at low intensity blasts while the honeycomb panels showed better performance at high intensity blasts. The sandwich panels with 1 mm thick face sheets showed better performance over the monolithic plates with the exception of Cymat foam core panels. The 29 mm honeycomb core panels performed better than the equivalent monolithic plate while the 13 mm honeycomb and Alporas foam core panels outperformed monolithic equivalents for impulse greater than 25 Ns. Alporas foam core performance increased with the use of thicker face sheets (Figure 2.39). The centrally loaded portion undergone significant local deformation while the outer boundaries showed negligible crushing in aluminum foam core panels while brittle failure modes were dominant in Cymat aluminum foams. Core crushing, folding of the cell walls and in-plane compression of cells close to boundaries were observed in 13 mm and 29 mm honeycomb cores (Figure 2.40). It was finally shown that 29 mm-thick honeycomb core sandwich panels had the best performance at low and high intensity blast tests.

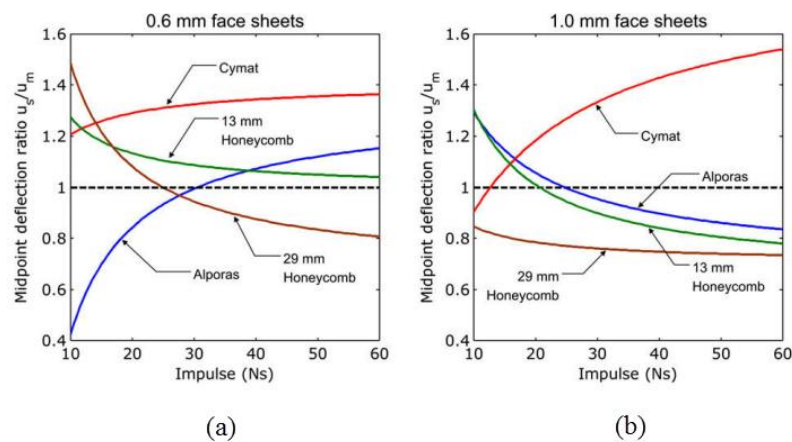


Figure 2.39. The sandwich panel and equivalent monolithic plate midpoint (back face) displacement ratio  $u_s / u_m$  for the various core materials with: (a) 0.6 mm face sheets and (b) 1.0 mm face sheets [93].

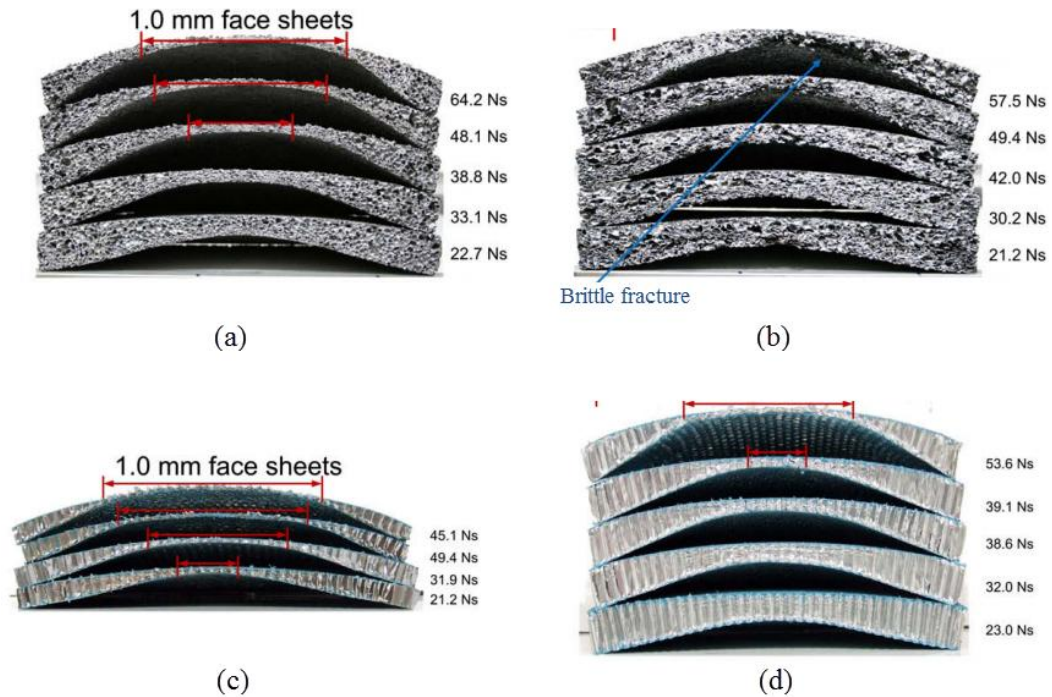


Figure 2.40. Deformed core materials: (a) Alporas foam, (b) Cymat foam, (c) 13 mm honeycomb and (d) 29 mm honeycomb [93].

Zhang et al. [94] studied the air blast response of laser welded triangular corrugated core (0.7 mm web thickness, 28 mm cell size and 14 mm core thickness) sandwich panels with 1.4 mm thick face sheets and mass equivalent solid plates made of 304 stainless steel. The blast experiments were conducted in an explosion tank with an inner diameter of 5 m and height of 7.5 m. The blast wave was generated by the detonation of a 55 g cylindrical TNT explosive with the stand-off distances of 50 mm, 100 mm and 150 mm from the top surface of the target test structures. The numerical models of the experiments were performed using quarter models to reduce the computation time in ANSYS/Autodyn explicit analysis code. Lagrangian reference frame was used to follow material movement, while Eulerian reference was used to describe the gas flow due to detonation. The face sheets, core materials and monolithic plates were modeled with Belytschko-Tsay shell elements while the surrounding air and explosive were modeled with multi-material Euler elements. TNT explosive was modeled with Jones-Wilkins-Lee model. A crack at the center with dimensions of 50x60 mm was found on the front face sheet of the sandwich structure loaded at the stand-off distance of 50 mm and the rest portion underwent a large bending deflection. At a stand-off distance of 100 mm, the core in the center remained in contact with the front face having a relatively small crack and web core folding at the center. Away from

the center, core buckling was formed due to stretching tension. At a stand-off distance of 150 mm, plastic buckling failure was found at the core webs of the panel. In solid monolithic plate, a large global dome superimposed with an inner dome was observed at 50 mm stand-off distance. At 100 mm and 150 mm stand-off distance the inner dome disappeared and only global dome was observed (Figure 2.41). The numerical model displacements and deformation modes showed good correlations with the blast experiments (Figure 2.42). The in-plane strain distribution in the numerical model indicated that the stretching deformation was evident at the center of the panel. The back face deflection was reduced with the increase of both face sheet and core web thicknesses. The increase in the thickness of front face enhanced the blast resistance of the panels.

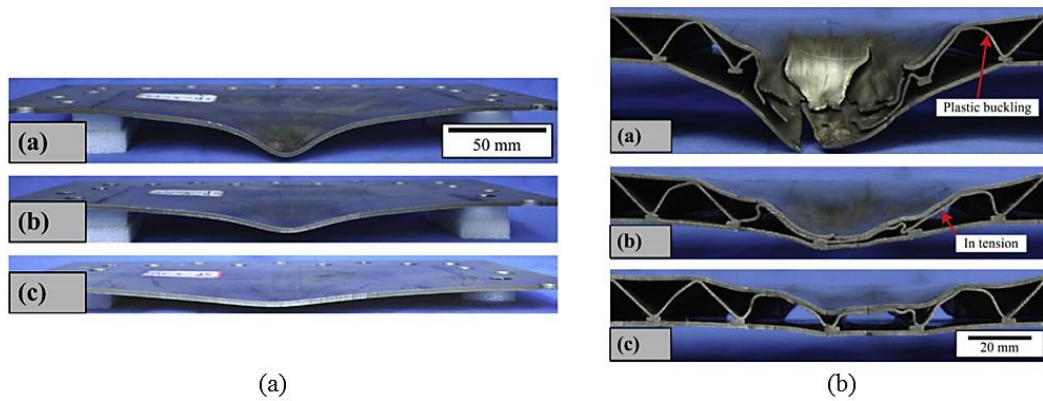


Figure 2.41. Experimentally deformed (a) monolithic solid plate and (b) corrugated core sandwich structures [94].

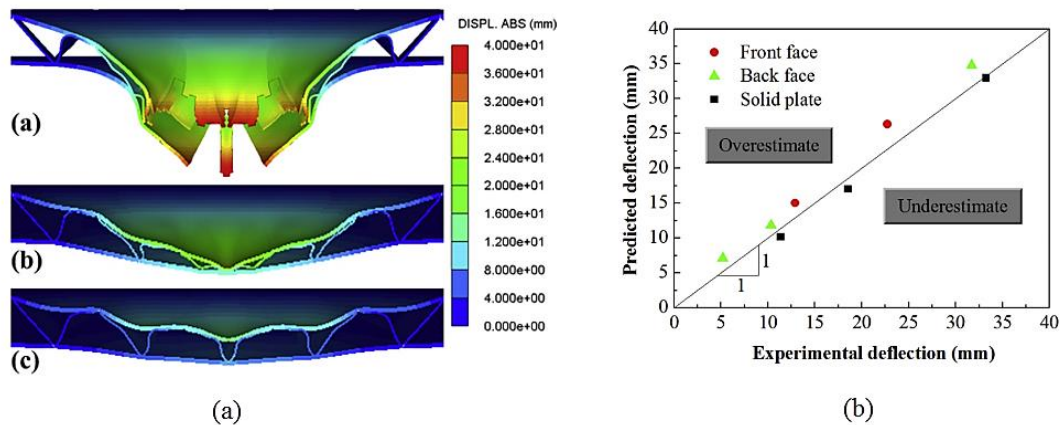


Figure 2.42. (a) numerical deformation of sandwich structures and (b) experimental and numerical deflections [94].

Wadley et al. [95] investigated the impulse response of square edge clamped triangular extruded 6061 T-6 aluminum alloy corrugated core sandwich panels and areal mass equivalent solid plates. The blast tests were conducted with wet sand test model consisting of 375 g of C4 explosive surrounded by a concentric shell of water saturated with 200  $\mu\text{m}$  diameter glass microspheres. The panels were fully edge clamped with a loading area of 406 x 406 mm at the stand-off distances of 15, 19, 22, 25 and 30 cm (Figure 2.43). The high explosive detonation was modelled using IMPETUS Afea Solver and its discrete particle based. The method worked with discrete, rigid spherical particles that transferred the forces between each other through contacts and collisions. The extruded aluminum sandwich panel was built-up from 26112 64-node 3rd-order and the frame was built-up from 2964 8-node linear hexahedra elements. A modified Johnson-Cook constitutive relation was chosen to model the target material. The fracture was modeled using Cockcroft and Latham (Figure 2.44). The maximum back face sheet deflection for sandwich panels was found to be lower than the equivalent solid plates. The global bending, localized core crushing and stretching, face sheet fracture and edge failures close to heat affected zones were detected in sandwich plates. The model showed that the local deformations resulted in increased sand reflections so this increased the impulse transferred to the concave surface regions. The numerical back face deflections and deformation modes showed well agreements with experiments (Figure 2.45).

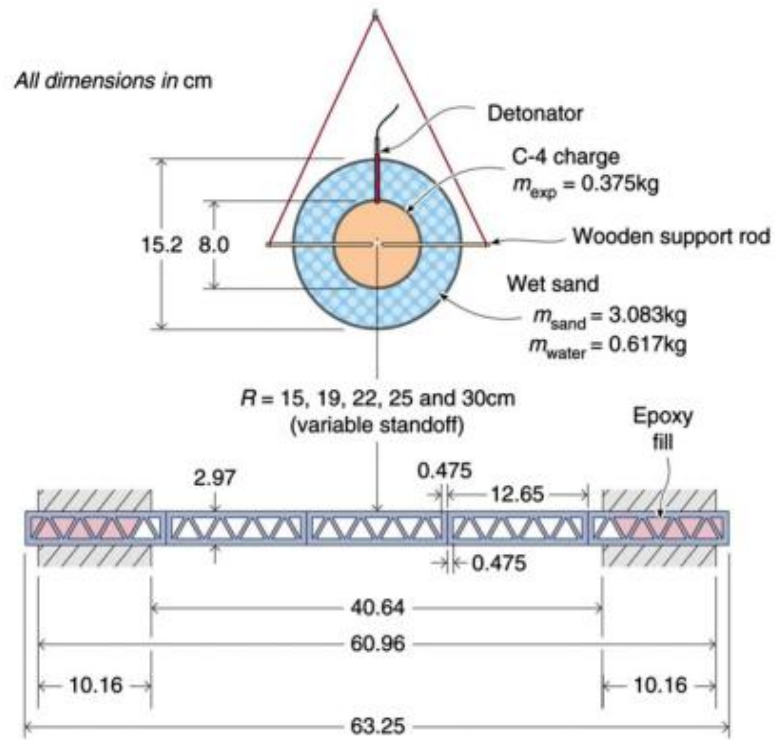


Figure 2.43. The sand impulse test geometry and dimensions of the sandwich panels [95].

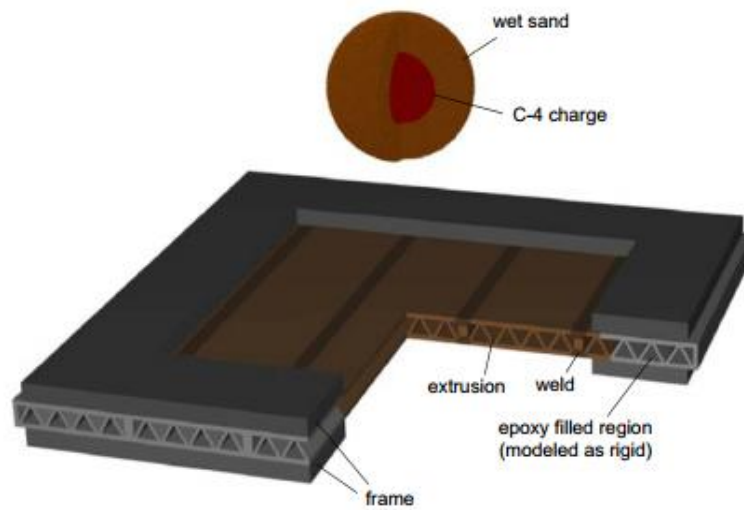


Figure 2.44. The finite element model prior to detonation [95].

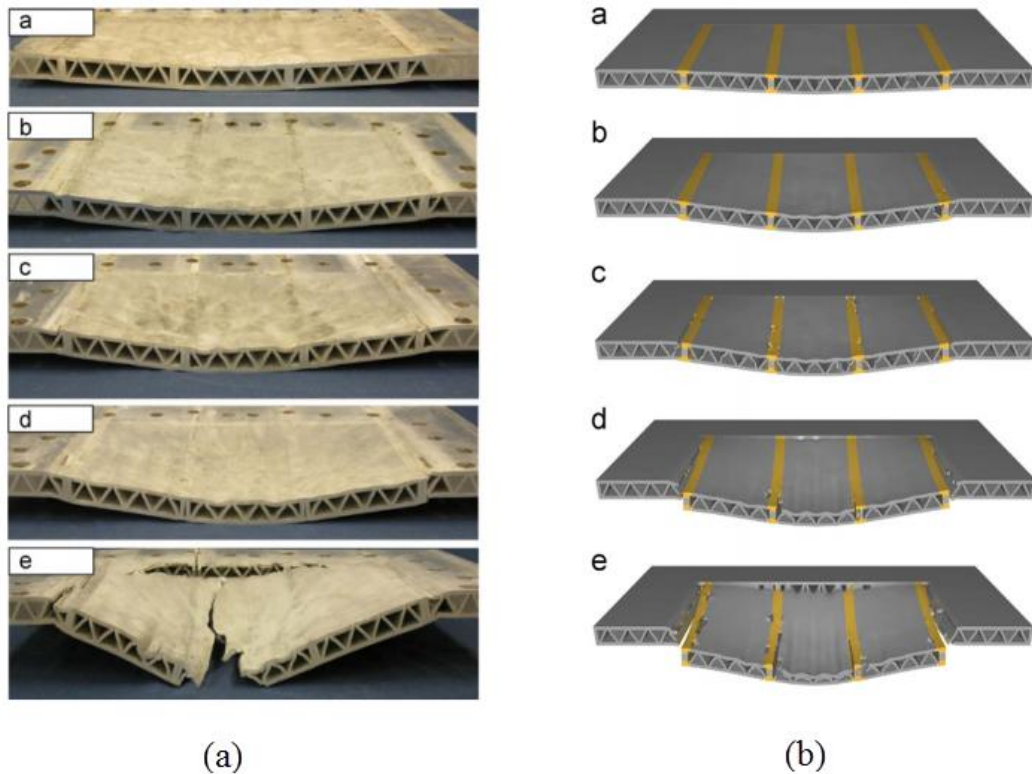


Figure 2.45. Deformation of sandwich structures (a) experimental and (b) numerical [95].

### 2.5.2. Blast-Like Loading of Plates and Sandwich Structures

Yazıcı et al. [96] investigated the effect of foam filling on the blast resistivity of corrugated steel core sandwich panels using a shock tube facility both experimentally and numerically. The corrugated core sandwich structures were produced from low carbon steel face sheets and galvanized low carbon steel sinusoidal corrugations in a four layer match up (Figure 2.46). The incident and reflected pressure profiles were recorded using two pressure transducers mounted at the end of muzzle (Figure 2.47(a-b)). The shock pressure profile was input into ABAQUS as tabular data and imparted onto the front face sheet. Johnson-Cook material model was used for corrugated core and face sheets while polyurethane foam was modeled with Ogden material model. The foam filling increased the buckling and bending rigidity of the core in both experiments and finite element simulations. The foam filling decreased the front and back face deflections more than 50%. Fully foam filling and increased face sheet and corrugated core thickness decreased the deflection by 77.5%. In fully clamped boundary

conditions, the face sheet properties were more dominant than the core properties under shock loading.

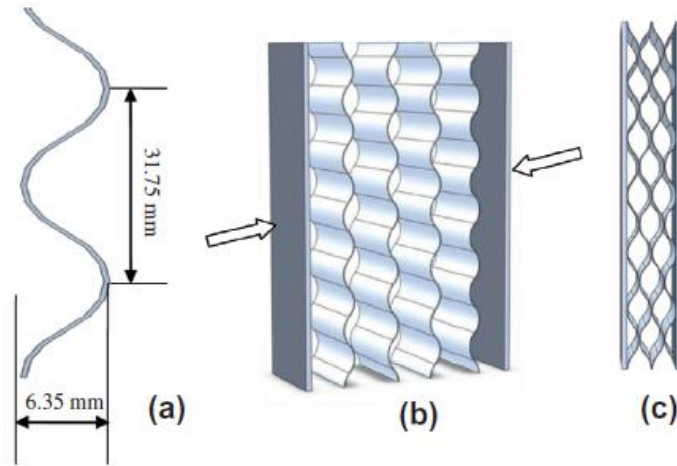
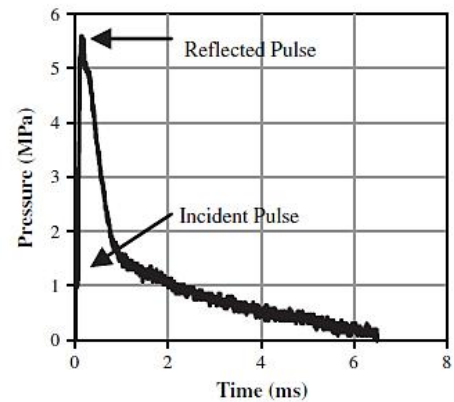


Figure 2.46. (a) Corrugated core sheet dimensions. (b) assembly procedure of corrugated steel core sandwich structures and (c) final sandwich panel side view [96].



(a)



(b)

Figure 2.47. (a) Shock tube apparatus and (b) experimental pressure profile [96].

Zhang et al. [97] studied the dynamic air shock response of corrugated sandwich structures. The corrugated cores were made from 1008 steel and the face sheets from 1018 steel. Three different types of core arrangements (thick, medium and thin) with identical core densities were tested. The blast-like shock loading was performed in a shock tube with 0.7 MPa incident peak pressure (Figure 2.48). The numerical study was performed in ABAQUS. The corrugated cores and rigid supports were meshed with first

order fully integrated C3D8I elements. The shock loading was applied to the front face sheet by using spatial load distribution. The sandwich plate with thick-medium-medium-thin core arrangement had the smallest back face deflection and absorbed the highest plastic energy in the core. The sandwich panel with thick-thick-thin-thin core arrangement transmitted the least impulse to the support. Furthermore, the thick-medium-medium-thin core arrangement outperformed the other two arrangements in energy absorption and back face deflection. The finite element damage modes and deflections showed well correlations with those of the experiments (Figure 2.49).

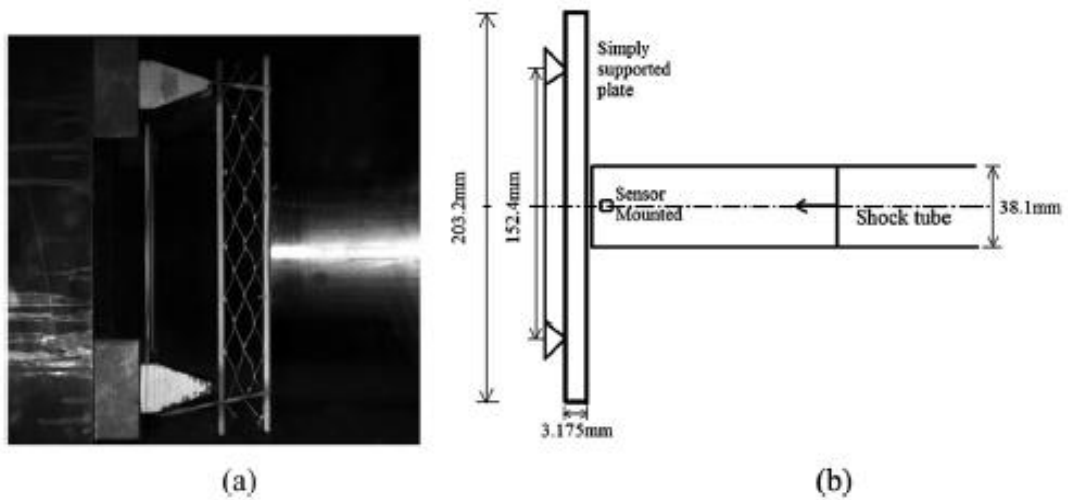


Figure 2.48. (a) Fixture of the corrugated sandwich plate and (b) a schematic of shock tube tester [97].

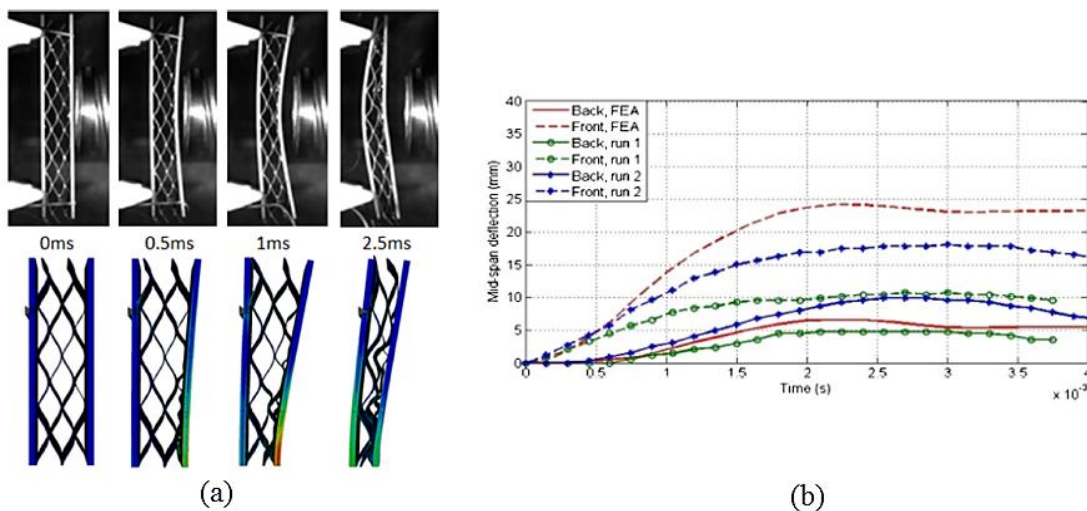


Figure 2.49. (a) Experimental and numerical damage and (b) mid-span deflections of face sheets [97].

Amini et al. [98] investigated the dynamic response and failure modes of circular DH-36 steel and DH-36 steel-polyurea bilayers subjected to impulsive loads using polyurea projectiles. The effects of location of polyurea coatings and bonding strength between the steel and polyurea against the blast loading were numerically investigated (Figure 2.50). The steel plate was modeled using eight-node brick elements with one integration point, while the rim was modeled using the fully integrated quadratic eight node brick elements in LS-DYNA finite element software. The steel plate-polyurethane and aluminum projectile-steel plate interaction was modeled with AUTOMATIC\_SURFACE\_TO\_SURFACE contact algorithm. DH-36 steel was modeled by the material model developed by Nemat-Nasser and Guo while polyurethane using Moony-Rivlin rubber constitutive model. The polyurethane projectiles launched on the steel and polyurea coated steel circular targets and the variations along the radial line of the three principal stretches were measured. Both Lagrangian and Arbitrary Lagrangian Eulerian (ALE) were applied and the results were compared. It was found that the results of ALE were more stable and accurate compared to Lagrangian. The polyurea coating on the back face of the steel reduced the effective plastic strain more than 53% when bonding was perfect, whereas the placing polyurea coating at the front face reduced the effective plastic strain less than 9%. When debonding between front face of the steel and polyurea occurred the effective plastic strain increased with respect to monolithic plate. When the polyurea was placed on the opposite to the impulse loaded side, the initial shock loaded the steel plate first and then a part of the shock was captured and dissipated by the polyurea layer, decreasing the back face displacement (Figure 2.51).

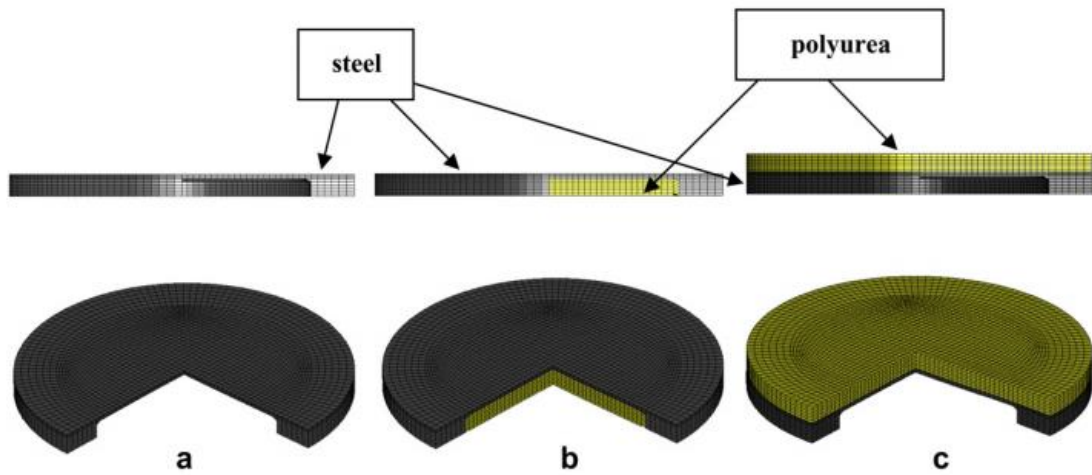


Figure 2.50. (a) Monolithic steel plate (b) bilayer plate with polyurea on the dish side and (c) bilayer plate with polyurea on the flat side [98].

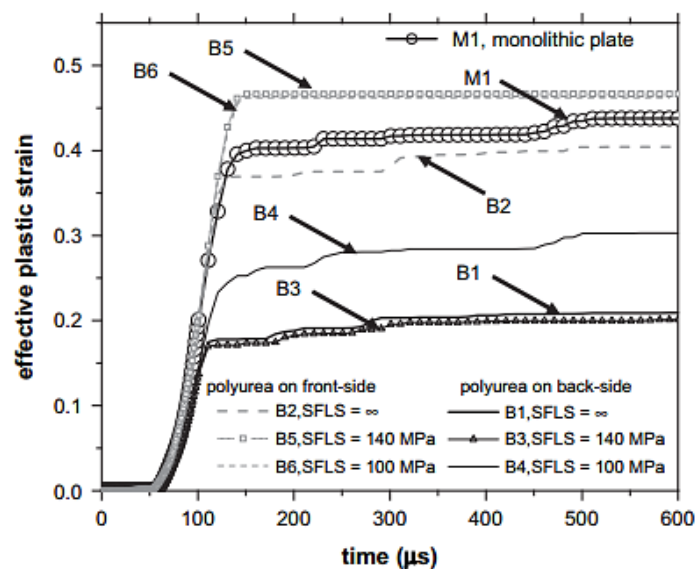


Figure 2.51. Average effective plastic strain history of a monolithic plate and bilayer plates of the indicated polyurea–steel interface bonding strengths [98].

Radford et al. [99] investigated the shock resistance of monolithic and sandwich beams using aluminum foam projectiles to represent the shock loading in air and underwater. Sandwich beams with three types of core topologies; corrugated, pyramidal and closed cell aluminum alloy foam and their mass equivalent monolithic beams were tested. The face sheets and corrugated and pyramidal cores were machined from Al-6XN stainless steel plates. In the shock loading tests, cylindrical aluminum foams with 28.5 mm diameter and 23-50 mm length were launched on the monolithic beams and

sandwich beams at an impact velocity range of 185-490 m/s. The deformation profiles of the specimens were recorded using a high speed camera (Figure 2.52). In the analytical solution part, core crushing for the sandwich beams and mid-span deflection for the monolithic beams were calculated and compared with those of experiments (Figure 2.53). Travelling hinges in the dynamic tests changed the deformation mode of specimens with respect to the quasi-static loading. Moreover, sandwich beams had better shock resistance than the monolithic beams at the same incident momentum. Considering longitudinal stretching resistance, the corrugated core and aluminum foam core sandwiches showed the best resistance against shock loading.

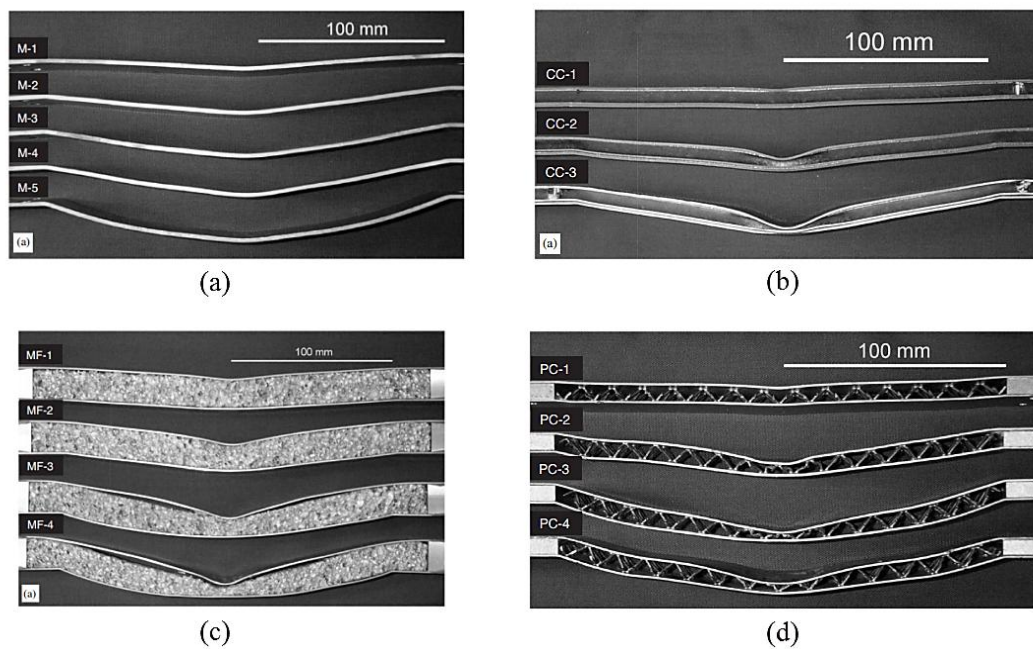


Figure 2.52. Shock loaded and deformed structures: (a) monolithic beams, (b) corrugated core sandwich beams, (c) foam core sandwich beams and (d) pyramidal core sandwich beams [99].

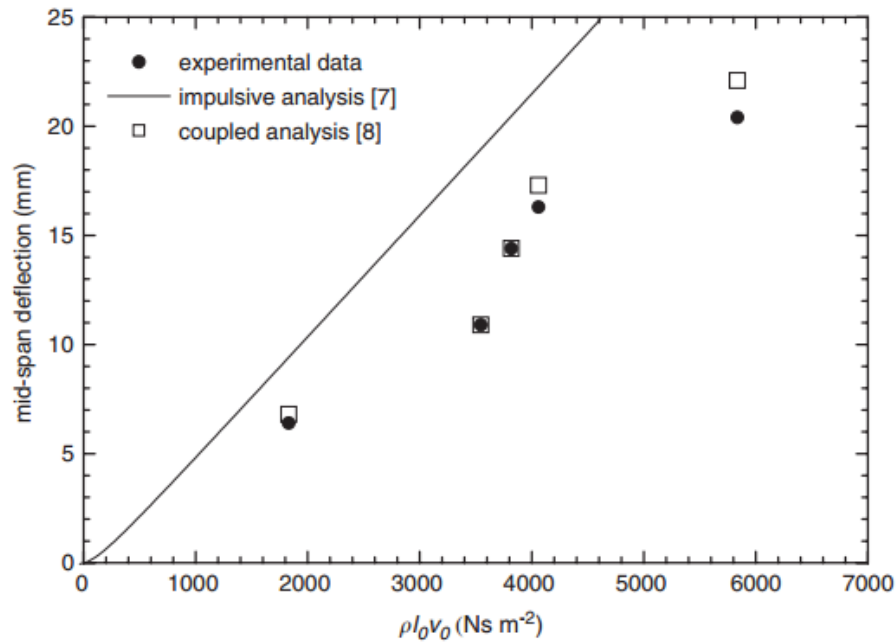


Figure 2.53. Comparison between experimental measurements and predictions of the mid-span deflections for the monolithic beams [99].

Chen et al. [100] developed a non-explosive blast like loading method using a crushable polymer foam projectile launched by a gas gun at velocities ranging from 30 to 60 m/s. The composite specimens and balsa cored sandwich specimens were subjected to projectile impact. The control of the pressure pulse was achieved by changing the density of the pressure generating crushable polymer foam, developing a peak pressure ranging from 3 to 6.5 MPa. The pressure-time history of the foam projectiles with densities of 80, 160 and 240  $\text{kg/m}^3$  were measured using a piezoelectric force sensor setup (Figure 2.54). The polymer foam projectile of 160  $\text{kg/m}^3$  was fired on carbon fiber vinyl ester composite beams at 42.7 m/s and surface cracks and delamination of the surface ply were observed in the high speed camera records (Figure 2.55). As the density of the projectile increased at constant velocity, the damage including fiber compression failure and delamination through the thickness increased. The polymer foam projectile of 160  $\text{kg/m}^3$  produced shear failure on the balsa wood core and core-face sheet separation in the sandwich beam. Polymer foam projectiles were found to produce pressure pulses of desirable profile but the magnitude of the pulses was higher than that would occur in air blast situations.

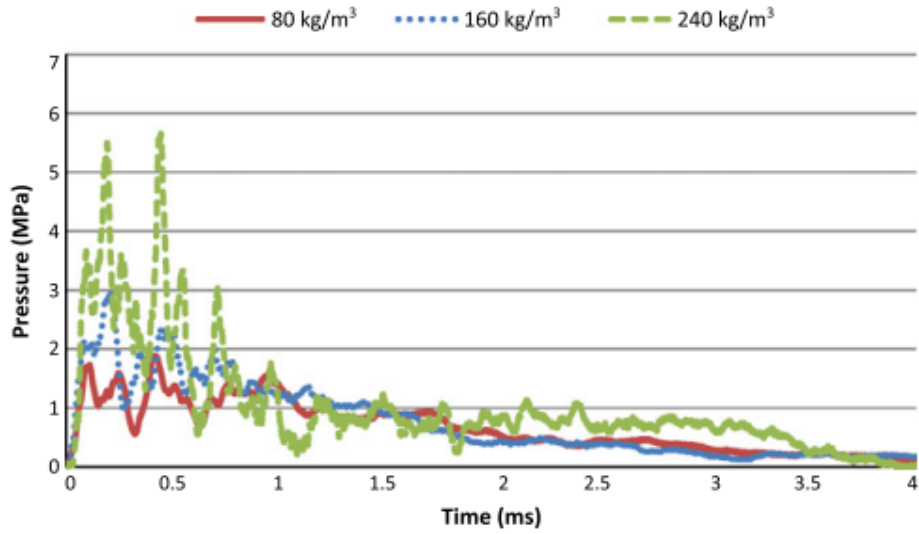


Figure 2.54. Piezoelectric force cell measurement of pressure history, impacts at 38.1 m/s [100].

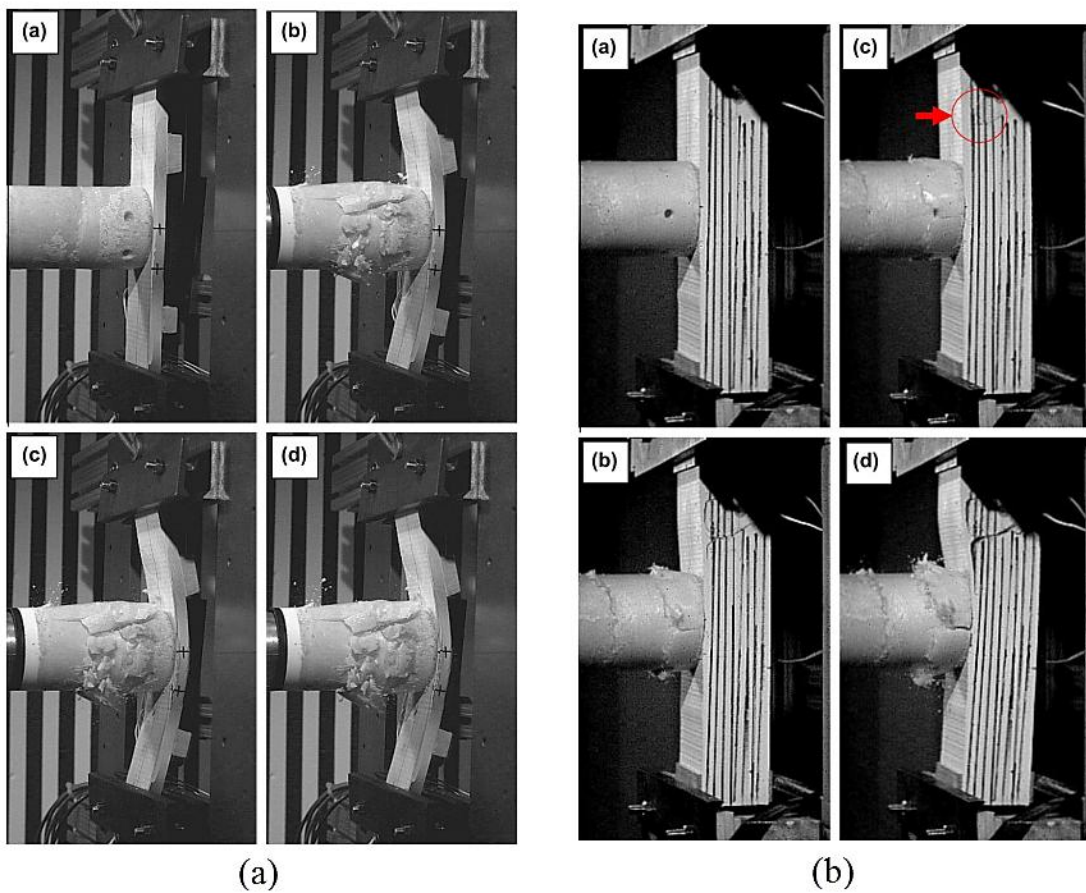


Figure 2.55. Deformation of shock loaded (a) composite plates and (b) sandwich structures [100].



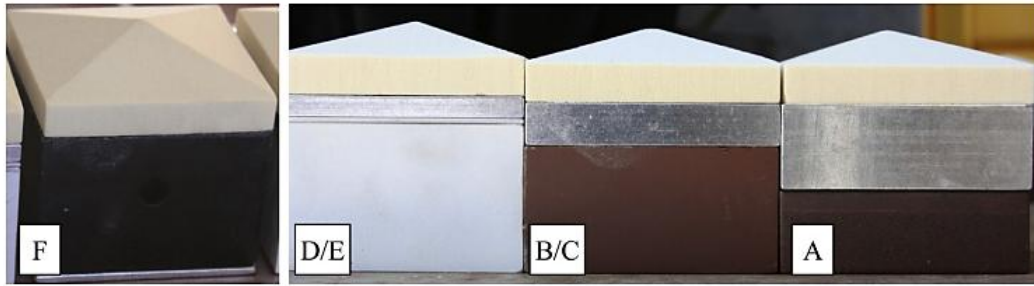


Figure 2.57. Foam tipped tile blocks shown from left: 50.8 mm steel block F and 3.18 mm spacer; 6.35 mm aluminum, 1.59 mm spacer, and 44.5 mm steel blocks D, E; 12.7 mm aluminum and 38.1 mm steel block B, C; 25.4 mm aluminum and 25.4 mm steel block A [101].



Figure 2.58. Deformation of double honeycomb core sandwich structures: (a) non-explosive blast test and (b) explosive blast test [101].

## CHAPTER 3

### EXPERIMENTAL

#### 3.1. Introduction

The composite material was mechanically tested to determine MAT\_162 material model parameters. The tests for material parameters determination were performed in accord with ASTM test standards for polymer composite materials. MAT\_98 material model parameters of the core material 1050 H14 aluminum alloy were determined through mechanical tests. The quasi-static and dynamic mechanical tests were applied to the corrugated sandwich structures and corrugated core composite sandwiches to determine their static and dynamic response and failure behavior.

#### 3.2. E-Glass/Polyester Composite Processing

E-glass/polyester composite samples were prepared using a Metyx biaxial E-glass fabric with an areal density of 954 g/m<sup>2</sup> and a Scott Bader Crystic 703 PA polyester resin (Figures 3.1 (a-b)). The composite plates were prepared in a VARTM set-up. The number of fabric layers for a given final thickness of composite plate was calculated using the following equation

$$n = \frac{h \rho_f V_f}{mof} \quad (3.1)$$

where,  $n$  is the number of fabric layers,  $h$  is the final thickness of the composite,  $\rho_f$  is the density of E-glass fiber (2600 kg/m<sup>3</sup>),  $V_f$  is the fiber volume fraction (0.6) and  $mof$  is areal density of the fiber. The mass of the polyester resin,  $m_p$ , was determined using

$$m_p = (\rho_m V_m) V_p \quad (3.2)$$

where,  $\rho_m$  is the density of polyester ( $1200 \text{ kg/m}^3$ ),  $V_m$  is the volume of the plate and  $V_p$  is the polyester volume fraction in the composite (0.4). The amount of hardener (MEKP) used in the composite preparation was 2 wt% of the polyester.

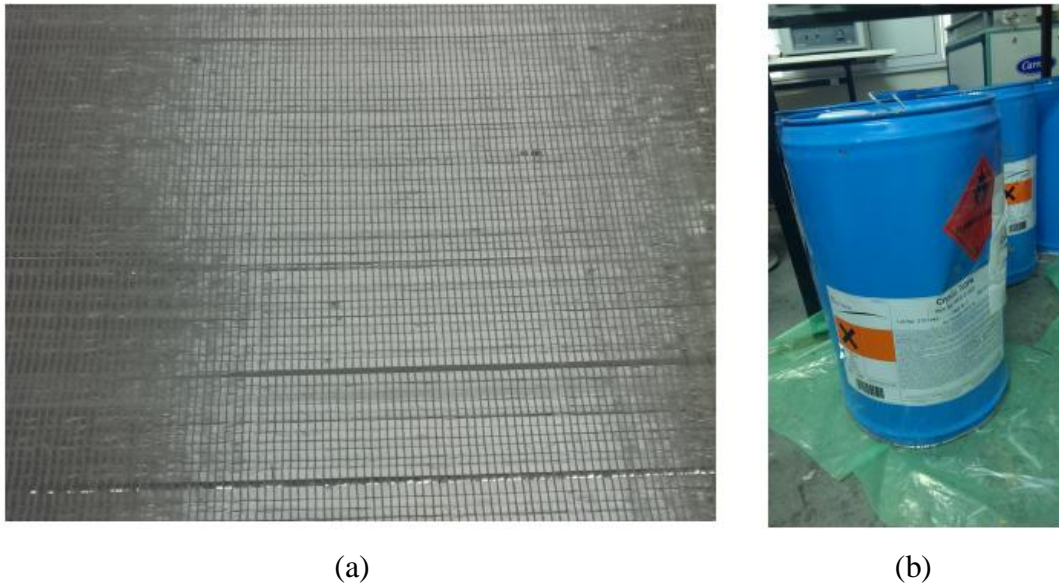


Figure 3.1. (a) Metyx biaxial E-glass fiber and (b) Scott Bader Crystic 703 PA polyester.

The used VARTM set-up is shown in Figure 3.2. The infusion process was performed on a glass plate. Initially, a thin layer of wax layer was deposited on the glass plate surface for the easy separation of the composite plate from the glass plate. Then, the fiber plies were sequentially placed. The fibers were covered with tear-off tissue and then draining tissue was placed on tear-off tissue. Additional fiber plies were placed on the tear-off tissue to slow down the flow of the resin. Vacuum ramps and resin ramps were placed and sealtex was applied peripheral to the fibers. Vacuum bag was cut in suitable dimensions and installed to form vacuum over the fiber plies. Vacuum pipes were connected and the vacuum was checked against leakage. Polyester resin was supplied to the system through flexible polyethylene pipes and wet fibers were kept under pressure until the curing process finished.

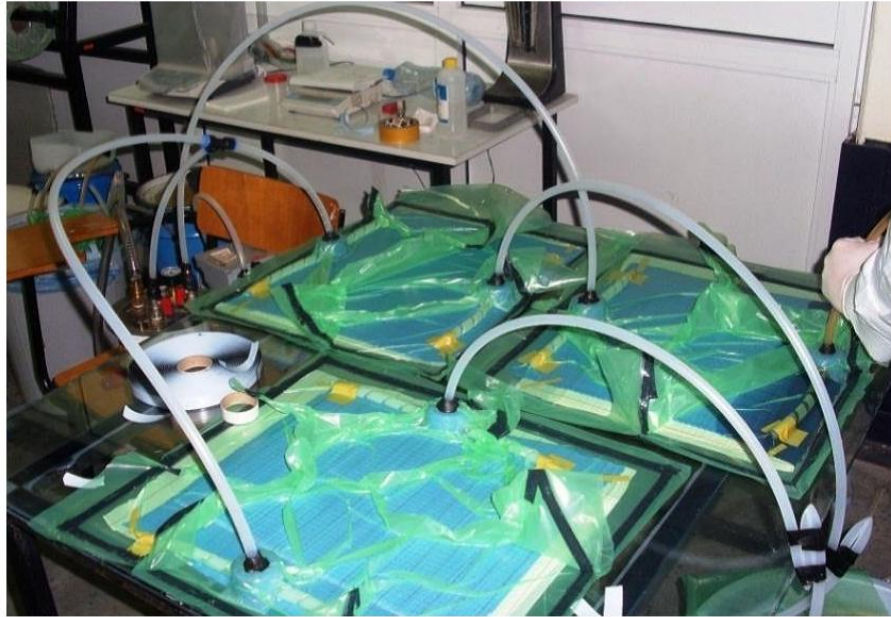


Figure 3.2. Vacuum assisted resin transfer molding set-up.

The cartesian coordinate system of the prepared E-glass/polyester composite plates in XYZ directions is shown in Figure 3.3. The X axis shows the warp fiber direction and the Y axis the weft fiber in plane orthogonal directions. The Z axis shows the through thickness direction, perpendicular to the in plane orthogonal directions. Since the fiber is balanced and symmetric, the properties of the composite in X and Y axes are nearly equal.

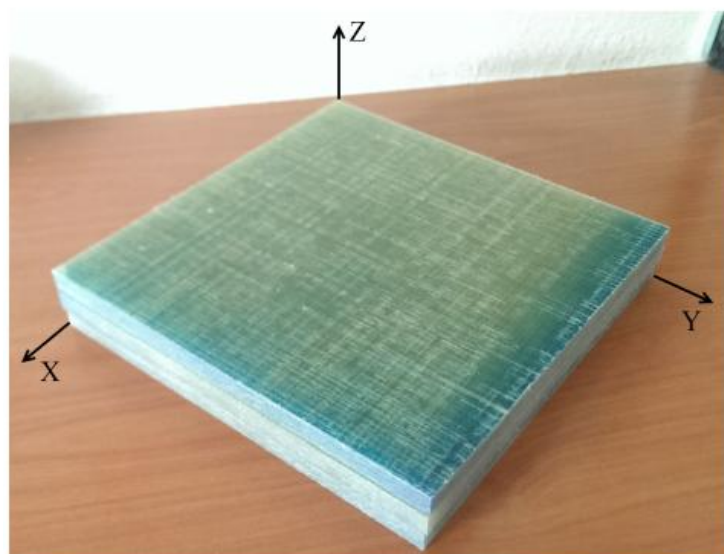


Figure 3.3. E-glass/polyester composite principal coordinate system.

### 3.3. Mechanical Testing of E-Glass/Polyester Composite

#### 3.3.1. In-Plane Tensile Tests

The quasi-static tension test samples of E-glass/polyester composite in  $[0^\circ/90^\circ]_s$  fiber orientation were prepared in accord with ASTM D3039M [1] test specimen geometry with end tabs using a Shimadzu universal testing machine at 2 mm/min cross-head speed. The displacement of the test sample was recorded using a video extensometer. Strain gages were mounted on the test sample to measure the longitudinal and axial strains to calculate the Poisson's ratio (Figure 3.4). The tensile tests were conducted both in X and Y principles axes. The rectangular tension specimens were 2.5 mm in thickness, 25 mm in width and 250 mm in length with a gage length of 150 mm (Figure 3.5). All the tension test specimens were in  $[0^\circ/90^\circ]_s$  stacking sequence with 3 layers of fibers. The end tab thickness was 1.5 mm, with a length of 50 mm and the tab bevel angle was  $90^\circ$  for all types of specimens. The tabbing material was E-glass/Polyester composite in the same orientation with the composite specimen and two component BISON epoxy was used to glue end tabs.

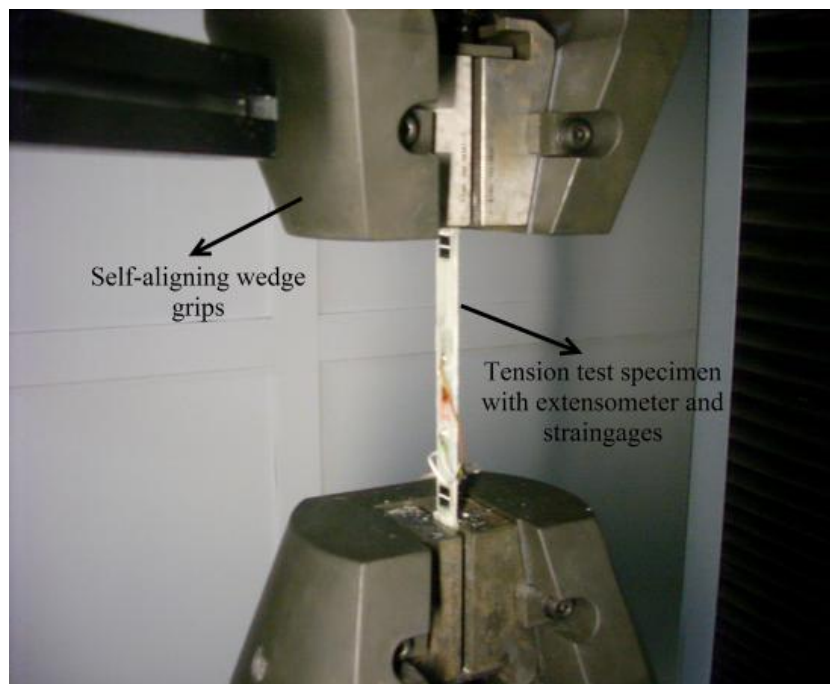


Figure 3.4. Tension test specimen with extensometer and strain gages.

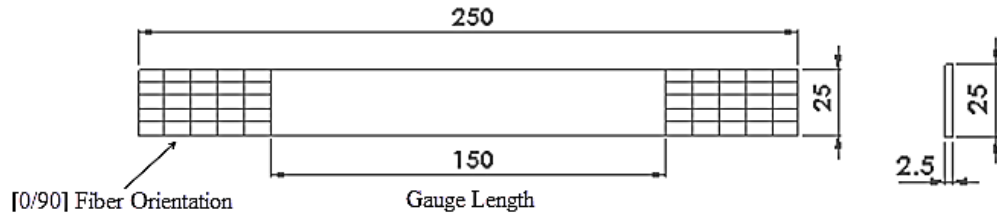


Figure 3.5. ASTM 3039M tensile test specimen.

The material properties obtained after the tensile tests are as follows;

- Young's modulus in the fiber direction,  $E_x$ .
- Young's modulus in the transverse to the fiber direction,  $E_y$ .
- Ultimate tensile stress and strain in the fiber direction,  $X_1^T, \varepsilon_1^T$ .
- Ultimate tensile stress and strain transverse to the fiber direction,  $X_2^T, \varepsilon_2^T$ .
- Poisson's ratio,  $\nu_{12}$ .

### 3.3.2. In-Plane Shear Test

Shear test samples were prepared in accord with ASTM D 3518 [102]. This test standard also recommends ASTM D 3039M test specimen geometry for shear test. The test was used to determine shear modulus and shear strength. To satisfy a pure and uniform shear region, tension test specimens of  $[\pm 45]_{ns}$  ( $n \geq 2$ ) were prepared and tested. The geometry for  $[\pm 45]_{ns}$  tensile coupon had the same geometry as ASTM D 3039 tension test specimen shown in Figure 3.6. The  $[\pm 45]_{ns}$  tension test provides an indirect measure of the in-plane shear stress-strain response in the fiber coordinate system. The strain data were recorded with 2 strain gages, one of them was placed in the fiber direction and the other one in the transverse to the fiber direction. The strain gages were bonded to the midspan of the test specimen. The width, length and thickness of the shear test specimen were sequentially 25, 250 and 2.5 mm as seen in Figure 3.7. The tabs used in these tests were 50 mm in length and 1.5 mm in thickness and the tab bevel angle was  $90^\circ$ . The specimen was tested in tension until fracture at a crosshead speed of 2 mm/min. The shear strength of the specimens,  $\tau_{xy}$ , was calculated using the laminated plate theory as

$$\tau_{xy} = \sigma_x / 2 \quad (3.3)$$

where,  $\sigma_x$  is the axial stress and the shear strain,  $\gamma_{xy}$ , was determined using the following relation

$$\gamma_{xy} = \varepsilon_x - \varepsilon_y \quad (3.4)$$

where,  $\varepsilon_x$  and  $\varepsilon_y$  are the axial and transverse strains recorded by the strain gages, respectively. The slope of shear stress vs. strain curve gives the shear modulus,  $G_{xy}$ . The ultimate shear stress is defined as the maximum value of  $\sigma_x / 2$ .

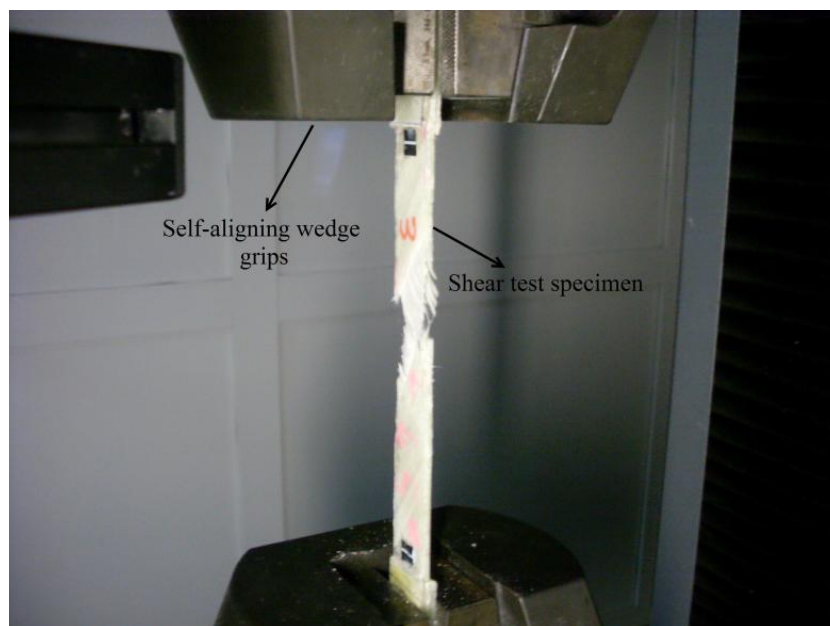


Figure 3.6.  $[\pm 45^\circ]$  shear test specimen.

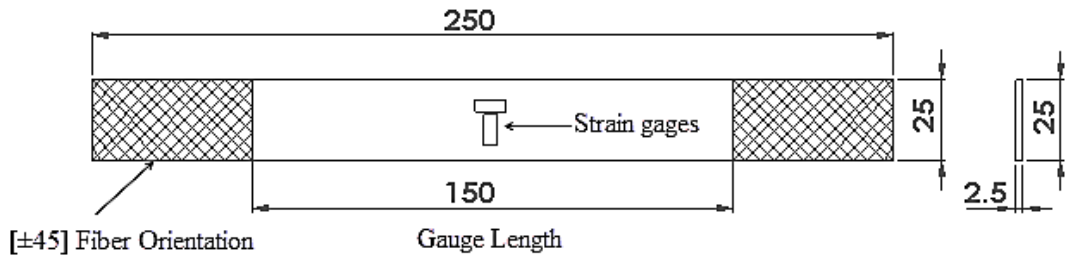


Figure 3.7. Shear test specimen dimensions according to ASTM D 3518.

### 3.3.3. Quasi-static Compression Tests

The quasi-static compression tests were conducted according to ASTM D 3410 compression test standard [103] in the principle X and Y directions. To investigate the strain rate sensitivity of composite material, cylindrical test specimens were core drilled from composite plates in X, Y and Z principle axes. The ASTM D 3410 and cylindrical test samples are shown in Figures 3.8 (a-b), respectively.

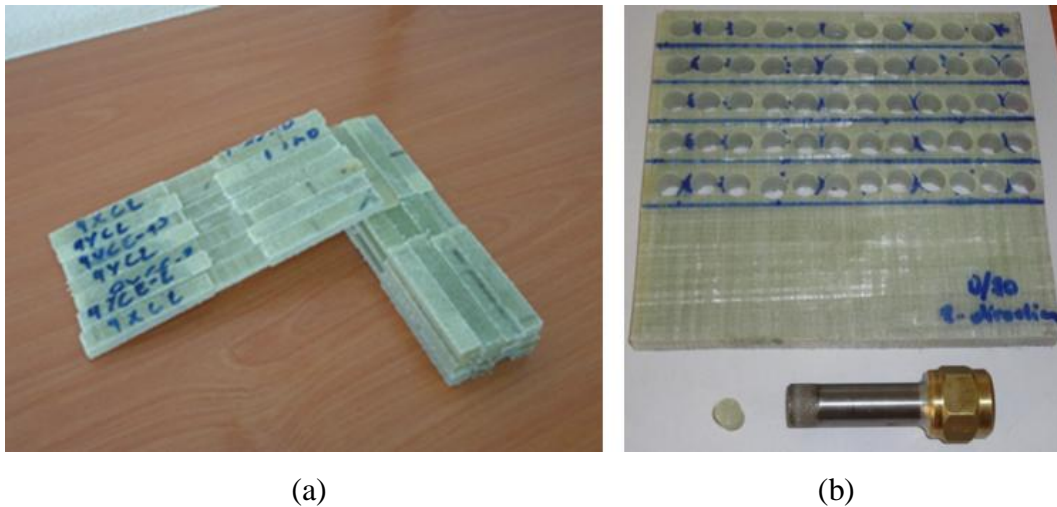


Figure 3.8. Quasi-static compression test specimens; (a) ASTM D3410 and (b) cylindrical test samples.

The compression test samples were 10 mm in width, 155 mm in length and 5 mm in thickness (Figure 3.9). The cylindrical tests specimens were 9.81 mm in diameter and 14 mm in length. The compression tests were performed at the strain rates of  $10^{-3}$ ,  $10^{-2}$  and  $10^{-1} \text{ s}^{-1}$ . The crosshead speed,  $V_{Cr}$ , was calculated using the following equation

$$V_{cr} = \dot{\varepsilon} L_0 \quad (3.5)$$

where,  $\dot{\varepsilon}$  is the strain rate and  $L_0$  is the initial length of the specimen. Material properties obtained from the compression test are:

- Young's modulus in the fiber direction,  $E_X$ .
- Young's modulus in the transverse to the fiber direction,  $E_Y$ .
- Young's modulus in the through thickness,  $E_Z$ .
- Ultimate compressive stress and strain in the fiber direction,  $X_X^C, \varepsilon_X^C$ .
- Ultimate compressive stress and strain transverse to the fiber direction,  $X_Y^C, \varepsilon_Y^C$ .
- Ultimate compressive stress and strain in the through thickness,  $X_Z^C, \varepsilon_Z^C$ .

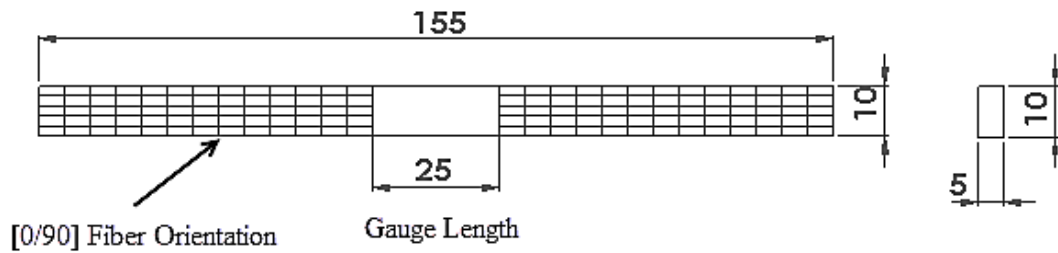


Figure 3.9. Technical drawing of compression test samples according to ASTM D3410.

### 3.3.4. Flexural Tests

Flexure tests (3-point bending tests) were conducted on  $[0^\circ/90^\circ]_s$  fiber oriented composite samples using the bending test fixture shown in Figure 3.10. The span to thickness ratio ( $L/h$ ) was chosen 16 based on the ASTM D 790-92 [104]. The diameter of the load noses and support pins should be at least 6.4 mm according to the specification. A load nose with 10 mm diameter was used to conduct the tests. Specimens were nominally 130 mm long and 12.7 mm wide. In flexure test, the top side of the specimen is under compression while the bottom side is tension. The mid-plane contains the neutral axis and is under zero bending stress. The interlaminar shear stress is maximum at the beam center. The stress level is dependent on the span to thickness ratio. Beams with a small  $L/h$  ratio are dominated by shear. At least five specimens from each thickness were tested using Shimadzu uniaxial test machine at a crosshead

speed of 2 mm/min. Force and deflection were recorded and the strength was calculated using the following relation

$$\sigma = \frac{3PL}{2wh^2} \quad (3.6)$$

where, P is the applied load, L is the span length; h is the thickness of the beam and w is the width of the beam. The strain at the mid-span of the beam is calculated as

$$\varepsilon = 6Dh/L^2 \quad (3.7)$$

where,  $\varepsilon$  is the strain of the fibers and D is the deflection of the beam. The flexural modulus,  $E_f$ , was calculated using the following equation

$$E_f = \frac{mL^3}{4wh^3} \quad (3.8)$$

where m is the slope of the load-deflection curve.

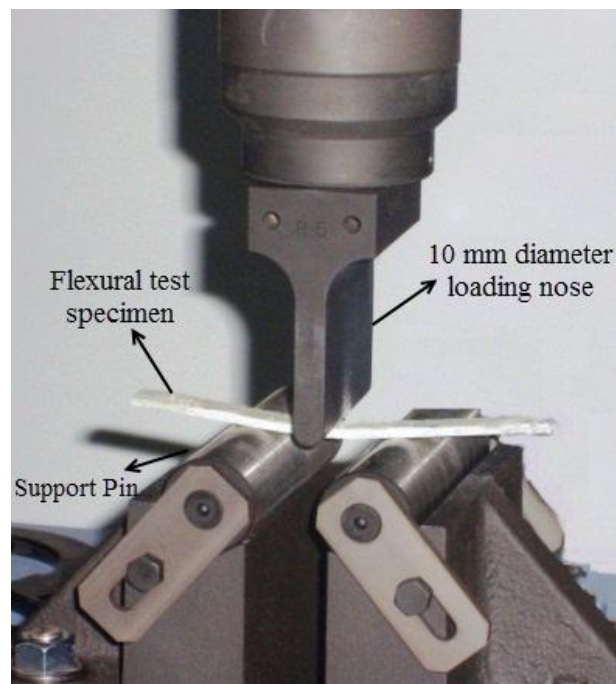


Figure 3.10. Flexural test set-up and flexural test specimen.

### 3.3.5. Curved Beam Tests

The curved beam strength tests were conducted according to ASTM D 6415 [105] standard to find the through thickness tensile strength of the composite. The test specimens were 25 mm in width, 90 mm in length and 5 mm in thickness. As explained in the standard, a constant crosshead speed of 1.5 mm/min was applied on the specimens to complete the deformation between 1 and 10 min. The applied load was transferred to the curved beam from symmetrically placed 10 mm diameter steel rods and supported by the symmetrically placed 10 mm diameter bottom rods. The data were recorded by the force transducer located on the universal compression testing machine. The test set-up and test sample are shown in Figures 3.11(a-b), respectively.

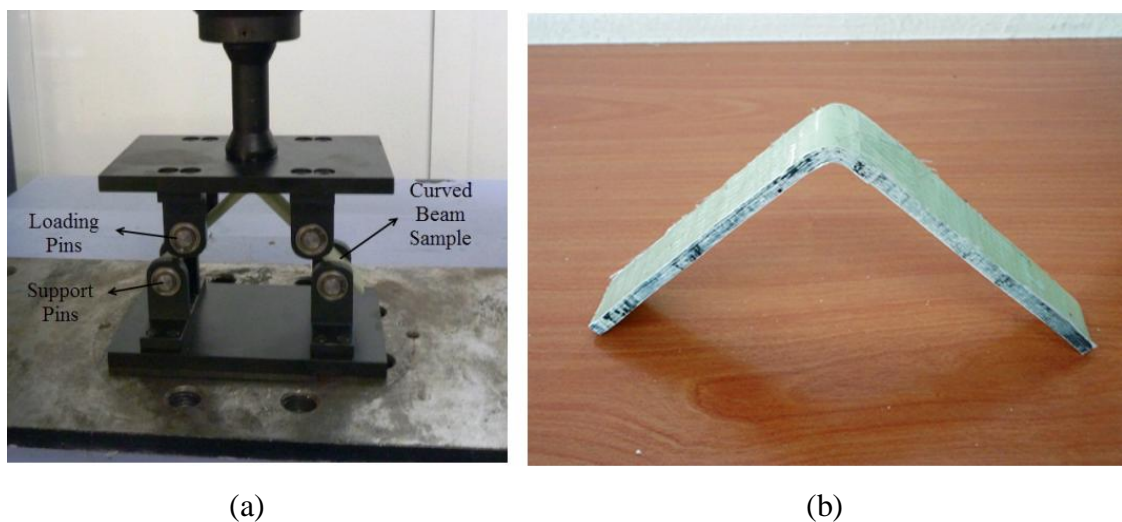


Figure 3.11. (a) Curved beam test set-up and (b) curved beam specimen.

### 3.3.6. Laterally Constraint Compression Tests

Laterally constraint compression test set-up and test samples (Figure 3.12) were used to determine the shear failure strength of the composite. In this test method, composite samples having dimensions of 12.7x12.7x12.7 mm were machined from composite plates in through thickness direction [61]. The compressive load was transferred to the specimen by a steel pillar at a cross-head speed of 1.5 mm/min (Figure 3.12).

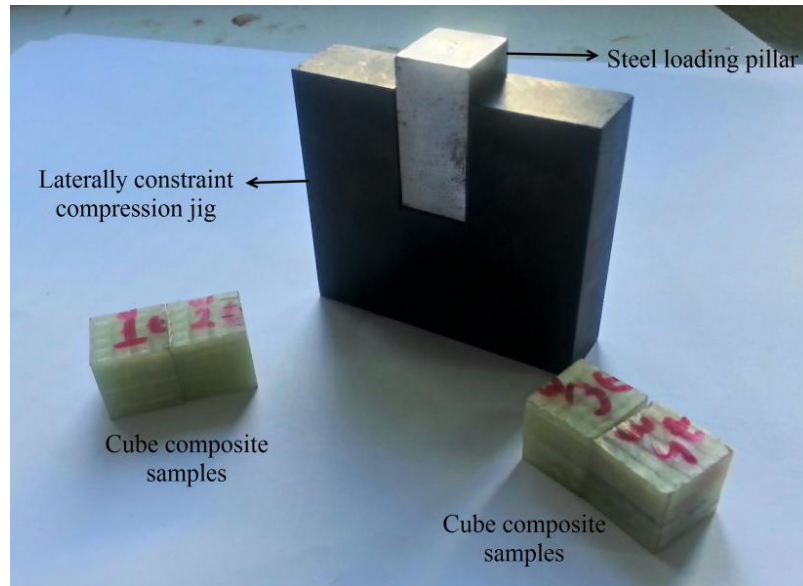


Figure 3.12. Laterally constraint compression test set-up and cube composite samples.

In laterally constraint compression test, fiber shear failure is initiated by the transverse compressive load. A failure surface cutting through the fibers with an inclined angle ( $\theta$ ) in the compressive loading direction typically results from such a compressive test. By loading the specimen in through-thickness direction and constraining laterally in one direction, failure occurs on certain preferred planes cutting the fibers. The failure angle can be determined after the test using an image processing program. The fiber mode shear strength (SFS) is

$$SFS = 0.5(SFC)\sin(2\theta) \quad (3.9)$$

where, SFC is the fiber crush strength.

### 3.3.7. Low Velocity Impact Tests

The low velocity impact tests were conducted using a FRACTOVIS drop weight tower (Figure 3.13 (a)). The equipment consisted of striker holder which accommodated additional weights, striker and the 20 mm diameter hemispherical impactor shown in Figure 3.13 (b). The hemispherical impactor was attached to the tip of the 90 kN capacity strain gage striker. The weights were added to alter the impact energy. The velocity of the impactor was measured by a photocell device placed in the path of the striker before the impactor strikes to the specimen. The force-time history was measured

from the point of initial contact with the specimen and the striker travels through the thickness of the specimen. Energy was calculated by integrating the force-time history. The load-displacement, force-time and energy-time histories were recorded by a Data Acquisition System. Totally 16000 points were recorded in a typical test. The sampling frequency was 1000 kHz with a 16 ms of test duration.

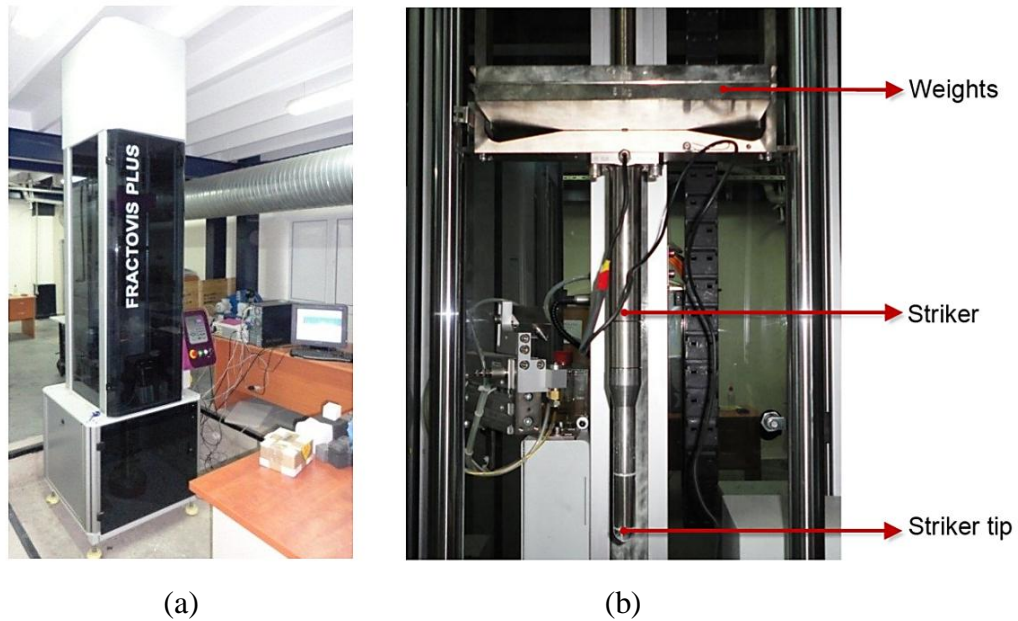


Figure 3.13. (a) FRACTOVIS low velocity impact test equipment and (b) striker holder, weights and the impactor.

In low velocity impact tests a total weight of 15.78 kg was used. Drop height changed during the test because of the variable impact velocity and in few tests additional energy system was used to reach the desired impact velocity. Impact velocities were between 4 m/s and 10 m/s. To avoid repeated impacts, two rebound arrestors were located on both sides of the specimen. The rebound arrestors were pneumatically actuated, and spring up and separated the striker from the specimen after the first impact. The composite  $[0^\circ/90^\circ]_s$  fiber orientation low velocity impact test samples were 100x100x3 in size. The specimen was fixed in a fully clamped support condition with a 76.2 mm diameter hole that allowed the impactor to strike the specimen. The applied clamping force on the specimen was 75 N which avoided the rotation and sliding of the specimen at the impact instant.

Various properties can be obtained from low velocity impact tests (Figure 3.14) including impact velocity and incipient energy ( $E_i$ ), total energy absorbed ( $E_t$ ), total deflection ( $I_t$ ), incipient damage point ( $P_i$ ), maximum load ( $P_{max}$ ), failure load point, total load point ( $P_t$ ), energy at maximum load ( $E_m$ ), deflection at maximum load ( $I_m$ ) and energy ( $E_p=E_t-E_m$ ) and deflection ( $I_p=I_t-I_m$ ) after maximum load. The point of incipient damage ( $P_i$  and  $E_i$ ) is the first significant deviation or break from the initial portion of the load-time curve. This point shows the onset delamination, matrix micro-cracking or fiber damage. At the point of maximum load and maximum energy, maximum penetration of the impactor occurs and then the rebound begins. In some cases, the incipient damage point coincides with the maximum load. The failure load and energy points indicate the specimen response up to the end of the rebound phase of the impactor. These parameters can be influenced by material thickness and geometry, boundary conditions, progression and sequence of damage accumulation, fiber orientation, interface variations and impactor geometry (sharp, blunt, and spherical). It should be noted that the heterogeneous and anisotropic nature of the fiber reinforced composites cause the different types of failure modes including (1) matrix cracking due to tension, compression or shear; (2) delamination between the plies because of the interlaminar shear stress; (3) fiber break and buckling and (4) penetration.

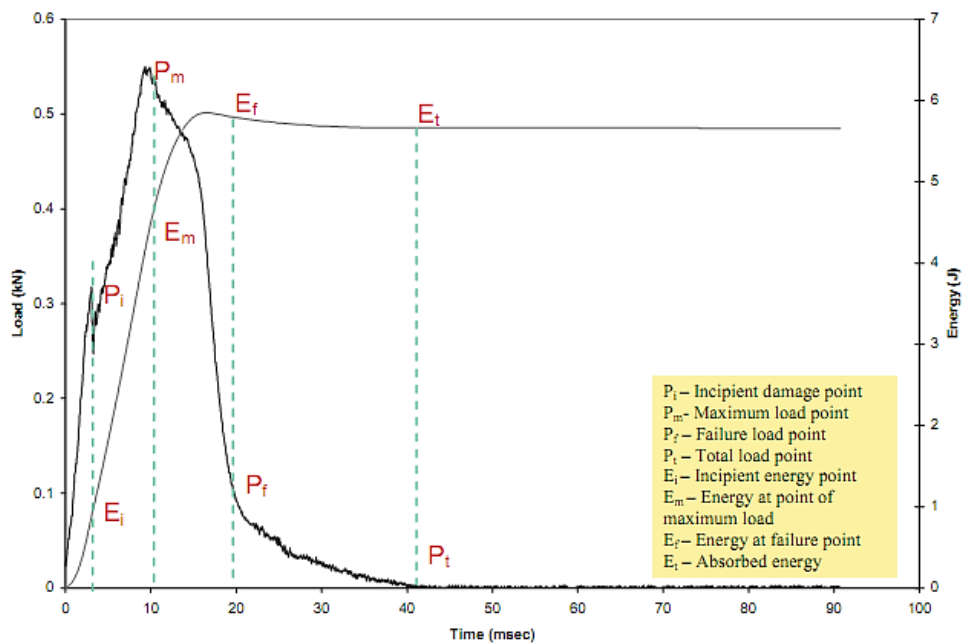


Figure 3.14. A typical load-energy-time curve for impact analyses [106].

### 3.3.8. Split Hopkinson Pressure Bar Compression Tests

The SHPB cylindrical test specimens were core drilled in three principal axis. The specimens were 9.81 mm in diameter and 14.715 mm in length with an L/D ratio of 1.5. The test specimen was sandwiched between the incident and transmitter bar by applying lubrication at specimen-bar interfaces (Figure 3.15). The used SHPB apparatus consisted of Inconel 718 bars, 500 mm striker, 3116 mm incident and 2080 mm transmitter bars, all with a diameter of 19.35 mm. A full bridge strain gage was used to measure the strains on the bars. The distance between the interface of the bar and the strain gage was 1010 mm on both transmitter and incident bars. The pulses measured by the strain gages were conditioned with a signal conditioner and the voltage versus time records were monitored by a digital oscilloscope. The voltage-time records were converted into stress-strain diagrams by using Eqns. 2.5 and 2.6, respectively. A high speed camera, 5000 fps, was used to record the SHPB tests in order to observe the deformation modes of the composite samples in all principal directions.

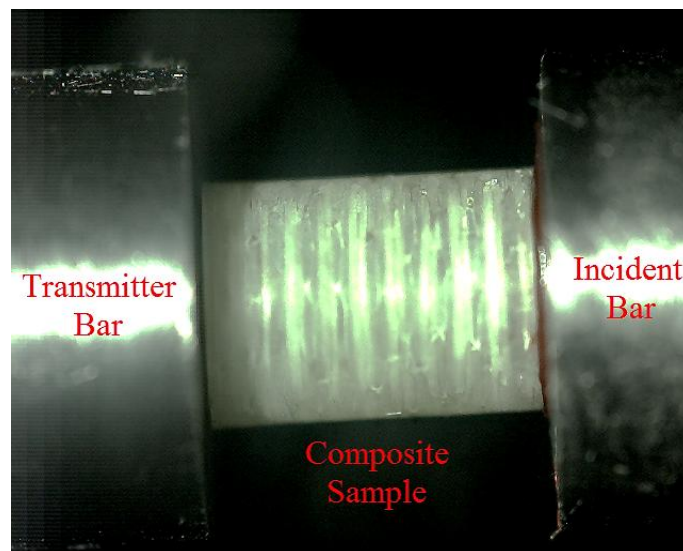


Figure 3.15. Incident bar, transmitter bar and composite sample prior to impact.

### 3.3.9. Projectile Impact Tests with Spherical Projectiles

The projectile impact tests were applied on  $0^\circ/90^\circ$  fiber oriented E-glass/polyester composite plates with thicknesses of 2, 3 and 5 mm by using a gas gun test system. The gas gun test system consisted of pressure vessel, specimen holder and laser barriers to measure the impact and residual velocities of the projectile. Pressurized air was used to accelerate the projectiles with the help of polyurethane sabots. A hardened steel sphere in 30 mm diameter and 110 g in weight was used as the projectile. The projectile was placed into the sabot housing tightly. At the exit side, the sabot impacted the anvil and the steel sphere projectile launched through the target (Figure 3.16). A high speed video camera was used to record the impact and the motion of the projectile before the penetration. The composite targets were cut in 200x200 mm plates of  $[0^\circ/90^\circ]_s$  fiber oriented composite laminates. The composite samples in 2 mm, 3 mm and 5 mm thicknesses were tested at the same pressure for both orientations. The impact velocity ranged between 127 m/s and 190 m/s normal to the plates.

The composite plates and sandwich structures were examined after the projectile impact tests. Furthermore, the ballistic limits for the composite plates were determined from the recorded impact and residual velocities. The energy absorbed by the composite plates was also calculated.

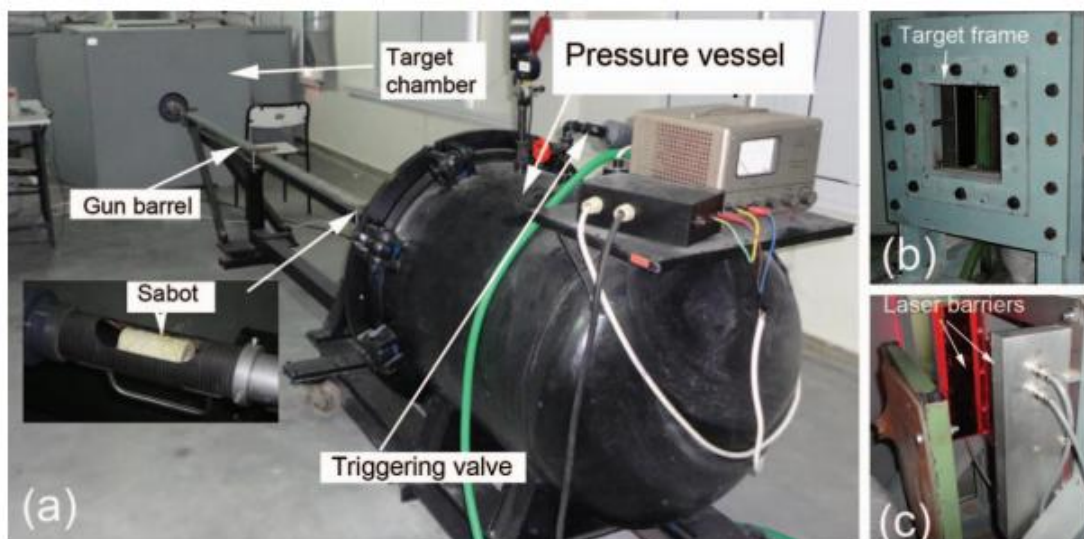


Figure 3.16. (a) Projectile impact test set-up, (b) target frame and (c) laser barriers [107].

### 3.4. Trapezoidal Corrugated Aluminum Fin Layers and Sandwich Structures

The trapezoidal corrugated aluminum core layers used in the sandwich constructions were commercially produced by a local factory in a specified fin geometry using a hydraulic press as shown in Figure 3.17. The hydraulic press was composed of hydraulic pressure unit, dies and machine frame. In this process, 1050 H14 Al alloy sheets with a thickness of 0.135 mm were punched and bent into a die cavity in which zig-zag form and trapezoidal shape were formed. The pictures of the forming machine and bottom die are shown in Figures 3.18 (a) and (b), respectively. These corrugated layers were fabricated to be used in heat exchanger to control heat flow and thermal conduction but the mechanical compression tests proved that these materials could also be used as load carrying units in sandwiches because the moment of inertia resulting from the geometry.



Figure 3.17. Hydraulic press used to form corrugated layers.



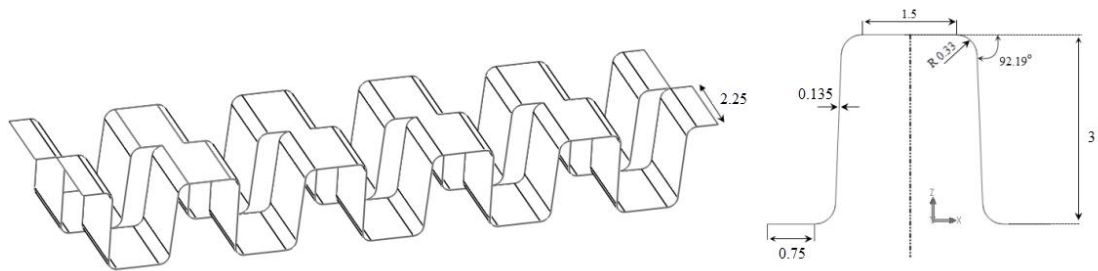
(a)



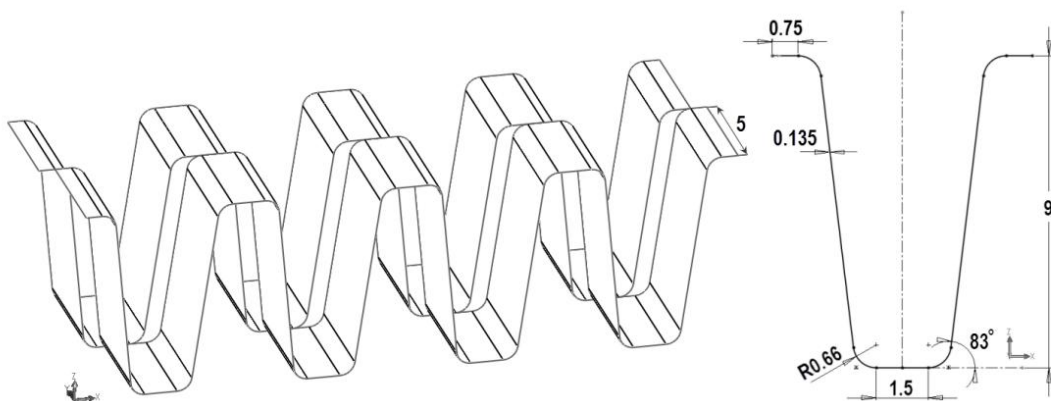
(b)

Figure 3.18. The pictures of (a) forming machine and (b) bottom die.

In the present study, two different types of corrugated structures were tested; the small fin type corrugated layer (Figure 3.19 (a)) was used as core layers in projectiles while the big fin type corrugated layers were used as core layers in composite sandwich structures (Figure 3.19 (b)). The small fin corrugated sandwich structure consisted of 1 mm thick 1050 H14 face sheets and 16 layers of 1050 H14 small fin (Figure 3.20 (a)). The sandwich panel components were brazed in a furnace at 600°C for 10 min under atmospheric pressure using a 4343 aluminum filler sheet (6.6-8.2 wt%), following the cleaning and flux slurry spraying of the surfaces. The second group of sandwiches consisted of big fin corrugated cores assembled using a polyurethane adhesive (Henkel Thomsit R710). The sandwich panels were kept under 5 kg loads for 2 h in order to satisfy full sticking between composite face sheets and cores. In three layers core composite sandwich structures 1050 H14 interlayer sheets with 0.5 mm thickness were inserted between the corrugated layers while there was no interlayer sheets in single layer core sandwich structure. (Figure 3.20 (b-c)).



(a)

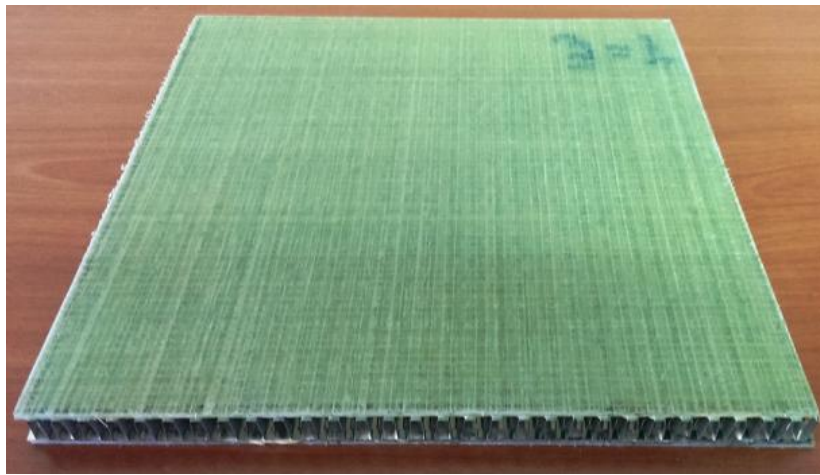


(b)

Figure 3.19. Picture and technical drawings of corrugated fin layers: (a) small fin corrugated layer and (b) big fin corrugated layer.



(a)



(b)



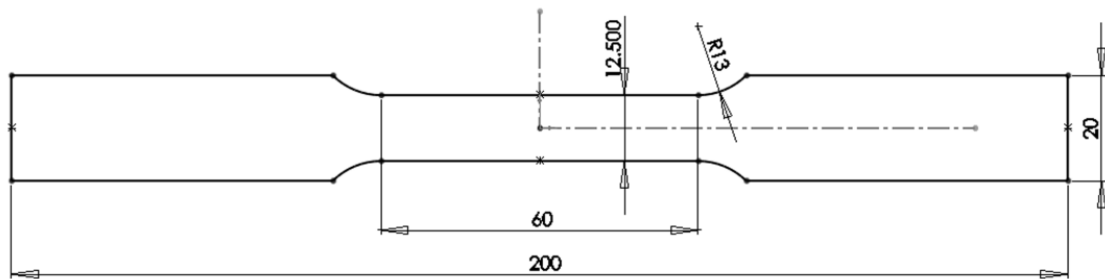
(c)

Figure 3.20. (a) Small fin corrugated core aluminum sandwich, (b) single layer big fin core composite sandwich and (c) three layers big fin corrugated core composite sandwich.

### 3.5. Mechanical Testing of 1050 H14 Aluminum Alloy and Corrugated Sandwich Structures

#### 3.5.1. Mechanical Testing of 1050 H14 Aluminum Alloy

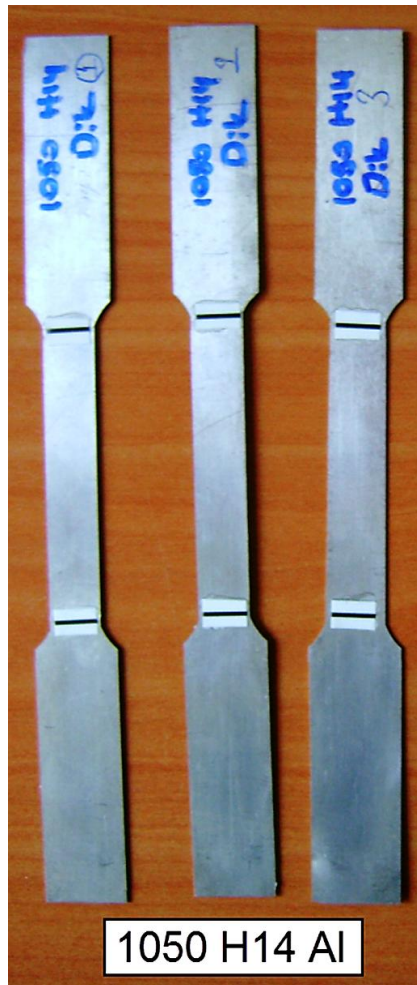
The quasi-static tensile stress-strain behavior of 1050 H14 Al alloy was determined at the strain rate of  $10^{-3} \text{ s}^{-1}$  using SHIMADZU universal testing machine. The tension test specimens, as shown in Figure 3.21 (a) and (b), were machined in accord with ASTM E8M-04 standard [108]: the gage length and thickness were 60 and 1.5 mm, respectively. A video extensometer synchronized with the mechanical testing machine was used to measure the displacement.



(a)

Figure 3.21. (a) Technical drawing and (b) picture of tensile test specimens [85, 109].

(cont. on next page)



(b)

Figure 3.21 (cont.).

In order to determine the effect of brazing on the stress-strain behavior, few tension test specimens were passed through a heat treatment process in a furnace (Figure 3.22), the same with the one applied in the brazing. These specimens were heated from 200 °C to 600 °C in 13 min, hold at 600 °C for 2 min; then, cooled to ambient temperature in air.



Figure 3.22. Furnace for heat treatment of 1050 H14 test samples.

### **3.5.2. Quasi-static Compression Tests on Corrugated Sandwich Structures**

The quasi-static compression tests on cylindrical sandwich structures with and without face sheets ( $\phi 48mm$ ) were conducted at the strain rates of  $10^{-3}$  and  $10^{-1} s^{-1}$ . The deformations of test samples were recorded using a high speed camera (Fastcam Photron) at 50 fps. The constraint compression tests were also performed on the cylindrical corrugated sandwich specimens with and without face sheets at the strain rate of  $10^{-1} s^{-1}$  using a cylindrical tube with 40 mm inner diameter shown in Figure 3.23. The sandwich specimen was placed inside the tube and with a punch the specimen was axially compressed in the tube. In order to reduce the friction between the tube and test sample, the surfaces of tube were lubricated using grease.



Figure 3.23. Constraint compression test apparatus and compression samples.

### 3.5.3. Direct Impact SHPB Tests

Direct impact tests were conducted using a 7075 T6 Aluminum Split Hopkinson Pressure Bar test apparatus having bar diameters of 40 mm. In the tests, the transmitter bar was removed and only incident bar was used as rigid target and the measurements were taken from the strain gages installed on the incident bar. In the tests, small fin corrugated sandwich structures with face sheets and without face sheets were used as projectiles at the impact velocities ranged between 105-200 m/s. The velocity of the projectiles was measured from the laser velocity measurement system located on the barrel of the pressure tank. Figure 3.24 shows the picture of direct impact SHPB test system. The incident bar had a length of 2000 mm, satisfying enough duration for the waves to travel. The strain gages were installed 500 mm away from the impacting end of the bar. The elastic modulus and density of bar material were 71.7 GPa and 2810 kg/m<sup>3</sup>, respectively.

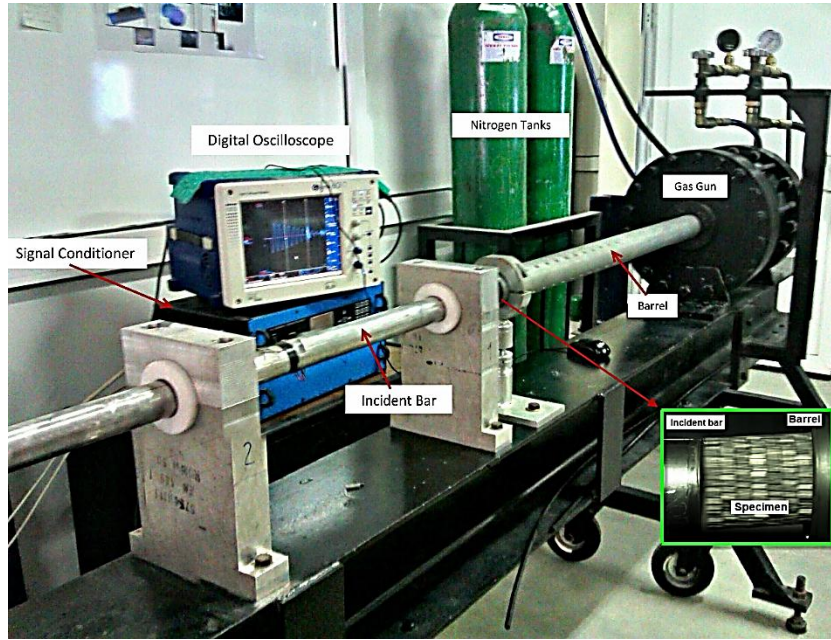


Figure 3.24. Direct impact SHPB test set-up.

The pressure generated by the corrugated sandwich structure on the aluminum SHPB was calculated by using the voltage records from the strain gages according to

$$\sigma = \left( \frac{D_b}{D_s} \right)^2 E_b \frac{2\varepsilon_t (V)}{G_g K_g V_e (1+\nu)} \quad (3.10)$$

where,  $D_b$  and  $D_s$  are the diameters of aluminum bar and corrugated sandwich structure, respectively.  $E_b$  is the elastic modulus of the bar,  $\varepsilon_t (V)$  is the recorded wave in terms of voltage,  $G_g$  is the gain,  $K_g$  is gage factor,  $V_e$  is the excitation voltage and  $\nu$  is the Poisson's ratio. In the experiments, the gain and the excitation voltage were set to 125 and 5 V, respectively.

### 3.5.4. Projectile Impact Tests with Corrugated Projectiles

Projectile impact tests were conducted on the composite and big fin corrugated core composite sandwich plates using the gas gun test set-up in order to simulate the blast-like non-explosive loading. In these tests, cylindrical small fin corrugated core sandwich projectiles ( $\phi 48mm$ ) with and without face sheets were fired on the targets. Two different types of chamber pressures were used to change the impact velocities (3 and 5 bars). The impact velocities were measured with the laser barrier located before the specimen holder and the impact event was recorded with high speed camera (20000 fps). The alignment of the corrugated projectile was difficult to control due to the corrugated structure of the projectile. Air flowed into porous structure and altered the direction of the projectiles before impact. This problem was minimized by applying a thin layer of tape through the thickness of the projectile in order to eliminate the air flow into the projectile. The displacements of the plates and sandwich structures after the tests were measured using caliper and also verified from the camera records (Figure 3.25).

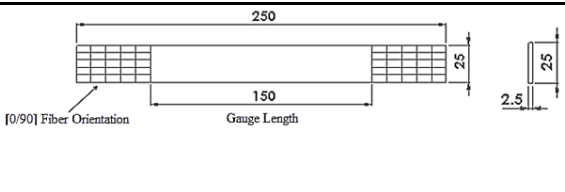
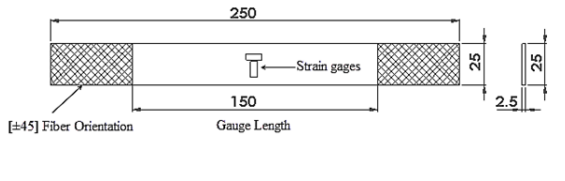
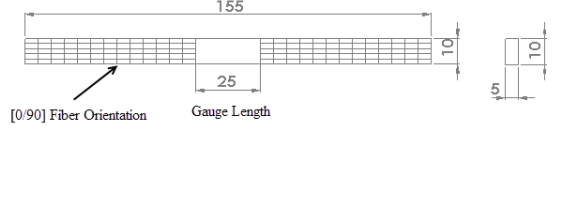
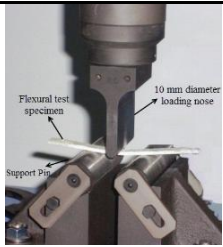
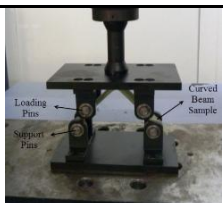
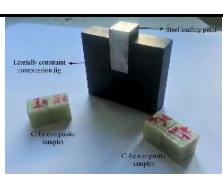


Figure 3.25. Projectile impact test set-up and high speed camera.

### 3.5.5. Summary of The Experimental Study

The experimental studies are summarized in the following tables.

Table 3.1. Summary of experimental tests on composite samples.

Test	Specimen dimensions	Figures
In-Plane Tensile Testing ASTM D 3039M		
In-Plane Shear Testing ASTM D 3518		
Quasi-static Compression Test ASTM D 3410		
Flexural Test ASTM D 790-92	130 mm long and 12.7 mm wide	
4 Point Bending Test ASTM D 6415	25 mm in width, 90 mm in length and 5 mm in thickness	
Laterally Constraint Compression Test	12.7x12.7x12.7 mm	
Low Velocity Impact Test	100x100x3 mm	

(cont. on next page)

Table 3.1 (cont.)

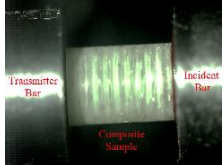
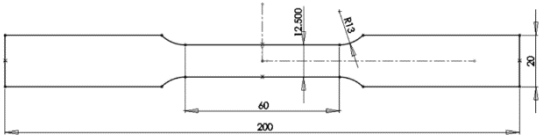
Test	Specimen dimensions	Figures
Projectile Impact Test	200x200 mm plates	
SHPB Test	9.81 mm in diameter and 14.715 mm in length with a L/D ratio of 1.5	

Table 3.2. Summary of experimental tests on corrugated sandwich structures.

Tensile Test ASTM E 8M-04		
Quasi-Static Compression	cylindrical 40 mm diameter, 48 mm in length	
Direct Impact Tests	cylindrical 40 mm diameter, 48 mm in length	
Projectile Impact Tests with Corrugated Projectiles	200x200 mm plates	

## CHAPTER 4

### NUMERICAL MODELS

#### 4.1. Introduction

MAT\_162 material model parameters were input to the impact damage simulation of E-glass/Polyester composite plates. This material model is capable of simulating matrix damage, fiber fracture, delamination and fiber crush. The determined material model parameters were first calibrated then validated. Finally, the optimized parameters were incorporated to the simulations to predict the damage in composite plates and big fin corrugated composite sandwich structures. The corrugated structures investigated were modelled using MAT\_98 material model.

#### 4.2. Modeling Tools and Methodology

The numerical modeling steps are shown in Figure 4.1 and consists of solid structure modeling, mesh application, pre-processing the simulation, the solution and verification of numerical results. The 3D modeling of the geometries were performed in Solidworks and saved as IGES files. These files were opened with Hypermesh meshing software. The composite samples were meshed with quad elements. The meshed structures were saved as .k files and exported to LS-PrePost software to define material properties, boundary conditions, contacts, test conditions, termination time and mass scaling for quasi-static testing. The solution was implemented in LS-DYNA SOLVER and the numerical results were compared with the experimental results. Inverse modeling techniques were applied to improve numerical results.

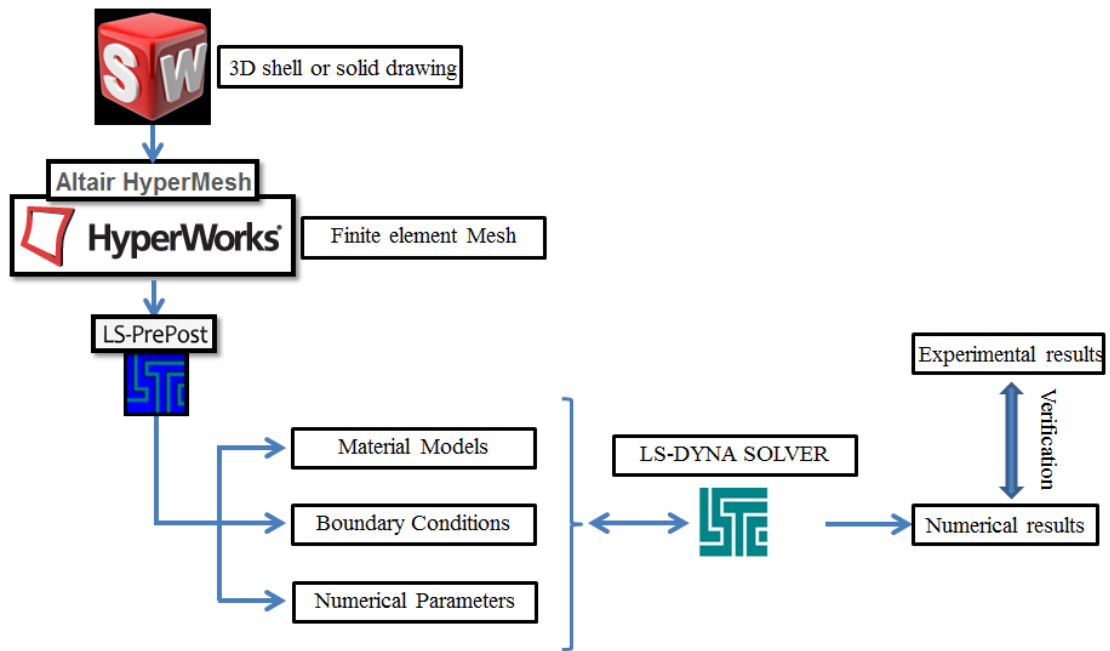


Figure 4.1. Steps in numerical model.

### 4.3. MAT\_162 Composite Material Model

In LS-DYNA PrePost software, the composite plates and composite test specimens were modeled using MAT\_COMPOSITE\_MSC\_DMG (MAT\_162) material model. The principle directions of X, Y and Z are represented as a, b and c in the material model, respectively. The MAT\_162 material model predicts the fiber fill tensile/shear failure, fiber warp tensile/shear failure, in-plane compressive failure in fiber fill and warp directions, the crush failure under compressive pressure and in-plane and through-thickness matrix failure modes.

#### 4.3.1. Failure Criteria

Unidirectional and fabric lamina models are the two model to simulate failure in composites, while fabric lamina model is used in the simulations since the fiber architecture in E-glass lamina is biaxial.

### 4.3.1.1. Tensile/Shear Failure Modes

The fill and warp fiber tensile/shear failure are given in the Hashin's failure criteria by the quadratic interaction between the associated axial and shear stresses as

$$f_1 = \left(\frac{\langle\sigma_a\rangle}{S_{aT}}\right)^2 + \frac{(\tau_{ab}^2 + \tau_{ca}^2)}{S_{aFS}^2} - 1 = 0 \quad (4.1)$$

$$f_2 = \left(\frac{\langle\sigma_b\rangle}{S_{bT}}\right)^2 + \frac{(\tau_{ab}^2 + \tau_{bc}^2)}{S_{bFS}^2} - 1 = 0 \quad (4.2)$$

where,  $S_{aT}$  and  $S_{bT}$  are the axial tensile strengths in the fill and warp directions,  $S_{aFS}$  and  $S_{bFS}$  are the layer shear strengths due to fiber failure in the fill and warp directions. These failure criterion are applicable when  $\sigma_a$  or  $\sigma_b$  is positive. It is assumed that

$$S_{aFS} = SFS \text{ and } S_{bFS} = SFS * \left(\frac{S_{bT}}{S_{aT}}\right).$$

### 4.3.1.2. Compression Failure Modes

When  $\sigma_a$  or  $\sigma_b$  is compressive, in-plane compressive failure are given by the maximum stress criterion in both fill and warp directions as

$$f_3 = \left(\frac{\langle\sigma_a^i\rangle}{S_{aC}}\right)^2 - 1 = 0, \quad \sigma_a^i = -\sigma_a + \langle-\sigma_c\rangle \quad (4.3)$$

$$f_4 = \left(\frac{\langle\sigma_b^i\rangle}{S_{bC}}\right)^2 - 1 = 0, \quad \sigma_b^i = -\sigma_b + \langle-\sigma_c\rangle \quad (4.4)$$

where,  $S_{aC}$  and  $S_{bC}$  are the axial compressive strengths in the fill and warp directions, respectively. The crush failure under hydrostatic pressure ( $p$ ) is

$$f_5 = \left(\frac{\langle p \rangle}{S_{FC}}\right)^2 - 1 = 0, \quad p = -\frac{\sigma_a + \sigma_b + \sigma_c}{3} \quad (4.5)$$

where,  $S_{FC}$  is the crush strength of the fiber in the through thickness direction.

#### 4.3.1.3. Shear Failure Mode

Plain weave fibers can fail under in-plane shear without fiber fracture. In-plane matrix failure mode is given as

$$f_6 = \left( \frac{\tau_{ab}}{S_{ab}} \right)^2 - 1 = 0 \quad (4.6)$$

where,  $S_{ab}$  is the layer shear strength due to matrix shear failure.

#### 4.3.1.4. Delamination Failure Mode

The delamination failure is expected to be a mainly matrix failure, which is due to the quadratic interaction between thickness stresses and given as

$$f_7 = S^2 \left\{ \left( \frac{\langle \sigma_c \rangle}{S_{cT}} \right)^2 + \left( \frac{\tau_{bc}}{S_{bc}} \right)^2 + \left( \frac{\tau_{ca}}{S_{ca}} \right)^2 \right\} - 1 = 0 \quad (4.7)$$

$$\begin{Bmatrix} S_{ca} \\ S_{bc} \end{Bmatrix} = \begin{Bmatrix} S_{ca}^{(0)} \\ S_{bc}^{(0)} \end{Bmatrix} + \tan(\varphi) \langle -\sigma_c \rangle \quad (4.8)$$

where,  $S_{cT}$  is through the thickness tensile strength,  $S_{bc}$  and  $S_{ca}$  are shear strengths which are assumed to depend on the compressive normal stress  $\sigma_c$  and  $\varphi$  is the internal friction angle.

### 4.3.2. Damage Model

The damage functions are derived from the failure criteria of fiber and matrix failure modes by ignoring the Poisson's effect. Elastic moduli reduction is expressed in terms of the associated damage parameters  $\bar{w}_i$  as

$$E'_i = (1 - \bar{w}_i) \cdot E_i \quad (4.9)$$

$$\bar{w}_i = 1 - \exp(-r_i^{m_i} / m_i); \quad r_i > 0, \quad i = 1, \dots, 6 \quad (4.10)$$

where,  $E_i$  is the initial elastic modulus,  $E'_i$  is the reduced elastic modulus,  $r_i$  is the damage thresholds computed from the associated damage functions for fiber damage, matrix damage and delamination and  $m_i$  is the material damage parameter. The damage function is formulated to account for the overall nonlinear elastic response of a lamina including the initial hardening and subsequent softening beyond the ultimate strength. Four damage parameters of  $m$  are used to model the post elastic damage response under different loading conditions. These are

- $m_1$  = Fiber damage in X direction,
- $m_2$  = Fiber damage in Y direction,
- $m_3$  = Fiber crush and punch shear damage,
- $m_4$  = Matrix failure and delamination damage.

### 4.3.3. Strain Rate Effect

Strain rate sensitivities in terms of the strength properties of composite are formulated as

$$\{S_{rt}\} = \{S_0\} \left( 1 + C_{rate1} \ln \frac{\dot{\epsilon}}{\dot{\epsilon}_0} \right) \quad (4.11)$$

$$\{S_{RT}\} = \begin{Bmatrix} S_{aT} \\ S_{aC} \\ S_{bT} \\ S_{bC} \\ S_{FC} \\ S_{FS} \end{Bmatrix} \quad \text{and} \quad \{\dot{\bar{\epsilon}}\} = \begin{Bmatrix} \dot{\epsilon}_a \\ \dot{\epsilon}_a \\ \dot{\epsilon}_b \\ \dot{\epsilon}_b \\ \dot{\epsilon}_c \\ (\dot{\epsilon}_{ca}^2 + \dot{\epsilon}_{bc}^2)^{1/2} \end{Bmatrix} \quad (4.12)$$

Strain rate sensitivities and damage parameters in terms of the elastic moduli of composites are given as

$$\dot{E}_i = (1 - \varpi_i)E_i \quad (4.13)$$

$$\{E_{rt}\} = \{E_0\} \left( 1 + \{C_{rate}\} \ln \frac{\dot{\bar{\epsilon}}}{\dot{\bar{\epsilon}}_0} \right) \quad (4.14)$$

$$\{E_{RT}\} = \begin{Bmatrix} E_a \\ E_b \\ E_c \\ G_{ab} \\ G_{bc} \\ G_{ca} \end{Bmatrix}, \quad \{\dot{\bar{\epsilon}}\} = \begin{Bmatrix} |\dot{\epsilon}_a| \\ |\dot{\epsilon}_b| \\ |\dot{\epsilon}_c| \\ |\dot{\epsilon}_{ab}| \\ |\dot{\epsilon}_{bc}| \\ |\dot{\epsilon}_{ca}| \end{Bmatrix} \quad \text{and} \quad \{C_{rate}\} = \begin{Bmatrix} C_{rate2} \\ C_{rate2} \\ C_{rate4} \\ C_{rate3} \\ C_{rate3} \\ C_{rate3} \end{Bmatrix} \quad (4.15)$$

There are 4 strain rate parameters. These are

- $C_1$  = Strain rate constant for strength properties,
- $C_2$  = Strain rate constant for elastic moduli in the X direction,
- $C_3$  = Strain rate constant for shear moduli,
- $C_4$  = Strain rate constant for elastic moduli in the Z direction.

#### 4.3.4. Delamination Factor

When failure occurs by delamination in the elements that are adjacent to the ply interface, the failure plane is expected to be parallel to the layering planes and thus can be referred to as the delamination damage mode. Scale factor of S is introduced to provide better correlation of experimental delamination. The adjacent planes of fiber

layers in the simulations were defined by BETA command in the material model. The beta values for adjacent ply layers were adjusted as  $0^\circ$  and  $90^\circ$  in the numerical models. A delamination scale factor was used to account for stress concentrations. The value of S are used to calibrate the predicted delamination area with the experiments. In the numerical models, the value of S was set to 1.2.

#### **4.3.5. Element Erosion**

There are three element erosion criteria in MAT\_162 material model. The erosion criterion is important since the eroded elements can cause negative volume errors, numerical instabilities and excessive computational time. The failed elements are eroded in any of three ways:

1. If the tensile strain in both in-plane directions X and Y exceeds the E\_LIMT value.
2. If compressive relative volume in a failed element is smaller than ECRSH value.
3. If tensile relative volume in a failed element is greater than EEXPN.

In the numerical models, EEXPN=E\_LIMT= 4 and E\_CRSH= 0.001 were chosen following the parametric studies.

#### **4.4. Quasi-static Tension Test Numerical Modeling**

In the tensile test numerical model (Figure 4.2), the mesh sensitivity of the composite material and the damage parameters of m1 and m2 were calibrated. The model test specimen had the same dimensions as the test specimens. The clamps of the test machine were simulated by SET\_NODE card. The bottom side of the composite material was fully constraint in three translational and rotational directions while the top side was only free to move in the X axis. The motion of the moving end was defined with PRESCRIBED\_MOTION\_SET in X direction with the same testing speed as the experiment. Each composite layer with a thickness of 0.6125 mm was modeled with constant stress solid elements. The fiber orientation of  $0^\circ$  and  $90^\circ$  was applied to the

composite layers using BETA option in MAT\_162 material card. The ERODING\_SINGLE\_SURFACE contact was defined and the static and dynamic coefficient of friction were taken 0.3 and 0.2, respectively. Square mesh elements were used to avoid localized and unbiased damage progression. The mesh element sizes were varied between 1 mm and 2.5 mm in axial and longitudinal directions in order to determine the optimum mesh size. The mesh size of 2.5x2.5 mm had shown the best agreement with experiments. The damage parameters m1 and m2 were assumed to be equal because of the biaxial nature of the E-glass fiber. In the simulations, the m1 and m2 damage parameters were varied between 1 and 4. The best agreement between experimental and numerical results was found when m1=m2=4. EXTENT\_BINARY option was also defined to determine failure modes.

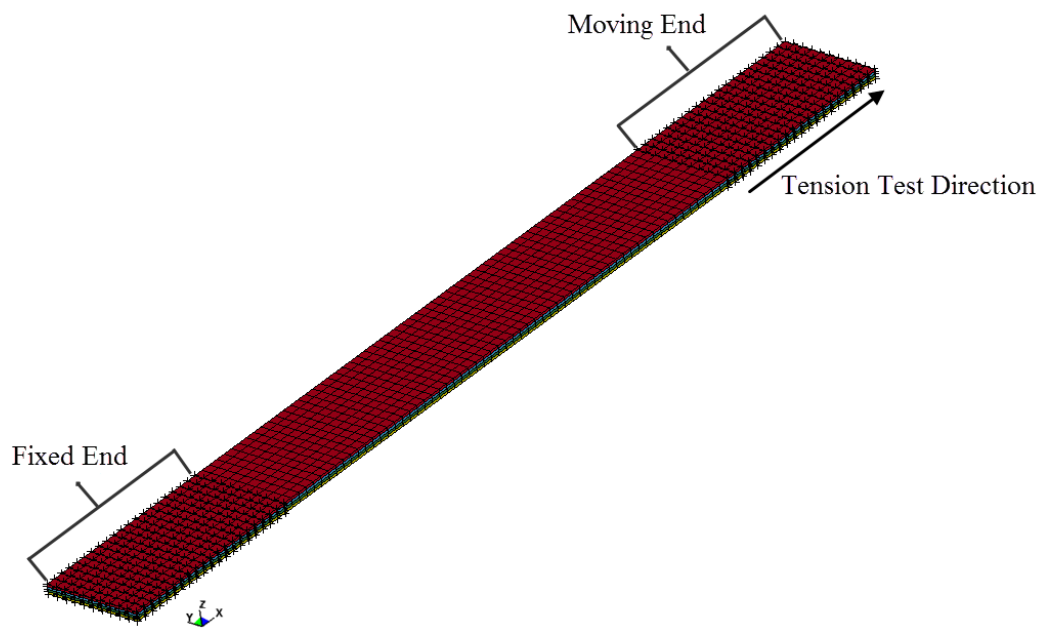


Figure 4.2. The numerical model of the composite tension test specimen.

#### 4.5. Quasi-static Compression Test Numerical Modeling

The quasi-static compression test simulations were conducted in accord with ASTM D3410 test standard [103]. The sample in the numerical model had the same dimensions as in the experiments (Figure 4.3). The testing fixtures and the loading column of the test machine were simulated by SET\_NODE card. The bottom side of the

composite material was fully constraint in three translational and rotational directions while the top side was only free to move in the X axis. The motion of the moving end was defined with PRESCRIBED\_MOTION\_SET in X direction with the same testing speed as in the experiment. Each composite layer with a thickness of 0.6125 mm was modeled with constant stress solid elements. The fiber orientation of 0° and 90° was applied to the composite layers using BETA option. The ERODING\_SINGLE\_SURFACE contact was defined for the composite material and the static and dynamic coefficient of friction were set to 0.3 and 0.2, respectively. The mesh size was 2.5 mm x 2.5 mm in in-plane directions and the damage parameters m1 and m2 were set to 4. EXTENT\_BINARY option was also defined to determine failure modes.

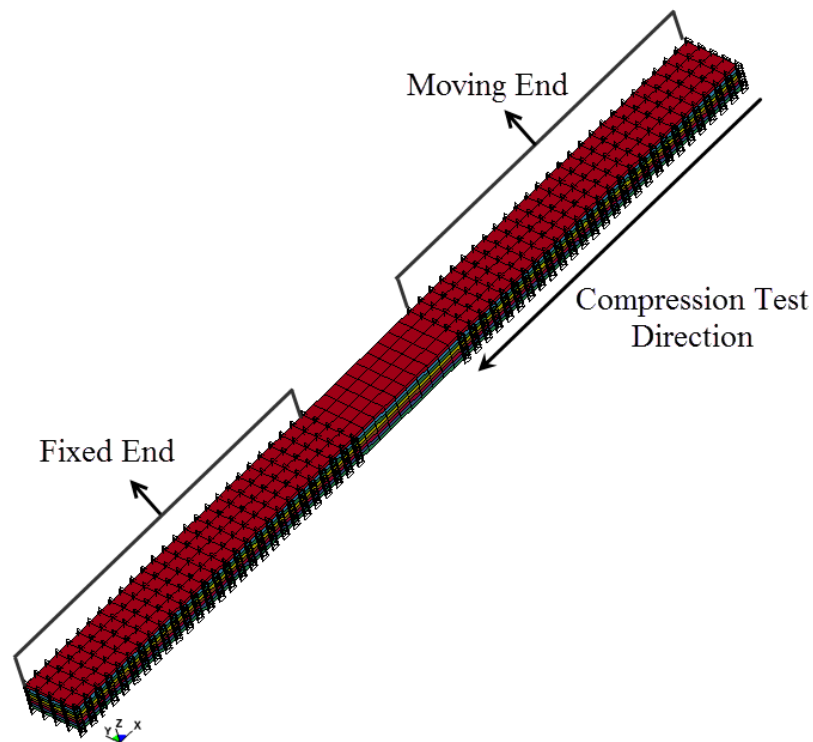


Figure 4.3. The numerical model of the composite compression test specimen.

#### 4.6. Quasi-static Shear Test Numerical Modeling

In the shear test numerical modeling (Figure 4.4), the matrix damage parameter m4 was calibrated. The shear test model was similar to the tension test model but the BETA option in the MAT\_162 material model was set to  $\pm 45^\circ$  for the adjacent

composite layers as stated in the ASTM D3518 test standard [102]. The boundary conditions and the motion of the cross-head were defined with the SET\_NODE card. The bottom side of the composite material was fully constraint while top side was free to move in X translational direction. The numerical model speed was the same as the experiments defined by the PRESCRIBED\_MOTION\_SET in X direction. Each composite layer with a thickness of 0.6125 mm was modeled with constant stress solid elements. The ERODING\_SINGLE\_SURFACE contact was defined for the composite material. The mesh sizes for both in-plane directions were 2.5 mm x 2.5 mm. A hardening stress-strain response was expected in the shear test therefore the value of m4 was selected less than zero. The optimum m4 value was determined to be -0.15 after iterations. EXTENT\_BINARY option was defined to determine failure modes.

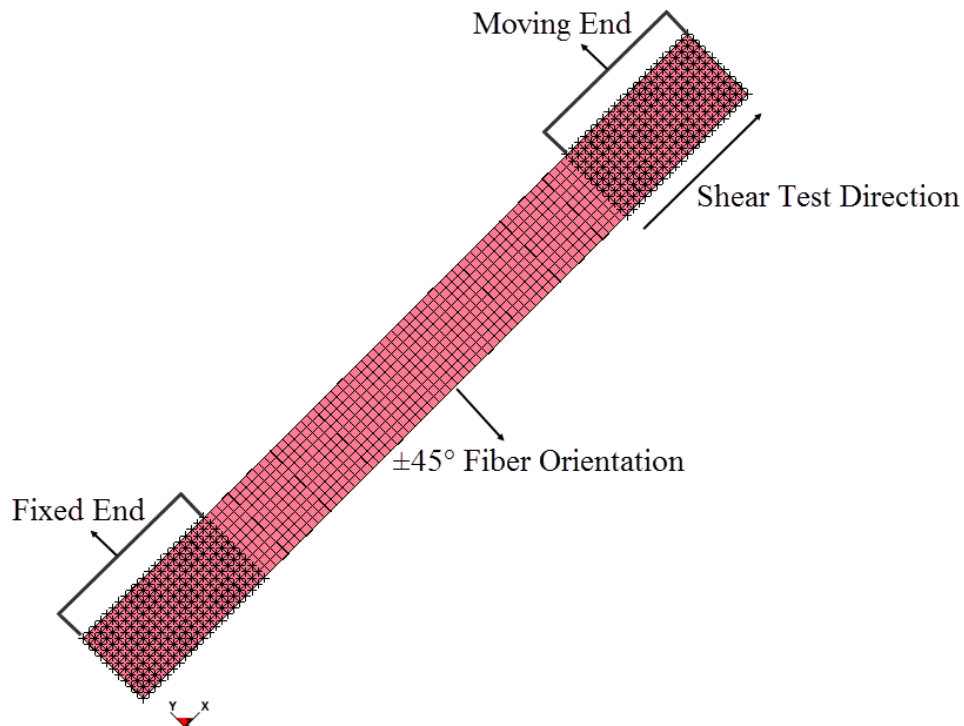


Figure 4.4. The numerical model of the composite shear test specimen.

## 4.7. Flexural Test Numerical Modeling

In the finite element model of the flexural test (Figure 4.5), the loading cross-head and the rigid supports were fully modeled using constant stress solid elements. The composite material consisted of solid element layers. The cross-head and the supports

were modelled using steel rigid material model. The supports were fully constrained in both translational and rotational directions, while the cross-head was only able to move in the Z translational direction. The motion of the cross-head was defined using PRESCRIBED\_MOTION\_RIGID with the input of the velocity time data obtained from the experiments. The simulation was terminated when the cross-head reached a total displacement of 5 mm. AUTOMATIC\_SINGLE\_SURFACE contact was defined for the composite material. AUTOMATIC\_SURFACE\_TO\_SURFACE contact was defined between composite material and the cross-head. The same contact algorithm was used between rigid supports and composite material. EXTENT\_BINARY option was defined to determine failure modes.

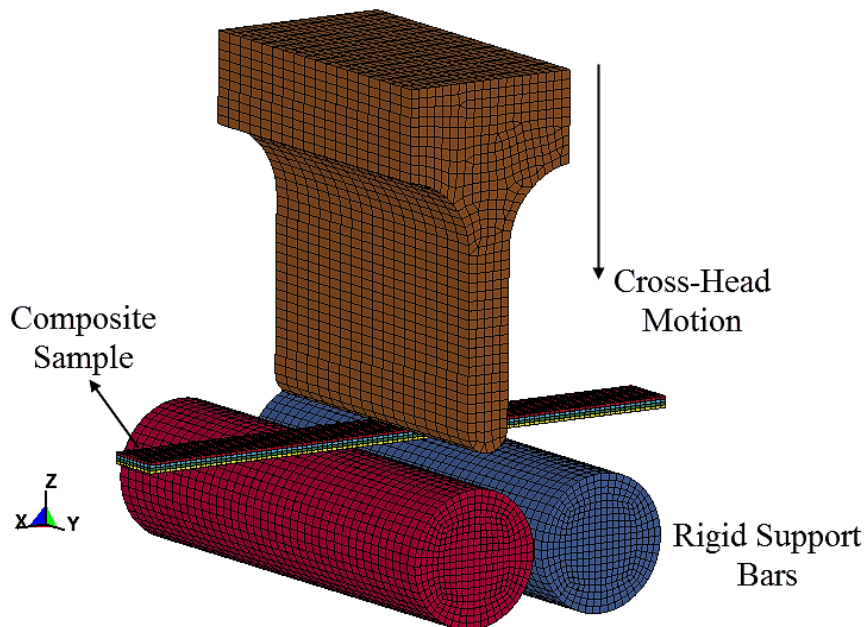


Figure 4.5. Finite element model of quasi-static flexural test.

#### 4.8. Low Velocity Impact Test Modeling

The modulus reduction parameter OMGMX was determined by the simulation of low velocity impact tests. The values of OMGMX were varied in the simulations in order to find the best agreement between model and low velocity tests. The OMGMX parameter varied between 0.994 and 0.999 by keeping the other parameters constant. The low velocity impact simulations were conducted on 3 mm thick composite samples

with two different velocities: 4.21 and 6.12 m/s. An AUTOMATIC\_SINGLE\_SURFACE contact definition was applied between composite sample plies. AUTOMATIC\_SURFACE\_TO\_SURFACE was applied between rigid supports and the composite sample while ERODING\_SURFACE\_TO\_SURFACE contact algorithm for penetration condition was applied between 20 mm diameter hemispherical indenter and the composite plate. The MAT\_162 material model requires solid elements be used in the analysis and there were 96904 constant stress solid elements in this model. A static coefficient of friction of 0.3 and a dynamic coefficient of friction of 0.2 were applied within all types of contact algorithms. The additional weights in the low velocity impact tests were not modeled in the simulation studies, the total weight was imposed on the indenter by increasing its density (Figure 4.6).

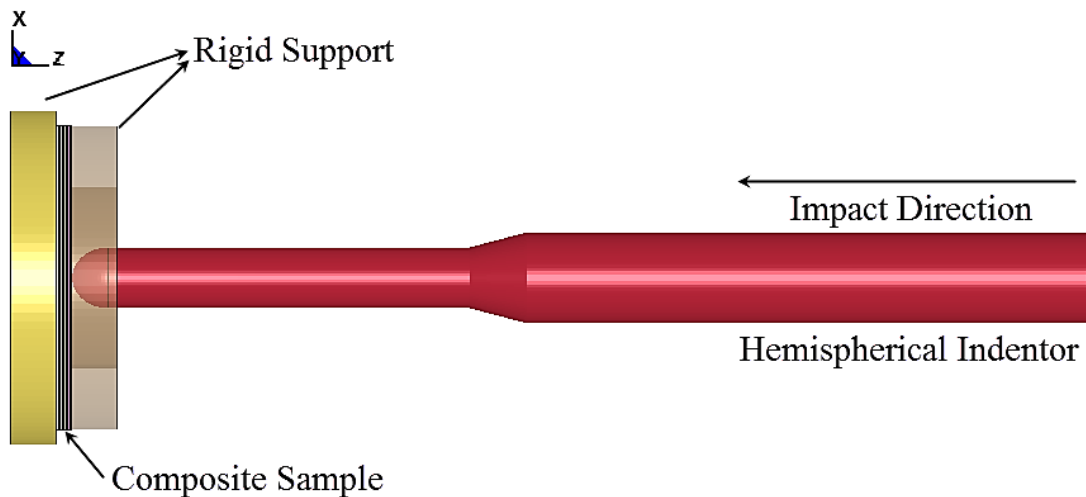


Figure 4.6. Low velocity impact model used in simulations.

#### 4.9. Projectile Impact Test Modeling

The penetration erosion parameters E\_LIMT and EEXPN were determined by simulating projectile impact tests (Figure 4.7). Both ECRSH and EEXPN erode elements based on the ratio of the initial volume of the element to the current volume of the element. For element expansion the element was eroded when the volume ratio was greater than the EEXPN value. Fiber tension in both in-plane directions controlled the value of E-LIMT, when the tension in both in-plane directions exceeded the value of E-LIMT, the elements were eroded. By setting the two values equal, the E\_LIMT erosion

criterion was suppressed and the volumetric strain EEXP<sub>N</sub> controlled the element erosion in the calculations. In the parametric study, E\_LIMT=EEXP<sub>N</sub> varied from 3 to 4. In the simulation, 131864 constant stress solid elements were used. An ERODING\_SINGLE\_SURFACE contact definition was applied between composite sample plies. AUTOMATIC\_SURFACE\_TO\_SURFACE was applied between rigid supports and the composite sample while ERODING\_SURFACE\_TO\_SURFACE contact algorithm for penetration condition was applied between 30 mm diameter sphere projectile and the composite plate. In the analysis, the residual velocity of the spherical projectile was compared with the experimental results in order to validate correct E\_LIMT and EEXP<sub>N</sub> values and also the remaining MAT\_162 material model parameters.

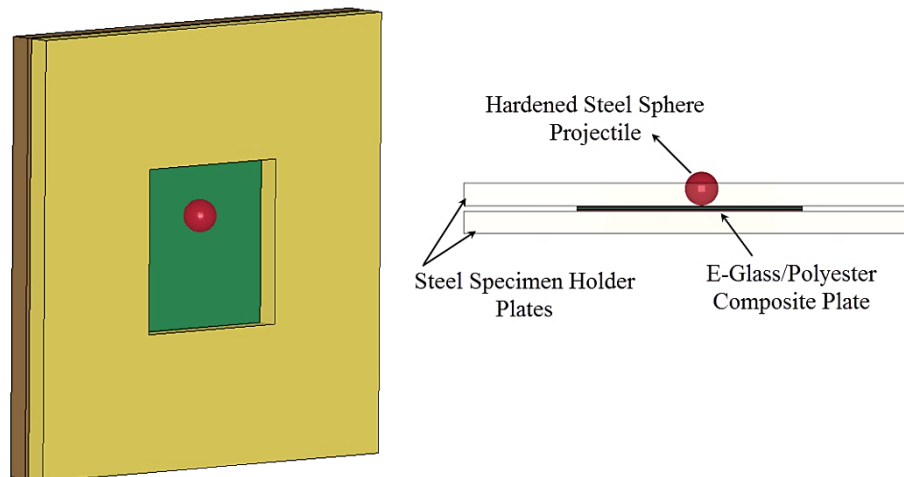


Figure 4.7. Projectile impact test model used in simulations.

#### 4.10. Trapezoidal Corrugated Fin Layers Geometric Modeling and Mesh Generation Studies

The three dimensional models of big and small fin corrugated layers were developed in Solidworks CAD software. The full geometrical numerical models of the experiments were developed in non-linear explicit FE code LS-DYNA. In both layer types, a unit fin was modeled at the beginning (Figure 4.8(a) and Figure 4.9(a)). The unit fins created in CAD software were meshed to predefined finite elements as shown in Figure 4.8 (b) and Figure 4.9(b). Then, generated mesh was duplicated in the direction of x-axis (Figure 4.8 (c) and Figure 4.9(c)). After that, whole structure was

uplicated in y-axis and moved in the direction of x-axis simultaneously to create zig-zag form (Figure 4.8(d) and Figure 4.9(d)).

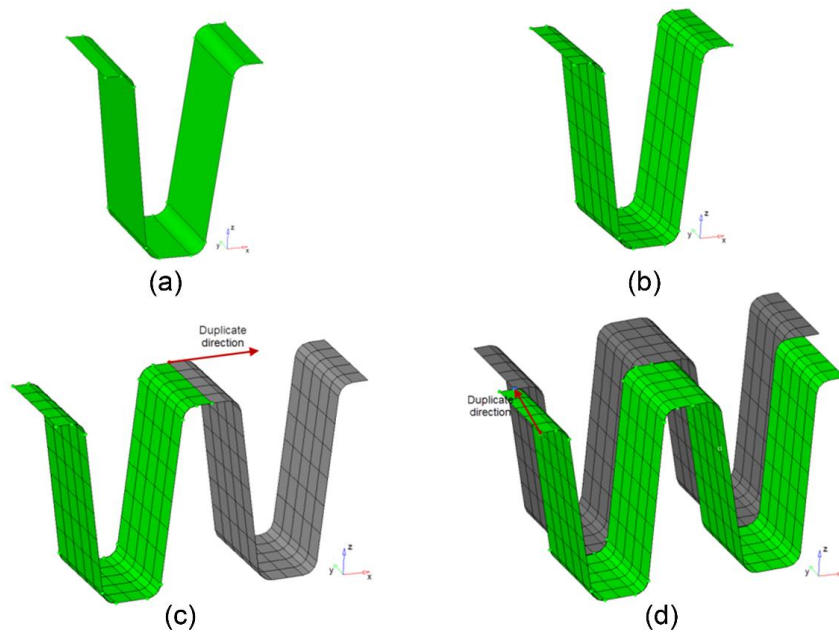


Figure 4.8. Mesh generation of a big fin corrugated core sheet; (a) CAD geometry, (b) meshing, (c) duplication in x-axis and (d) duplication in y-axis.

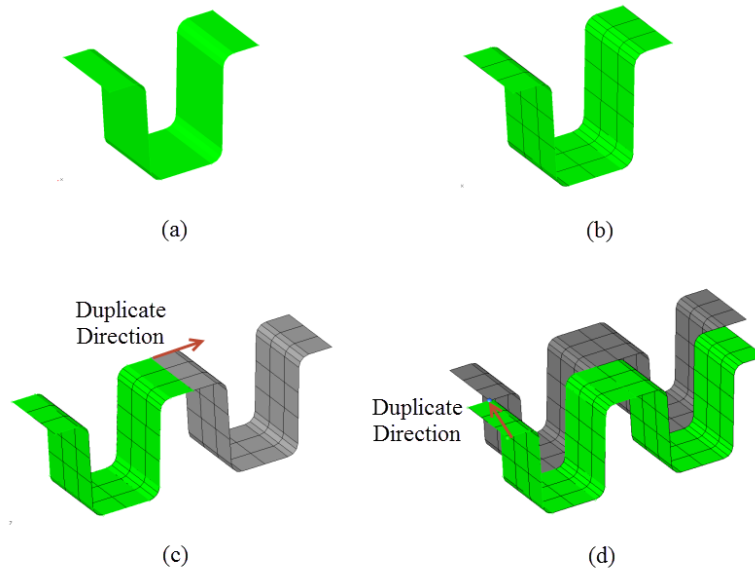


Figure 4.9. Mesh generation of a small fin corrugated core sheet; (a) CAD geometry, (b) meshing, (c) duplication in x-axis and (d) duplication in y-axis.

## 4.11. Material Models

### 4.11.1. Simplified Johnson-Cook (JC) Material Model

MAT\_SIMPLIFIED\_JOHNSON\_COOK material model, material type 98 in LS-DYNA, was used to model the flow stress of 1050 H14 Al alloy in numerical simulations. Johnson and Cook (JC) flow stress model is given as [110]

$$\sigma = \left[ A + B\varepsilon^n \right] \left[ 1 + c \ln \left( \frac{\dot{\varepsilon}}{\dot{\varepsilon}_0} \right) \right] \left[ 1 - \left( T^* \right)^m \right] \quad (4.16)$$

where  $\sigma$ ,  $\varepsilon$ ,  $\dot{\varepsilon}$  and  $\dot{\varepsilon}_0$ , respectively, the effective stress, effective plastic strain, strain rate and reference strain rate;  $A$ ,  $B$ ,  $n$ ,  $c$  and  $m$  are the model parameters. The last term  $T^*$  is expressed as

$$T^* = \frac{T - T_r}{T_m - T_r} \quad (4.17)$$

where,  $T$  is the temperature and  $T_r$  and  $T_m$  are the reference and melting temperatures, respectively. Material type 98 does not take into account temperature effect expressed in the last bracket of Eqn. 4.16. As aluminum alloys are known to have negligible strain rate dependent flow stresses: the second bracket of Eqn. 4.16 is omitted in the material model.

## 4.12. Numerical Models of Compression of Multi-layer Corrugated Sandwiches

The handling of the fin layers, during brazing process and later cutting with electro discharge machine induced random imperfections on the fin walls. Two types of imperfections were detected on the test samples: fin wall bending and fin wall bulge formation as shown by arrows in Figure 4.10.

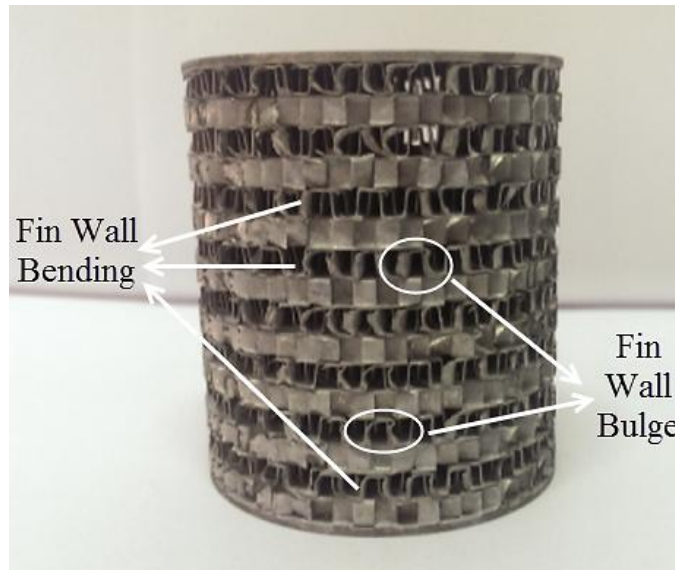


Figure 4.10. Imperfections in corrugated sandwich structures.

The effect of induced fin wall imperfection was simulated by the implementation of imperfect models. In the imperfect model, bending type imperfection (3 mm in length) was introduced to the half of the fin walls, with a radius of 1.4 mm and an angle of  $26.92^\circ$  from the original fin wall as depicted in Figure 4.11. The numerical imperfect models were implemented using the bending type imperfection, while the effect of the length of the imperfection was assessed by bulge type imperfection with a radius of 1.25 mm and length of 0.8 mm as shown in Figure 4.12.

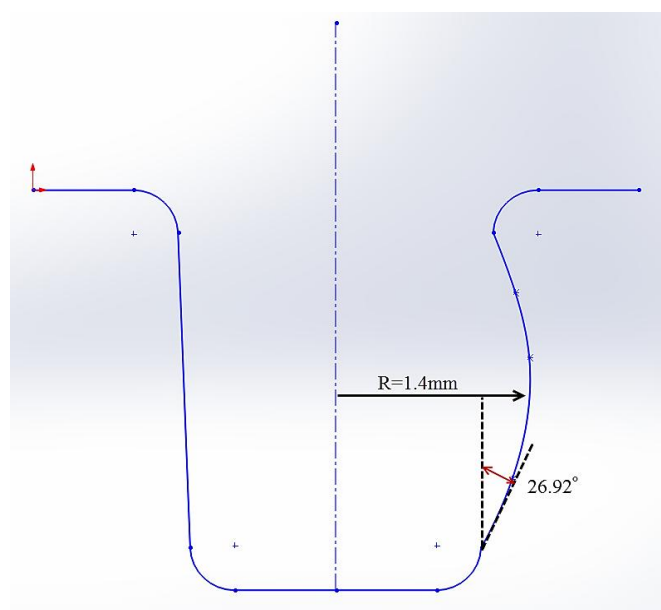


Figure 4.11. Fin wall bending type of imperfection in a unit fin.

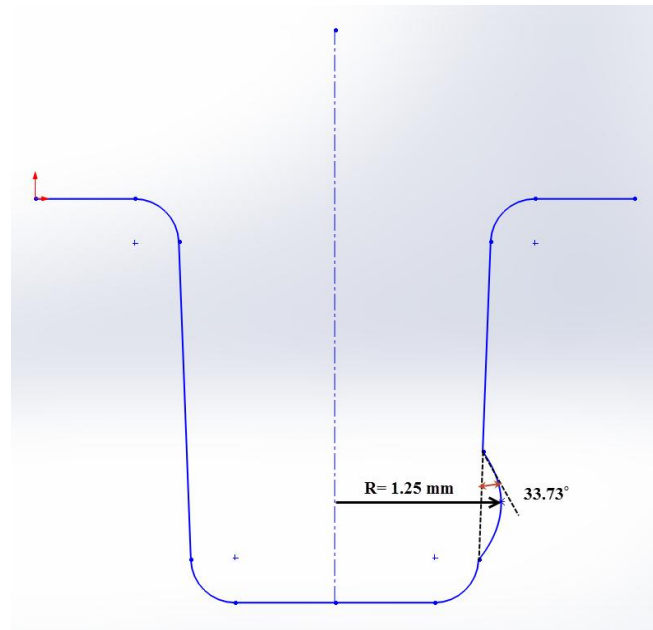


Figure 4.12. Fin wall bulge imperfection in a unit fin.

The numerical perfect models of the multilayer corrugated core sandwich structures with face sheets and without face sheets are sequentially shown in Figures 4.13 (a) and (b). The corresponding imperfect models with all fin wall bending and mixed imperfection with fin wall bending and fin wall bulge formation are sequentially shown in Figures 4.14 (a) and (b). Furthermore, by inspecting the quasi-static compression test results from the camera records that the deformation starts in certain core layers and another model was prepared only applying imperfections to these certain layers (Figure 4.14(c)). The adhesive effect was given to the numerical models by using duplicate node tool in LS-DYNA since the adhesive locations are local and move by adhesion and cohesion forces between the contacting surfaces. The contacts between the core layers and face sheets were given by AUTOMATIC\_SINGLE\_SURFACE contact algorithm.

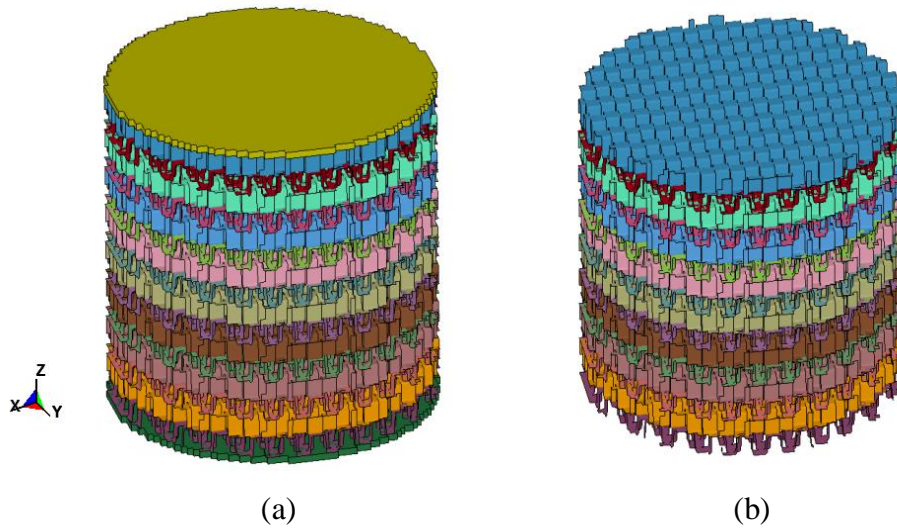


Figure 4.13. Perfect numerical models of small fin corrugated sandwich structures: (a) with and (b) without face sheets.

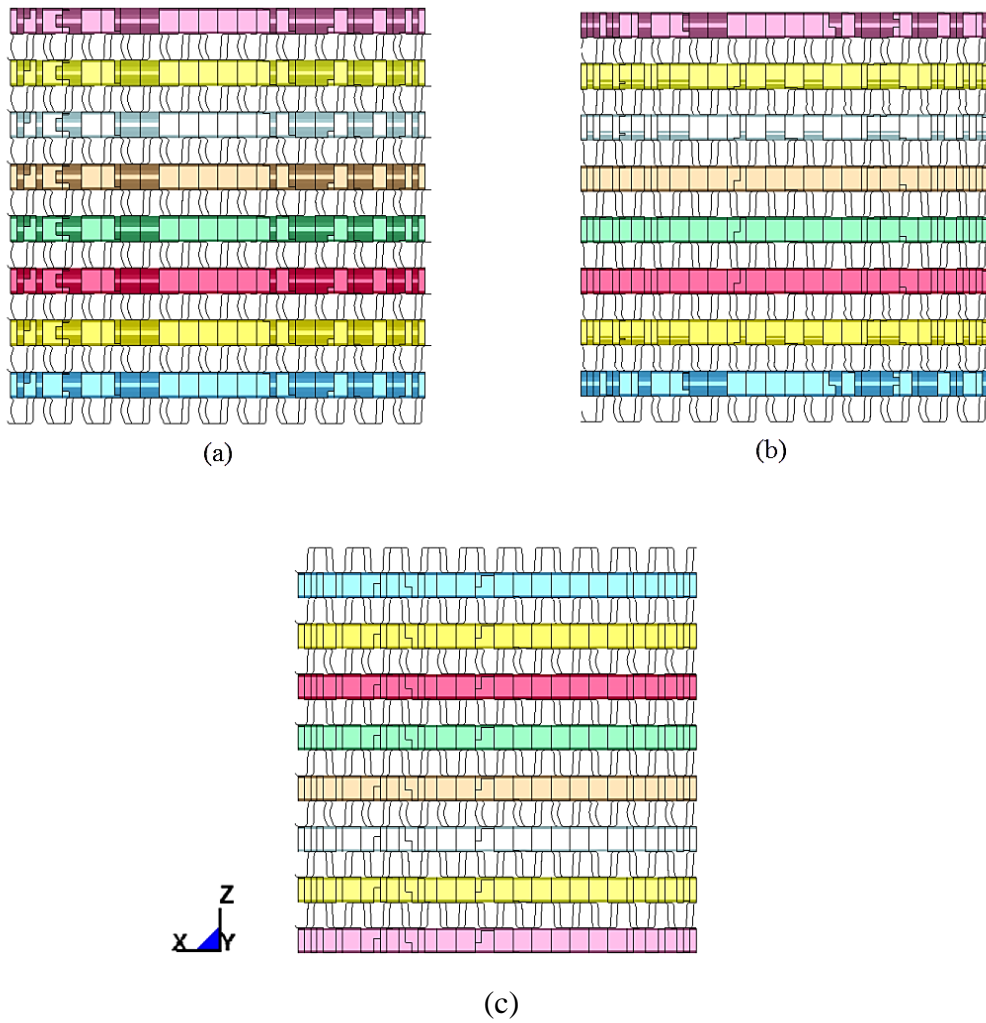


Figure 4.14. Imperfect models: (a) fin wall bending in all layers, (b) mixed imperfection and (c) layers 6 and 12 fin wall bending.

The trapezoidal corrugated fin layers were meshed using Belytschko-Tsay shell elements with five integration points and the face sheets were modeled using the constant stress solid elements. The increased number of integration points in shell elements generally leads to prolonged CPU calculation times. On the other side, in order to increase the accuracy of the models, the number of integration points should be higher than two when the buckling is the dominant deformation mode [111]. In addition, the FE meshes of the corrugated fin layers and face sheets have to coincide with each in order to be able to define contacts. This naturally limits the use of arbitrary-defined mesh distribution and element sizes. The effect of mesh size on the modeling was investigated by three types of element sizes (Figures 4.15(a-c)): (i) fine mesh consisting of 1164168 shell elements, (ii) medium mesh consisting of 527176 shell elements and (iii) coarse mesh consisting of 87350 shell elements in quasi-static compression test modeling of 16 layered sandwich structure without face sheets.

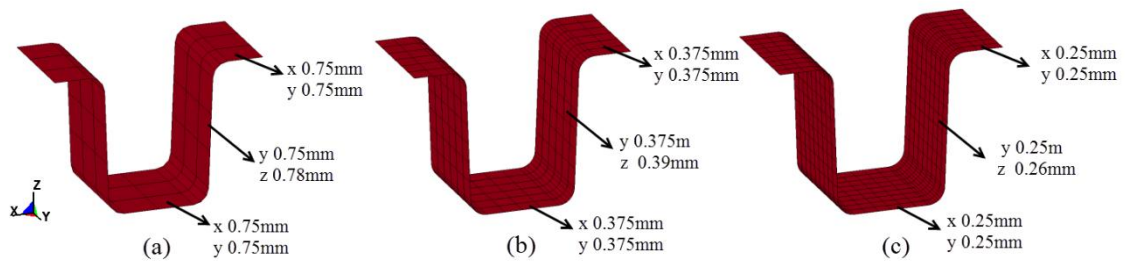


Figure 4.15. Unit fin mesh size: (a) coarse mesh, (b) medium mesh and (c) fine mesh sizes.

Figure 4.16 shows the numerical model of quasi-static compression test set-up. The model consists of the top and bottom compression test platens and specimen. Each compression test platen was modeled using 19200 constant stress solid elements. The compression platens were modeled with MAT20\_RIGID material model ( $E=210$  GPa and  $\nu=0.3$ ). In the model, the rotations and the movement of the compression platens were fully constrained, except the axial motion of the top platen in the z-direction. The axial velocity of the top platen was kept constant, the same as the experiments and defined by PRESCRIBED\_MOTION\_RIGID card. The contact between compression test platens and specimen was defined by AUTOMATIC\_SURFACE\_TO\_SURFACE contact. Since the total CPU time for the quasi-static test solutions are relatively long

[112], the mass scaling was applied in the quasi-static simulations by defining a positive time step value in CONTROL\_TIMESTEP card.

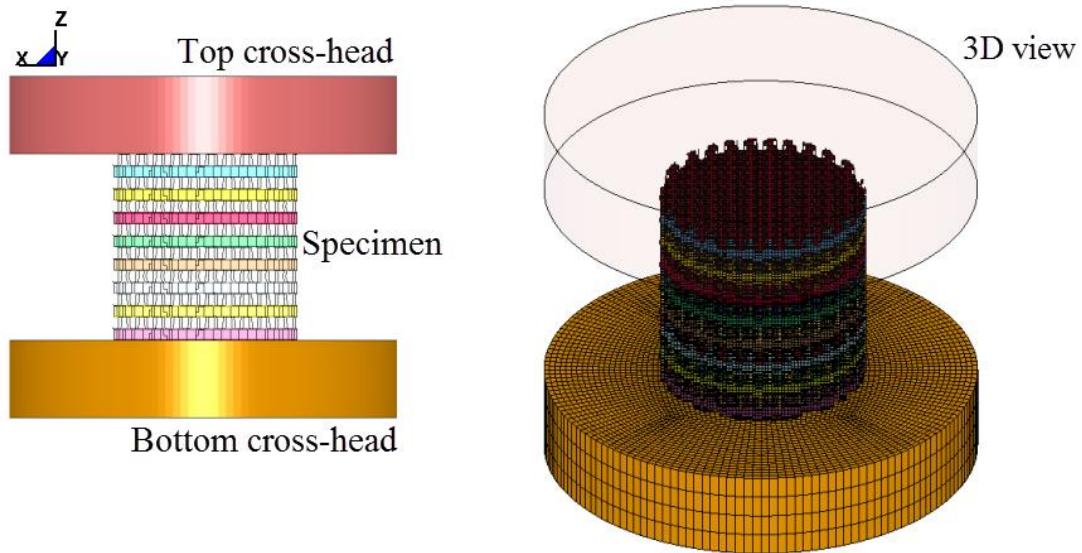


Figure 4.16. The numerical model of quasi-static compression test set-up.

The numerical model of the direct SHPB impact testing is shown in Figure 4.17. The incident bar was modeled using 20 mm size elements. The incident bar consisted of 30000 constant stress solid elements and the deformation was modeled using MAT01\_ELASTIC material model. The axial movement and the rotation of the incident bar were constrained in all directions, except the axial movement of the incident bar in the z-direction. The experimental corrugated sandwich projectile velocity, 105-200 m/s, was defined in the model using VELOCITY\_GENERATION in LS-DYNA. The contact between bar and specimen was defined by AUTOMATIC\_SURFACE\_TO\_SURFACE contact. The contact between the layers of corrugated sandwich projectile and face sheets was defined by AUTOMATIC\_SINGLE\_SURFACE contact algorithm. The static and dynamic friction coefficients were set to 0.3 and 0.2 in all contact definitions, respectively. The stress on the incident bar was calculated on the bar from an element located at the same distance with the strain gages in the experiment. FORCE\_TRANSDUCER\_PENALTY contact algorithm was applied between the layers of corrugated sandwich structure to measure the reaction forces in each layer.

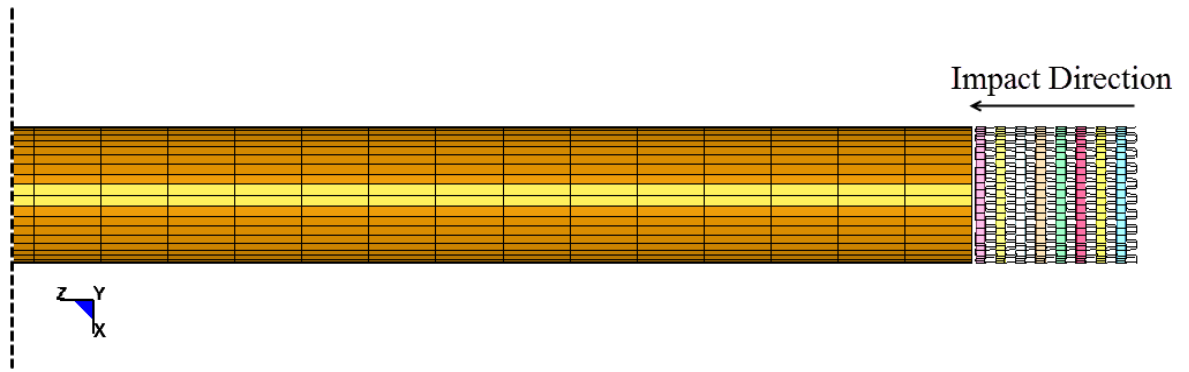


Figure 4.17. Direct SHPB impact test model with corrugated projectile.

The numerical models of the mass impact moving with the corrugated sandwich projectile and mass impact on stationary corrugated sandwich attached to the SHPB are shown in Figures 4.18 (a) and (b), respectively. In the models, the incident bar consisted of 30000 constant stress solid elements. The incident bar was modeled using MAT01\_ELASTIC material model. The axial movement and the rotations of the incident bar were constrained in all directions, except the axial movement of the incident bar in the z-direction. For the mass, rigid non-deformable 9368 solid elements were used. The impact velocity was defined to the mass by VELOCITY\_GENERATION card in LS\_DYNA. The impact velocities in the numerical models varied from 1 m/s to 200 m/s. The contact between bar and specimen was defined by AUTOMATIC\_SURFACE\_TO\_SURFACE contact. The contact between the layers of corrugated sandwich projectile and face sheets was defined by AUTOMATIC\_SINGLE\_SURFACE contact algorithm. The static and dynamic friction coefficients were set to 0.3 and 0.2 in all contact definitions, respectively. The stress values on the incident bar were calculated on the bars from an element located at the same distance with the strain gages in the experimental set-up. FORCE\_TRANSDUCER\_PENALTY contact algorithm was applied between the layers of corrugated sandwich structure to measure the each layers reaction forces.

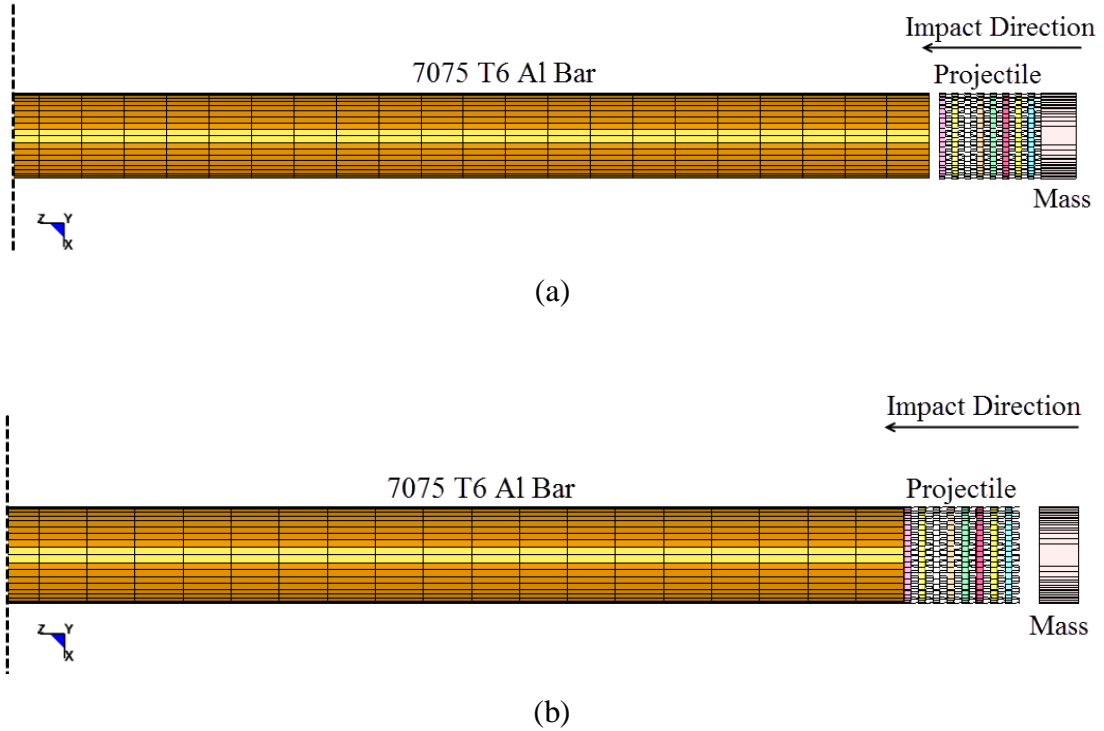


Figure 4.18. Mass impact with SHPB: (a) moving projectile and (b) stationary projectile.

The numerical model of the corrugated sandwich projectile impact on composite plate is shown in Figure 4.19. The model consisted of top-bottom frames, projectile and composite plate specimen. The frames were considered to be rigid and each frame was comprised of 11232 solid elements. The composite plate and corrugated projectile were modelled using 35532 constant solid and 187968 shell elements, respectively. In the actual test, sandwich specimen was placed between the frames and fixed by bolts. The generated compression force due to screwing,  $\sim 500$  N, was attained in the model to the top frame by defining `LOAD_SEGMENT_SET` card in LS-DYNA. The impact velocity of the corrugated projectile was defined with the `VELOCITY_GENERATION` card in LS\_DYNA. `ERODING_SINGLE_SURFACE` contact algorithm was defined for the composite layers and `AUTOMATIC_SINGLE_SURFACE` was defined for the projectile. `AUTOMATIC_SURFACE_TO_SURFACE` contact was defined between specimen and the rigid rings. The interaction between the composite and projectile was defined with `ERODING_SURFACE_TO_SURFACE` contact type. In this type of simulations, the composite plate thicknesses were 2 mm, 5 mm and 8 mm and the projectile without face sheets were used to investigate the difference between in responses.

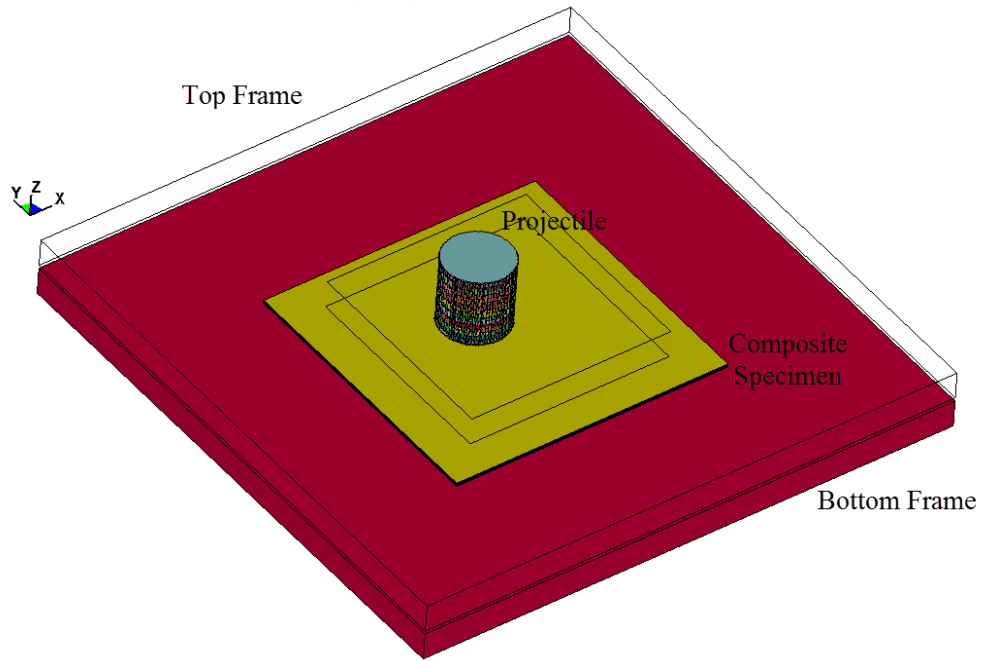


Figure 4.19. The numerical model of projectile impact on composite specimen.

The numerical model of the corrugated sandwich projectile impact on corrugated core single layer composite sandwich and 3 layer corrugated core composite sandwich are shown in Figures 4.20 (a) and (b), respectively. The models consisted of top-bottom frames, projectile and composite sandwich specimens. The frames were considered to be rigid and each frame comprised of 11232 solid elements. For the sandwich structure with 3 layers of corrugated core 343488 shell elements and 116236 constant solid stress elements including 22464 rigid elements were used. On the other hand, for the sandwich structure with single layer corrugated core, 239808 shell elements and 87116 constant solid stress elements including 22464 rigid elements were used. In the actual test, sandwich specimen was placed between frames and compressed by bolts. The generated compression force due to screwing,  $\sim 500$  N, was attained in the model to the top frame by defining `LOAD_SEGMENT_SET` card in LS-DYNA. The impact velocity of the corrugated projectile was defined with the `VELOCITY_GENERATION` card in LS-DYNA. `ERODING_SINGLE_SURFACE` contact algorithm was defined for the composite, corrugated cores and interlayer sheets and `AUTOMATIC_SINGLE_SURFACE` was defined between the corrugated layers of projectile. `AUTOMATIC_SURFACE_TO_SURFACE` contact was defined between specimen and the rigid rings. The interaction between the composite sandwich and projectile was defined with `ERODING_SURFACE_TO_SURFACE` contact type. In

this type of simulations, the projectile without face sheets was also used to investigate the difference between in responses. The impact positions of the corrugated sandwich projectiles were determined from the test specimens in order to validate and compare the test results.

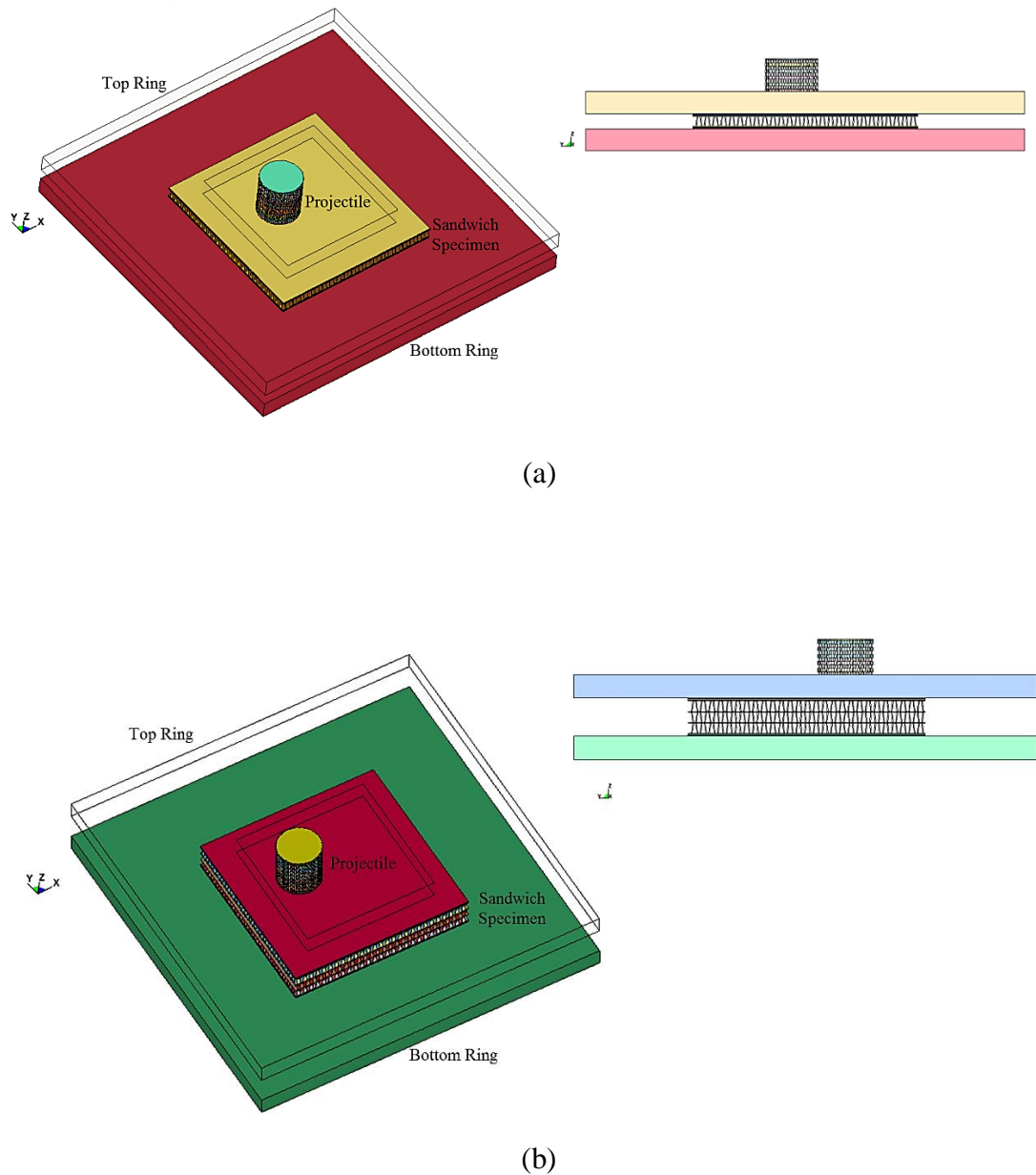


Figure 4.20. Projectile impact on sandwich structures with; (a) single corrugated core and (b) 3 layered corrugated core.

### 4.13. Summary of The Numerical Study

The numerical studies conducted on both composites and corrugated structures are summarized in the following tables.

Table 4.1. Summary of the numerical models on composite samples.

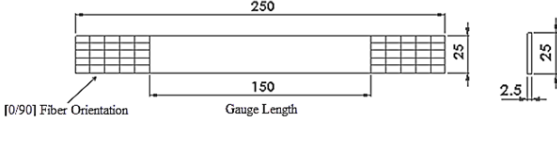
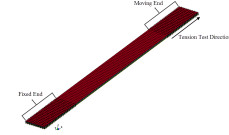
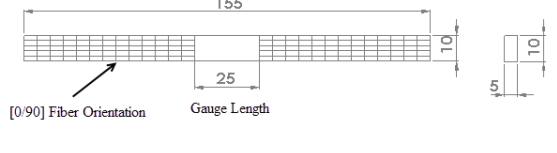
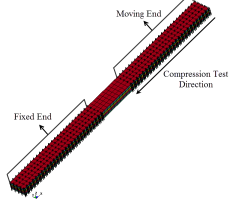
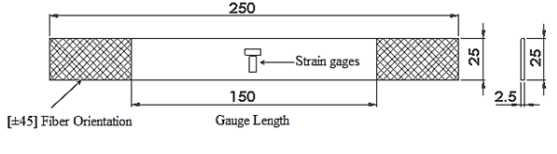
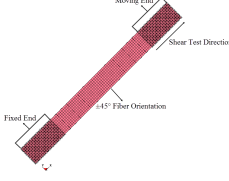
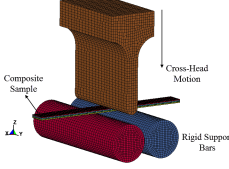
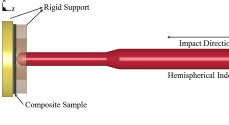
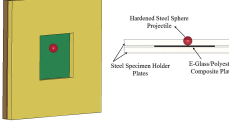
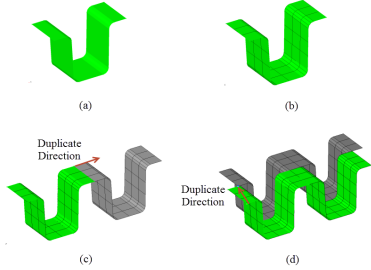
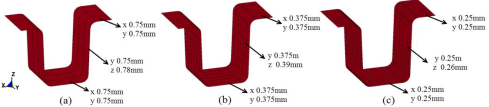
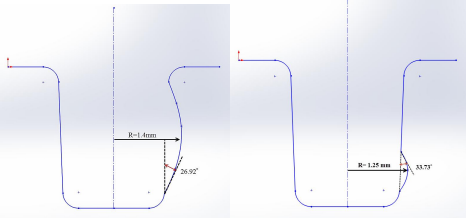
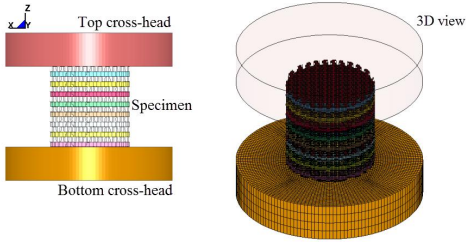
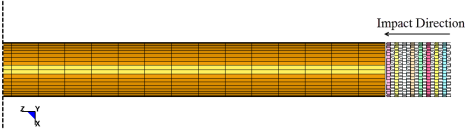
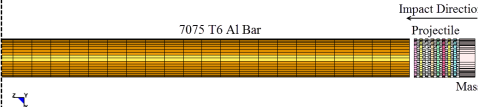
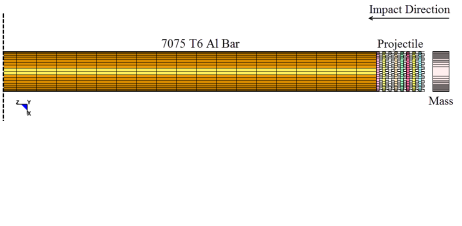
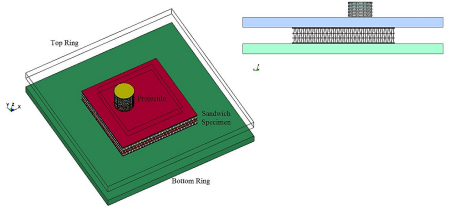
Numerical Study	Specimen Dimensions	Figures
Quasi-static tensile test		
Quasi-static tensile test		
Quasi-static shear test		
Flexural Test	130 mm long and 12.7 mm wide	
Low velocity impact test	100x100x3 mm	
Projectile impact test	200x200 mm plates	

Table 4.2. Summary of the numerical models on composite samples.

Numerical Study	Ambition	Figures
Mesh Generation	<p>To generate unit fin mesh.</p> <p>To generate unit fin layer.</p>	
Mesh Size	<p>To see the effects of mesh size on deformation.</p>	
Imperfection	<p>To see the effect of imperfection on deformation results.</p> <ul style="list-style-type: none"> <li>• Fin wall bending.</li> <li>• Fin wall bulge.</li> </ul>	
Compression test	<p>To optimize the mesh size and imperfection sensitivity.</p>	
Direct impact test without backing mass	<p>Investigate the shock wave formation and propagation in corrugated sandwich projectiles.</p>	
Direct impact test with backing mass	<p>Investigate the shock wave formation and propagation in corrugated sandwich projectiles.</p>	

(cont. on next page)

Table 4.2 (cont.)

<p>Stationary impact test with backing mass</p>	<p>Investigate the shock wave formation and propagation in corrugated sandwich projectiles.</p>	
<p>Projectile impact test</p>	<p>To simulate blast-like loading of composite plates and sandwich structures.</p>	

# CHAPTER 5

## ANALYTICAL SOLUTIONS

### 5.1. Introduction

Three different idealized material models are available: elastic perfectly plastic, elastic linear hardening and rigid perfectly plastic models (Figures 5.1(a-c)). When the materials undergo large plastic deformation, as the plastic strain is relatively large, the elastic strain is neglected; the elastic modulus becomes infinite so the material exhibits plastic deformation before yielding starts. The direct impact responses of the corrugated structures were modeled using the rigid perfectly plastic material model.

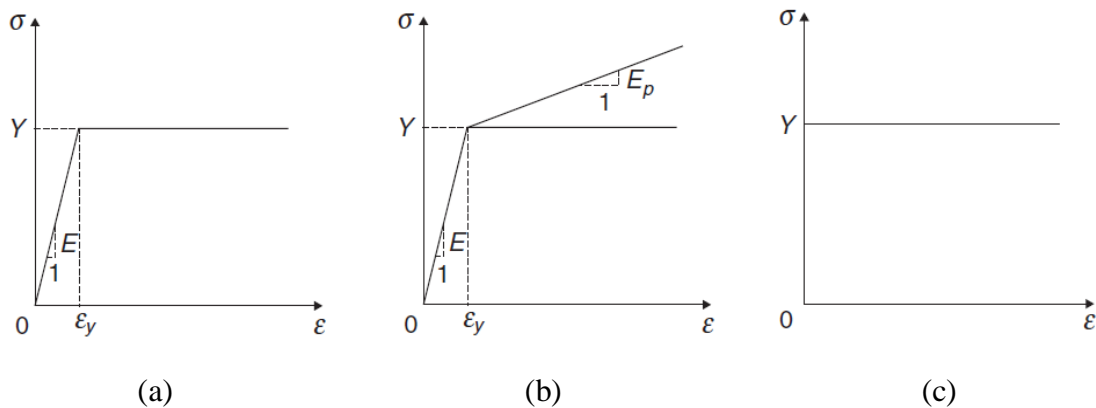


Figure 5.1. Idealized material models: (a) elastic perfectly plastic, (b) elastic linear hardening and (c) rigid perfectly plastic [113].

When the impact velocity is high enough, planar shock waves develop in the cellular materials. The planar shock wave generates two regions in the cellular materials: upstream and downstream. In the upstream region, the material deforms at a stress below the yield stress (plateau stress) while in the downstream region (behind the shock wave), the material is compacted at the densification strain or above the densification strain depending on the impact velocity. The stress values in both regions can be calculated by using 1D shock wave theory, Lagrangian framework and rigid perfectly plastic material model theoretically.

The deflections of composite plates and sandwich structures were calculated using upper and lower bound theorems. The strain hardening and geometric changes were assumed negligible and the structures were assumed perfectly plastic. In the lower bound theorem, the applied load was assumed smaller than the statically admissible load limit. On the other hand, in the upper bound theorem, the magnitude of the external load must be an upper bound of the actual limit loads.

## 5.2. Rigid Perfectly Plastic Shock Theory

In Figure 5.2, the sketch of 1-D shock wave formation and propagation in corrugated core sandwich projectile impacting on an aluminum bar is shown. Prior to impact, the sandwich projectile has an initial length of  $L$ , cross-sectional area of  $A_0$  and density of  $\rho_0$ . The projectile is launched on the aluminum bar and shock wave propagates to the impacting end with an impact velocity  $V_0$  over the critical impact velocity. As the shock wave propagates through the corrugated projectile the stress jumps to  $\sigma_D$  with a compressive strain of  $\varepsilon_D$  at the downstream end. However, in the upstream end the material stays at the yield stress  $\sigma_y$  with a zero plastic strain. Since it is assumed that plastic Poisson's ratio of the projectiles under shock loading is zero, the momentum conservation of the projectile and target mass can be calculated as in Eqn. 5.1

$$mV_0 = (M + m\frac{s}{L})V_i + m(1 - \frac{s}{L})V_D \quad (5.1)$$

where  $m$  is the projectile mass and  $M$  was the mass of aluminum bar.  $V_i$  and  $V_D$  are the particle velocities in the upstream and downstream end of face of the shock wave, respectively. The plastic wave speed across the shock front can be calculated by Eqn. 5.2 as

$$c = \frac{v_D - v_i}{\varepsilon_D} \quad (5.2)$$

By simultaneously solving the Eqns. 5.1 and 5.2, the plastic wave speed in terms of downstream particle velocity is

$$c = \frac{(1 + \frac{m}{M})V_D - \frac{m}{M}V_0}{\varepsilon_D(\frac{m}{M}\frac{s}{L} + 1)} \quad (5.3)$$

By applying the equation of motion to the upstream face of the shock wave over the undeformed range, the yield strength in the upstream end over a unit cross-sectional area can be calculated as

$$m(1 - \frac{s}{L})\dot{V}_D = -\sigma_Y \quad (5.4)$$

Importing Eqn. 5.3 into Eqn. 5.4 and integrating it with the initial conditions of  $V_D = V_0$  and  $s = 0$ , the upstream end particle velocity in terms of impact velocity and yield strength becomes

$$V_D = \sqrt{V_0^2 + \frac{2\sigma_Y\varepsilon_D}{\rho} (Ln(1 - \frac{s}{L}))} \quad (5.5)$$

The stress in the downstream face of the shock wave can be obtained from 1-D shock wave theory as

$$(\sigma_D - \sigma_i) = -\rho c(v_i - v_D) \quad (5.6)$$

Substituting Eqns. 5.1, 5.2 and 5.5 into Eqn. 5.6 the jump stress in the downstream end of the corrugated projectile can be calculated in terms of impact velocity, yield strength and densification strain as

$$\sigma_D = \sigma_Y + \frac{\rho_0}{\varepsilon_D} (\frac{2\sigma_Y\varepsilon_D}{\rho_0} Ln(1 - \frac{s}{L}) + V_0^2) \quad (5.7)$$

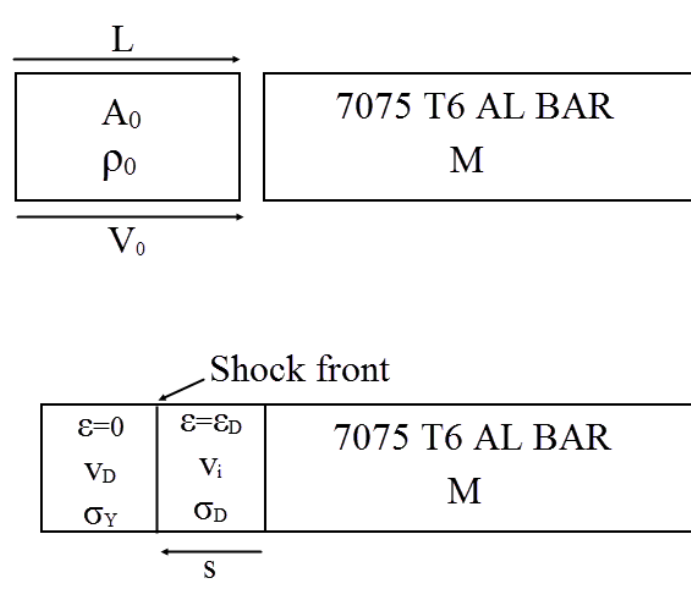


Figure 5.2. Sketch of corrugated sandwich corrugated projectile impacting on aluminum bar.

Figure 5.3 shows a corrugated core sandwich cylinder with an initial length of  $L_0$ , cross-sectional area of  $A_0$  and density of  $\rho_0$  and a mass  $G$  striking on the corrugated sandwich with an initial impact velocity of  $V_0$ . When the mass impact on the cylinder over a critical velocity, a plastic shock develops and travels through the other end with a wave velocity of  $c_p$ . In the upstream region the material is stationary with a stress of  $\sigma_p$  while at the downstream end the material is compacted at a density of  $\rho_D = \rho/(1 - \epsilon_D)$  and the stress level jumps to  $\sigma_D$  which varies with the instantaneous velocity,  $v_D$ . Applying conservation of energy yields

$$\frac{1}{2} \left( G + \frac{\rho_0}{1 - \epsilon_D} A_0 l \right) v_D^2 + \sigma_p \epsilon_D A_0 \frac{1}{1 - \epsilon_D} = \frac{1}{2} G V_0^2 \quad (5.8)$$

where  $l$  is the length of compacted cylinder. The plastic wave speed is

$$c_p = \sqrt{\frac{(\sigma_D - \sigma_p) / \epsilon_D}{\rho_0}} \quad (5.9)$$

Applying conservation of momentum by using Lagrangian framework at the upstream end gives

$$(\sigma_D - \sigma_p)A_0 \delta t = \frac{\rho_0 A_0 c_p v_D}{1 - \varepsilon_D} \quad (5.10)$$

After simplifying Eqn. 5.10, the stress jump becomes

$$\sigma_D = \sigma_p + \frac{\rho_0 c_p v_D}{1 - \varepsilon_D} \quad (5.11)$$

Solving Eqn. 5.8 and Eqn.5.11 simultaneously, the downstream stress in terms of impact velocity is

$$\sigma_D = \sigma_p + \frac{\rho_0 V_D^2}{\varepsilon_D} \quad (5.12)$$

The velocity in the downstream, by applying change of momentum of the end mass  $G$  and undeformed region in the corrugated cylinder, is given by the following relation

$$v_D = \sqrt{V_0^2 + \frac{2\sigma_p \varepsilon_D}{\rho_0} \ln\left(1 - \frac{\rho_0 A_0 u}{G^* \varepsilon_D}\right)} \quad (5.13)$$

where  $G^* = G + \rho_0 A_0 L_0$  and substituting Eqn. 5.13 into Eqn.5.12 the downstream shock stress can be found by

$$\sigma_D = \sigma_p + \frac{\rho_0}{\varepsilon_d} \left[ v_0^2 + \frac{2 \cdot \sigma_p \cdot \varepsilon_d}{\rho_0} \ln\left(1 - \frac{\rho_0 A_0 u}{G^* \cdot \varepsilon_D}\right) \right] \quad (5.14)$$

The same results of analytical solutions were given by Radford et al [7], Tan et al [114] and Reid and Peng [115] where the planar shock wave theory was applied on the cylinder aluminum foams.

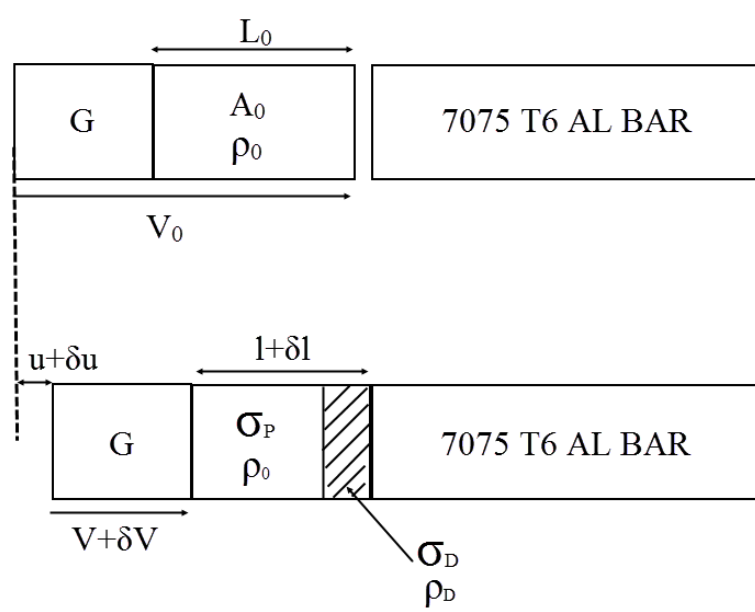


Figure 5.3. Mass impact on a rigid perfectly plastic corrugated cylinder.

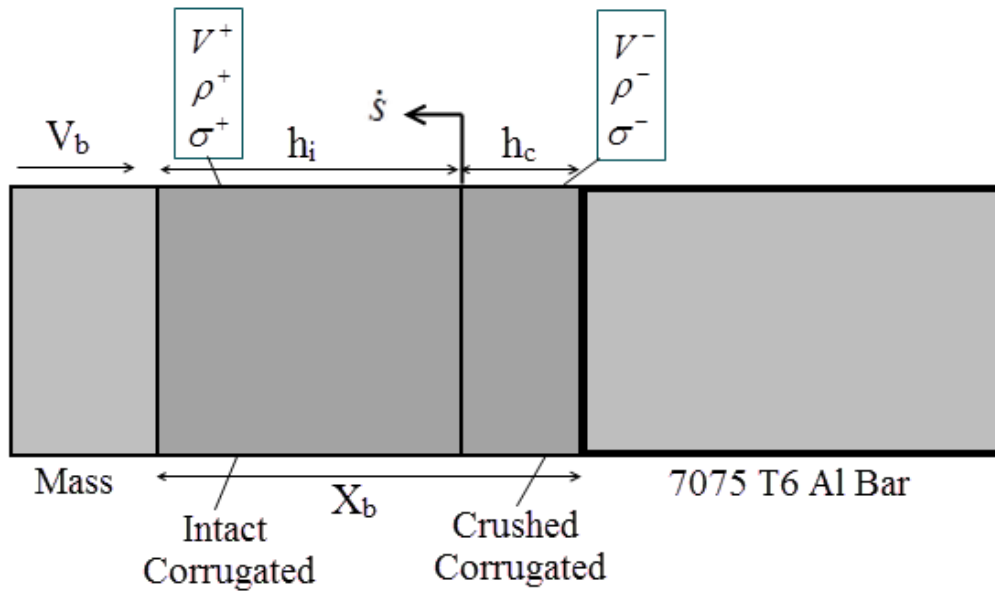
### 5.3. Application of Hugoniot Jump Equations to Corrugated Sandwiches

The planar shock wave generation in corrugated sandwiches can be analytically investigated by applying Hugoniot Jump relations for two cases [116]; mass attached corrugated sandwich impact on aluminum bar (Figure 5.4(a)) and mass impact on corrugated sandwich attached to the aluminum bar (Figure 5.4(b)). In the same figures, the initial length of the corrugated sandwich is represented by  $h_0$  and the crushed section is represented by  $h_c$  while the intact section of the sandwich length is shown by  $h_i$ . The velocities of mass, crush front and the shock are represented by  $V_b$ ,  $V_c$  and  $\dot{s}$ , similar with ref. [116]. The classical jump conditions in Lagrangian form representing conservation of mass, momentum and energy applied to plane longitudinal shocks are expressed as, respectively [117].

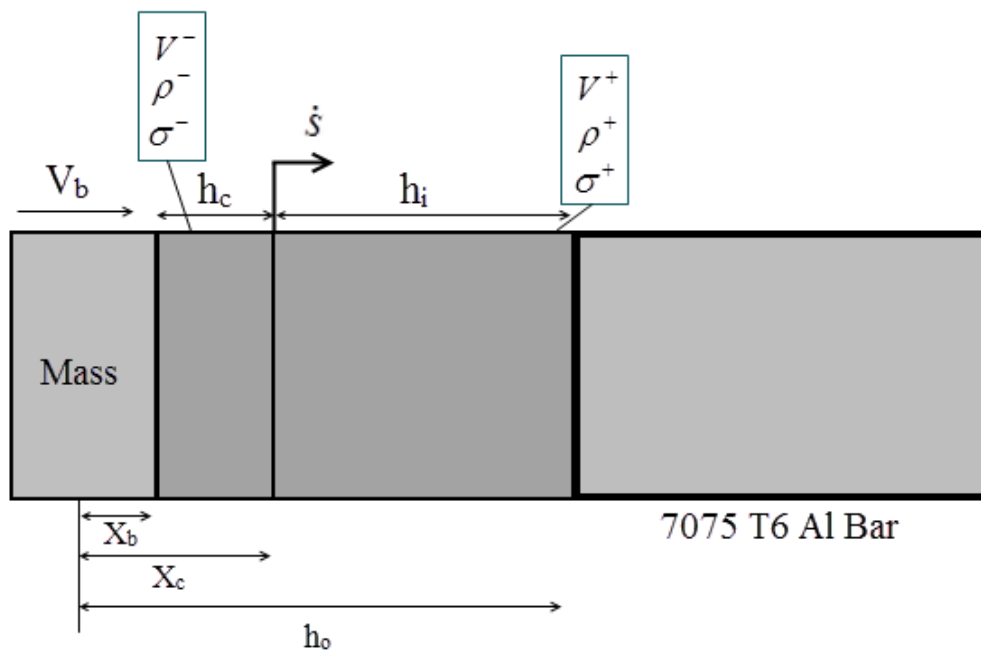
$$\rho_0 \dot{s} [\rho^{-1}] + [V] = 0 \quad (5.15)$$

$$\rho_0 \dot{s} [V] + [\sigma] = 0 \quad (5.16)$$

$$\rho_0 \dot{s} \left[ U + \frac{1}{2} V^2 \right] + [\sigma V] = 0 \quad (5.17)$$



(a)



(b)

Figure 5.4. (a) Impact of mass attached corrugated sandwich on aluminum bar and (b) impact of mass on corrugated sandwich attached to the aluminum bar.

The variables  $\{\rho^+, V^+, \sigma^+\}$  represent the values head of the shock (upstream) while the variables  $\{\rho^-, V^-, \sigma^-\}$  represent the values behind the shock (downstream). In both conditions,  $\rho$  represents the density,  $V$  represents the particle velocity and  $\sigma$  represents the nominal stress. By using the initial  $\{\rho^+, V^+, \sigma^+\}$  conditions,  $\{\rho^-, V^-, \sigma^-\}$  and  $\dot{s}$  can be calculated from the Eqns. 5.15, 5.16 and 5.17. The shock state can be established by performing experiments or numerical models at different impact velocities to develop the  $V - \dot{s}$  Hugoniot curves. Through the experiments and numerical models the impact velocity and the one of the stresses will be measured for direct mass impact and stationary mass impact conditions. By this way, impact velocity and shock speed relationship can be established from the experiments.

The density jump ( $\rho^{-1}$ ) can be expressed when the transverse strain is negligibly small as

$$\left(\frac{1}{\rho^+} - \frac{1}{\rho^-}\right) = \left(\frac{1}{\rho_0} - \frac{h_c}{\rho_0 s}\right) = \frac{1}{\rho_0} \left(\frac{s - h_c}{s}\right) = \frac{\varepsilon_H}{\rho_0} \quad (5.18)$$

where  $\rho_0$  is the initial density of the material assumed to remain unchanged ahead of the shock,  $s = h_0 - h_i$  and  $\varepsilon_H$  is the strain behind the shock that will be referred to as Hugoniot strain. By inserting the conservation of mass into Eqns. 5.15-5.17, the following relations are obtained

$$\dot{s}\varepsilon_H = (V^+ - V^-) \quad (5.19)$$

$$\sigma^+ = \sigma^- - \rho_0 \dot{s}(V^+ - V^-) = \sigma^- - \rho_0 \frac{(V^+ - V^-)^2}{\varepsilon_H} \quad (5.20)$$

$$\rho_0(U^+ - U^-) = \frac{1}{2}(\sigma^+ + \sigma^-)\varepsilon_H \quad (5.21)$$

A linear relationship between the particle velocity and shock speed was observed experimentally nearly for all types of materials. The shock speed in terms of the backing mass velocity can be obtained by

$$\dot{s} = A + BV_b \quad (5.22)$$

The constant A generally corresponds to the bulk wave speed of the solid and B is the slope of the shock Hugoniot obtained from the fitting the experimental results with simulation results. The relation between the backing mass velocity and the Hugoniot strain,  $V_b - \varepsilon_H$ , can be defined by combining Eqn. 5.19 with the linear fit of the  $V_b - \dot{s}$  Hugoniot that gives

$$\varepsilon_H = \frac{V_b}{A + BV_b} \quad (5.23)$$

The stress value behind the shock ( $\sigma^-$ ) can also be obtained from the initiation stress ( $\sigma_I$ ), the quasi-static crushing stress, with the combination of linear fits of  $\dot{s}$  by

$$\sigma^- = \sigma_I + \rho_0 V_b (A + BV_b) \quad (5.24)$$

The relationship between the stress and strain behind the shock ( $\varepsilon_H - \sigma^-$ ), can be obtained by eliminating  $V_b$  from the Eqn. 5.24,

$$\sigma^- = \sigma^+ + \rho_0 \varepsilon_H \left( \frac{A}{1 - B\varepsilon_H} \right)^2 \quad (5.25)$$

#### 5.4. Analytical Model for Clamped Composite Plates

The analytical models of Jones [118] that predict the permanent transverse deflections of solid rectangular plates subjected to large dynamic loads were used as the basic equations and that was combined with the Qiu et al. [119] yield criterion approach for the clamped monolithic beams. The dynamic impulse loads are generated launching corrugated sandwich projectiles on composite plates at different impact velocities. The schematic representation of the loading type and composite plate is shown in Figure 5.5.

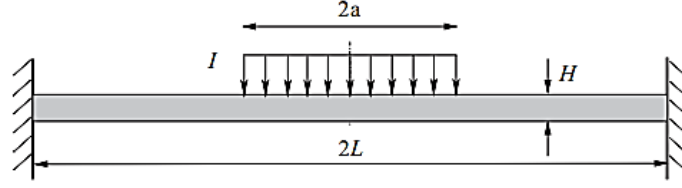


Figure 5.5. Clamped composite plate loaded by corrugated projectile [119].

The composite plates are assumed to satisfy the rigid ideally plastic material law with a yield strength of  $\sigma_{fy}$ , and a density of  $\rho_f$  so all elastic effects are neglected, strain rate sensitivity and small geometry changes are also excluded. These effects can be neglected when the total energy dissipated is much larger than the stored elastic energy. It is assumed that the yield of the plate was due to the resultant longitudinal force  $N$  and bending moment,  $M$  so the yield locus can be defined as [118]

$$\left(\frac{M}{M_0}\right)^2 + \frac{|N|}{N_0} = 1 \quad (5.26)$$

where  $N_0 = \sigma_{fy} \cdot H$  was the circumferential plastic membrane force and  $M_0 = \sigma_{fy} \cdot H^2 / 4$  is the plastic bending moment and  $H$  represented the thickness of the plate. The yield locus can be solved by using circumscribing or inscribing yield criterions.

The deflection estimation for rigid perfectly plastic beams subjected to high intensity dynamic loads were investigated by Martin and Symmonds [120] and a trial velocity and free body diagram solution were established. The solution consisted of three phases based on the plastic hinge locations and free body equilibrium. Since modal solution analysis was used in the present thesis, phase I and phase II deflections were neglected and only phase III deflection was calculated. In phase III, all plastic hinges were stationary and located at the supports and mid-span of the beam for the loading patch size ratio smaller than 0.5 (Figure 5.6(a)). The bending moments were also located at the supports and mid-span of the half beam (Figure 5.6(b)).

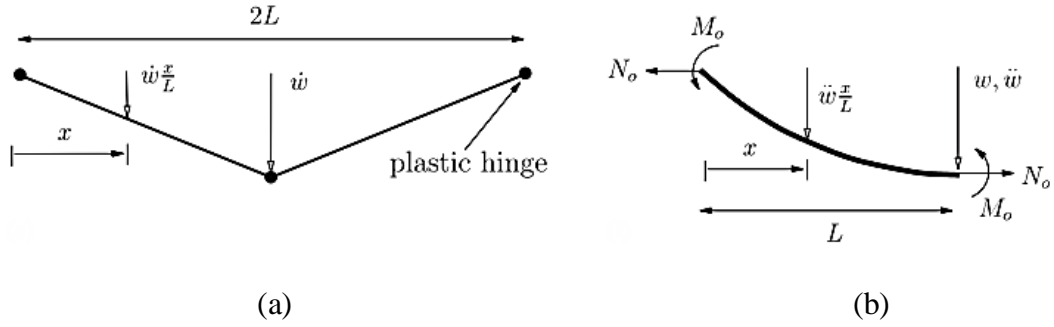


Figure 5.6. Monolithic beam impulsive response analysis for Phase III; (a) velocity profile and (b) half beam free body diagram.

Considering the moment of momentum about a fixed support for half beam yields (Figure 5.6(b))

$$2M_o + N_o w = -\frac{\ddot{w}}{L} \int_0^L m x^2 dx = -m \frac{L^3}{3} \frac{\ddot{w}}{L} \quad (5.27)$$

where  $m = \rho_f \cdot H$ . In order to solve the ODE in Eqn. 5.27, non-dimensional forms of the variables have to be defined as

$$\bar{I} = \frac{I}{L\sqrt{\sigma_{fy}\rho f}} = \frac{mV_0}{L\sqrt{\sigma_{fy}\rho f}} = \frac{\rho_0 L_0 V_0}{L\sqrt{\sigma_{fy}\rho f}} \quad (5.28)$$

$$\bar{w} = \frac{w}{L} \quad (5.29)$$

$$\bar{H} = \frac{H}{L} \quad (5.30)$$

$$r = \frac{a}{L} \quad (5.31)$$

where  $\bar{I}$  is the impulse imparted on the central patch of the beam,  $\bar{w}$  is the non-dimensional deflection,  $\bar{H}$  is non-dimensional plate thickness and  $r$  is the loading patch size ratio. The deflection of the plate impulsively loaded by the corrugated projectiles

from central patch can be obtained by assuming that all the momentum of the projectiles are imparted to the beam thus the initial conditions become

$$\bar{w}(0) = 0 \quad (5.32)$$

$$\dot{\bar{w}}(0) = \frac{2\bar{I}r}{\bar{H}} \quad (5.33)$$

Assuming the circumscribing yield criterion and using the Eqns. 5.32 and 5.33, the solution of the Eqn. 5.27 gives the mid-span deflection of the plate as

$$\bar{w} = \frac{\bar{H}}{2} \left( \sqrt{1 + \frac{16\bar{I}^2 r^2}{\bar{H}^4}} - 1 \right) \quad (5.34)$$

## 5.5. Analytical Model for Clamped Sandwich Structures

The analytical solutions of fully clamped corrugated core composite sandwich structures subjected to the impulsive loading in the central patch were developed for large deflections (Figure 5.7). The face sheet is assumed rigid perfectly plastic with a yield strength of  $\sigma_{fy}$  and a density of  $\rho_f$ . The corrugated core is assumed rigid perfectly plastic locking material with a constant crushing stress of  $\sigma_n$ , a densification strain of  $\varepsilon_D$  and a longitudinal tensile strength of  $\sigma_l$ . The sandwich structure span length is represented as  $2L$ , core thickness as  $c$  and the face sheet thickness as  $h$  (Figure 5.7).

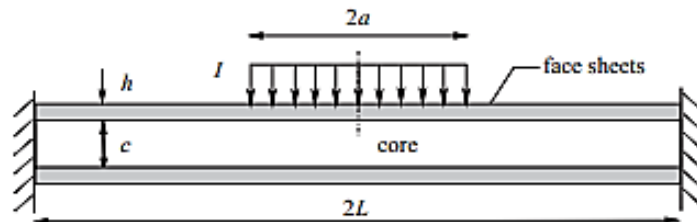


Figure 5.7. Fully clamped sandwich structure under impulsive loading [119].

Fleck and Deshpande [121] analytically investigated the response of shock loaded sandwich structures over the entire beam span and split the solution in three stages. The stage I was one dimensional fluid structure interaction which was neglected in the present study. The stage II and stage III involved the core compression and beam bending and stretching. In core compression, the impulsive load applied on the front face sheet compress the core and accelerates the back face sheet and entire structure reaches a common velocity of  $v$  that is

$$v = \frac{I}{2\rho_f h + \rho_c c} = \frac{m_f \cdot v_0}{2m_f + \rho_c \cdot c} \quad (5.35)$$

The ratio of energy dissipated  $U_{lost}$  to the initial kinetic energy of the top face sheet can be found by

$$\phi = \frac{U_{lost}}{I^2 / (2\rho_f h)} = \frac{1+q}{2+q} \quad (5.36)$$

where  $q = \rho_c c / (\rho_f h)$  is mass ratio of the core and face sheet. Assuming that the core compression occurs in 1D and at a constant stress,  $\sigma_n$ , the average core compression strain  $\varepsilon_c$  is given as

$$\varepsilon_c = \frac{\bar{I}^2}{2\bar{\sigma}_n \bar{c}^2 \bar{h}} \frac{\bar{h} + \bar{\rho}}{2\bar{h} + \bar{\rho}} \quad (5.37)$$

where  $\bar{h} = h/c$ ,  $\bar{c} = c/L$ ,  $\bar{\rho} = \rho_c / \rho_f$ ,  $\bar{I} = I / (L\sqrt{\sigma_{fY}\rho_f})$  and  $\bar{\sigma}_n = \sigma_n / \sigma_{fY}$ . If the dissipated energy is too much and exceeds the densification strain  $\varepsilon_D$ , the average core compression strain  $\varepsilon_c$  is set equal to  $\varepsilon_D$ . The final core height at the end of the phase is reduced to  $c' = (1 - \varepsilon_c)c$ . In beam bending and stretching phase as the impulse levels increase the deflection of the fully clamped sandwich structure increase [121-123]. The deflection increase eliminates the bending effect and axial force stretching effect without shear yielding becomes dominant. Furthermore, since the structure reaches a

common velocity, the core crushing is eliminated and the structure can be assumed as monolithic beam. The core compression in the sandwich structure does not affect the longitudinal plastic membrane force and can be found by

$$N_0 = 2h\sigma_{fy} + \sigma_l c \quad (5.38)$$

The mid-span velocity given in Figure 5.7(a) is calculated as

$$\dot{w} = \dot{w} \frac{x}{L}, \quad 0 \leq x \leq L \quad (5.39)$$

where  $\dot{w}$  was velocity of the mid-span of the beam. The conservation of moment of moment around the support with respect to time  $t$  (Figure 5.8(a)), one gets

$$N_0 w = -\frac{d}{dt} \int_0^L (2\rho_f h + \rho_c c) \dot{w} x dx \quad (5.40)$$

where  $w$  is the mid-span deflection. The solution can be generalized by applying non-dimensional parameters for the sandwich beam as

$$\hat{c} = \bar{c}(1 - \varepsilon_c) \quad \text{and} \quad \hat{h} = \frac{\bar{h}}{1 - \varepsilon_c} \quad (5.41)$$

and the non-dimensional parameters for the core material is

$$\bar{\sigma}_l = \frac{\sigma_l}{\sigma_{fy}} \quad \text{and} \quad \hat{\sigma}_l = \frac{\sigma_l}{1 - \varepsilon_c} \quad (5.42)$$

and the structural deflection of sandwich beam by modal analysis including the non-dimensional parameters can be calculated by substituting non-dimensional parameters into Eqn. 5.40.

$$\bar{w} = \alpha_1 \alpha_3 \left( \sqrt{1 + \frac{64}{3} \frac{\alpha_2^2}{\alpha_1^2} \bar{I}^2 r^2} - 1 \right) \quad (5.43)$$

where

$$\alpha_1 = c^2 ((1 + 2\bar{h})^2 - 1 + \bar{\sigma}_1) + \hat{c}^2 ((1 + 2\hat{h})^2 - 1 + \hat{\sigma}_1) \quad (5.44)$$

$$\alpha_2 = \sqrt{\frac{2\bar{h} + \bar{\sigma}_1}{2\bar{h} + \bar{\rho}}} \quad (5.45)$$

$$\alpha_3 = \frac{1}{4\bar{c}(2\bar{h} + \bar{\sigma}_1)} \quad (5.46)$$

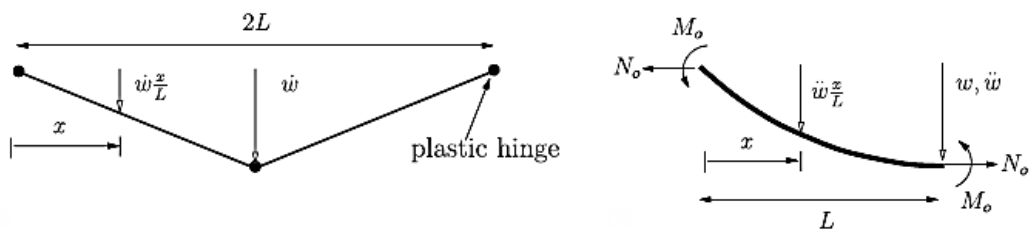


Figure 5.8. Sandwich beam impulsive response analysis for Phase III; (a) velocity profile and (b) half beam free body diagram.

## CHAPTER 6

# TESTING AND MODELLING OF E-GLASS COMPOSITE MATERIALS

### 6.1. Introduction

In this section, the results of quasi-static, low velocity impact, high strain rate and projectile impact tests on E-Glass/Polyester materials were given. The parameters in MAT\_162 material model were determined from these experiments. The experimentally obtained numerical model parameters were validated by comparing the results of the experiments and simulations.

### 6.2. The Experimental and Numerical Results of Composite Materials

#### 6.2.1. Experimental Tension Test and Numerical Model Results

Figure 6.1 shows the X- and Y-direction (in-plane) tensile stress-strain curves of E-Glass/Polyester composite. In both directions, the stress-strain response is nearly linear up to the tensile strength and a sudden failure occurs at an average strain of 0.022. The composite shows a linear behavior between 0 and 0.005 strain and between 0.005 and failure strain. The elastic modulus is calculated by linear fitting the stress-strain values between 0.005 and tensile failure strain as depicted in Figure 6.2. The average tensile strength, modulus and failure strain (three tests) in the X-direction are sequentially 385 MPa, 16.6 GPa and 0.0247. The average tensile strength, modulus and failure strain in the Y-direction are sequentially 409 MPa, 17.3 GPa and 0.0244. These results indicate that the composite has similar mechanical properties in in-plane directions. Therefore average properties are calculated for these directions. As a result the average strength, elastic modulus and failure strain are sequentially 397 MPa, 16.9 GPa and 0.023. The composite failure is composed of fiber fracture in the warp

direction, fiber pull-out in the weft direction, delamination in the adjacent layers and matrix cracking (Figures 6.2(a) and (b)).

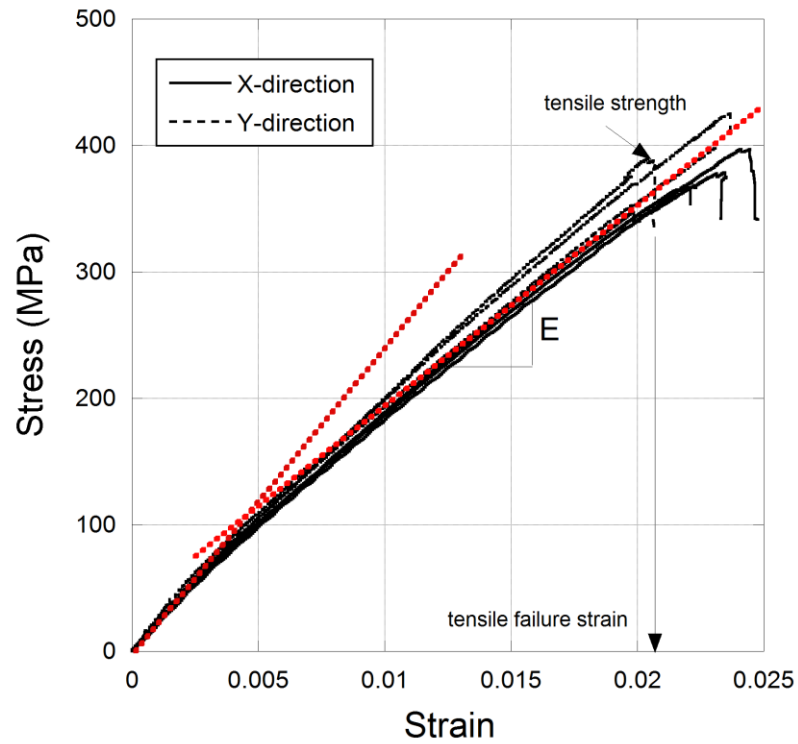


Figure 6.1. In-plane tensile stress-strain curves of E-Glass/Polyester composite.

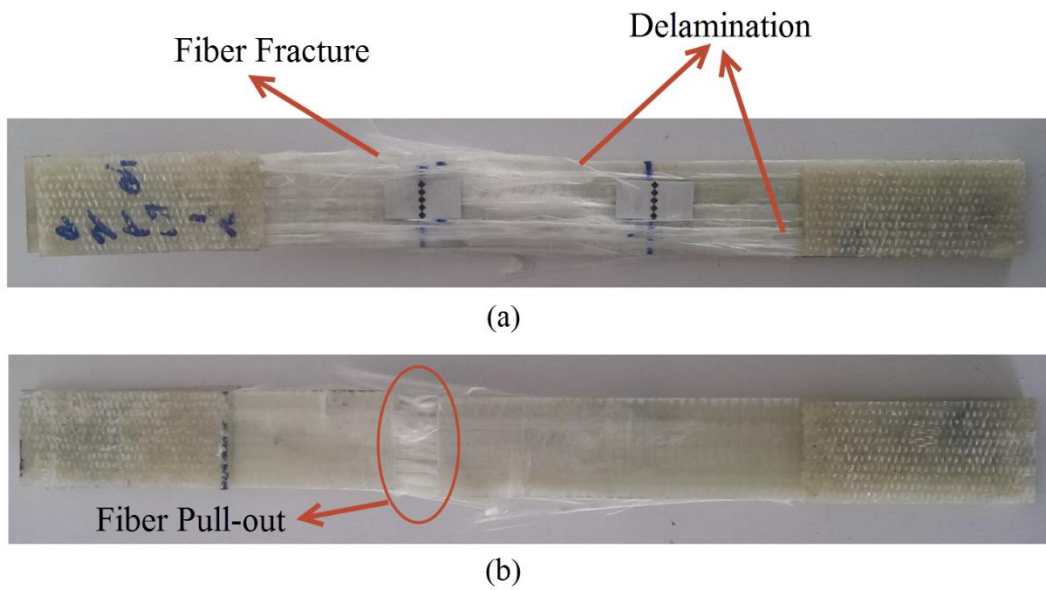


Figure 6.2. Damages in in-plane tensile tested specimen: (a) X- and (b) Y-directions.

The mesh sensitivity and damage parameter ( $m_1$ ,  $m_2$ ,  $m_3$  and  $m_4$ ) calibration studies were performed with in-plane tensile test models. The mesh sizes of the tensile test models for both in-plane directions were selected 1, 2.5 and 5 mm as shown in Figure 6.3. The experimental and numerical stress-strain curves and deformation modes for all mesh densities are shown in Figures 6.4 and 6.5, respectively. The mesh size has an obvious effect on the elastic behavior and the peak stresses of the composite. The small mesh size (1 mm) cannot predict the tensile strength, while large mesh size (5 mm) over predicts the elastic modulus. The medium mesh size however shows the best fitting to the experimental stress-strain behavior of the composite as shown in Figure 6.4. The best agreement between numerical and experimental softening part of the stress-strain curves was achieved when  $m_1$  and  $m_2$  was equal to 4. Lower damage values,  $m_1$  and  $m_2$ , resulted in a more brittle stress-strain behavior than that of experiment. The experimental damage occurred between the moving end tabs, near one of the end tabs, and this was only validated numerically with 2.5 mm mesh size when  $m_1=m_2=4$ . The numerical failure with these parameters initiated near the moving end tab and proceeded to the stationary end tab. The failure locations and modes of numerically and the experimentally tested samples were found very much similar.

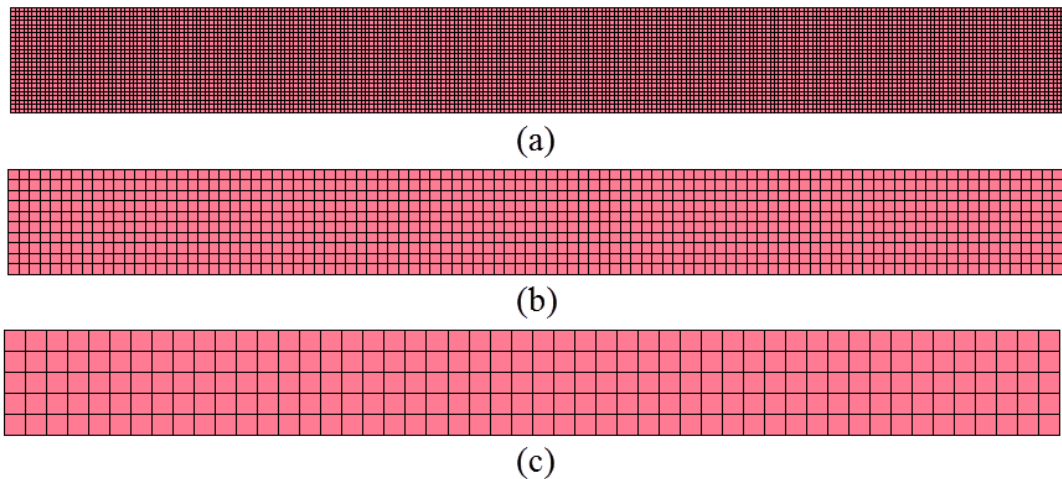


Figure 6.3. Tensile test models with different mesh sizes: (a) 1, (b) 2.5 and (c) 5 mm.

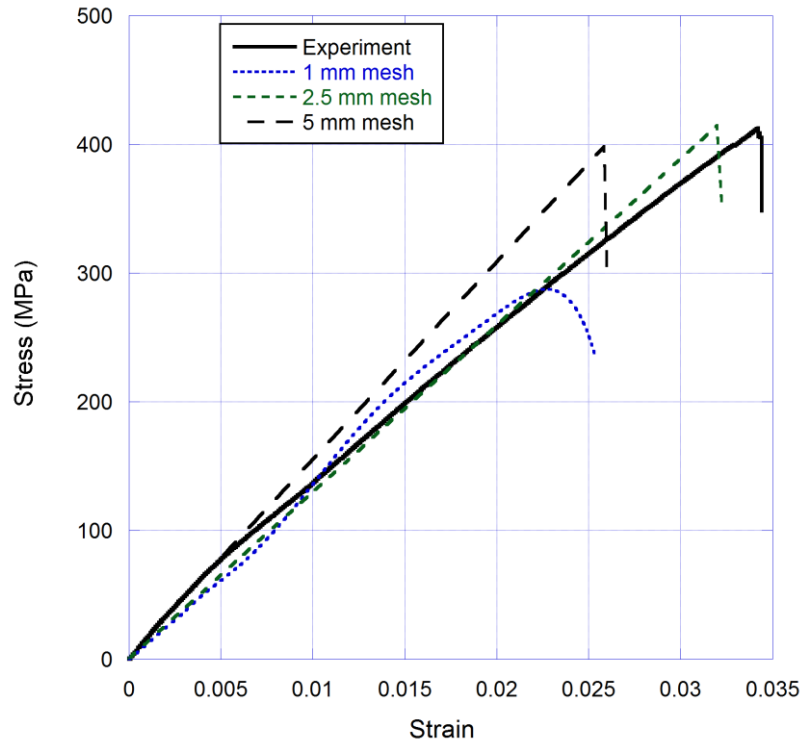


Figure 6.4. The stress-strain curves of experimentally and numerically tested composites.

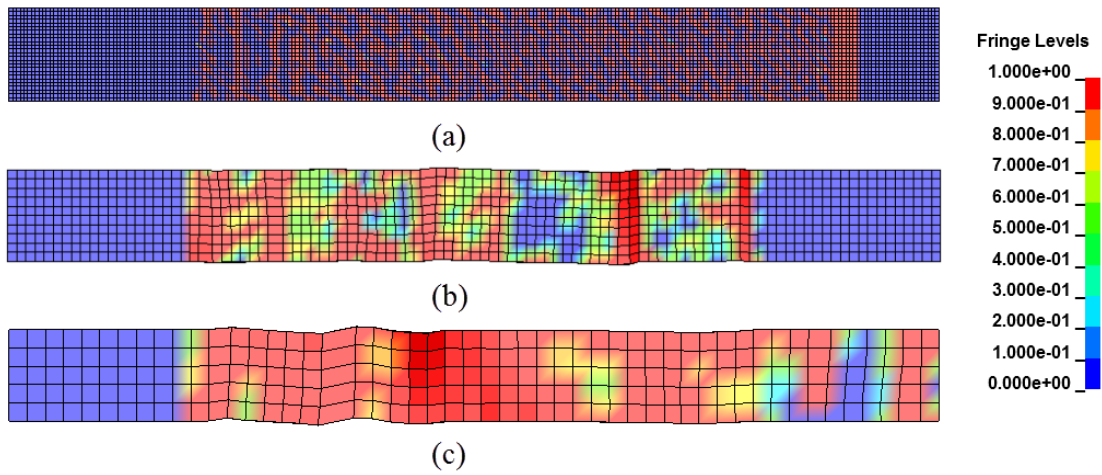


Figure 6.5. The deformation modes of the tensile test samples with  $m_1=m_2=4$  for different mesh sizes: (a) 1, (b) 2.5 and (c) 5 mm.

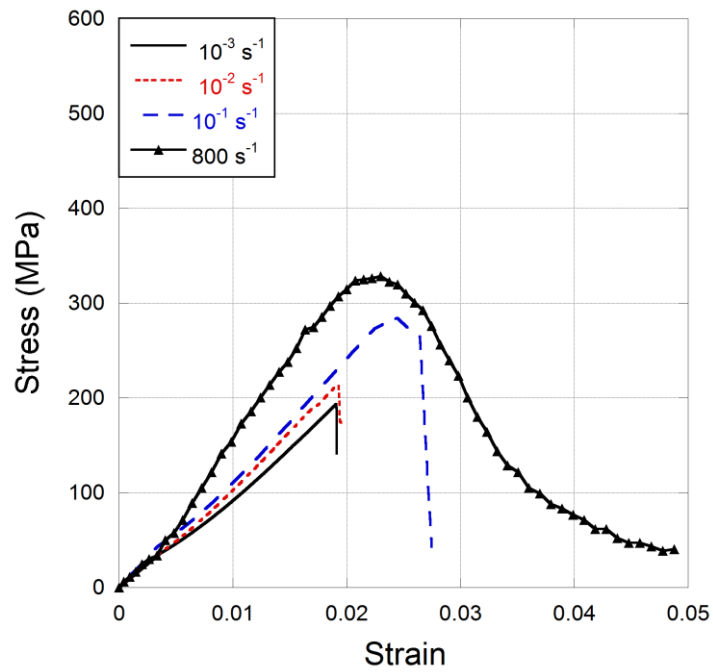
## 6.2.2. Experimental Compression Tests and Numerical Model Results

The preparation of tensile specimens and testing in tensile SHPB are rather difficult as small size specimens are tested in SHPB. Therefore; the strain rate sensitivity and rate dependent parameters of the E-Glass/polyester composite was investigated through quasi-static ( $10^{-3}$ ,  $10^{-2}$  and  $10^{-1}$   $s^{-1}$ ) and compression SHPB (600-800  $s^{-1}$ ) tests. Figures 6.6(a-c) show the experimental compression stress-strain curves of the composite at quasi-static and dynamic strain rates for X-, Y- and Z-direction, respectively. The composite shows a dynamic stress-strain behavior very much similar to that of the quasi-static strain rate; it fails following a non-linear elastic deformation region. As the strain rate increases however the elastic modulus, compression strength and failure strain increase, except the SHPB samples tested in Z-direction (Figure 6.6(c)). In the Z- direction, although compression strength and failure strain increase with increasing strain rate at quasi-static strain rate regime, the compression strength and strain decrease as compared with quasi-static strain rates at 600  $s^{-1}$ . It is also noted that following the compression strength a softening behavior is seen in the composite stress-strain curve of the samples tested in SHPB (Figures 6.6(a-c)).

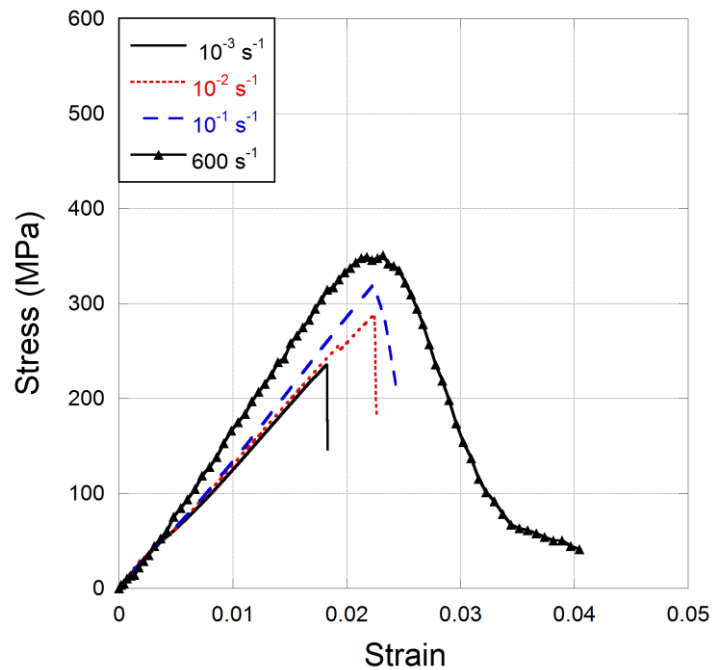
The average elastic modulus increases from 10.175 GPa at  $10^{-3}$   $s^{-1}$  to 18.283 GPa at 800  $s^{-1}$  for the samples tested in the X-direction, from 12.844 GPa at  $10^{-3}$   $s^{-1}$  to 19.32 GPa at 600  $s^{-1}$  for the samples tested in the Y-direction and from 5.556 GPa at  $10^{-3}$   $s^{-1}$  to 9.831 GPa at 700  $s^{-1}$  for the samples tested in the Z-direction. Similar increases are also found in the average compression strength values when the strain rate increases from quasi-static to dynamic rates except the samples tested in the Z-direction in the SHPB. The X-direction average compression strength increases from 194.09 MPa to 311.67 MPa, the Y-direction average strength increases from 229.33 MPa to 335.67 MPa when the strain rate increases from  $10^{-3}$   $s^{-1}$  to dynamic strain rates. While the Z-direction average compression strength decreases from 592.67 MPa to 436.67 MPa when the strain rate increases from  $10^{-3}$   $s^{-1}$  to 700  $s^{-1}$ .

Figures 6.6(a-c) clearly indicate that the composite shows different compressive mechanical responses in three principal axes. The composite shows the highest strength and failure strain in the Z-direction. The lowest strength is in the X-direction. When compared with tensile mechanical response, the composite in-plane strength and modulus values are lower, while the failure strain values are higher. Apart from

anisotropy in mechanical response in three principal axis, the composite is also strain rate sensitive in compression strength, modulus and failure strain.



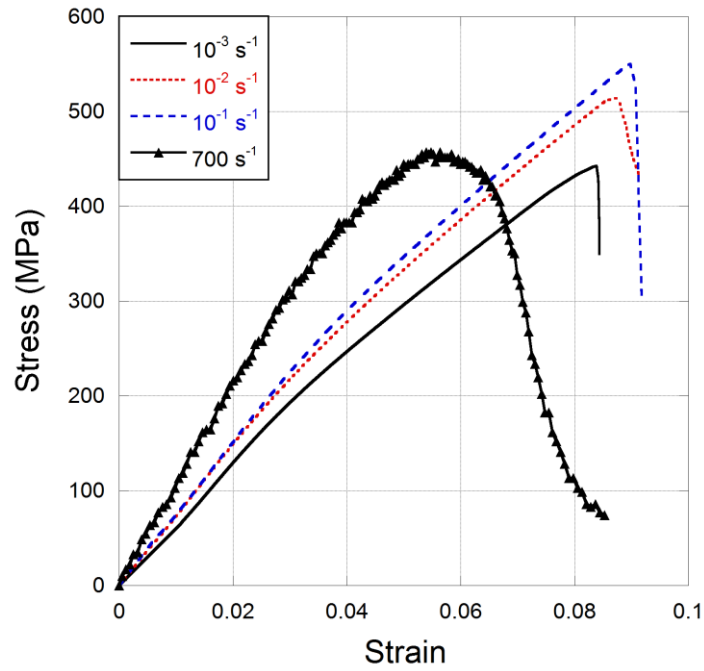
(a)



(b)

Figure 6.6. Quasi-static and SHPB compression stress-strain curves of the composite: (a) X-, (b) Y- and (c) Z-direction.

(cont. on next page)



(c)

Figure 6.6. (cont.)

The pictures of the failed but recovered quasi-static test samples tested in X-, Y- and Z-direction are shown in Figures 6.7(a-c), respectively. Although, the primary failure modes are fiber-matrix splitting and fiber buckling in the samples tested in-plane directions (Figures 6.7(a) and (b)), the main failure mode in Z-direction is the matrix dominant shear failure, as similar with the ref. [36]. The deforming high speed camera pictures of the sample tested in SHPB in X-, Y- and Z-directions are shown at various deformation times in Figures 6.8(a-c), respectively. The dynamic failure modes of these specimens are very much similar with those of quasi-statically tested samples; axial splitting in the samples tested through in-plane and matrix shear failure in the samples tested through thickness (Figures 6.8(a-c)). The shear failure bands range from  $30^\circ$  to  $44^\circ$  for all tested specimens. The average shear band angle is  $42^\circ$ . The main deformation mechanism is supposed to be the fiber kinking which leads to the matrix dominant shear failure in through thickness specimens.

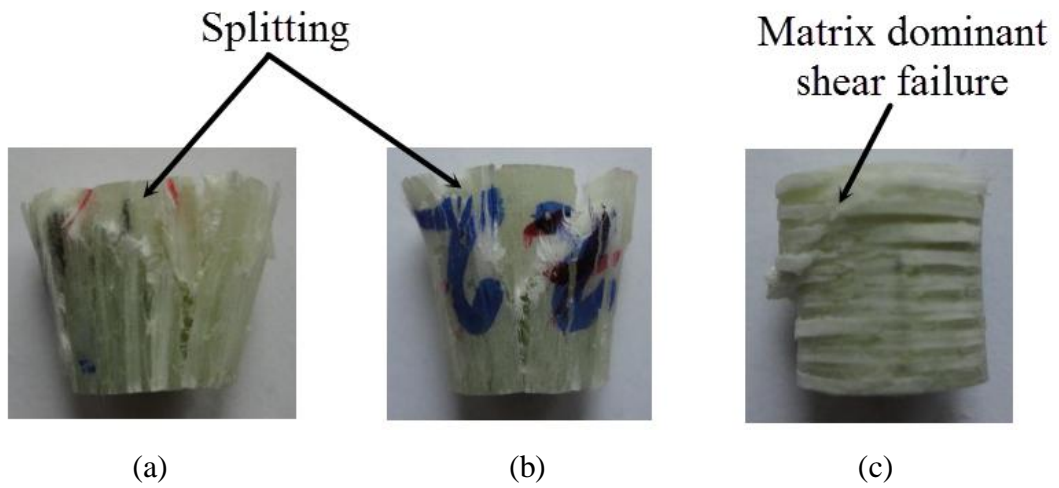


Figure 6.7. The failed quasi-static composite samples tested in (a) X-, (b) Y- and (c) Z-direction.

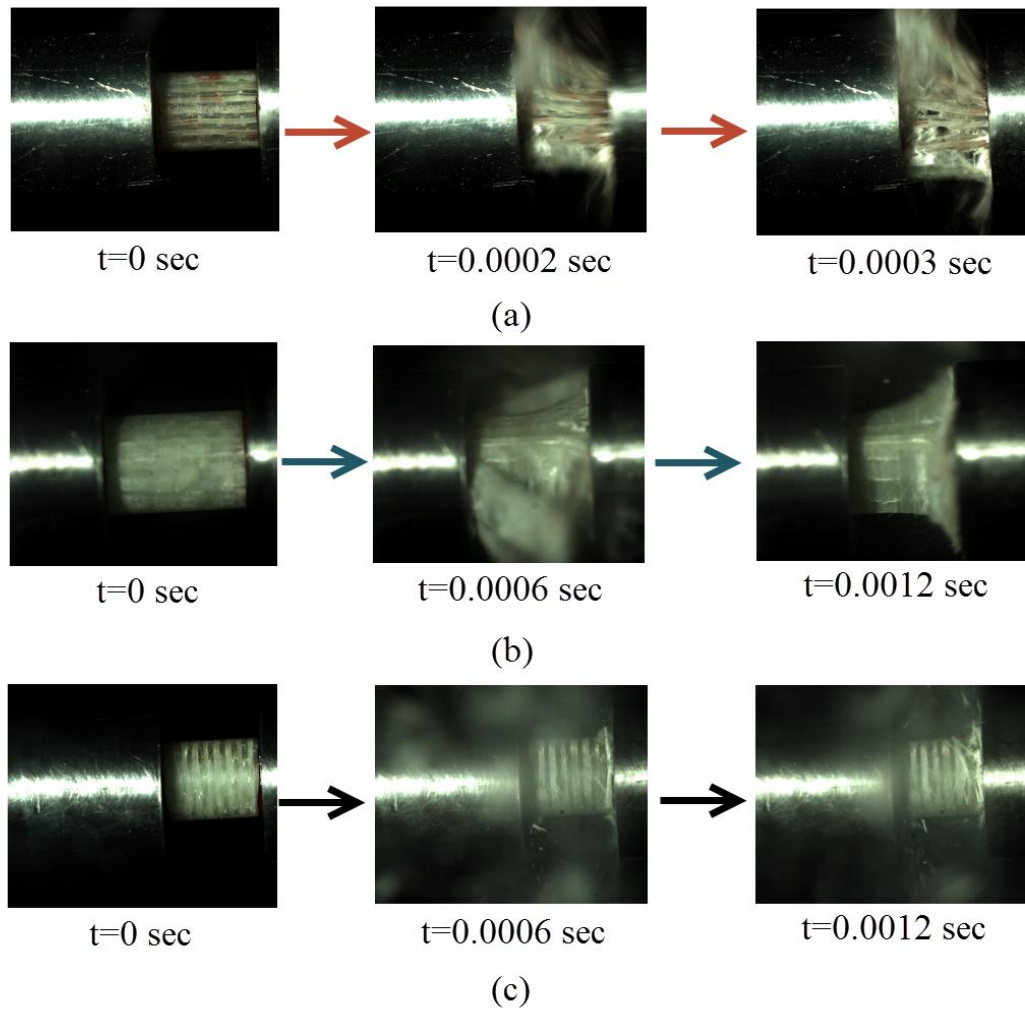


Figure 6.8. The deforming composite sample pictures in SHPB tested in (a) X-, (b) Y- and (c) Z-direction.

The variations of the compression strength with strain rate for three principal axes are shown in Figure 6.9. The compression strength values in the same figure are fitted with Eqn. 4.11 for three principal axes. The fitting results are shown in the inset of the same figure. The value of  $m_2$  in the inset gives the  $C_1$  value in Eqn. 4.11. The value of  $C_{rate1}$  for X, Y and Z axis are sequentially 0.043, 0.035 and 0.022. An average value of  $C_{rate1}$ , 0.033, is calculated for three principal axis. The strength values of  $S_{ac}$  and  $S_{bc}$  (the strength values at the reference strain rate of  $1s^{-1}$ ) in Eqn. 4.12 are determined to be the same, 285 MPa on the average. It is assumed that the strength values are equal in X- and Y-direction as the fibers are nearly biaxial. The values of  $C_{rate}$  in Eqn. 4.14 are calculated by fitting Eqn. 4.14 with the elastic modulus vs. strain rate graph shown in Figure 6.10. The fitting results are also shown in the inset of the same figure. The value of  $m_2$  corresponds to the value of  $C_{rate}$  in Eqn. 4.14. The value of  $C_{rate2}$  in Eqn. 4.14 are calculated 0.036 by averaging  $m_2$  values for X- and Y-directions and the value of  $C_{rate4}$  ( $m_2$  for Z-direction) in Eqn. 4.14 is 0.042. The tensile elastic modulus for X and Y directions is determined to be  $E_a=E_b=16$  GPa due to the absence of high strain rate tension tests and for Z direction  $E_c=7.74$  GPa is obtained from the fit of the quasi-static and high strain rate compression test results.

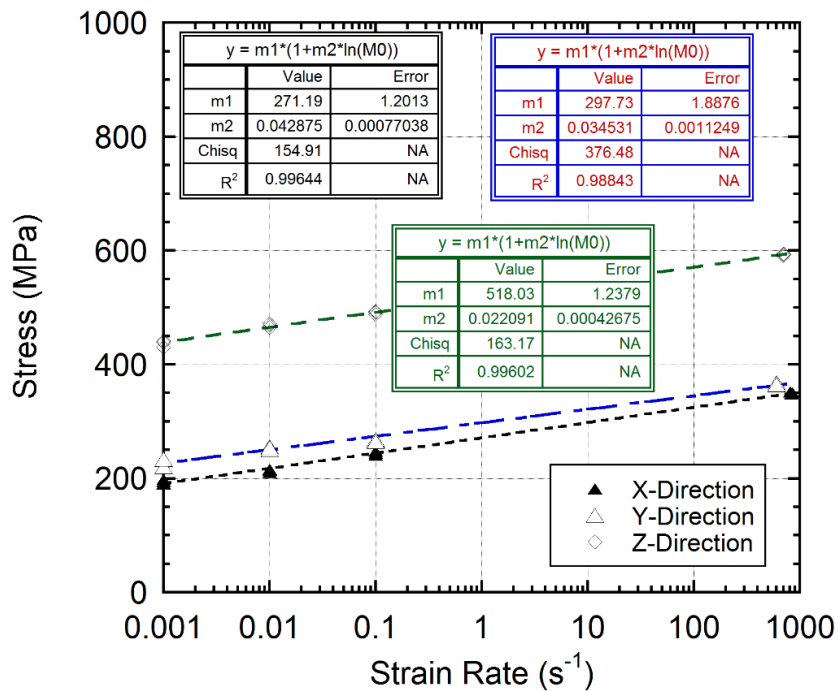


Figure 6.9. Determination of the strain rate sensitivity parameter of  $C_{rate1}$ .

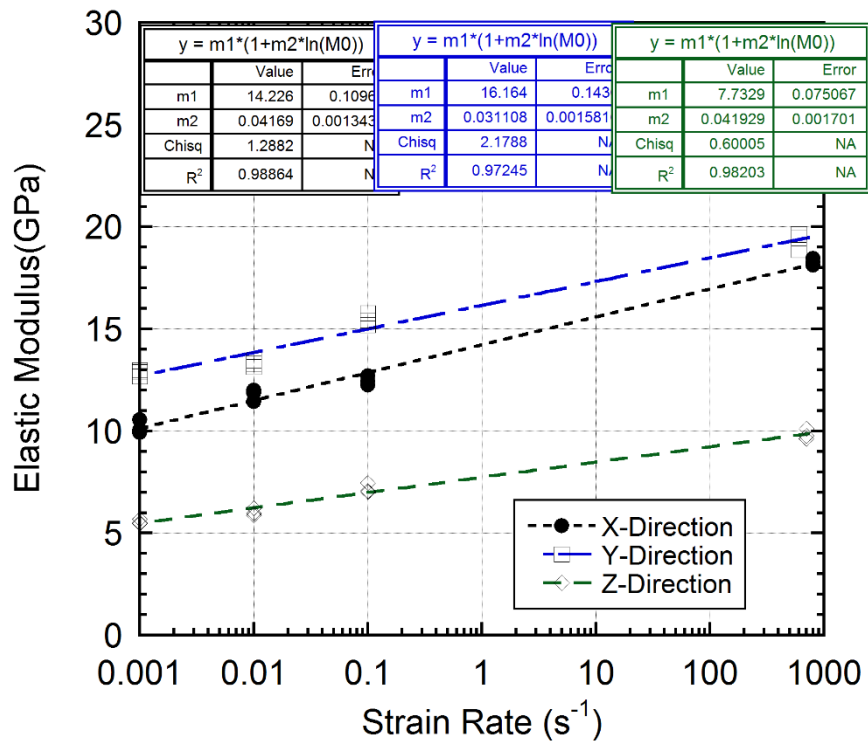


Figure 6.10. Determination of strain rate sensitivity parameters of  $C_{rate2}$  and  $C_{rate4}$ .

The compression numerical simulations were performed using ASTM D3410 compression test sample since the cylindrical specimens cut from the main plate deformed the mesh geometry, leading to improper simulation results. The damage parameters of  $m_1$  and  $m_2$  were determined by iteration using the experimental softening part of the compression stress-strain curves; a value of 0.5 gave very similar softening behavior with the experiments. The experimental and numerical quasi-static ( $10^{-1} \text{ s}^{-1}$ ) ASTM D3410 compression test sample stress-strain curves with  $m_1=m_2=0.5$  values are shown in Figure 6.11. The experimental and simulation stress-strain curves seen in the same figure are very much similar, while the simulation stress-strain curve show slightly higher compression strength than the experiment. The main reason for this difference is the slight variation in the compression strength and modulus of the composite in X- and Y-directions. The test was performed in X-direction, while in the numerical model the properties in the X- and Y-directions are taken as the average of two directions. Figures 6.12(a) and (b) show the pictures of the experimentally and numerically tested compression samples, respectively. In both tests, experimental and numerical, the damage is seen to occur in a fairly localized region on the gage length near the one of the end tab. Later, the damage proceeds through the gage length of the

sample. Shortly, the damage values of 0.5 show well agreements between the quasi-static compression experimental and numerical stress-strain curves and deformation modes.

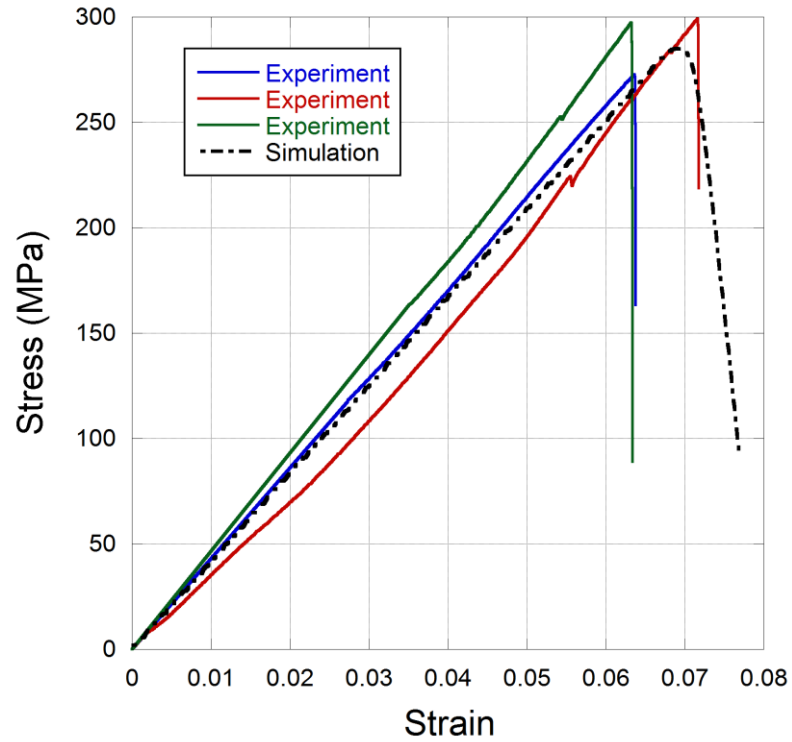


Figure 6.11. The experimental and numerical quasi-static ( $10^{-1} \text{ s}^{-1}$ ) ASTM D3410 compression test sample stress-strain curves with  $m_1=m_2=0.5$  values.

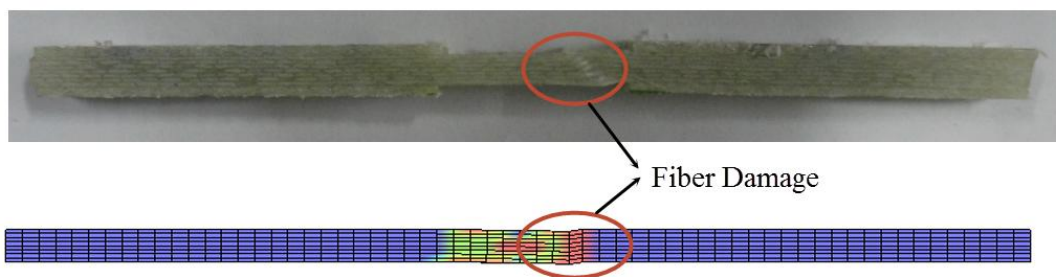


Figure 6.12. Quasi-static (a) experimentally and (b) numerical tested compression samples showing damage modes and locations.

### 6.2.3. Experimental Flexural Tests and Numerical Model Results

In Figure 6.13, experimental and numerical simulation results of three point bending test are shown. There is a 10% difference in the displacement values between test and simulation. This difference may be resulted from the elastic modulus of in-plane directions and the mass scaling. It was found that the mesh size did not have significant effect on the displacement values. On the other side, well agreements are found between test and simulation force values. The damage occurs at the cross head-specimen region in the simulation as seen in Figure 6.14. In initial stages, the matrix damage becomes dominant and in the preceding damage modes compression and shear stress become dominant on the top surface failure. In the bottom surface, tensile stresses cause failure in the specimen. The damage parameters of  $AM1=AM2=0.5$  show well agreements with tests as in the compression test simulations.

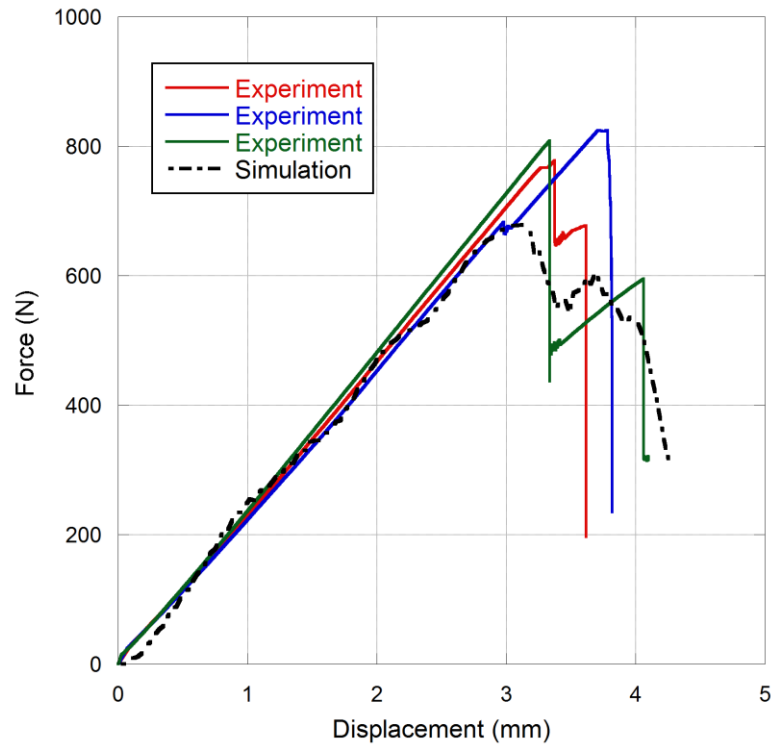


Figure 6.13. Experimental and numerical simulation force-displacement responses of three point bending test.

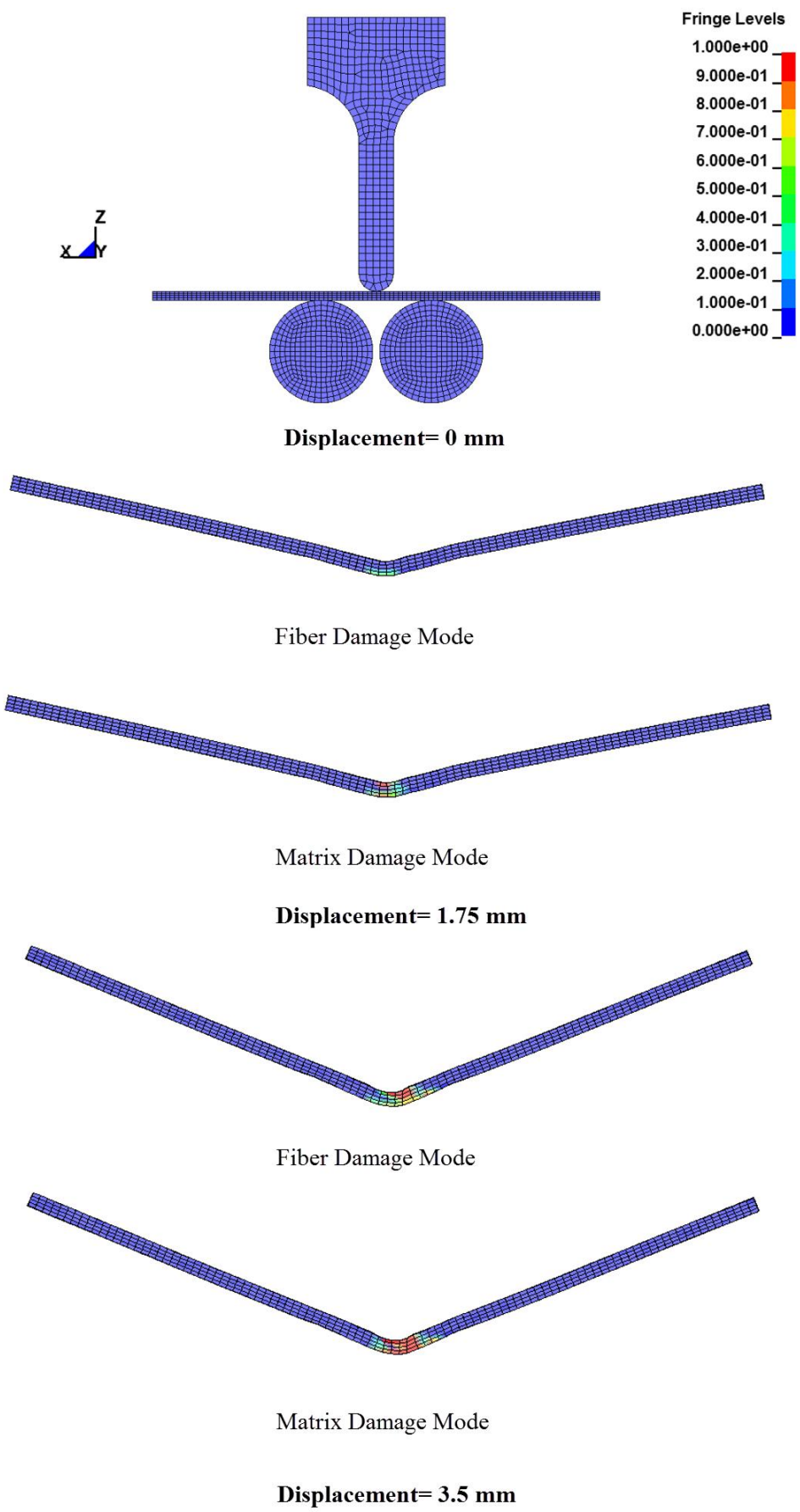


Figure 6.14. Sequential deformation modes of three point bending test simulation.

## 6.2.4. Curved Beam Test Results

The curved beam strength tests were carried out to find the out-of plane tensile stress produced in the curved region when force was applied. The curved beam was loaded in four point bending to apply a constant bending moment across the curved cross section where out-of plane tensile stresses caused the specimen failure. The curved beam strength can be calculated from the force, P, and the displacement value,  $\Delta$ , where the load suddenly drops. The experimental results of curved beam specimens are shown in Figure 6.15, the failure forces are around 1100N with a displacement value of around 2.8 mm. The curved beam strength of the samples can be calculated by using Eqns. 6.1- 6.4.

$$CBS = \left( \frac{P}{2w \cos(\phi)} \right) \left( \frac{d_x}{\cos(\phi)} + (D+t) \tan(\phi) \right) \quad (6.1)$$

$$dy = d_x \tan(\phi_i) + \frac{D+t}{\cos(\phi_i)} - \Delta \quad (6.2)$$

$$\phi = \sin^{-1} \left( \frac{-d_x(D+t) + dy \sqrt{d_x^2 + d_y^2 - D^2 - 2Dt - t^2}}{d_x^2 + d_y^2} \right) \quad (6.3)$$

$$\sigma = \frac{3 \cdot CBS}{2t \sqrt{r_i r_0}} \quad (6.4)$$

where  $\phi_i$  is the initial angle between loading arm and the horizontal ( $45^\circ$ ),  $d_x$  is the distance between the rollers (12.5mm), D is the diameter of the loading bars (10mm), t is the specimen thickness (2mm),  $\Delta$  is the displacement where the first force drop occurs and w is the width of the specimen (25mm). A short Matlab code was written to calculate the curved strength of samples by using the data in Figure 6.15. The through thickness tensile strength of the samples was found to be 30 MPa.

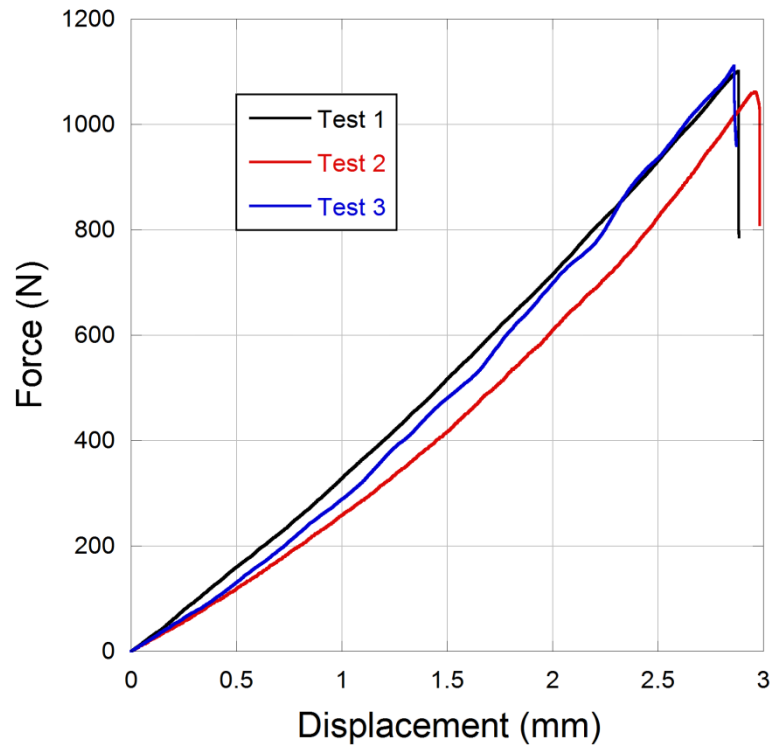


Figure 6.15. The curved beam force-displacement responses of the composite samples.

In the macroscopic damage analysis of the samples, two different deformation regions are inspected. In the bottom part of the curved section there is delamination in the sample due to the acting tensile stresses on the composite layer. In the middle portion of the curved section there is delamination between the adjacent layers due to compression loading and the dominant failure type is matrix dominant delamination. The deformation types are shown in Figure 6.16. In the same figure, it is seen that there are more than one delaminated adjacent layers and each delamination results in force drops. However, in calculations, only the first delamination corresponding to the first force drop in the force-displacement curve is taken in the through thickness stress calculations.

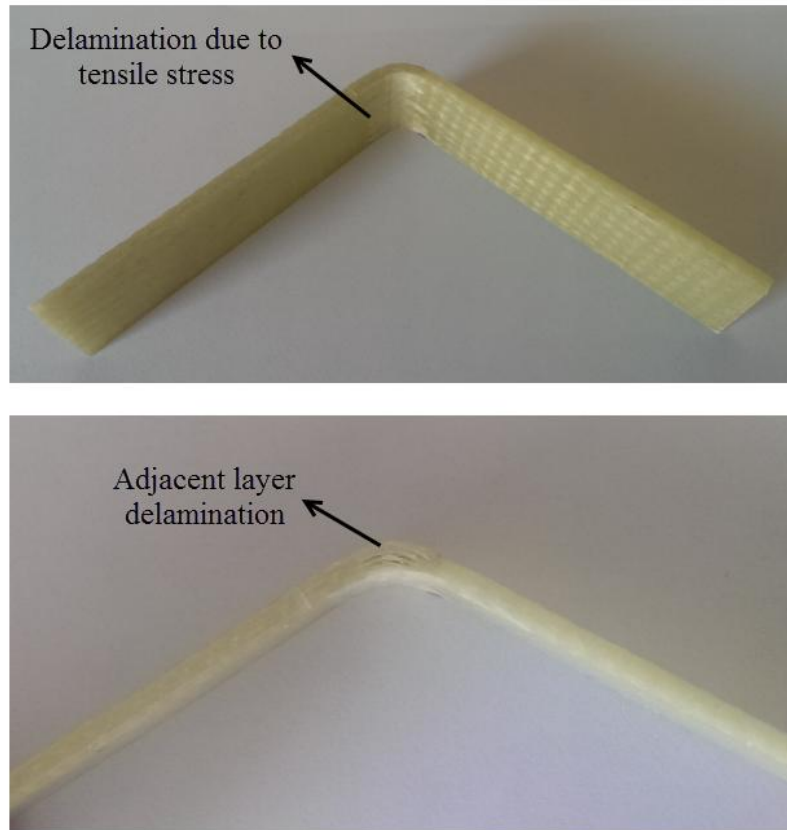


Figure 6.16. Deformation types in curved beam strength test specimen.

### 6.2.5. Laterally Constraint Compression Test Results

Lateral constraint compression tests were performed to find the shear failure dependent SFS and SFC material model parameters. In this test method, the material was loaded from the through thickness direction and constrained in the transverse direction in order to obtain a failure surface cutting through the fiber with an inclined angle in the compressive loading direction. The fiber crush strength (SFC) of the composite sample was just found by measuring stress response along the through thickness direction. The lateral constraint compression tests stress-strain curves of the composite are shown in Figure 6.17. The average value of the SFC parameter was calculated 625 MPa. The value of fiber punch shear strength, SFS can be calculated by determining the SFC and the failure plane angle,  $\phi$ . The failure plane angle can be found by measuring the failure angle on the composite sample. Figure 6.18 shows the measured failure angle from the composite sample and the average of the  $\phi$  with other measurements is found to be  $44^\circ$ . By using Eqn. 3.9, the SFS values is found 325 MPa.

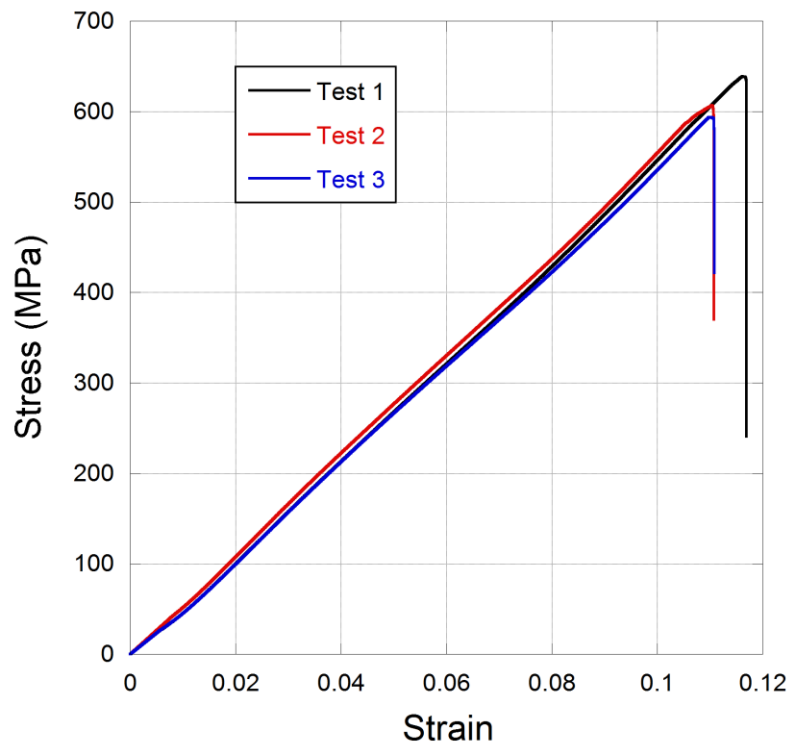


Figure 6.17. Lateral constraint compression test results.

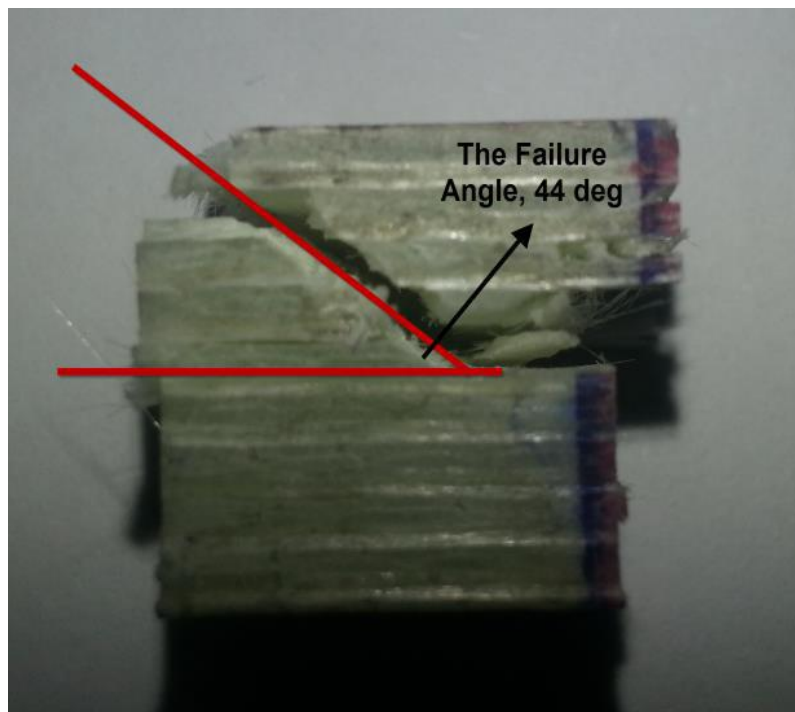


Figure 6.18. Lateral constraint test specimen failed with inclined shear plane.

## 6.2.6. Experimental Shear Test and Numerical Model Results

The quasi-static shear test numerical simulation studies were performed for  $m_4$  parameter calibration in accordance with the shear test experimental results. In shear tests, there was a non-linear hardening behavior in stress-strain response of the composite samples. Since the controlling parameter for this behavior was  $m_4$ , many calibration studies were conducted to obtain good agreement with the experimental results. In the studies, it was recognized that negative  $m_4$  parameters satisfied better agreement with the experimental results. The numerical simulation shear stress-strain curve using  $m_4 = -0.15$  is shown in Figure 6.19 together with experimental shear stress-strain curves. This value of  $m_4$  showed the best agreement with the experiment. As in the tension test simulation,  $m_1 = m_2$  parameters were set to 4 in order to obtain good agreement in in-plane fiber damages. The value for the maximum shear strength was measured as 43 MPa from the experimental results.

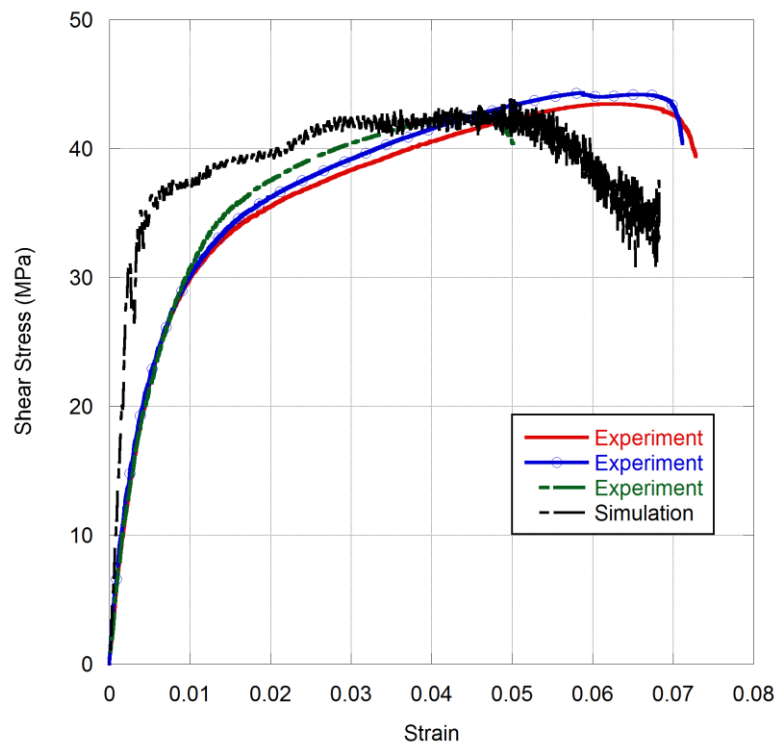


Figure 6.19. Quasi-static shear test experimental and numerical simulation stress-strain responses.

The simulation damage propagation through the shear test sample with proceeding strain values is shown in Figure 6.20. The damage starts from the pulling end and propagates through the stationary end in a V shaped profile. The shear strength in tension is the highest in the principal in-plane directions and lowest in principal out-of plane directions. This is attributed to the fiber/matrix interface debonding in these directions. The failure modes in shear testing include matrix cracking, fiber pull-out, fiber bundle pull-out and delamination. The picture of a failed test specimen is shown in Figure 6.21. The test specimen also fails in a V shaped profile with a 45° angle. The adjacent layer delamination and fiber bundle pull-out are also observed.

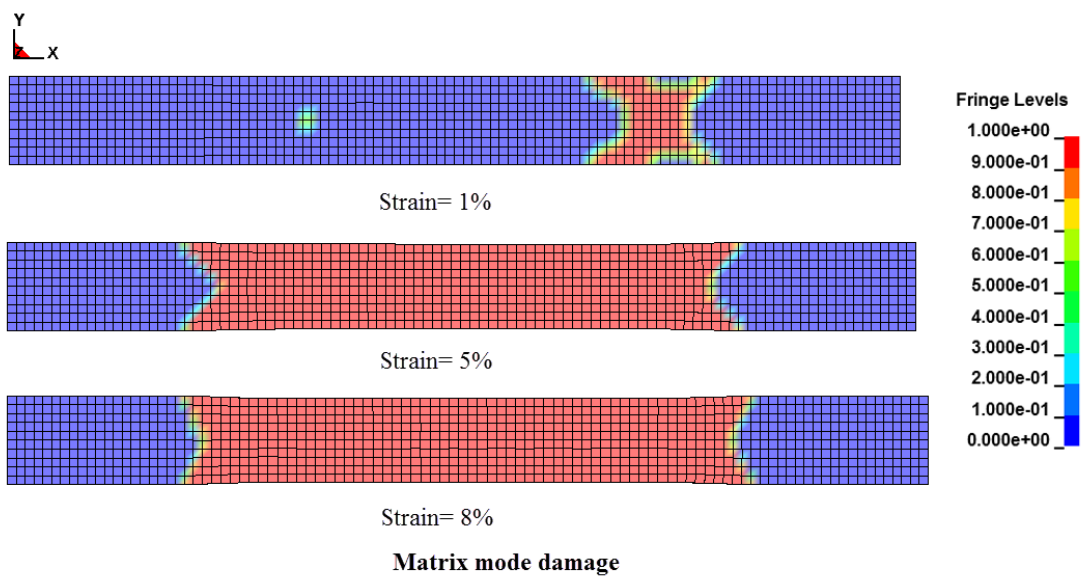


Figure 6.20. Matrix mode damage patterns in quasi-static shear test numerical simulation.



Figure 6.21. Failed composite sample after quasi-static shear testing.

### **6.2.7. Experimental Low Velocity Impact Test and Numerical Model Results**

Low velocity impact test simulations were conducted in order to validate the MAT 162 material model post damage softening parameters (m1-m4) and also to calibrate the modulus reduction parameter OMGMX. In the numerical simulations OMGMX varied from 0.994 to 0.999 while the other parameters were kept constant. The impact velocities used in experiments and simulations were 4.21 m/s to 6.12 m/s, which were chosen for rebound case and perforation case, respectively. The rebound case (4.21 m/s) force-time response for 3 mm thick composite samples at various values of OMGMX are shown in Figure 6.22. As is seen in the same figure that, as the OMGMX value decreases, the predicted peak load and the duration of the unloading decrease. It is also noted in the same figure, the simulation force-time profile with OMGMX=0.999 show the closest match to the experimental force-time profile. The perforation force-time response (6.12 m/s) is shown in Figure 6.23. In the same figure, the effect of reduction of the modulus parameter at different damage values are also shown. Similar to the rebound case, the peak load and the unloading duration decrease as the OMGMX parameter decreases. The initial slope of the perforation case is steeper than the rebound case, resulting from the strain rate sensitivity of composite, however, the loading and the unloading durations are lower than those of the rebound case due to the fiber failure in the sample. In both cases, there is a mismatch between the unloading part of the experimental and simulation force-time graphs due to the linear elastic unloading in the model as opposed to unloading with residual plastic strain in the experiments. The displacement values of the indenter in the experiments and simulation are shown for both rebound and perforation cases in Figure 6.24. In the rebound case, the indenter reaches a maximum displacement, 19.44 mm, in experiment and simulation and after releasing the whole energy it starts to move backwards. The perforation occurs at 22.86 mm for both experiment and simulation and the indenter continues its motion because of its residual kinetic energy. The simulation pictures of the deformed composite plates with displacement fringe levels are shown in Figure 6.25 for rebound and perforation. In perforation case, the elements are eroded, resulting from the excessive ECRSH parameter. The force-time, displacement-time and the damage images clearly indicate that the model is able to capture the low velocity impact tests, validating the used MAT 162 material model parameters.

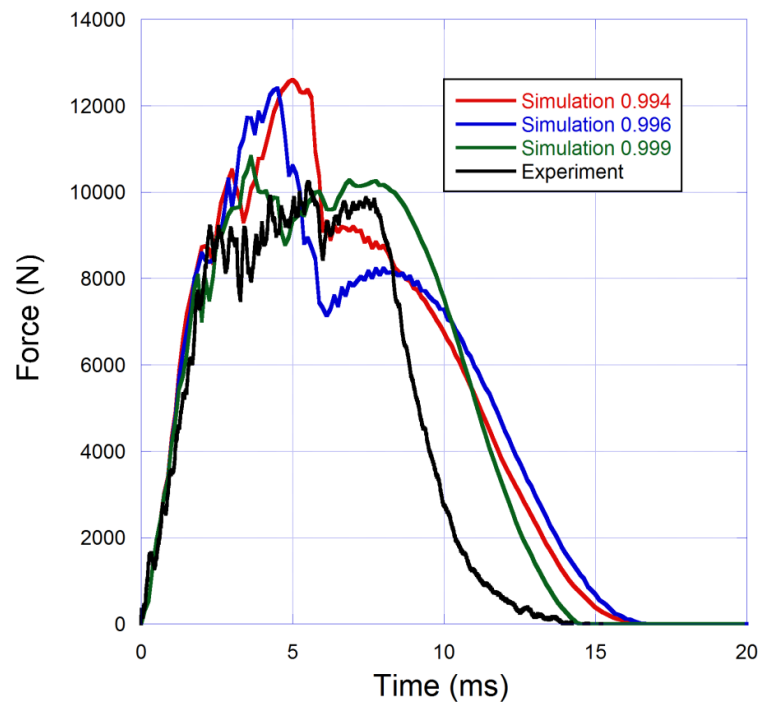


Figure 6.22. Force-time response of low velocity impact test and numerical studies at 4.21 m/s impact velocity.

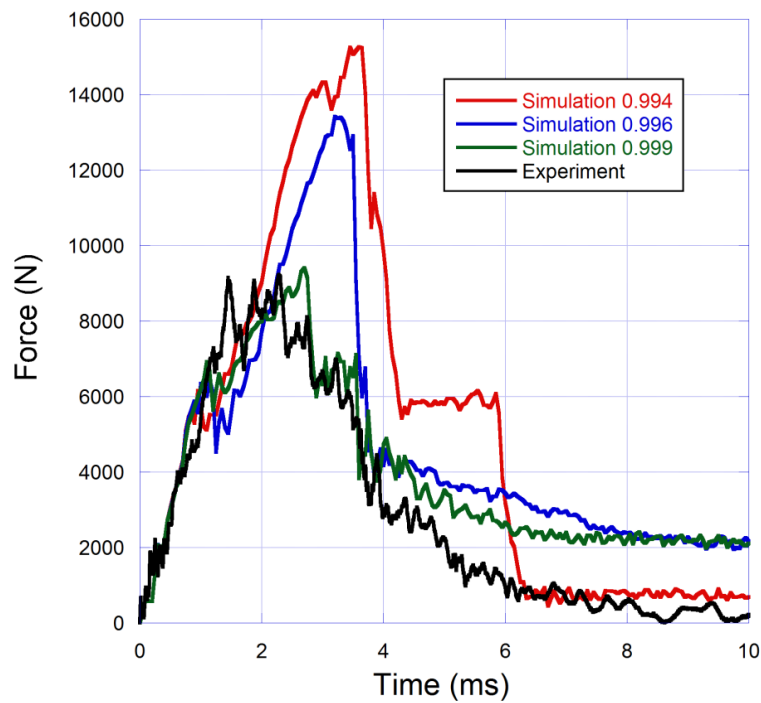


Figure 6.23. Force-time response of low velocity impact test and numerical studies at 6.12 m/s impact velocity.

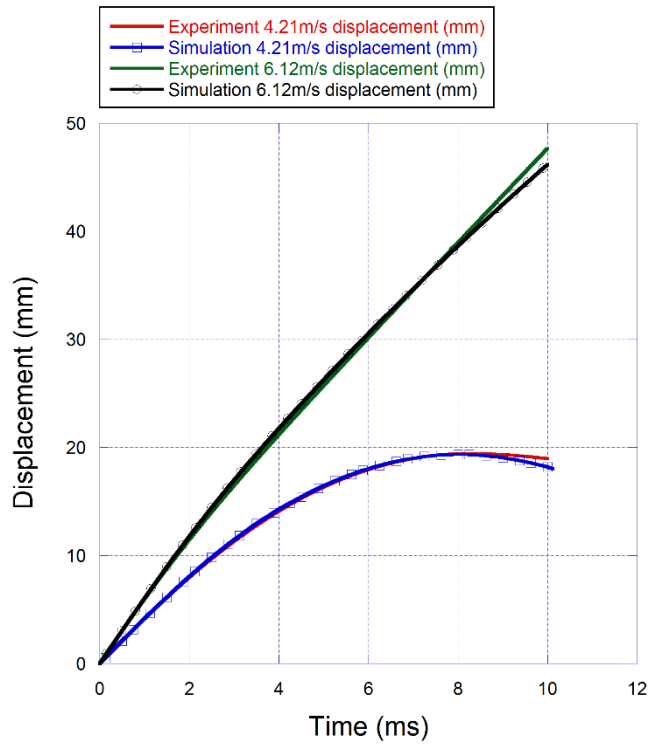


Figure 6.24. Experimental and numerical simulation displacement-time curves of rebound and perforation cases.

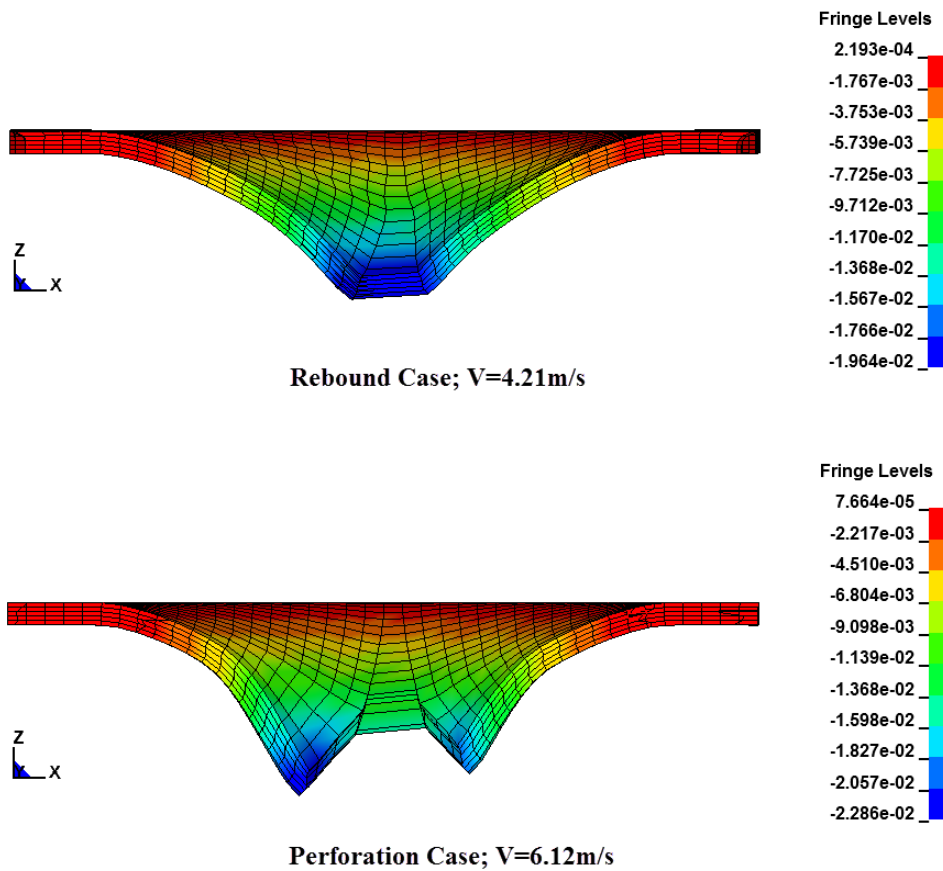


Figure 6.25. Displacement levels of rebound and perforation cases.

### 6.2.8. Experimental Projectile Impact Tests and Numerical Model Results

The projectile impact tests and simulations were conducted to verify the element eroding axial strain,  $E\_LIMT$  and limit tensile volume strain,  $EEXPN$ . In the numerical studies,  $E\_LIMT$  and  $EEXPN$  values varied between 3 and 4 with 0.5 increments in order to capture the residual velocity of the projectile, deformation in the composite plates and the ballistic limits calculated as in the experiments. In the experiments, 2 mm, 3 mm and 5 mm thick composites plates were used as targets and projectiles were fired on the plates at an average impact velocity of 150 m/s. The ballistic limits for the perforated composite plates were calculated from difference of the initial kinetic energy and residual kinetic energy of the projectile based on the conservation of the mass of the plates since mass of the plates slightly change after the experiments. The average calculated ballistic limits for the composite plates are tabulated in Table 6.1.

Table 6.1. Calculated ballistic limits for 2 mm, 3 mm and 5 mm thick composite plates.

<b>Specimen Type</b>	<b>Initial Projectile Velocity (m/s)</b>	<b>Residual Projectile Velocity (m/s)</b>	<b>Calculated Ballistic Limit (m/s)</b>
2 mm	152.10	90.43	126.60
3 mm	175.20	114.40	132.80
5 mm	154.82	65.41	140.32

In the numerical studies, the  $E\_LIMT$  and  $EEXPN$  parameters were determined with 2 mm thick composite plates. In the simulations, only  $E\_LIMT$  and  $EEXPN$  values were changed and the other parameters were kept constant. The averages of the experimental results were calculated for the projectile impact velocity and residual velocity. The projectile impact velocity was set 152.10 m/s and the simulation residual velocity compared to experimental ones. Experimental and numerical comparison of projectile residual velocity for 2 mm thick composite plates is shown in Figure 6.26. As is seen in the same figure,  $EEXPN=E\_LIMT=3$  and  $EEXPN=E\_LIMT=3.5$  over estimates the experimental residual velocity of the projectile while  $EEXPN=E\_LIMT=4$  nearly predicts the experimental residual velocity of the projectile. The values set to 3

and 3.5 limit the motion of projectile-composite plate interaction and cause the element erosion earlier than the expected so the simulation residual velocity of the projectile is higher than that of the experiment.

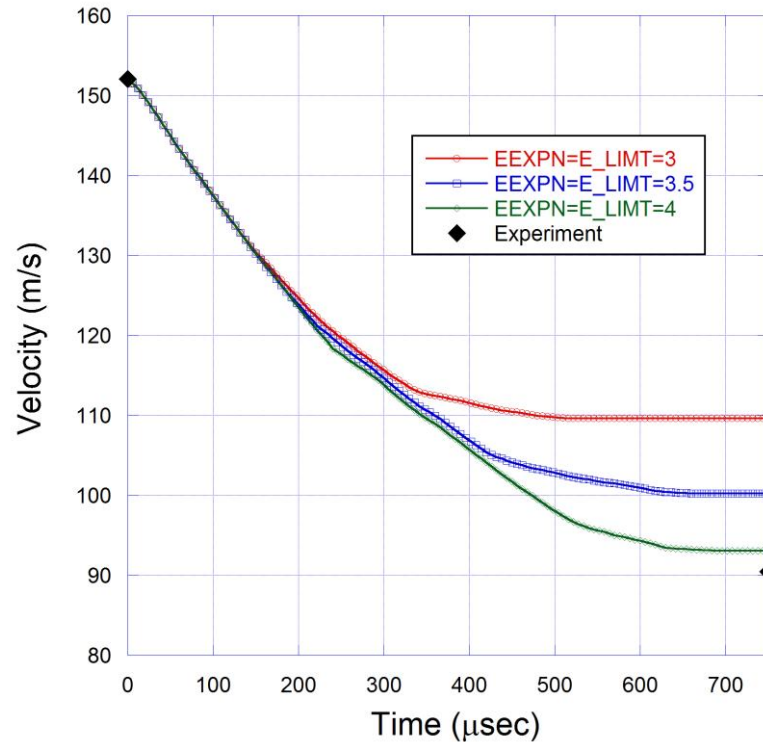


Figure 6.26. Experimental and numerical comparison of projectile residual velocity for 2 mm thick composite plates.

The numerical simulations with EEXPN=E\_LIMT=4 were also conducted for 3 mm and 5 mm thick composite plates. The experimental and numerical ballistic limits as function of plate thickness are shown in Figure 6.27. Linear fits are applied on the experimental and simulation data. The simulation and experimental ballistic limits show only slight differences between each other: for 2 mm, 3 mm and 5 mm thick composite plates the differences are 2.8%, 1.65% and 0.97%, respectively. The projectile displacement-time curve for three plate thicknesses plate thickness are shown in Figure 6.28 for the same impact velocity (152.10m/s). The displacement time curves in Figure 6.28 consist of two different regimes; the first region is bilinear region which shows the projectile-composite plate interaction and the second region is linear region where the projectile moves with a constant velocity proving the progressive damage occurs. It can be concluded from the same figure that the bilinear region increases with increasing plate thickness as the ballistic limit increases.

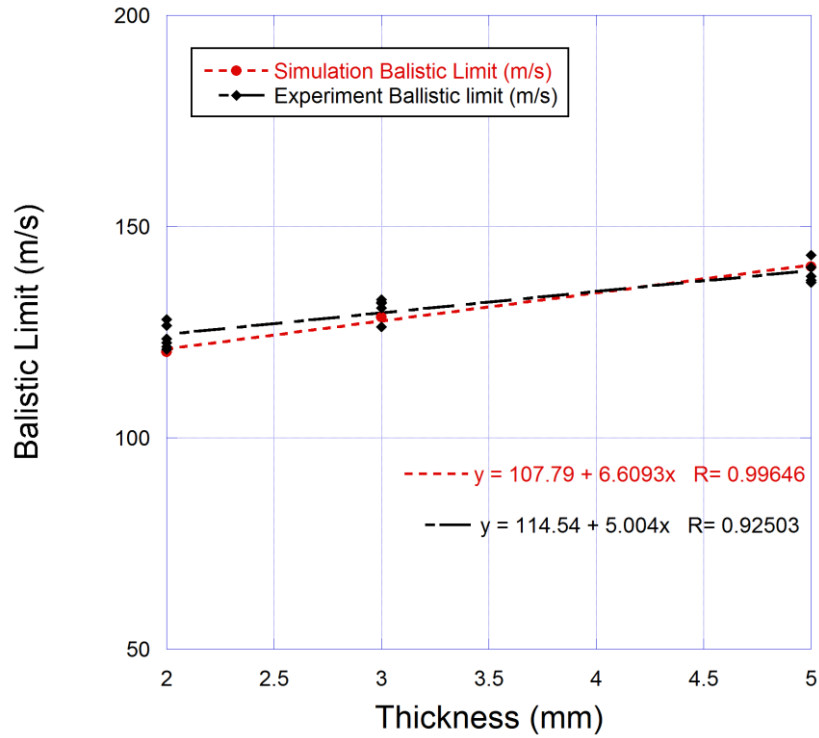


Figure 6.27. Experimental and numerical calculated ballistic limits for composite plates.

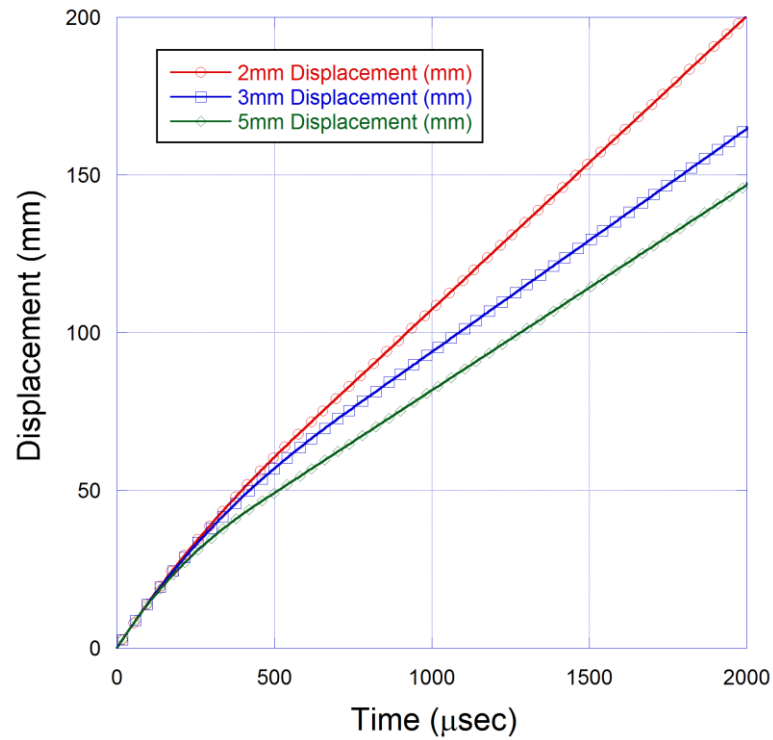


Figure 6.28. Displacement-time response of the projectile against composite plates.

The force-time response of the composite plate with 2 mm thickness at different EEXPN and E\_LIMT values is shown in Figure 6.29. The initial contact force does not change with the different EEXPN and E\_LIMT values, however; when the projectile-composite plate start to move together the elements are eroded and the force values decreases. EEXPN and E\_LIMT values set to 3 and 3.5 under predict the force and duration which cause higher projectile residual velocity. On the other hand, when EEXPN=E\_LIMT=4, the simulation projectile residual velocity shows close agreement with the experimental residual velocity. The sudden force drops and small oscillations in the force-time curves, are attributed to the element erosion.

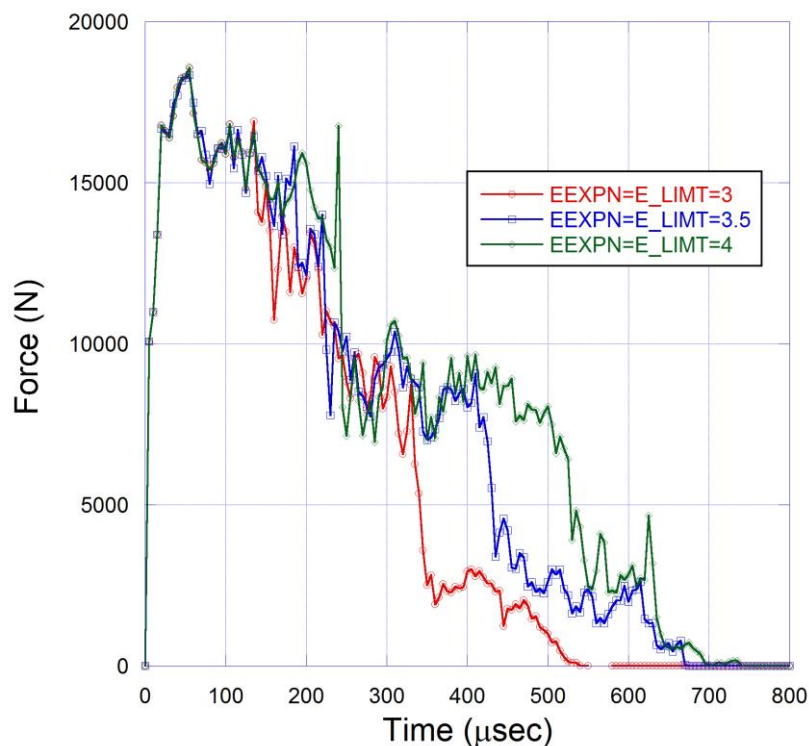


Figure 6.29. Force-time response of the composite plates.

The simulation damage progression of the composite plate at different impact times  $t_i$  is shown in Figure 6.30. The projectile induces a peak stress on the composite initially. Then, the projectile starts to induce compressive stress on the subsequent layers and the fibers start to break followed by the shear deformation. The compressive and tensile stresses also act on the front and back surfaces resulting in delamination. Finally, shear plugging occurs which is mainly caused by the dynamic friction between the projectile and the target.

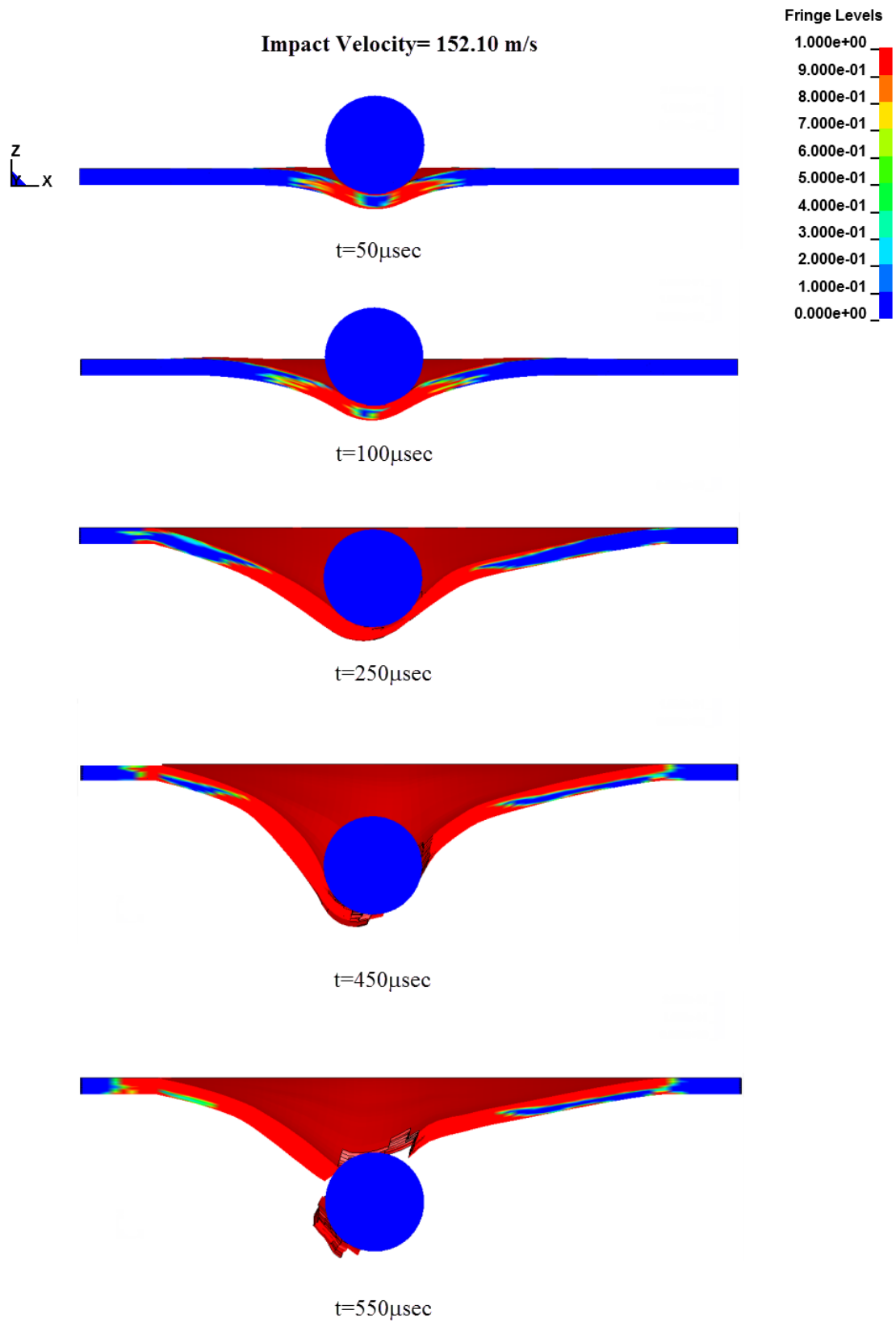


Figure 6.30. Finite element simulation damage progression of 5 mm thick composite.

The optimized MAT\_162 material model parameters of the tested composite are tabulated in Table 6.2. The determined material model parameters can be used in the simulations of static, impact and blast loading since the parameters are identified for the principal directions at both quasi-static and dynamic strain rates. Based on the type of the experiments, the damage parameters (m), ELIMIT, EEXPN and SDELM can be modified using different values.

Table 6.2. Optimized MAT 162 material model parameters.

<i>MID</i>	$\rho, \text{kg/m}^3$	$E_1, \text{GPa}$	$E_2, \text{GPa}$	$E_3, \text{GPa}$	$\nu_{21}$	$\nu_{31}$
162	1850	16	16	7.74	0.13	0.23
$G_{12}, \text{GPa}$	$G_{23}, \text{GPa}$	$G_{31}, \text{GPa}$	$S_{12}, \text{MPa}$	$S_{23}, \text{MPa}$	$S_{31}, \text{MPa}$	$\nu_{32}$
1.79	1.66	1.66	43.4	43.4	43.4	0.23
$S_1^T, \text{MPa}$	$S_1^C, \text{MPa}$	$S_2^T, \text{MPa}$	$S_2^C, \text{MPa}$	$S_3^T, \text{MPa}$	$S_{FC}, \text{MPa}$	$S_{FS}, \text{MPa}$
400	285	400	285	30	650	325
$S_{FFC}$	$\varphi, \text{deg}$	$e_{Limit}$	$S_{Delam}$	$\omega_{max}$	$e_{Crush}$	$e_{Expn}$
0.3	10	4	1.2	0.999	0.55	4
$C_{rate1}$	$M 1$	$M 2$	$M 3$	$M 4$	$C_{rate2}$	$C_{rate 3}$
0.033	4	4	0.5	0.2	0.036	0.03
$C_{rate 4}$						
0.042						

## CHAPTER 7

### TESTING AND MODELLING OF CORRUGATED STRUCTURES

#### 7.1. Simplified Johnson Cook Material Model of 1050 Al

The true tensile stress-strain curves of as-received sheet and heat-treated 1050 Al alloy are shown in Figure 7.1(a). At least three tests were performed for both as-received and heat treated alloy. The heat treatment naturally reduces the yield strength and flow stress and increases the failure strain of the alloys as seen in the same figure. The yield strength,  $\sigma_y$ , of the alloys are determined by the proportional limit as shown in Figure 7.1(b). This method gives a yield strength of 102 MPa for 1050 H14 alloy and 24 MPa for heat-treated alloy. The average tensile strength of 1050 H14 is 150.6 MPa (147-153 MPa), while the average tensile strength is reduced to 98.6 MPa (96.6-100.5 MPa) after annealing. The average tensile strain of 1050 H14 alloy is 0.042 (0.037-0.051), while heat treatment increases the tensile strain to 0.143 (0.10-0.18). The experimental true stress-strain curves were further fitted with the simplified Johnson-Cook material model in the first bracket of Eqn. 4.16. For the fitting, the strain values are converted into plastic strain ( $\varepsilon_p$ ) using the following relation

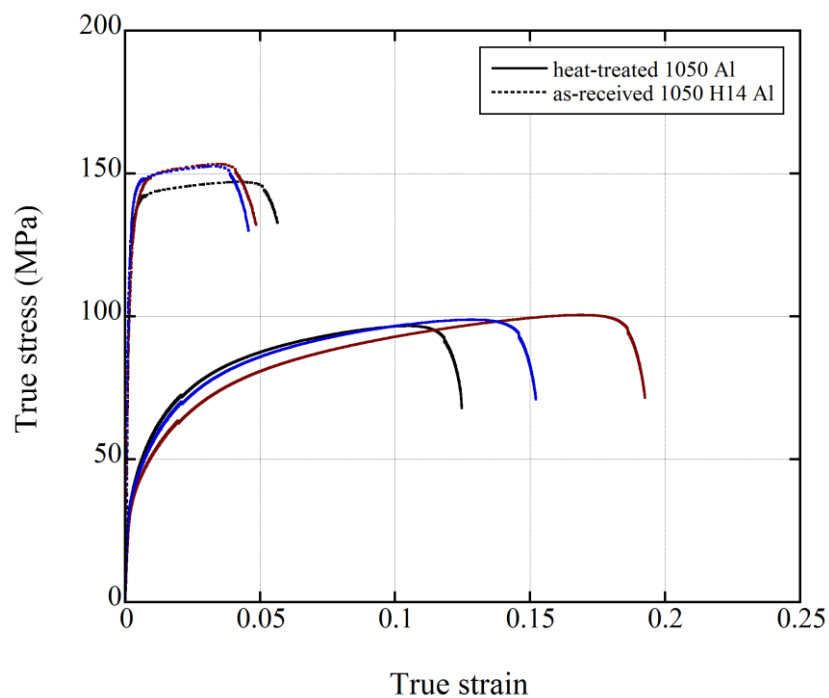
$$\varepsilon_p = \varepsilon - \frac{\sigma_y}{E} \quad (7.1)$$

The elastic modulus in Eqn. 7.1 is 70 GPa for both alloys. The fitting was done on a true stress-plastic strain curve, which is average of three tests. The resultant average true stress-plastic true strain curves of the alloys are shown in Figure 7.2. In the same figures, the results of fitting of the stress-strain curves with Eqn. 4.16 are also shown. The fitting results of m1 and m2 refer to B and n parameters, respectively, while the value of A corresponds to yield strength of the alloys. The strain hardening parameter of n increases after heat treatment. The simplified Johnson-Cook material

model parameters and the tensile failure strains ( $\epsilon_f$ ) of the alloys are summarized in Table 7.1. The failure strains of as-received and heat treated alloys were calculated using the following relation

$$\epsilon_f = \ln\left(\frac{A_0}{A_f}\right) \quad (7.2)$$

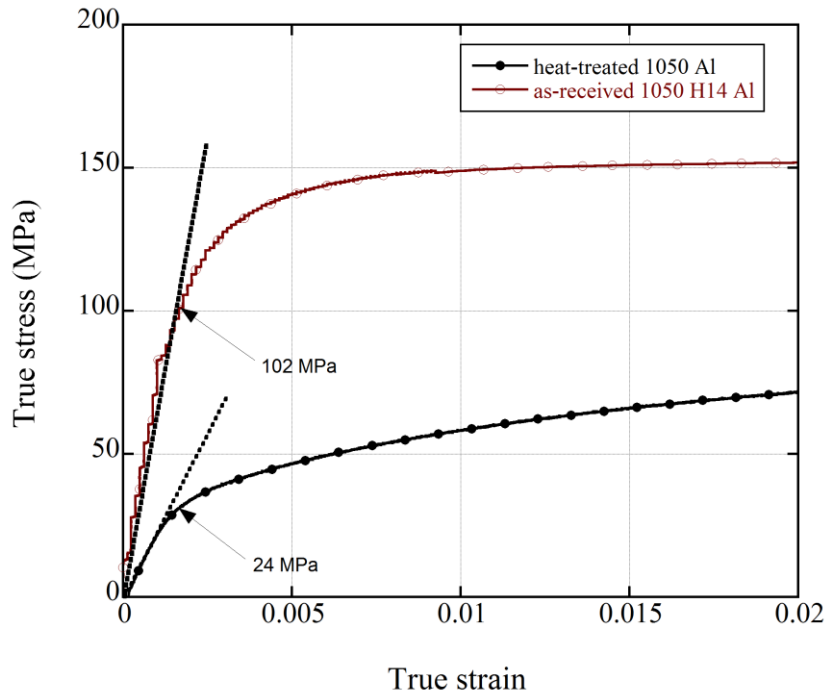
where  $A_0$  and  $A_f$  are the initial and fracture cross-sectional area of the specimen. The final fracture areas were measured from the fractured specimens.



(a)

Figure 7.1. (a) Tensile true stress-true strain curves and (b) yield strength of as-received and heat-treated 1050 Al.

(cont. on next page)



(b)

Figure 7.1. (cont.)

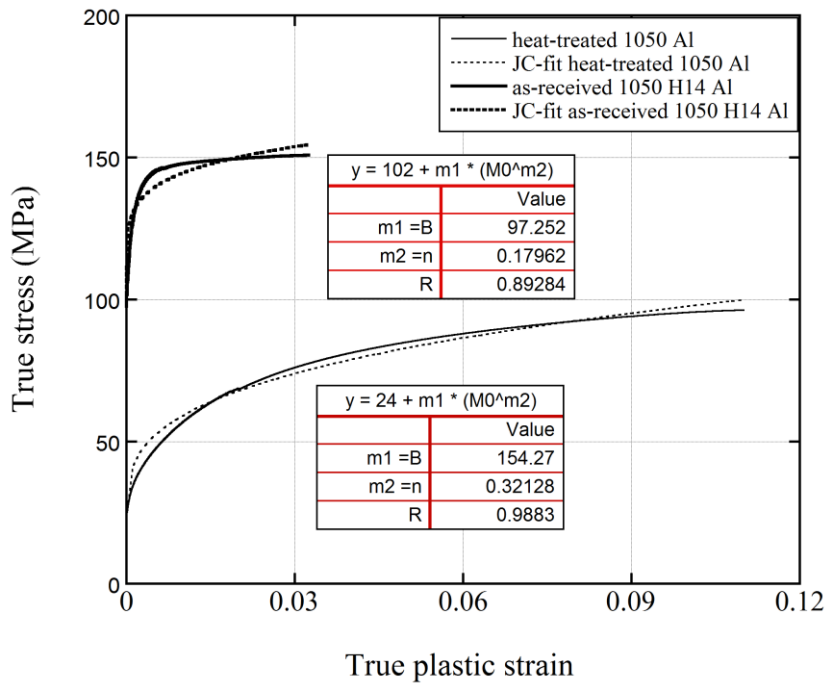


Figure 7.2. True stress-plastic true strain curves and JC parameters fitting of as-received and heat-treated 1050 Al.

Table 7.1. Determined simplified JC model parameters and failure strain of as-received and heat-treated 1050 Al alloys.

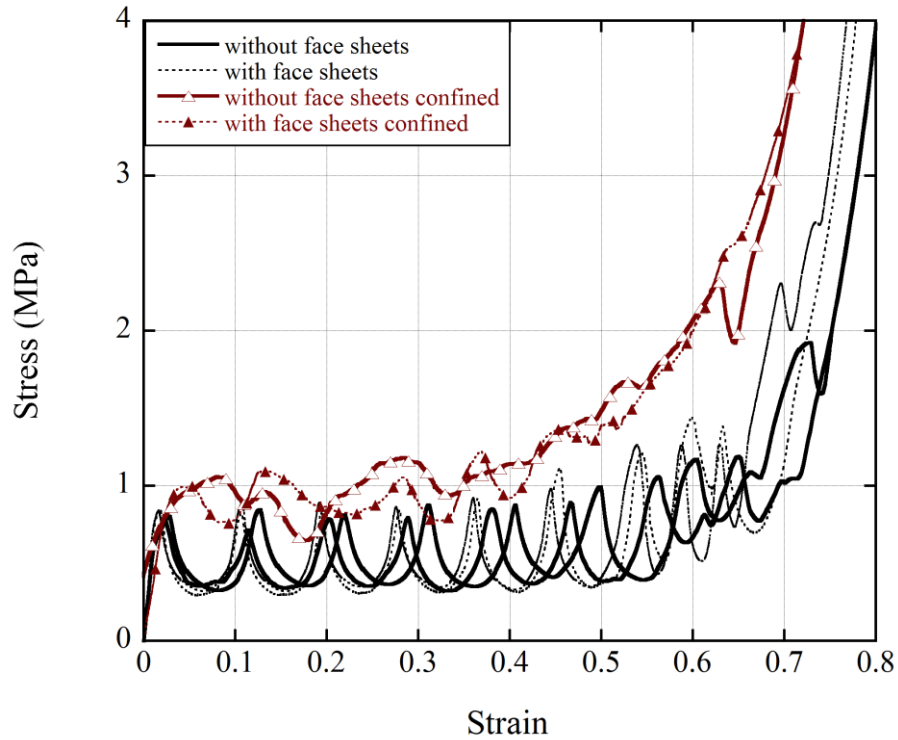
<b>Material</b>	<b>A (MPa)</b>	<b>B (MPa)</b>	<b>n</b>	<b><math>\epsilon_f</math></b>
1050 H14 Al	102	97.25	0.18	0.62
Heat-treated 1050 H14 Al	24	154.27	0.32	0.865

## 7.2. Compression of Corrugated Sandwiches

The quasi-static compression stress-strain curves of small fin corrugated sandwiches with and without 1050 Al face sheets at  $10^{-1} \text{ s}^{-1}$  are shown in Figure 7.3. The tests at  $10^{-3} \text{ s}^{-1}$  were also performed. Since the simulations at this quasi-static strain rate took very long time, only the quasi-static strain rate tests at  $10^{-1} \text{ s}^{-1}$  were simulated. In Figure 7.3, the stress-strain curves of two tests for the specimens are shown together in order to show repeatability of the tests. Despite slight differences in the location of the peak stress, the separate tests show well agreement between each other. Both with and without face sheets sandwiches, the inelastic deformation presumably is started with the buckling of one or couple of corrugated layers at a stress of 0.70 MPa as shown in Figure 7.3. The quasi-static crushing response of the tested corrugated sandwiches is very much similar to that of aluminum foams in that the stress strain curve is composed of three sequential deformation regions, namely elastic, collapse and densification regions [73, 74, 83]. In the collapse region the oscillations in the stress values arise from the sequential collapse of the individual corrugated layers. The densification starts at the strain of 0.74 in the corrugated sandwiches without face sheets and at a strain of 0.68 with face sheets. In the confined tests, the initial buckling stress is about 1 MPa for both without and with face sheets sandwiches. The intensity of the stress oscillations decline in confined tests and the structures densify earlier. The mean stress of both corrugated structures is about 0.46 MPa, while the means stresses of confined tests are  $\sim 0.85$  MPa. This values of mean stress nearly matches with the initial buckling stresses and stress peak values of without and with face sheets structures. As elaborated in the following sections, the shearing of the corrugated layers are prevented in the confined tests, while the layers in unconfined tests are partly sheared. This also results in early densification or abrupt stress rise in confined tests. Therefore, the crushing stress of the studied

corrugated structure is taken 0.70 MPa throughout this study and also in analytic investigations.

The big fin corrugated structure investigated in the present study were however previously tested and modelled in other studies [85, 109]. The optimum mesh size, correct imperfection geometry and size were determined from the experiments and applied to the numerical models.



(a)

Figure 7.3. (a) The experimental compression and confinement stress-strain curves of corrugated sandwiches at  $10^{-1} \text{ s}^{-1}$ .

In order to further clarify the quasi-static deformation characteristics of the studied corrugated sandwich structures, the tested samples were microscopically analyzed. The deformed samples were mounted into polyester and the mounted samples were cut through the cross-section in two sections using a diamond saw and a relatively low cutting speed. This prevented the corrugated layers from damaging during slicing. The cross-sectional view of corrugated core sandwich structures with face sheets compressed until about 0.4 strain before the densification region is shown in Figure 7.4. The deformation in Figure 7.4 is localized by crushing of corrugated layers, while noting the crushing of layers is not sequential. The localized deformation starts with fin

wall buckling, bending, followed by the folding of buckled walls, forming plastic hinges. The crushing also proceeds with the buckling of several layers simultaneously. This is also reflected in the stress-strain curves, in which each peak stress corresponds to the buckling of the layers. The stress-strain curve accommodates only 7 stress peaks, while there are 16 corrugated layers in the test sample.



Figure 7.4. The quasi-static confined test sample compressed until about 0.4 strain.

### 7.3. Mesh Sensitivity

The buckling mode is the most important parameter that is directly sensitive to the mesh and imperfection. Three mesh sizes were investigated: fine mesh of 1164168 shell elements, medium mesh of 527176 shell elements and coarse mesh of 87350 shell elements. Mesh size analysis was applied to perfect fin geometry without face sheets. Figures 7.5(a-c) show sequentially the numerical stress-strain curves of fine, medium and coarse mesh sizes together with experimental stress-strain curve at  $10^{-1} \text{ s}^{-1}$ . As the mesh size increases, the model better predicts the initial buckling stress. The coarse mesh predicts nearly the initial buckling stress (Figure 7.5(c)), while fine and medium mesh predicts 10 and 20% higher initial peak stresses (Figures 7.5(a) and b)). The stress peaks are also better predicted with medium meshes. As the mesh size increases the model predict lower stress valleys, but it converges the experimental densification strain. The effects of mesh size and imperfection on the buckling behavior of shell cylinders under axial loading were previously investigated using different mesh sizes in

perfect models [124]. The coarser mesh captured the experimental stress values better than fine mesh. The difference between fine mesh model and experiments was found  $\sim 15\%$ , while when imperfect model was used the difference was reduced to  $\sim 1\%$ . It was reported that the buckling modes of the imperfect cylinder were mainly characterized by the imperfection pattern and size.

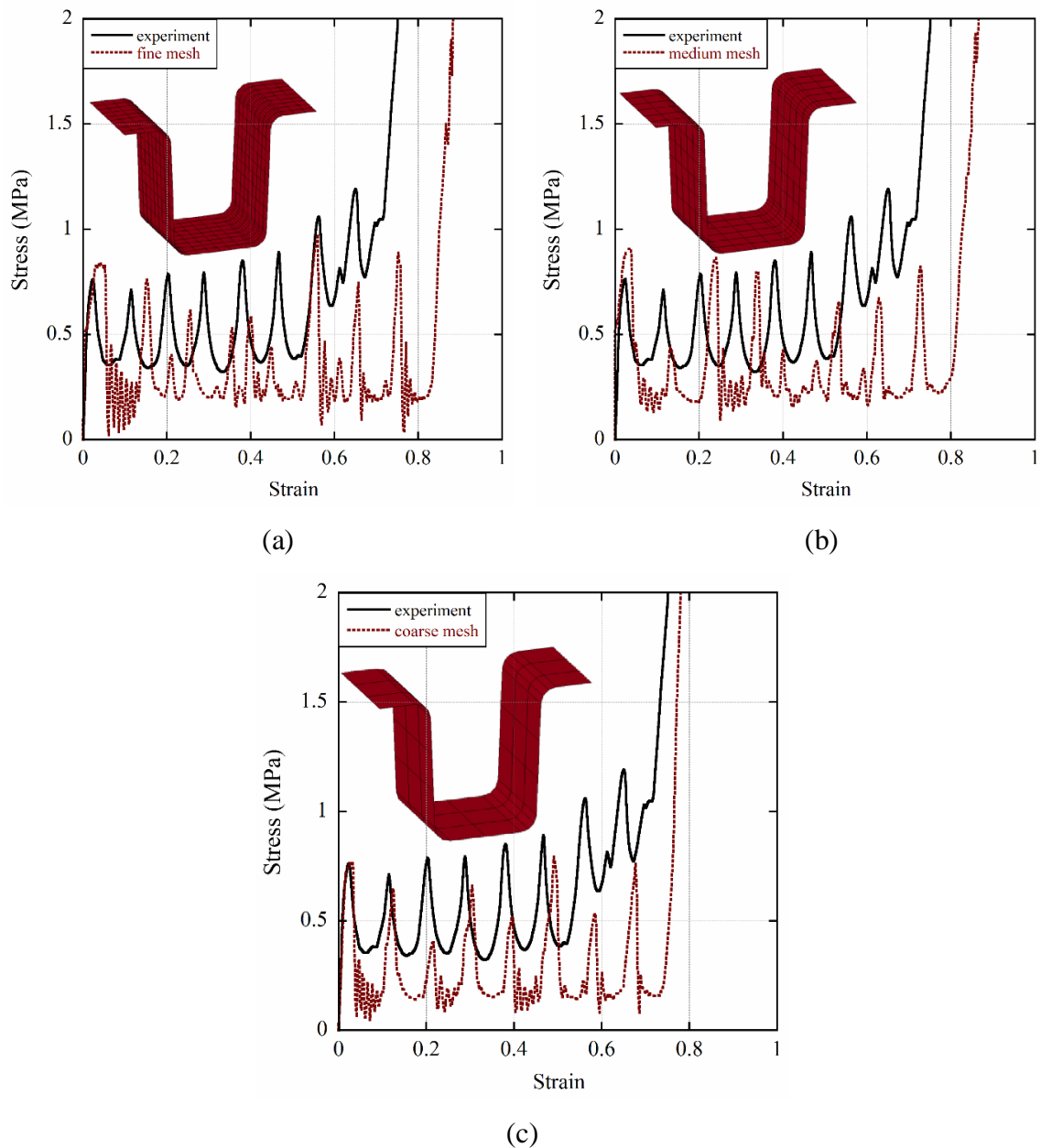


Figure 7.5. Mesh sensitivity analysis of perfect fin geometry at  $10^{-1} \text{ s}^{-1}$ : (a) fine, (b) medium and (c) coarse mesh size.

## 7.4. Imperfection Sensitivity

Different imperfection configurations were implemented. First, fin wall bending imperfection was applied to each corrugated layer. Second, half of the total layers had fin wall bending and half bulge type imperfection. From camera records of a compression tests, it was determined that the plastic instability started from the mid-section layers, usual simultaneous buckling of two distant fin layers. Based on this observation, imperfections were inserted to the intermediate layers. Two imperfections in the mid-section of half-length of the sample, layer 6 and layer 12, were inserted. The first two imperfect models were modelled using coarse mesh and third one using both fine and coarse meshes.

Applying bending type imperfection to all the fins of the corrugated layers results in reduced stress peak level with increased stress valleys as shown in Figure 7.6(a). The model although converges to experimental stress valley levels, the peak stress values stay much lower than those of the experiments. Note also bending type imperfection reduces the densification strain as compared with perfect model. The mixed type imperfection, second type, increases the peak stress values, but it decreases valley stresses as compared with bending type imperfection (Figure 7.6(b)). The mixed imperfection further increases the densification strain to the level of perfect model. The third type localized bending type imperfection with fine mesh increases the peak stress values but reduces the initial buckling stress (Figure 7.6(c)). It also increases the densification strain. The third type localized bending type imperfection with coarse mesh both increases the peak stress and valley stress values (Figure 7.6(d)). It converges both experimental initial buckling stress and densification strain.

Throughout the mesh size and imperfection analysis, the best fit is found with the coarse mesh and localized bending imperfection. The model however cannot match with the experimental stress values between 0.5 and densification strain. This discrepancy may be attributed to several factors. First, the increase in the fin wall thicknesses of the corrugated layers after brazing is not included in the model. This may lead to earlier densification of the corrugated sandwiches experimentally. The increased strength of the brazed sections may lead to increased buckling strength near the densification causing higher experimental stress. Although not observed experimentally the corrugated layer sequence of 0/90 layer may result in varying buckling stresses of

the layers, leading to buckling of 0 layer first, thereafter buckling of 90 layers or vice versa, which will be elaborated in a separate study. The further modelling of corrugated sandwiches however continued with coarse mesh and type 3 imperfection.

Figures 7.7 (a-d) show the experimental and simulation deformation sequences of sandwich structures at different strains. It is seen from the same figure that the simulation with coarse mesh size and fin wall bending imperfections at 6th and 12th fin layers results in similar deformation sequences of the layers with the experiment. Shortly, the small fin corrugated core sandwich structures are both mesh and imperfection type and location sensitive.

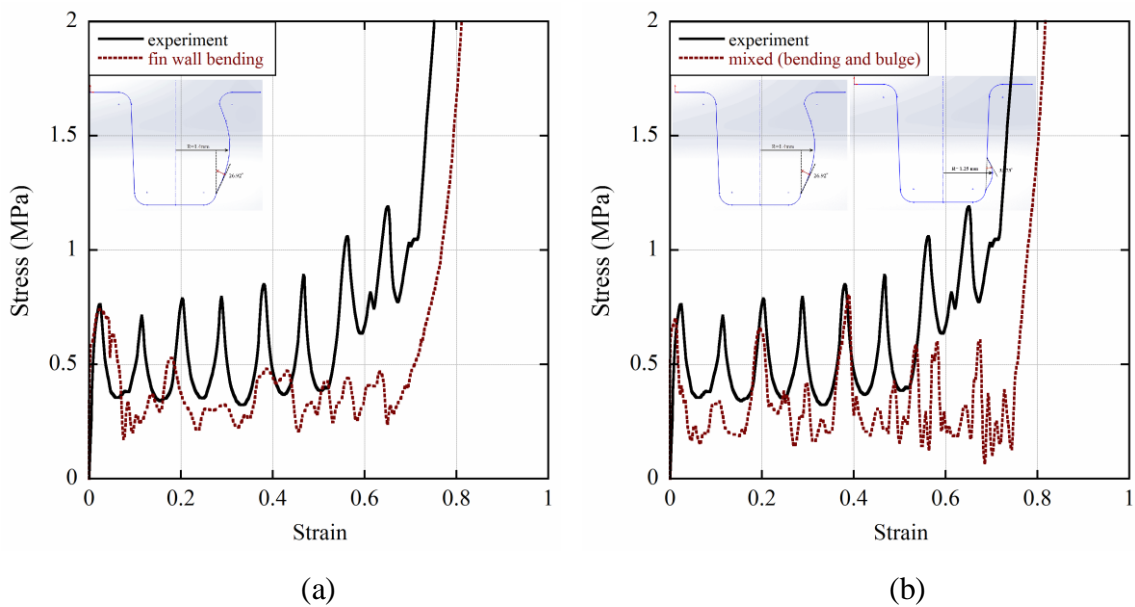


Figure 7.6. The stress strain curves of the imperfect corrugated sandwiches (a) fin wall bending, (b) fin wall bending and bulging and fin wall bending in the layers of 6 and 12; (c) fine mesh and (d) coarse mesh.

(cont. on next page)

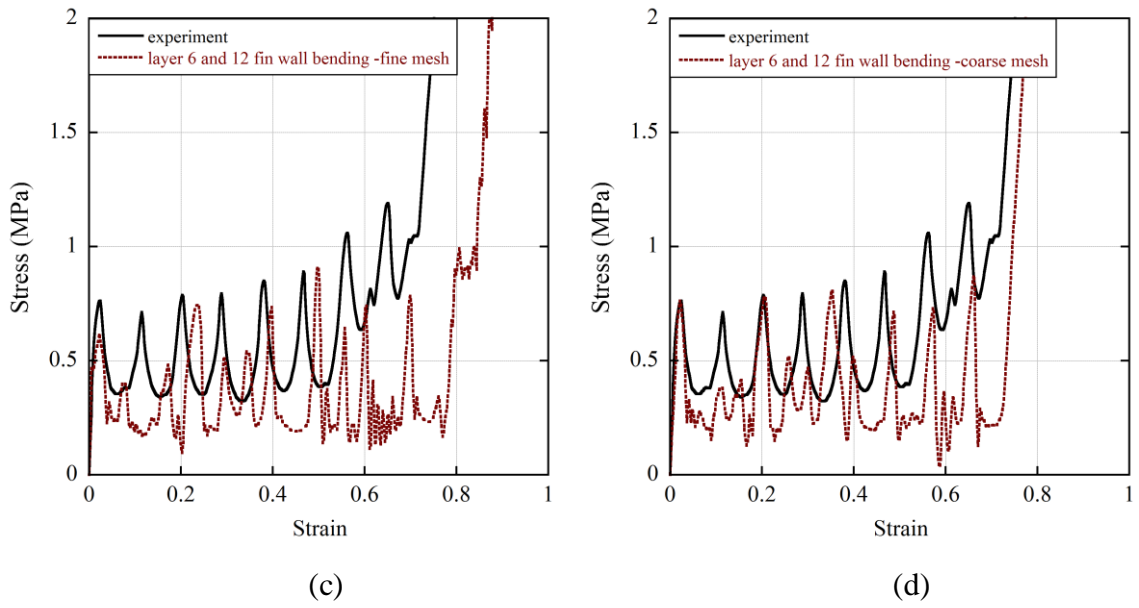


Figure 7.6. (cont.)

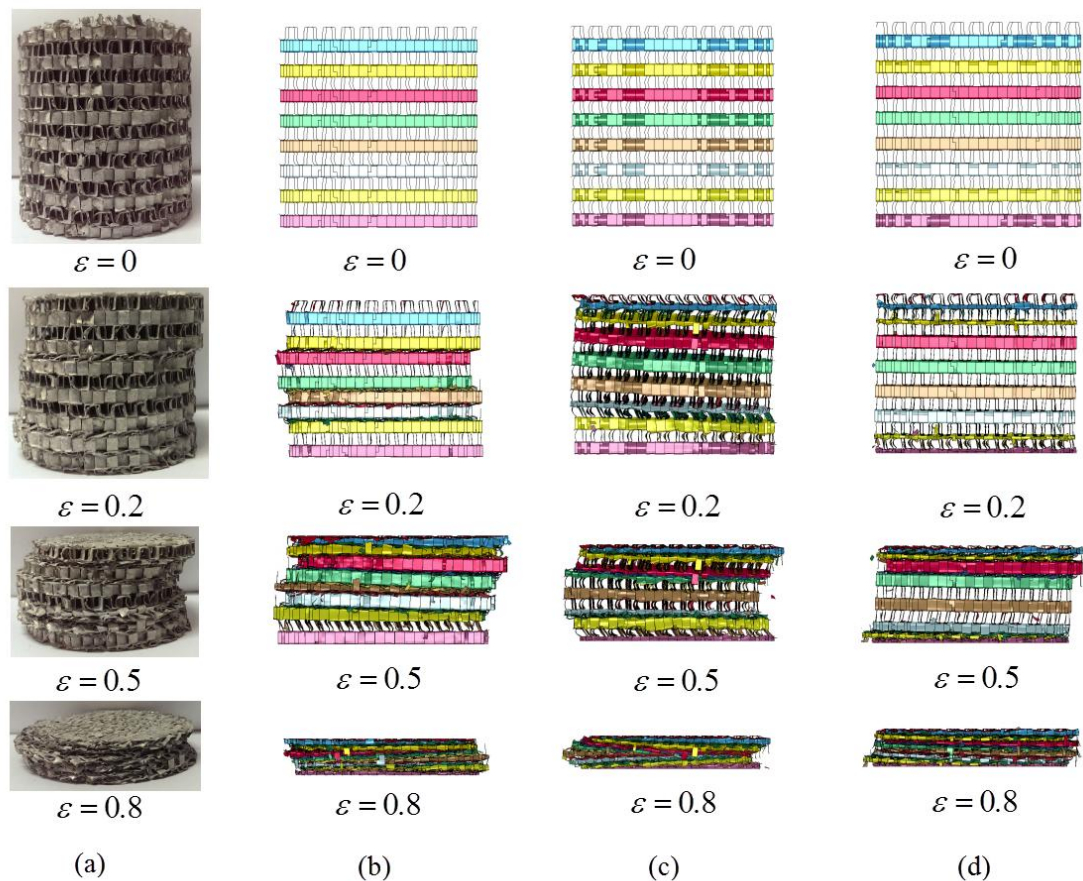


Figure 7.7. Quasi-static deformation of corrugated sandwich without face sheets at various strains: (a) experimental, (b) fin wall bending imperfection in the 6<sup>th</sup> and 12<sup>th</sup> layers, (c) fin wall bending in all layers and (d) mixed type of imperfection.

## CHAPTER 8

### SHOCK LOADING OF CORRUGATED STRUCTURES

#### 8.1. Direct Impact Testing

The cylindrical corrugated sandwich projectiles, 48 mm (w/o face sheets) and 50 mm (w face sheets) in length and 40 mm in diameter with and without face sheets were prepared through electro-discharge machine. The projectiles were tested in a modified SHPB test set-up as explained previously in Chapter 3. The corrugated sandwich projectiles without face sheets had a density of  $260 \text{ kg/m}^3$ , while the corrugated sandwich projectiles with face sheets had a density of  $320 \text{ kg/m}^3$ .

By considering all the internal energy is due to the loss of the kinetic energy, the following equation is used to calculate the critical velocity [114, 125].

$$v_{cr} = \left( \frac{2\sigma_{cr}\varepsilon_d}{\rho_o} \right)^{1/2} \quad (8.1)$$

Using the following values,  $\sigma_{cr} = 0.7 \text{ MPa}$ ,  $\rho_o = 260 \frac{\text{kg}}{\text{m}^3}$  and  $\varepsilon_d = 0.5 \text{ and } 0.74$  the critical velocity is calculated as 52 m/s and 63 m/s, respectively. Above this critical values, shock wave formation is expected.

The direct impact pressure-time curves of the corrugated sandwich with face sheets tested at 105, 140 and 200 m/s are shown in Figures 8.1(a-c), respectively. Two direct impact tests are shown in the figures for each velocity to show the repeatability of the tests. Despite the slight differences in pressure values between each test, the pressure-time profiles of the tests are very much similar. The peak pressure seen at  $\sim 600 \text{ } \mu\text{s}$  is the wave reflected from the free end of the incident bar. As seen in the same figures, the peak pressures of the tests increase with increasing impact velocity and are 32.7, 41.25 and 47.25 MPa for 105, 140 and 200 m/s tests, respectively. The peak pressures are comparably high compared to crushing stress of the corrugated sandwiches due to the impact of the face sheets. The impact of face sheet is

superimposed on the crushing of the corrugated sandwich, leading to a relatively high initial pressures. The post-peak pressure values also increase with increasing velocity and the lowest post-peak pressures are found in 105 and the highest pressures at 200 m/s velocities. The arrest time (see Figure 8.1(a)) defined as the time at which the projectile comes to rest decreases as the velocity increases and is 580, 377 and 283  $\mu\text{sec}$  at 105, 140 and 200 m/s, respectively.

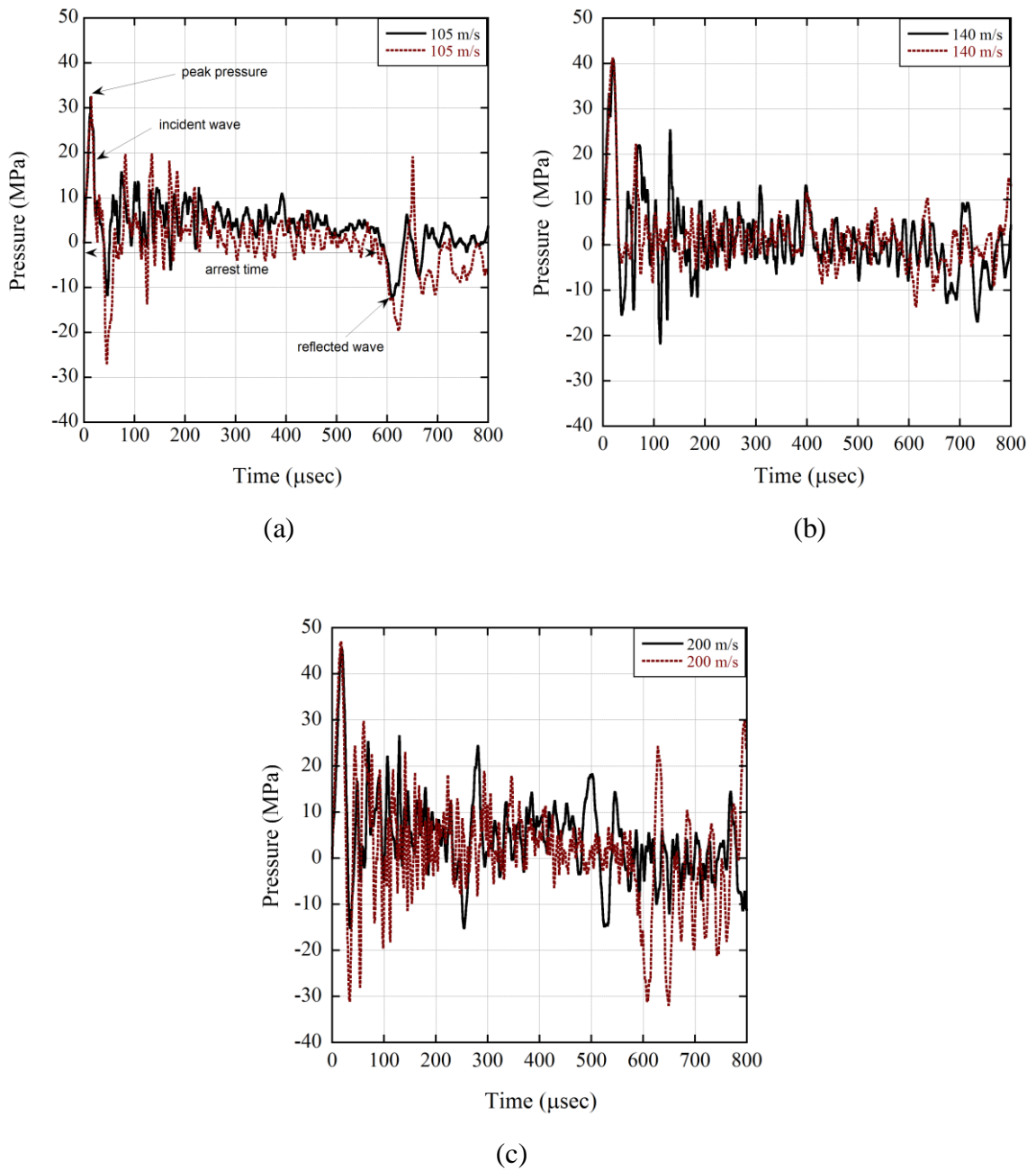


Figure 8.1. Direct impact pressure-time curves of the corrugated sandwich with face sheets tested at (a)105, (b) 140 and (c) 200 m/s.

The direct impact pressure-time curves of the corrugated sandwich without face sheets tested at 105, 140 and 200 m/s are shown in Figures 8.2(a-c), respectively. As in the case of the specimens with face sheets, the pressure-time profiles of the specimens tested at the same velocity are very much similar. The initial comparably high pressures are absent in the pressure-time profile as the face sheets are removed. The crushing pressure values increase with increasing velocity and are found 6, 7.5 and 12.8 MPa at 105 m/s, 140 m/s and 200 m/s, respectively. Inversely, the arrest time decreases as the velocity increases. The arrest time is measured from the time when the pressure has attained half of the initial peak value to the time when the pressure has dropped half way down the trailing edge of the pressure history. With this method, the arrest time is 325–320  $\mu\text{sec}$  at 105 m/s, 271–269  $\mu\text{sec}$  at 140 m/s and 229-238  $\mu\text{sec}$  at 200 m/s.

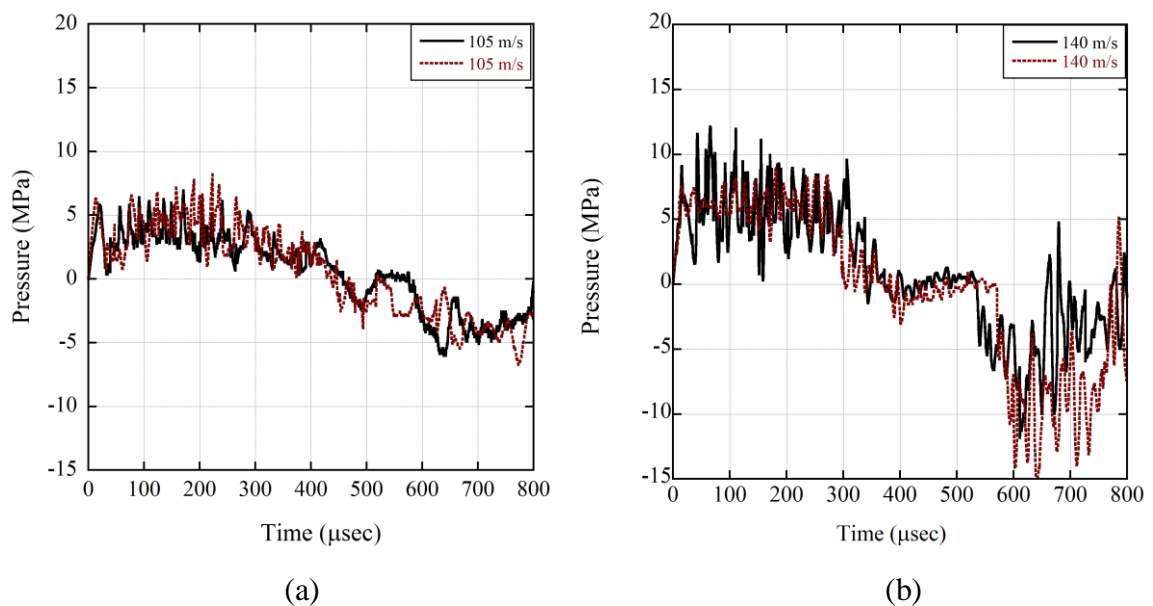
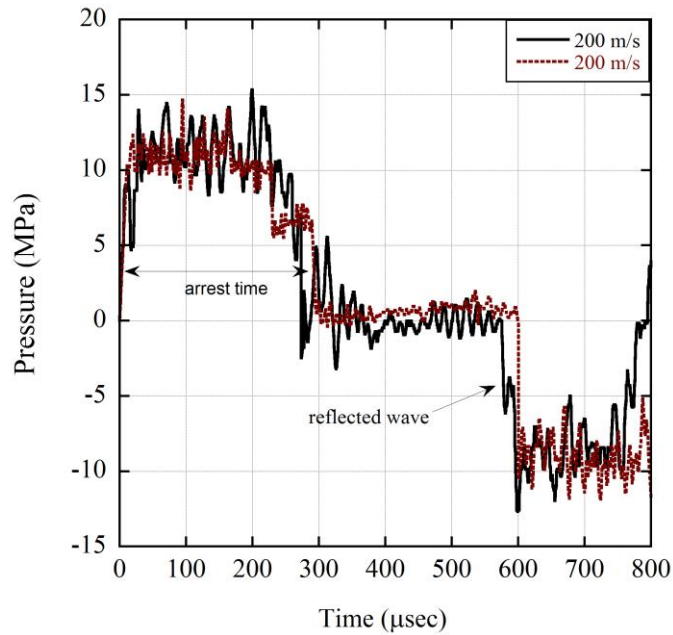


Figure 8.2. Direct impact pressure-time curves of the corrugated sandwich without face sheets tested at (a)105, (b) 140 and (c) 200 m/s.

(cont. on next page)



(c)

Figure 8.2. (cont.)

## 8.2. Direct Impact Test Simulations

The effect of imperfection on the quasi-static compression of the investigated corrugated sandwiches was elaborated previously in Chapter 7. The quasi-static simulations were performed, based on these studies, by forming two bending imperfections in structure; at the middle of the half of the length, 6<sup>th</sup> and 12<sup>th</sup> corrugated layers. The same imperfection was investigated using the coarse mesh in direct impact test simulations. The sandwich projectiles without face sheets were also modeled using the perfect geometry to identify comparatively the effect of imperfection on the dynamic response. Figure 8.3 shows perfect and imperfect model simulation pressure-time curves together with experimental curve at 105 m/s. The imperfect model shows large pressure oscillations between positive and negative values as compared with the imperfect model and experiment, while the perfect model pressure-time curve, despite slight shifts in time scale, shows a close agreement with experimental curve as seen in Figure 8.3. Similar simulation results were also obtained when the velocity was increased to 140 and 200 m/s. Further modelling in direct impact tests were therefore continued with the perfect model using coarse mesh.

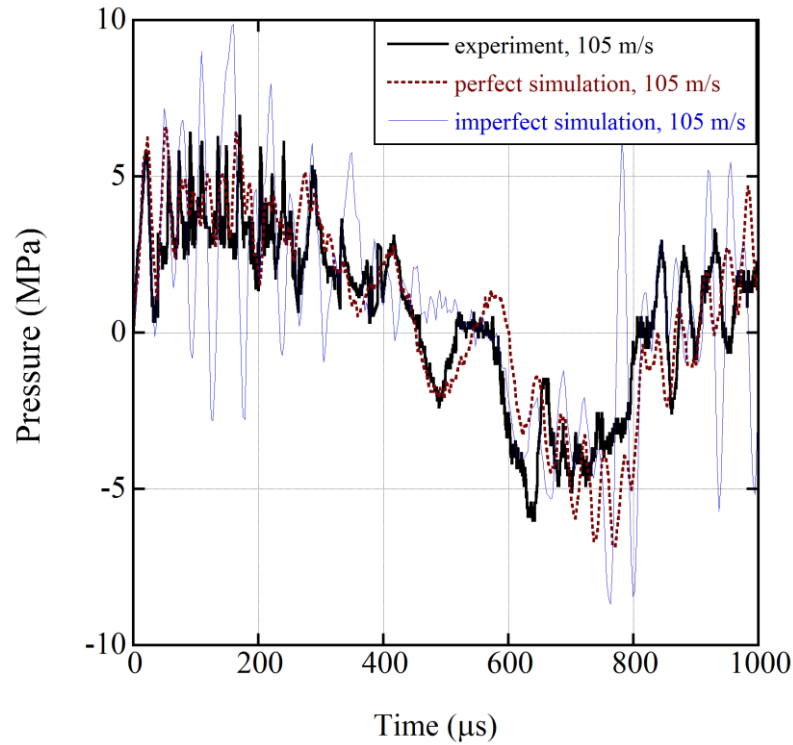
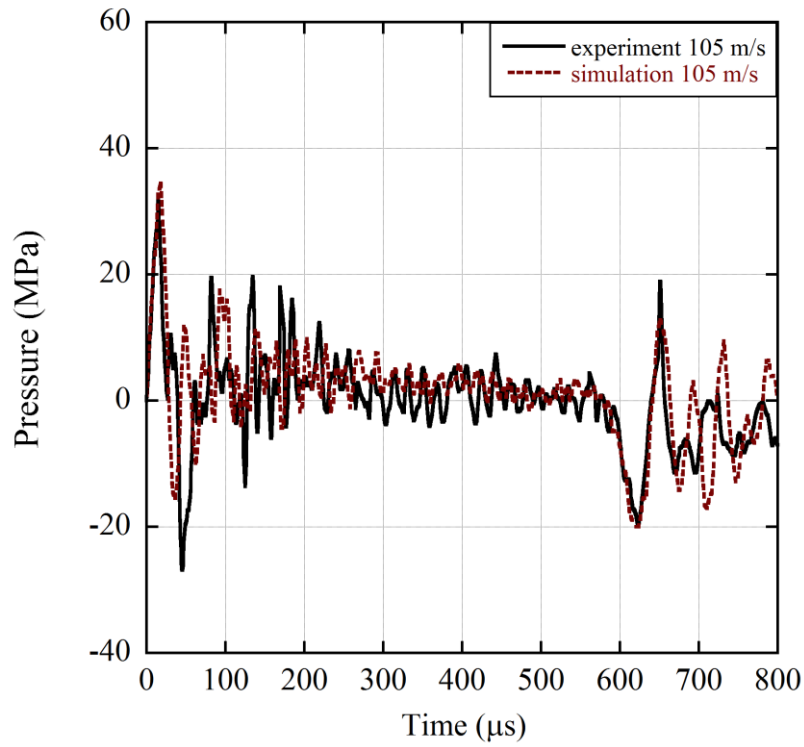
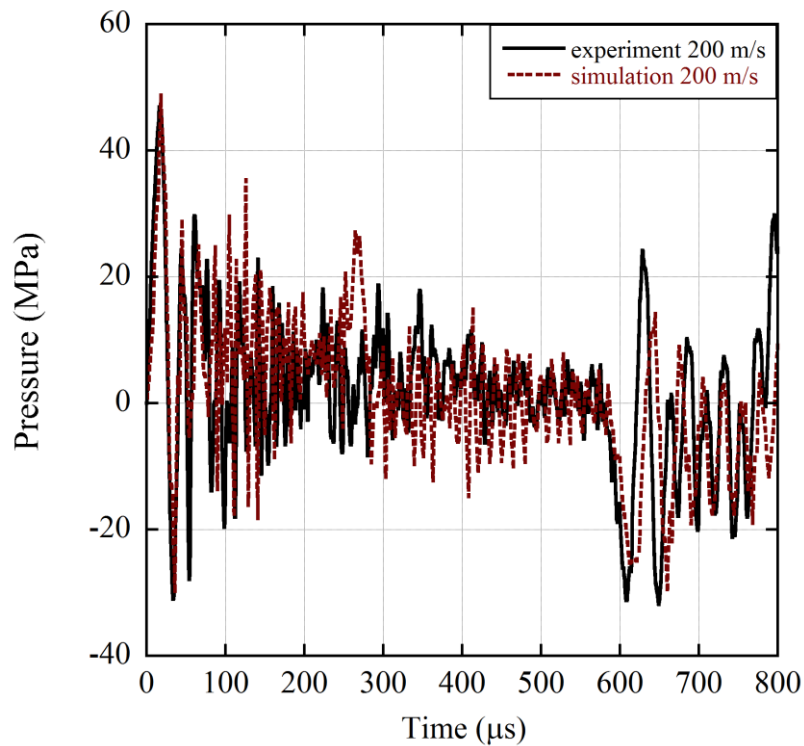


Figure 8.3. The pressure-time response of perfect and imperfect numerical models and experiment of corrugated projectiles without face sheet at 105 m/s.

The experimental and simulation pressure-time curves of corrugated projectiles with face sheets at 105 m/s and 200 m/s are shown in Figures 8.4(a) and (b), respectively. For all investigated projectile velocities, the numerical simulation and experimental pressure-time curves showed good agreements. The numerical peak stresses and loading durations are very much similar with those of the experiments as seen in Figures 8.4(a) and (b). The experimental and simulation pressure-time curves of corrugated projectiles without face sheets at 140 m/s and 200 m/s are shown in Figure 8.5. The simulation pressure time responses of all tests performed at three different velocities showed well correspondences to those of the experiments. The initial peak pressures (crushing strength) and arrest times are 6.22 MPa and 333  $\mu$ s at 105 m/s, 7.38 MPa and 281  $\mu$ s at 140 m/s and 13.44 MPa and 220  $\mu$ s at 200 m/s.



(a)



(b)

Figure 8.4. The experimental and numerical simulation pressure-time curves of the corrugated projectiles with face sheets tested at (a) 105 and (b) 200 m/s.

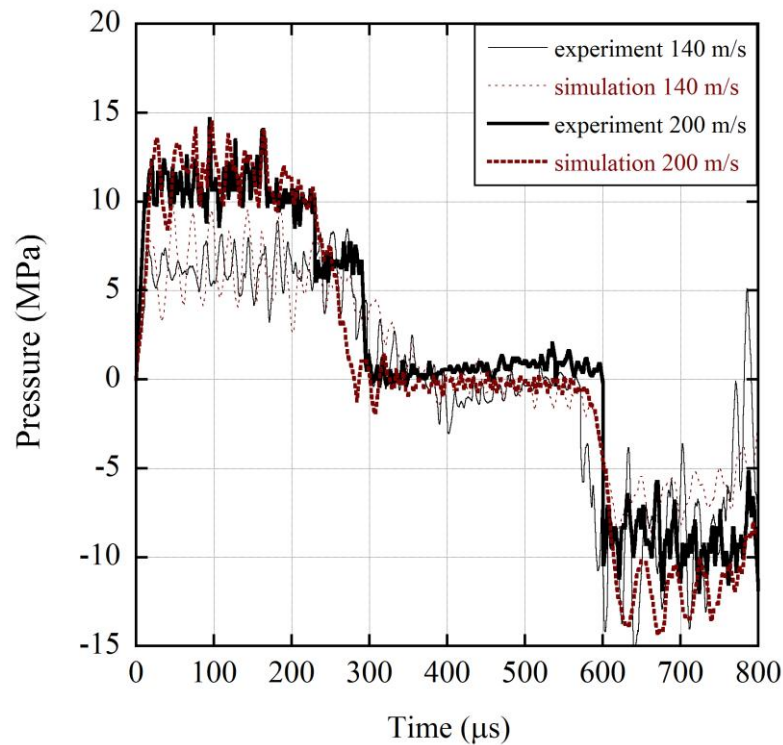


Figure 8.5. The experimental and numerical simulation pressure-time curves of the corrugated projectiles without face sheets tested at (a) 140 and (b) 200 m/s.

Figures 8.6(a) and (b) show sequentially the deformation pictures of the high speed camera and numerical model of corrugated projectiles with face and without face sheets at various times in 105 m/s projectile impact loading. The crushing of both numeric and test samples starts from the proximal end, end of the incident bar, and proceeds through the distal end. Although the deformation in quasi-static test proceeds with the discrete, non-contiguous bands of crushed (shearing and partly bending) fin layer, the deformation in direct-impact test proceeds with the sequential, in-planar crushing of the fin layer starting from the impact, showing shock deformation characteristic. It was noted experimentally that two corrugated layers collapse concurrently at quasi-static strain rate and as a result of this, only 7 peaks (after initial peak) were seen in the stress-strain curve of the quasi-static tests despite to the fact there are 16 corrugated layers. A similar reduced number peak stresses were also seen in the simulation stress-strain curve of the quasi-static tests. The increased number of stress peaks in direct impact test in Figure 8.5, corresponding to the crushing of each layer starting from the impact end, also proves the progressive crushing of the fin layer.

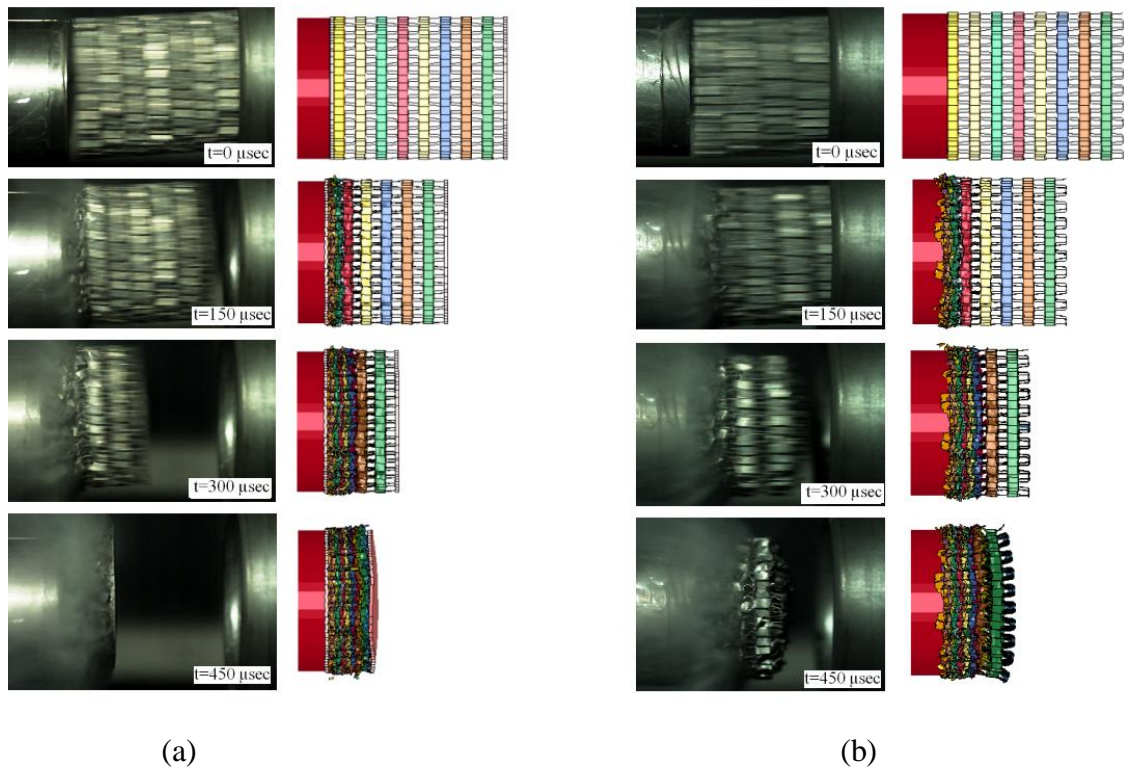


Figure 8.6. The deformation pictures of the high speed camera and numerical model of corrugated projectiles at 105 m/s: (a) with and (b) without face sheets.

The simulation deformation pictures of corrugated projectile without face sheets at 50 and 105 m/s are shown in Figures 8.7(a) and (b) at various times. The fin layers at both velocities deform in a sequential order starting from impact end as seen in the same figures. However, the deformation at 105 m/s is more localized than that at 50 m/s. In other words, the deformation at 50 m/s is more diffusive, while at 105 m/s it is very much localized. The arrows in Figure 8(a) shows diffusive nature of the deformation at 50 m/s. The diffusive nature of the deformation was more clear when the impact velocity decreases and the localized or shock deformation becomes more dominant when the impact velocity increases. When shock wave propagation occurs within the material, a visible boundary between the densified and non-densified region is formed. This boundary region can be regarded as the proof of the shock wave model [125]. However, in the direct impact tests without a backing mass, the final deformations obtained at relatively low velocities are relatively small, preventing the determination of the shock wave formation.

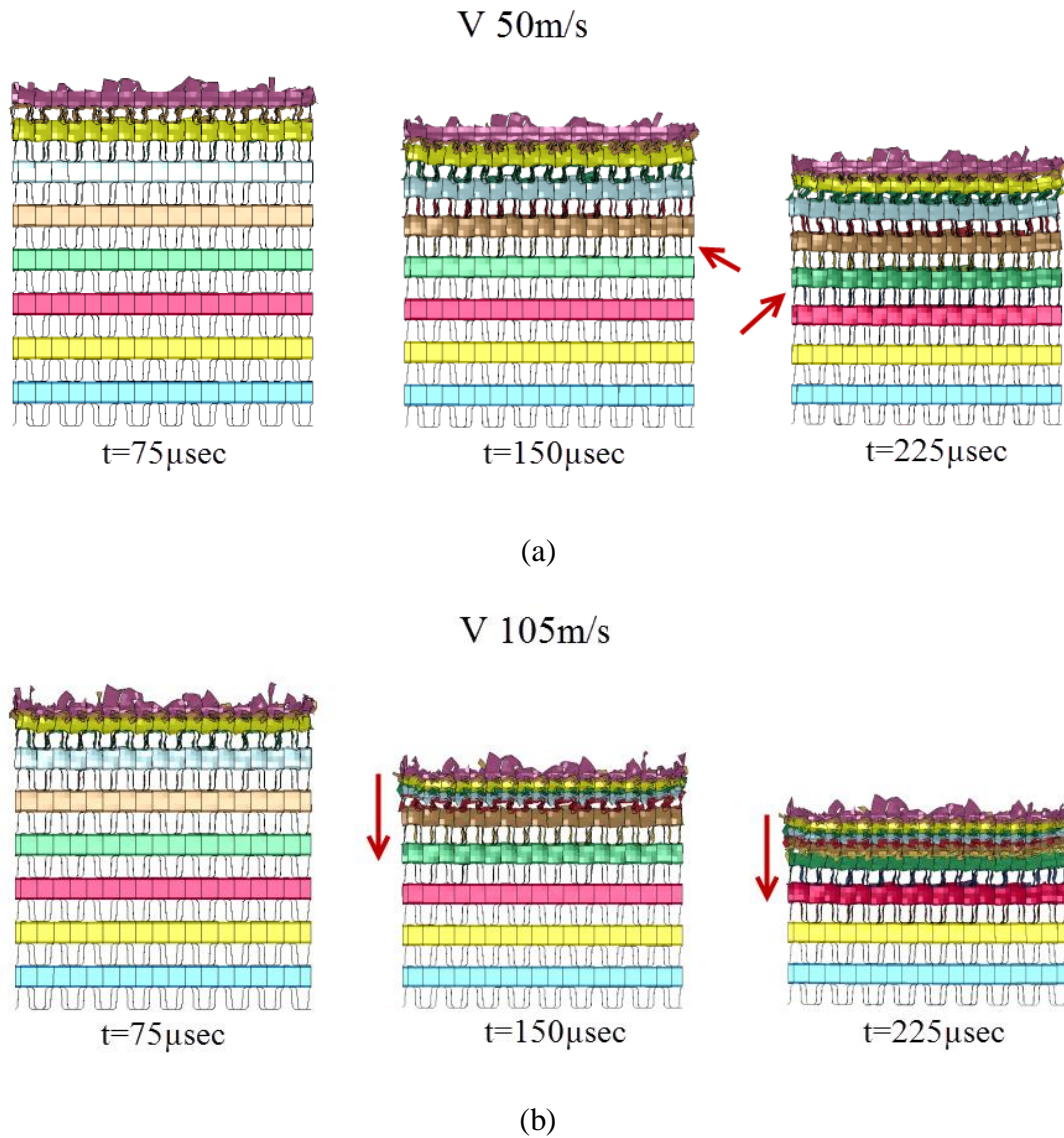


Figure 8.7. The simulation deformation pictures of corrugated projectile without face sheets at various impact time: (a) 50 and (b) 105 m/s.

Figure 8.8 shows sequentially the pictures of deformed corrugated projectiles at various velocities till different final lengths. The final lengths of the samples deformed at 1, 10, 25 and 50 m/s are relatively low and 48, 47, 45 and 38 mm respectively. The sample tested at 1 m/s only shows elastic deformation till end of the impact. The effect of impact velocity on the localized deformation is however clearly seen in Figures 8.8(e) and (f). Although final length of the samples in these figures are the same (30 mm), the localized deformation is clearer at 105 m/s (Figure 8.8(f)) than 75 m/s (Figure 8.8(e)). The same observation also applies to the samples tested at 140 and 200 m/s. When the velocity increases from 140 m/s to 200 m/s, the deformation at the same final length (20 mm) localizes further as seen in Figures 8.8(g) and (h).

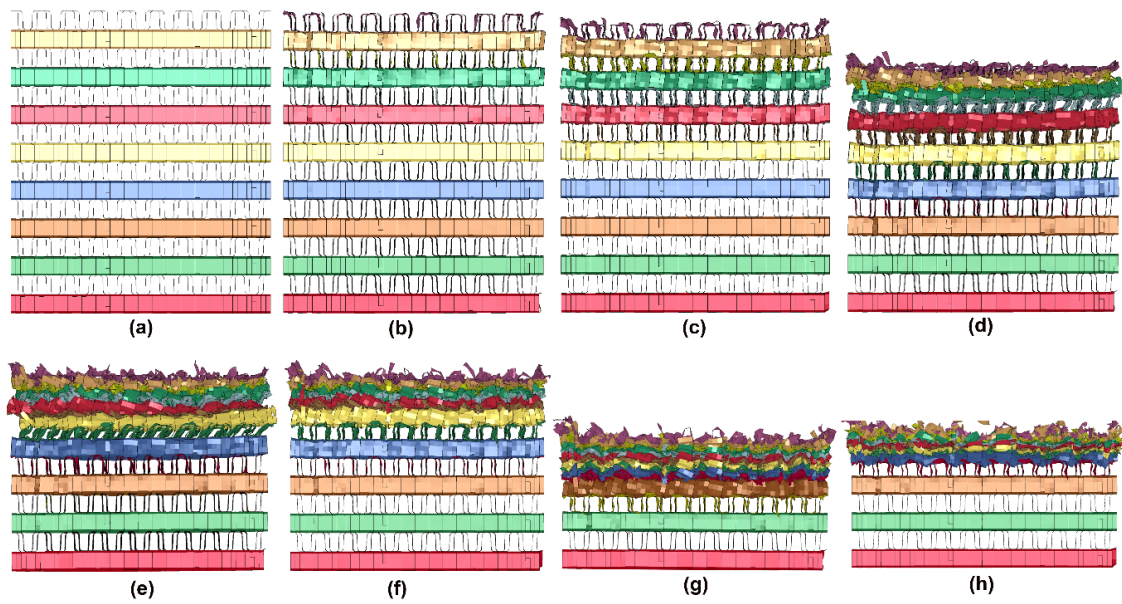


Figure 8.8. The simulation deformation pictures of corrugated projectile without face sheets (a) 1 m/s, (b) 10 m/s (final length= 47 mm), (c) 25 m/s (final length= 45 mm), (d) 50 m/s (final length= 38 mm) , (e) 75 m/s (final length= 30 mm), (f) 105 m/s (final length= 30 mm), (g) 140 m/s final length= 20 mm and (h) 200 m/s final length= 20 mm).

### 8.3. Direct Impact with Backing Mass and Stationary Impact Simulations

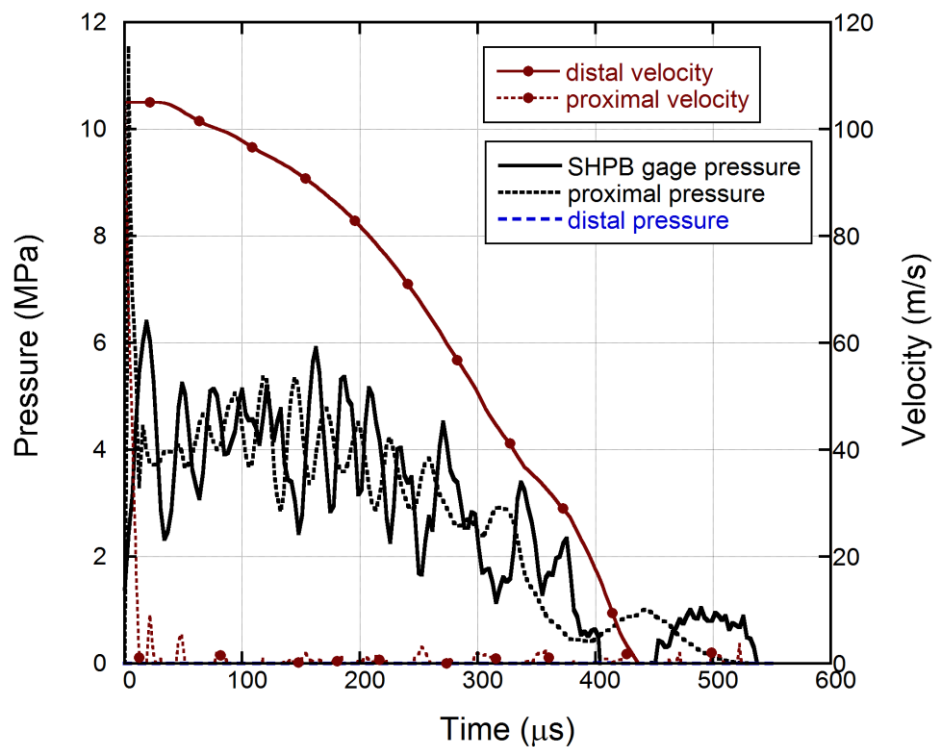
As stated in previous section, the direct impact tests without backing mass cannot produce enough strain to initiate shock wave at relatively low velocities. In order to attain large final strains, particularly in the simulations near subcritical velocities, aluminum backing masses were added to the direct impact tests and these masses were fired directly to the stationary corrugated projectile inserted at end of the incident bar. The backing mass weights used in the simulations at various impact velocities are tabulated In Table 8.1. The masses were calculated to produce densification in the projectile.

Table 8.1. Direct and stationary impact numerical simulation parameters.

Impact Velocity (m/s)	Numerical Simulation Type	Backing Mass, (g)	Corrugated Mass, (g)	Initial Length, (mm)
1	Direct/Stationary	9336	16.31	48
10	Direct/Stationary	810	16.31	48
25	Direct/Stationary	249	16.31	48
50	Direct/Stationary	124.5	16.31	48
75	Direct/Stationary	82.9	16.31	48
105	Direct/Stationary	59.2	16.31	48
140	Direct/Stationary	29.6	16.31	48
200	Direct/Stationary	15	16.31	48

In these numerical simulations, the generated pressure values were initially numerically measured from the strain gage locations on the SHPB to verify the constancy of aluminum backing mass models with the models without aluminum backing mass. The direct impact simulations of corrugated structures with and without backing mass are expected to show similar pressure-time profiles until about the densification of corrugated projectile. The numerical pressure and velocity time responses of corrugated projectiles with and without backing masses at 105 m/s and 200 m/s are shown in Figures 8.9 and 8.10, respectively. In testing without backing mass at 105 m/s, the distal end velocity gradually decline from the beginning of impact to the end, as the time increases, while the proximal end velocity sharply reduces to zero at the beginning of impact (Figure 8.9(a)). The pressure read from the SHPB gage and proximal end are very much similar in profile and magnitude, while the distal end attains no pressure throughout the impact as seen in the same figure. On the other hand, when testing with backing mass at the same velocity, the proximal end velocity increases to 10 m/s near the end of the impact (Figure 8.9(b)). The SHPB gage and proximal and distal end pressures increase abruptly after about 350  $\mu$ s, representing the projectile densification. The distal end pressure are almost zero until about 350  $\mu$ s, thereafter fin layer plastic collapse initiates at the distal end also. The SHPB gage pressures and distal end velocities of the tests with and without mass are shown together in Figure 8.9(c) for comparison. The distal end velocity decline quickly in without backing mass numerical test, while the distal end velocity almost stays constant until about distal end collapse initiates in backing mass numerical test (Figure 8.9(b)). The SHPB gage pressures of both tests are almost identical until about 200  $\mu$ s; thereafter the pressure of the test with backing mass increases over that of the test without backing

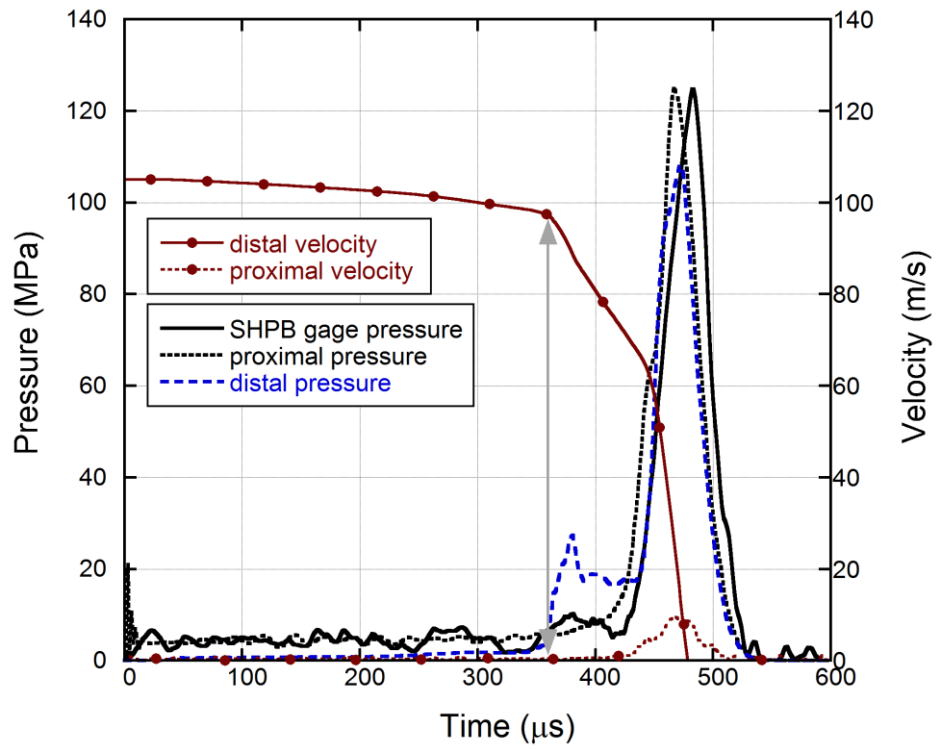
mass. The pressure in the test without backing mass gets zero, while the pressure in the test with backing mass increases sharply near the end of the arrest time. The same profile is also seen in proximal end pressures shown in Figure 8.9(d). In the direct impact numerical simulations of corrugated projectiles without backing mass, it is stated in the previous section that the shock wave cannot reach the other end of the projectile, while with backing mass the wave reaches the end of the projectile, leading the full densification of the projectile.



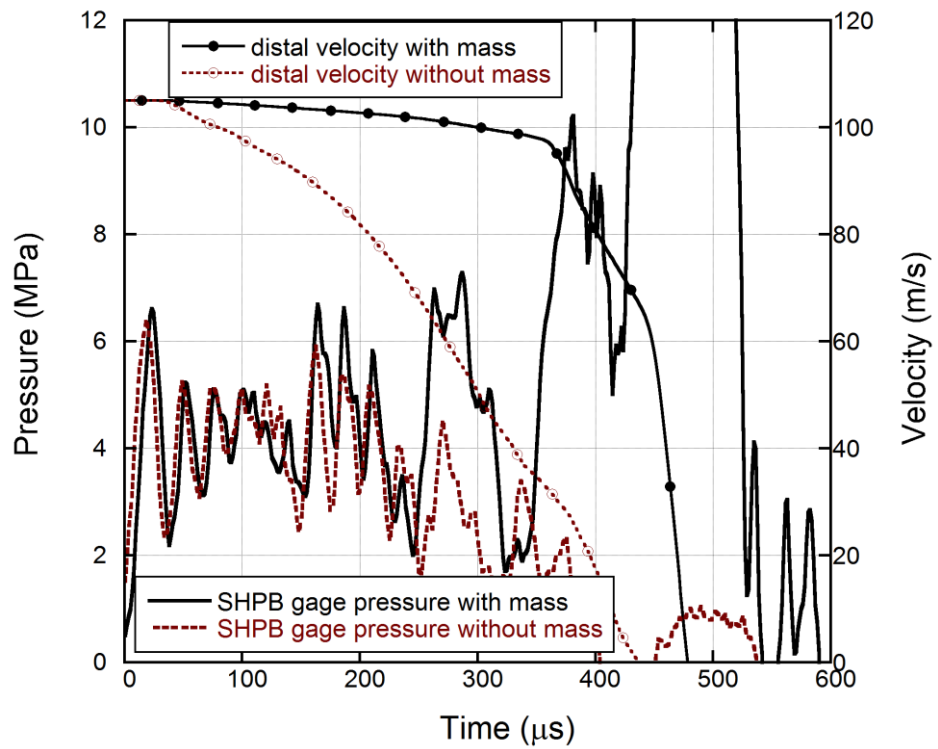
(a)

Figure 8.9. Pressure and velocity time profile of the projectile impacted (a) without and (b) with backing mass and (c) SHPB gage pressure-time profile and (d) proximal pressure-time profile of the projectile impacted with and without backing mass at 105 m/s.

(cont. on next page)

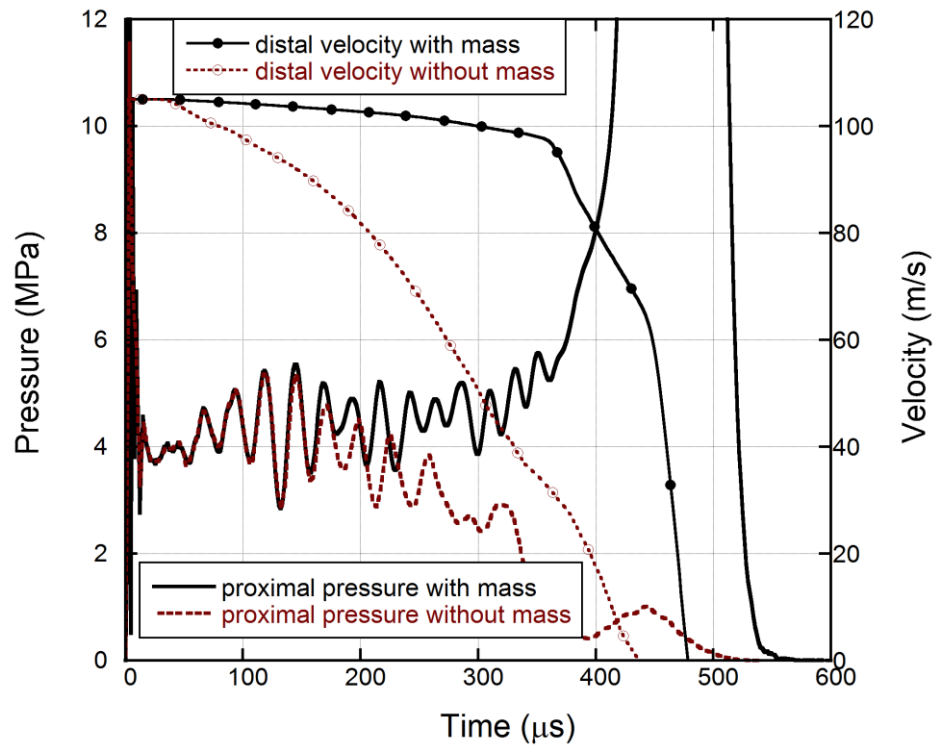


(b)



(c)

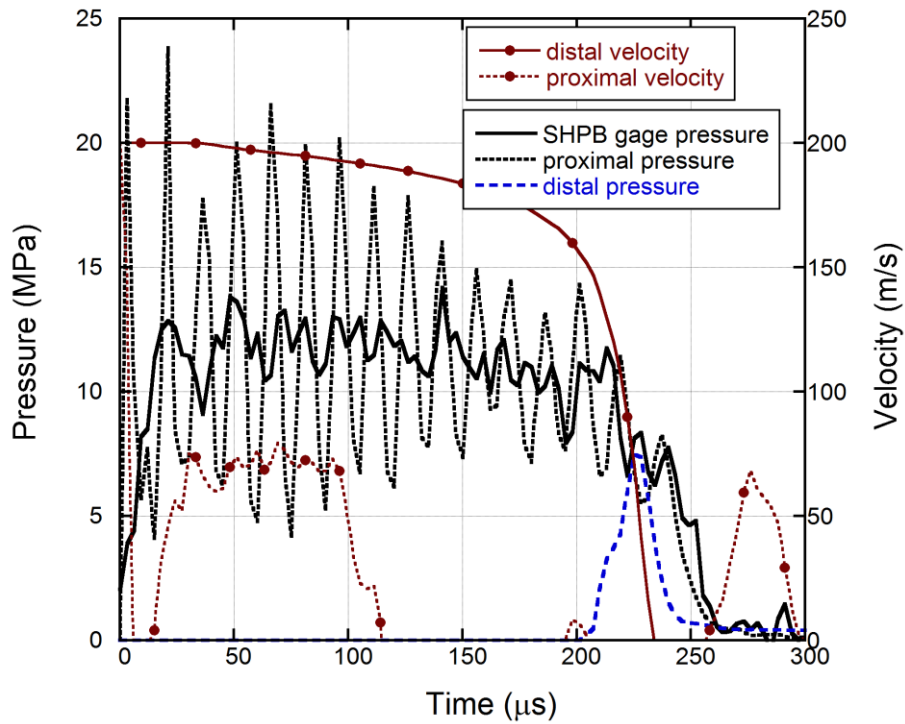
(cont. on next page)



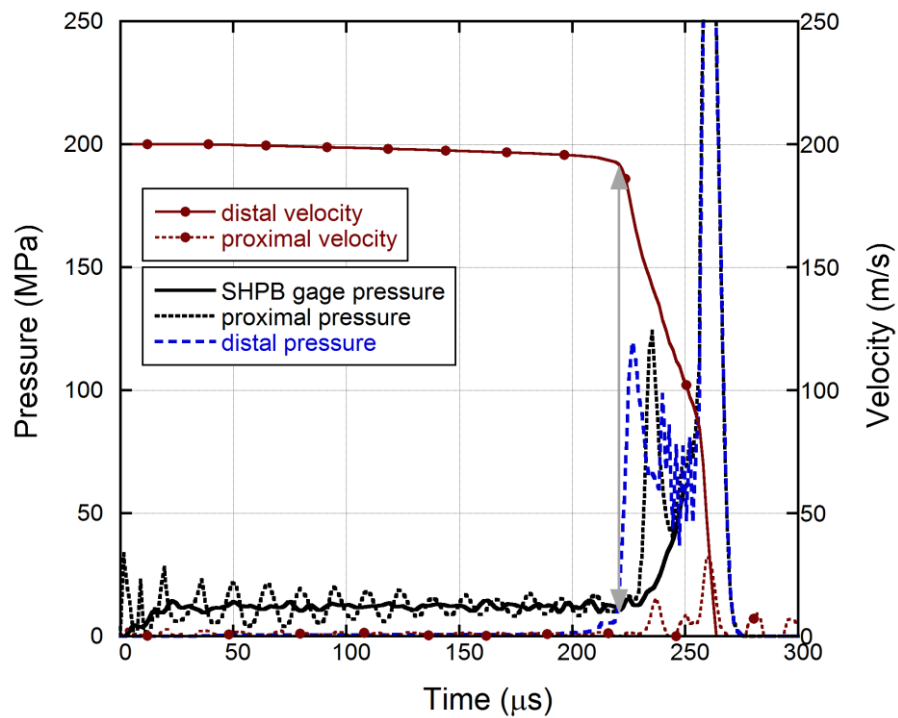
(d)

Figure 8.9. (cont.)

Nearly similar impact characteristics are detected in testing without and with backing mass at 200 m/s, Figures 8.10(a-d), except the distal end velocity decline is more gradual and fluctuations of the proximal end pressure increase significantly as compared with 105 m/s test (Figures 8.10(a) and (d)). It is found that these large stress fluctuations are filtered out when the pressure measurements are taken from the SHPB gage (Figures 8.10(a) and (c)). The SHPB gage pressure is found to correspond to the mean pressure of the proximal end (Figure 8.10(d)).



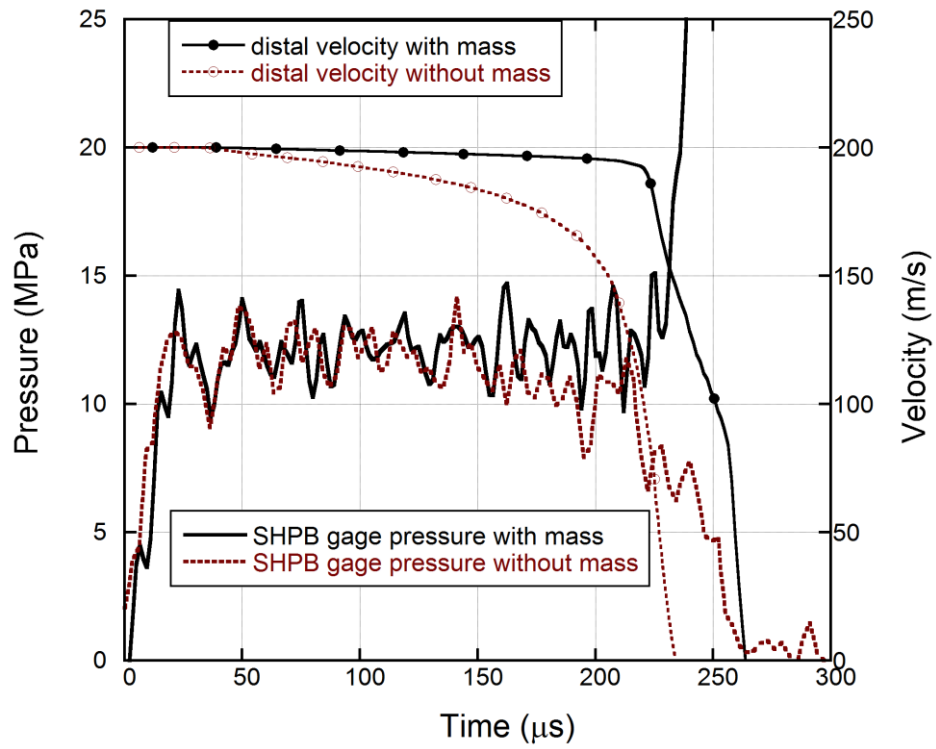
(a)



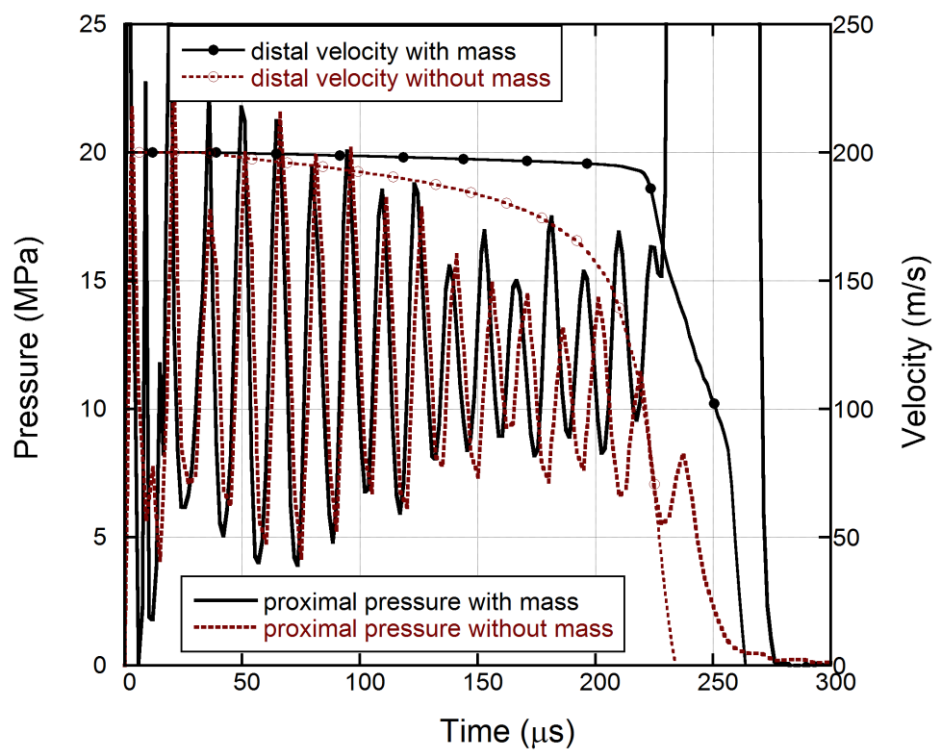
(b)

Figure 8.10. Pressure and velocity time profile of the projectile impacted (a) without and (b) with backing mass and (c) the velocity time profile and SHPB gage pressure-time profile and (d) proximal pressure-time profile of the projectile impacted end with and without backing mass at 200 m/s.

(cont. on next page)



(c)



(d)

Figure 8.10. (cont.)

The proximal end pressure-strain curves of direct impact test simulations with backing mass are shown in Figure 8.11(a). The proximal end pressures of the test at 200 and 140 m/s are represented by the SHPB gage pressures which show the mean pressures of proximal end in the same figure. The nominal strain is calculated by dividing the total displacement to the initial length of the projectile. The proximal pressure including initial peak and plateau pressure increases with increasing impact velocity as seen in Figure 8.11(a). The plateau pressure increase however becomes evident only after a subcritical velocity of 50 m/s as shown by an arrow in Figure 8.11(a). Till that velocity, the initial peak pressure increases with increasing impact velocity without increase in plateau pressure. It is also noted that the densification strain shown broadly by the dotted lines in the same figure increases as the impact velocity increases from quasi-static velocity (0.74) to 200 m/s (0.92). The distal end pressure-nominal strain curves above and below the subcritical velocity are shown together with quasi-static pressure-strain curve for comparison in Figures 11(b) and (c), respectively. The distal end pressure starts to increase after a critical nominal strain which increases with increasing impact velocity. This critical strain is 0.125 for 200 m/s, 0.0875 for 140 m/s, 0.0675 for 105 m/s, 0.05 for 75 m/s, 0.032 for 50 m/s, 0.018 for 25 m/s, 0.09 for 10 m/s and 0.0033 for 1 m/s (Figures 8.11(b) and (c)). Distal end pressure starts from zero and increases to a value of 0.52-0.62 MPa, which clearly showing an elastic deformation. It is noted that before the shock wave reaches the end of the projectile, no buckling of the distal end corrugated layers are detected at 200 m/s, while buckling of the end layers are observed when the impact velocity decreases; when the velocity is 75 m/s one and half distal end corrugated layer and 50 m/s two and half distal end layers buckle. The simulation deformed pictures of the projectile tested at 50 and 200 m/s at a nominal strain of 0.6 are shown in the inset of Figure 8.11(b). At a strain of 0.6, the simulations pictures show no distal end layer crushing at 200 m/s, while one end layer completely crushed (red one) and the next layer (blue one) partially crushed at 50 m/s. This is also reflected by the peak pressures in pressure-nominal strain curves: no peak pressures are seen at 200 m/s and one complete peak pressure and one half seen at 50 m/s at a strain of 0.6. It is also further noted that the corrugated layers shear 50 m/s, which is also seen at quasi-static strain rates. In inset of Figure 8.11(c), the simulation deformed pictures of the projectile tested at 25 and 10 m/s at a nominal strain of 0.6 are shown. The corrugated layer shearing become clearer at these subcritical velocities as seen in the same figure. The layer crushing starts from both distal and proximal end and

as a result the number of peak pressures increases and the projectile deformation approaches to the quasi-static deformation. Figure 8.11(d) shows the distal pressure-time curves at all impact velocities. The initial elastic wave develops at the distal end at about  $32 \mu\text{s}$  for 200 m/s (circle a), the plastic collapse at the distal end presumably starts at a pressure between 0.52-0.62 MPa (circle b) and finally the densification of the distal end begins at about 0.8 MPa (circle c).

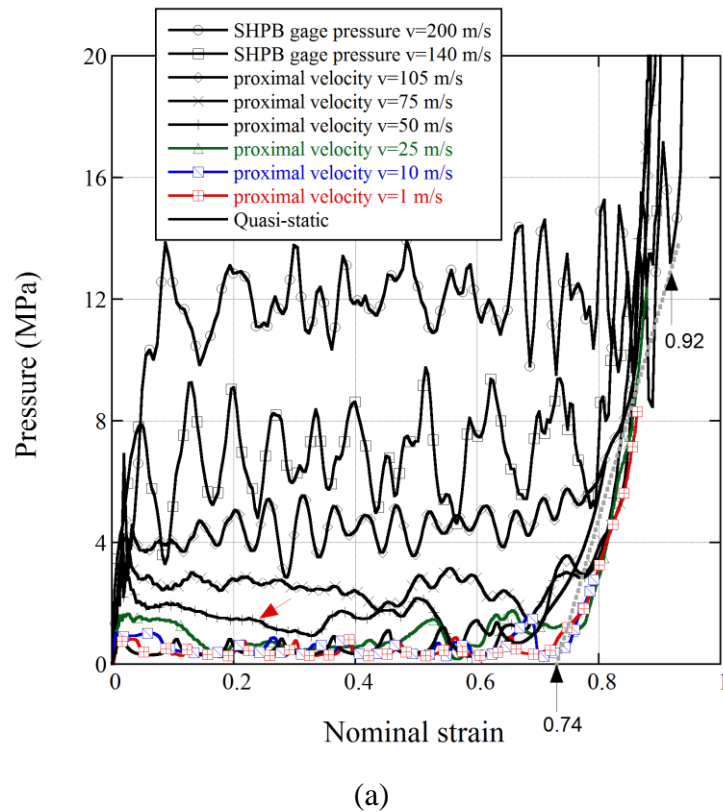
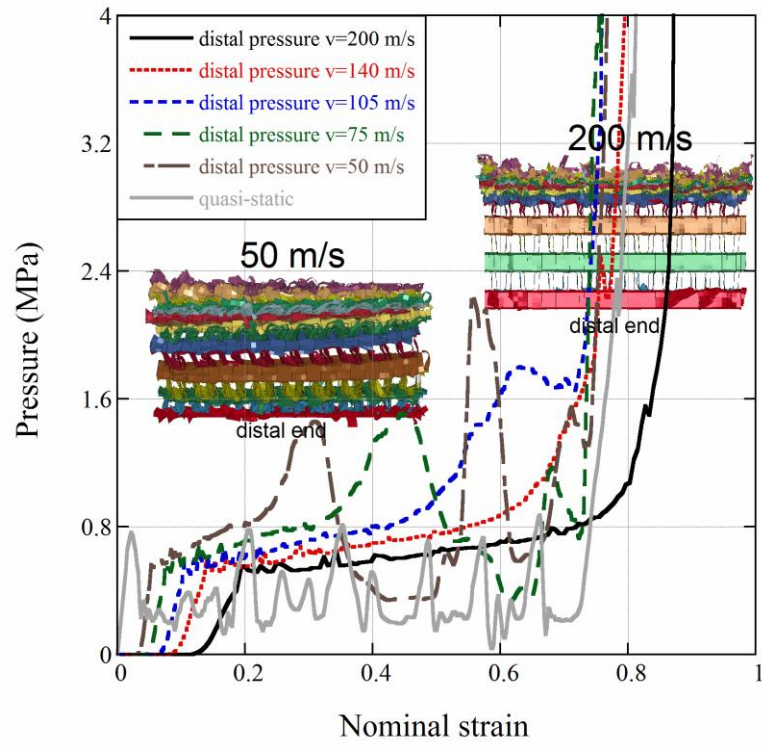
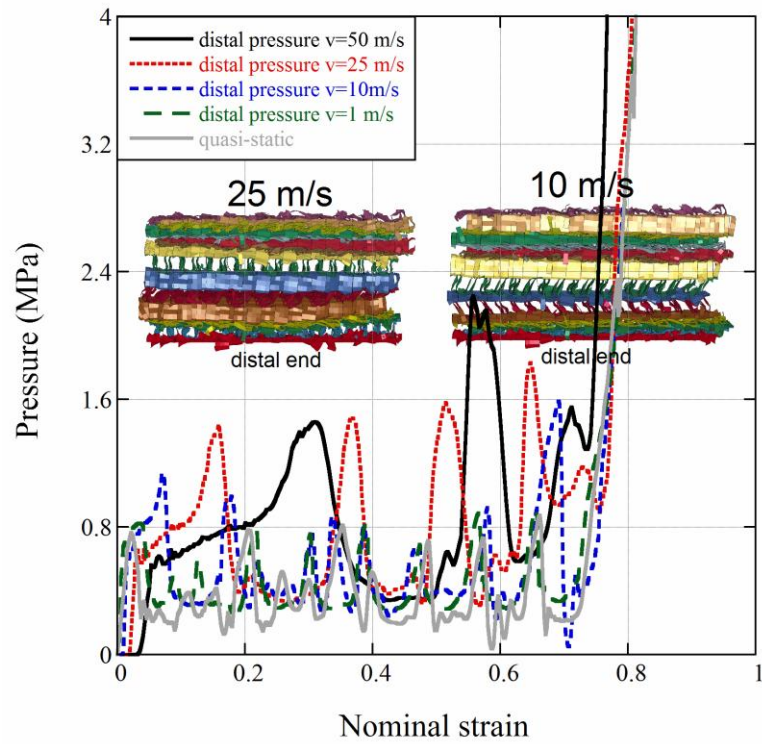


Figure 8.11. (a) SHPB gage and proximal end pressure-nominal strain and distal end pressures-strain curves: (b) above and (c) below the subcritical velocities and (d) distal end pressure-time curves of corrugated sandwich projectiles with backing mass.

(cont. on next page)

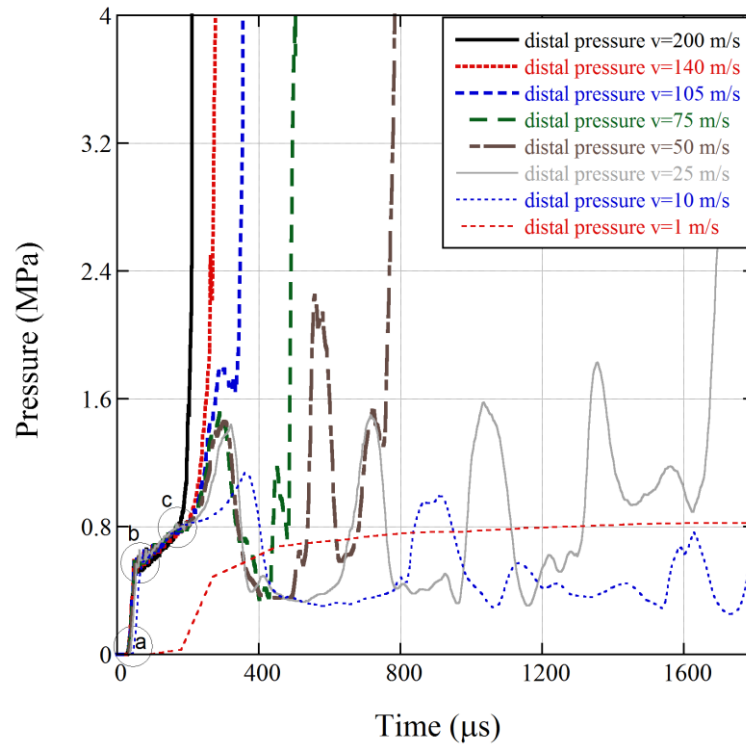


(b)



(c)

(cont. on next page)



(d)

Figure 8.11. (cont.)

The increase in impact velocity increases the initial peak and plateau pressures as the results of the shock formation and progression in the corrugated projectile. The average stress responses above the critical impact velocity are higher than that of the quasi-static crushing due to the plastic shock wave formation. The distal end pressure results from the elastic wave reflection and consequently it is delayed somewhat until the stress wave traversed the length of the specimen. The deformation sequences of direct impact test simulation of 105 m/s and 200 m/s impact velocity at various impact times till full densification are shown in Figures 8.12(a) and (b), respectively. Note that these velocities are well above the subcritical velocities (52-63 m/s) and consequently clearly a shock front develops at the proximal end (projectile-incident bar interface) which proceeds through the distal end (projectile-backing mass interface). The deformation sequences of direct impact test simulation of 10 m/s and 50 m/s impact velocities at various deformation times till full densification are shown in Figures 8.13(a) and (b), respectively. The corrugated projectile deformation is seen to be nonhomogeneous at 10 m/s (Figure 13(a)), starting from the distal end ( $t=100 \mu\text{s}$ ). The crushing is also not sequential at this velocity; it proceeds with the crushing of intermediate layers ( $t=300 \mu\text{s}$ ). The shearing of the layers as similar with the quasi-static

deformation is also noted at later time ( $t=300$  and  $400 \mu\text{s}$ ). When the impact velocity increases to  $50 \text{ m/s}$  (Figure 8.13(b)), the initial layer crushing initiates from the proximal end ( $t=200 \mu\text{s}$ ), while shearing of the layers near the distal end is also noted ( $t=400 \mu\text{s}$ ). At this velocity, the deformation may be considered in between shock and quasi-static deformation.

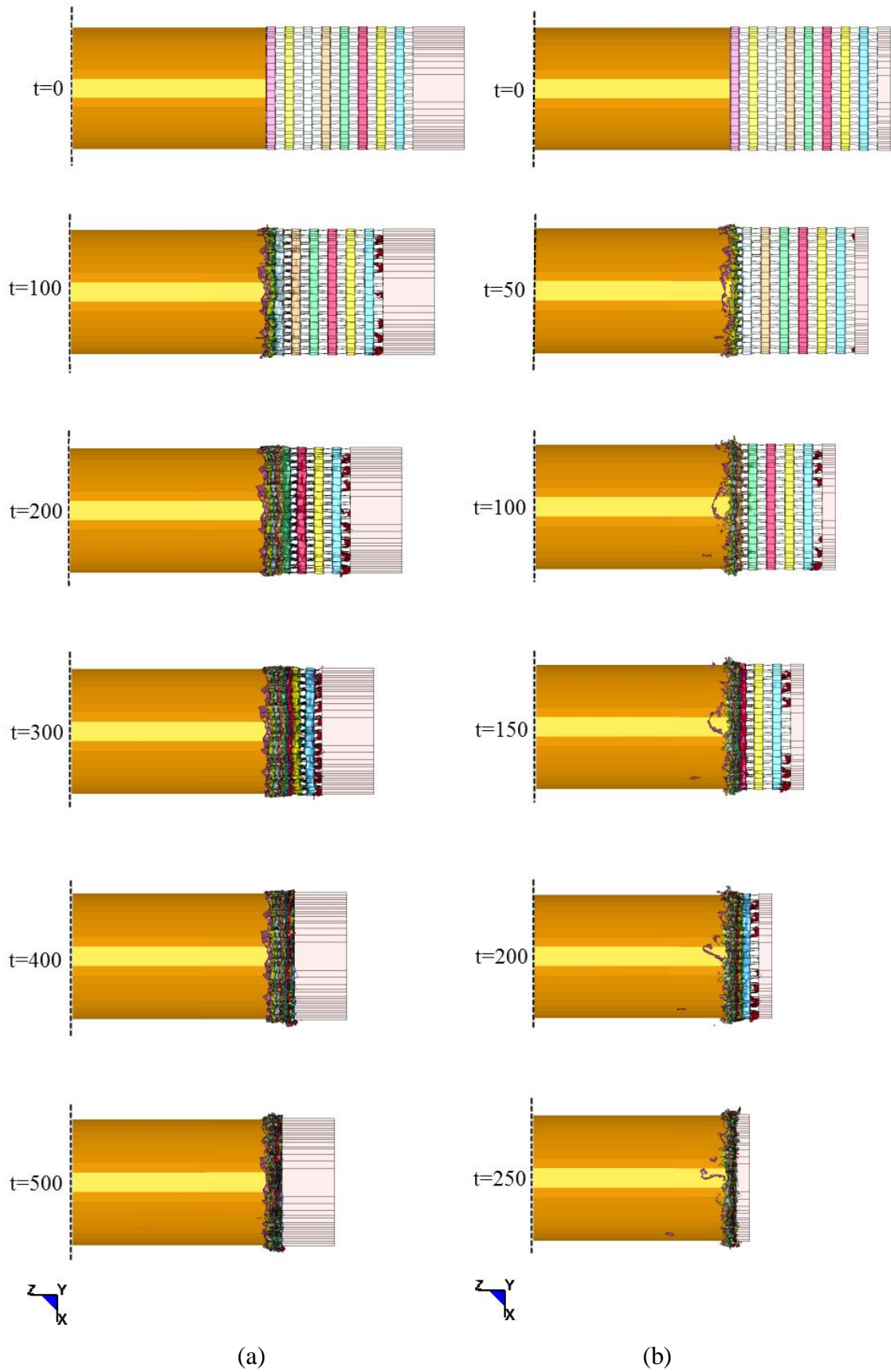


Figure 8.12. The numerical simulation deformation sequence of corrugated projectile fired with a backing mass at (a) 105 and (b) 200 m/s.

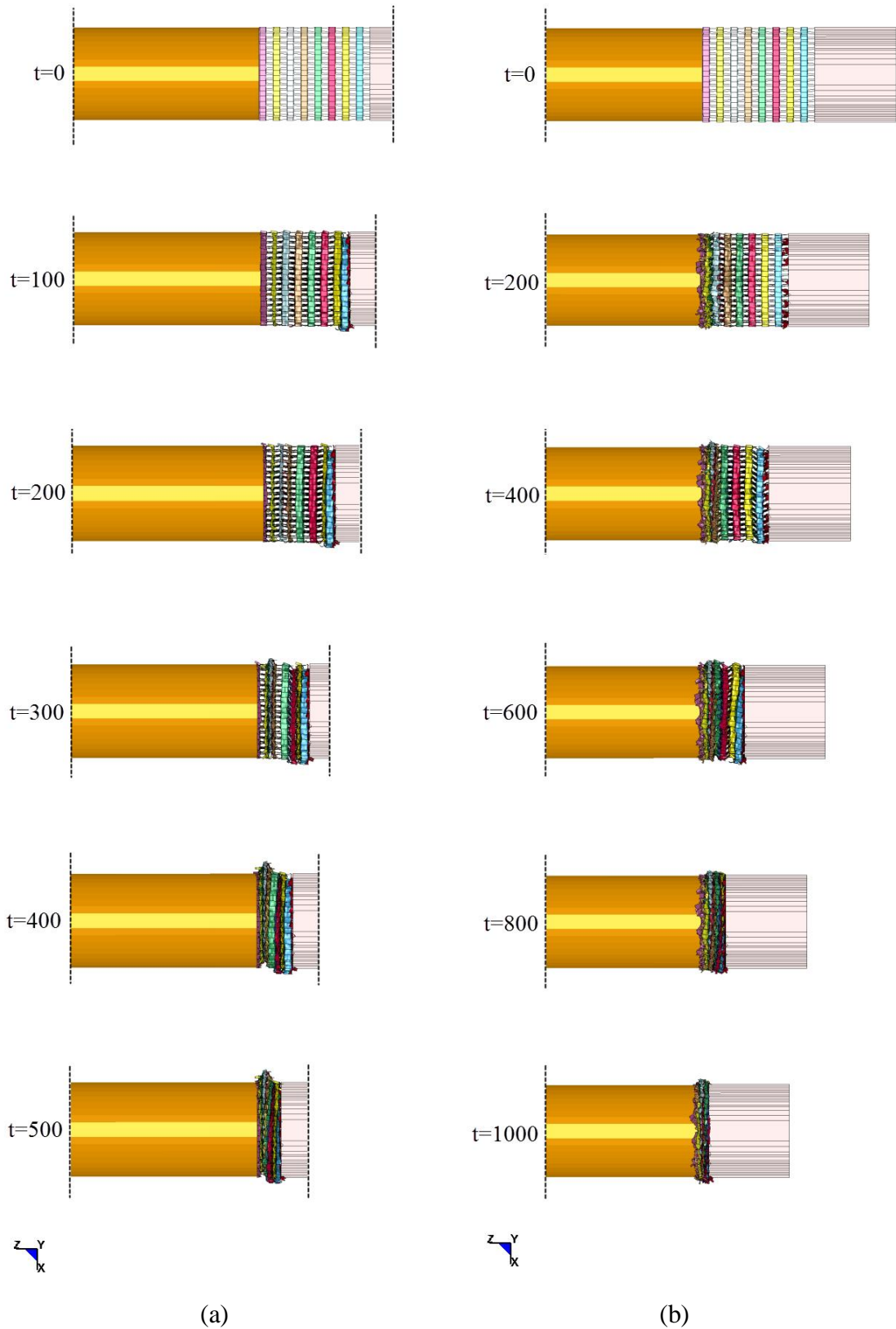
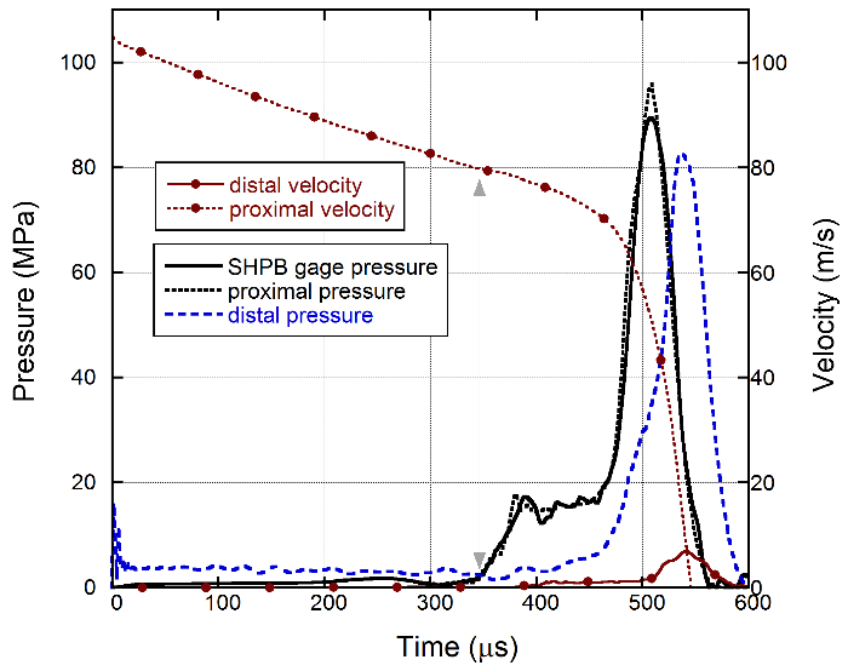


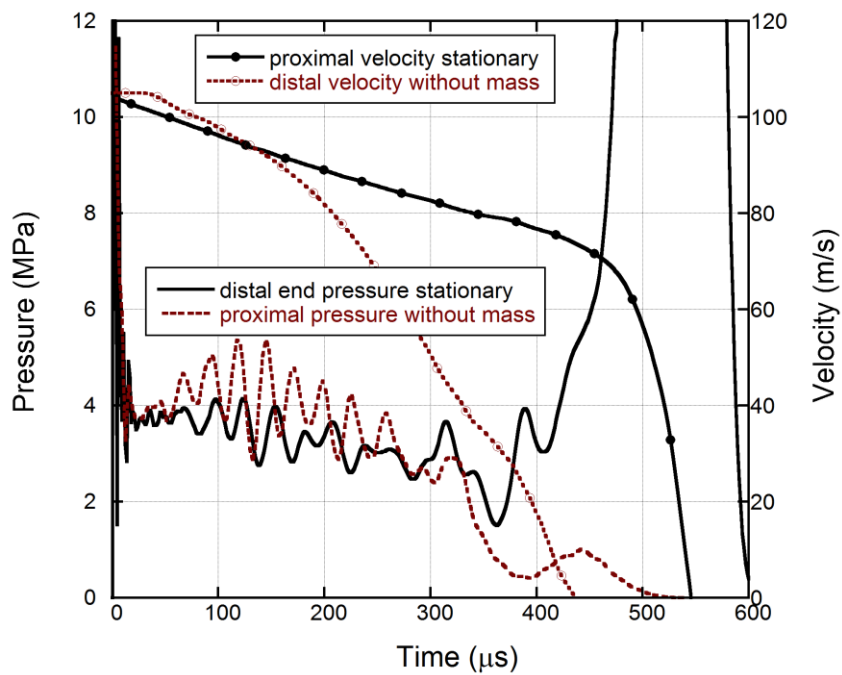
Figure 8.13. The numerical simulation deformation sequence of corrugated projectile fired with a backing mass at (a) 10 and (b) 50 m/s.

The SHPB gage and proximal and distal end pressure- and distal and proximal velocity-strain curves of stationary test simulation at 105 m/s are shown in Figure 8.14(a). Different from the impact tests with and without backing mass, the crushing of the projectile starts from the distal end where the mass hits the projectile and proceeds through the proximal end (projectile-incident bar interface). The proximal end pressure is zero until about 350  $\mu$ s; thereafter it reaches the level of the distal end pressure when the shock wave reaches the proximal end (Figure 8.14(a)). The similar opposite behavior is also seen in distal and proximal end velocities as shown in Figure 8.14(a). The distal end pressure and proximal end velocity of stationary impact at 105 m/s are compared with proximal end pressure and distal end velocity of impact without mass at 105 m/s in Figure 8.14(b). The velocity decline of the stationary impact is more gradual than that of the impact without mass, while the impact without mass generates slightly higher pressures as seen in Figure 8.14(b). The distal pressure-nominal strain curves of stationary impact shown in Figure 8.14(c) clearly indicate that plateau pressures increase with the impact velocity above 50 m/s. The proximal pressure reaches the quasi-static pressures when the velocity decreases as shown in Figure 8.14(d). The initial elastic wave develops at the proximal end and the proximal end plastic deformation starts at a pressure between 0.52-0.62 MPa and finally the densification of the proximal end begins at about 0.8 MPa.

The deformation sequences of stationary impact test simulation at 105 m/s and 200 m/s impact velocity and various impact times till full densification are shown in Figures 8.15(a) and (b), respectively. In stationary impact, the shock wave develops at the distal end and proceeds to the proximal end at both velocities as seen in Figures 8.16(a) and (b). The deformation sequences of stationary impact test simulation at 10 m/s and 50 m/s impact velocities and various deformation times till full densification are shown in Figures 8.16(a) and (b), respectively. As with the direct impact test with backing mass, the projectile deformation is nonhomogeneous at 10 m/s (Figure 8.16(a)) and the shearing of the layers as similar with the quasi-static deformation is also noted. At 50 m/s velocity, the deformation is in between shock and quasi-static deformation (Figure 8.16(b)).



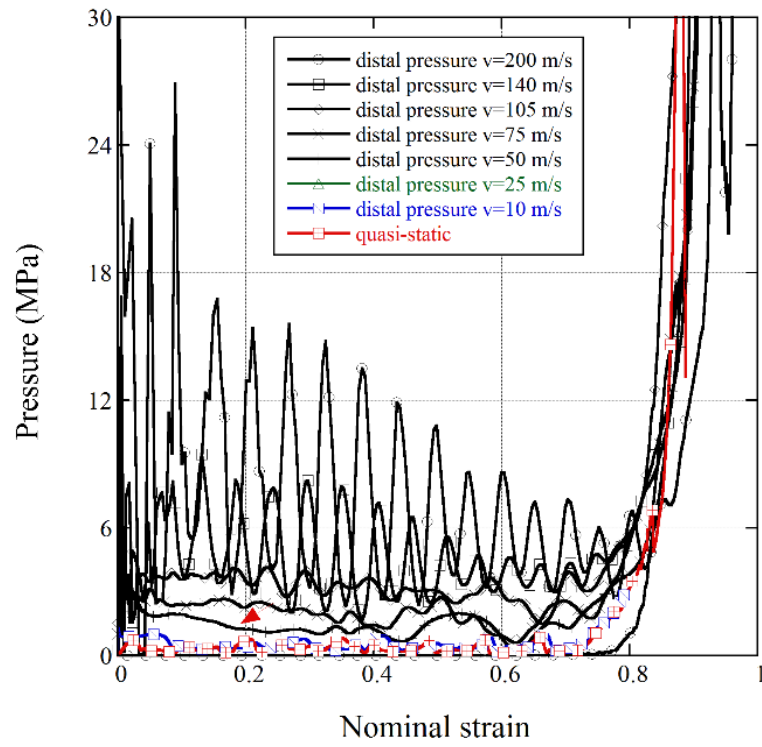
(a)



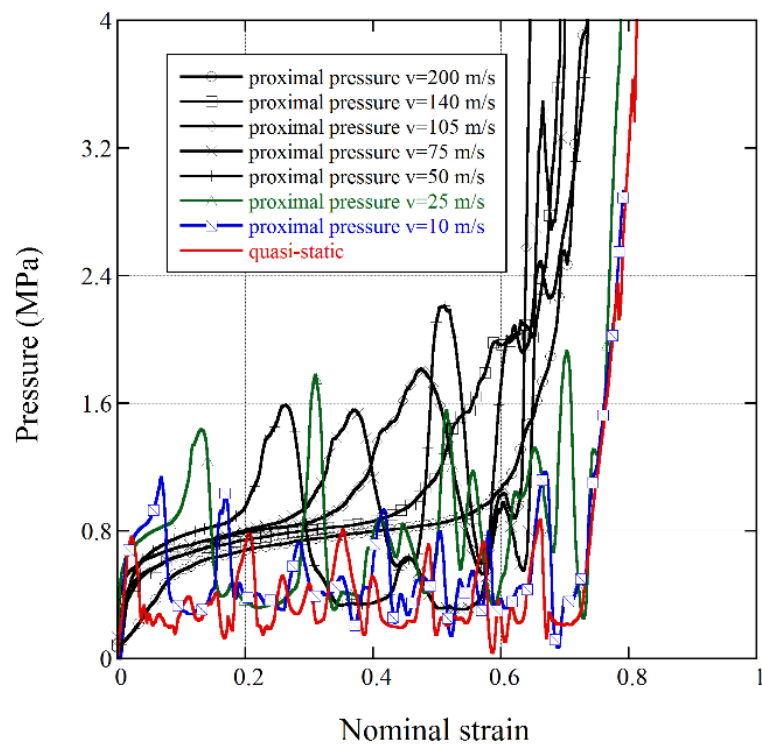
(b)

Figure 8.14. (a) SHPB gage, proximal and distal end pressure and distal and proximal velocity-nominal strain curves of stationary impact, (b) proximal and distal end pressure, distal and proximal velocity-nominal strain curves of stationary and backing mass impact, (c) distal end pressure and (d) proximal end pressure nominal strain curves of stationary impact.

(cont. on next page)



(c)



(d)

Figure 8.14. (cont.)

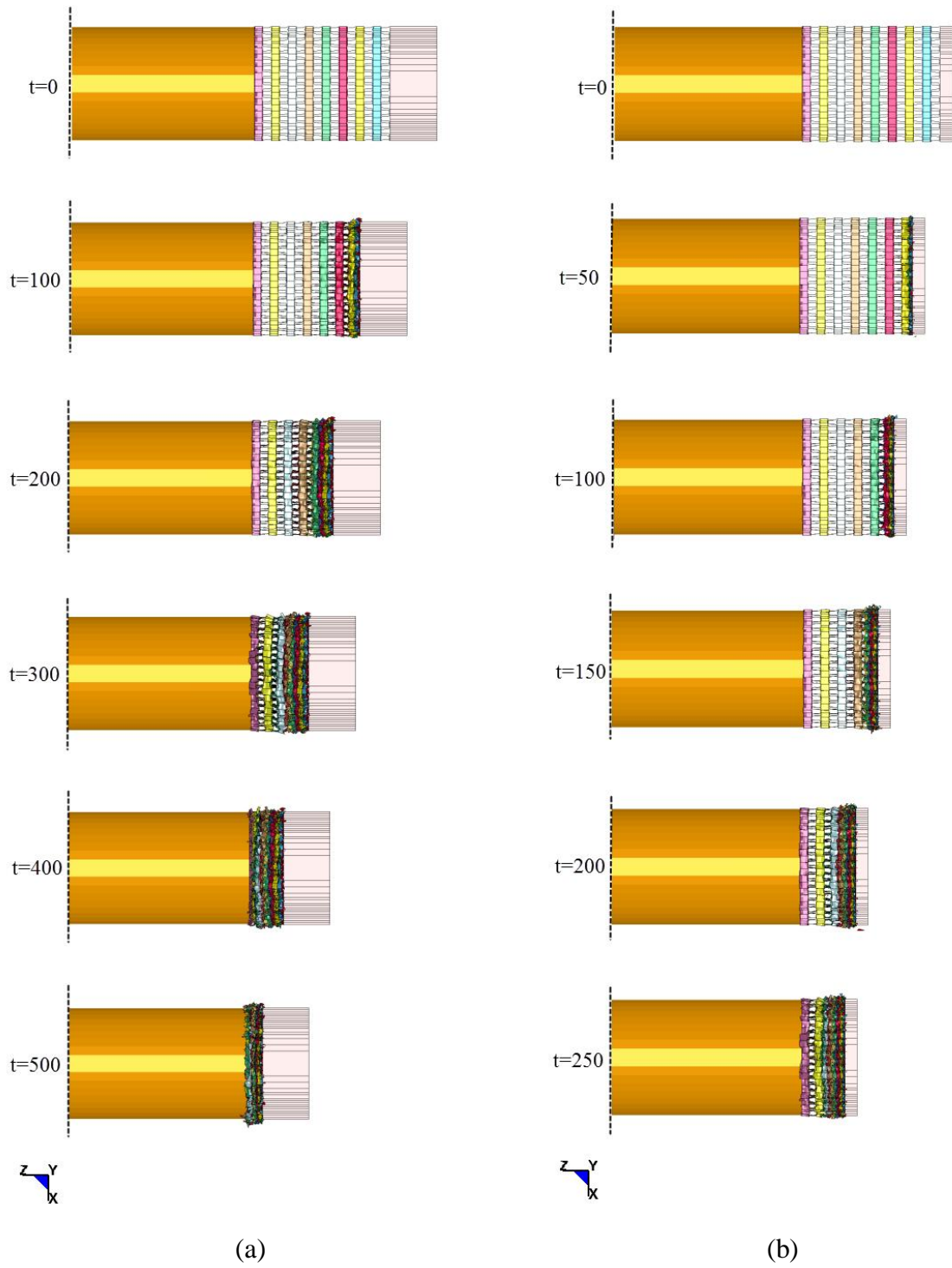


Figure 8.15. The numerical simulation deformation sequence of corrugated projectile subjected to stationary impact at (a) 105 and (b) 200 m/s.

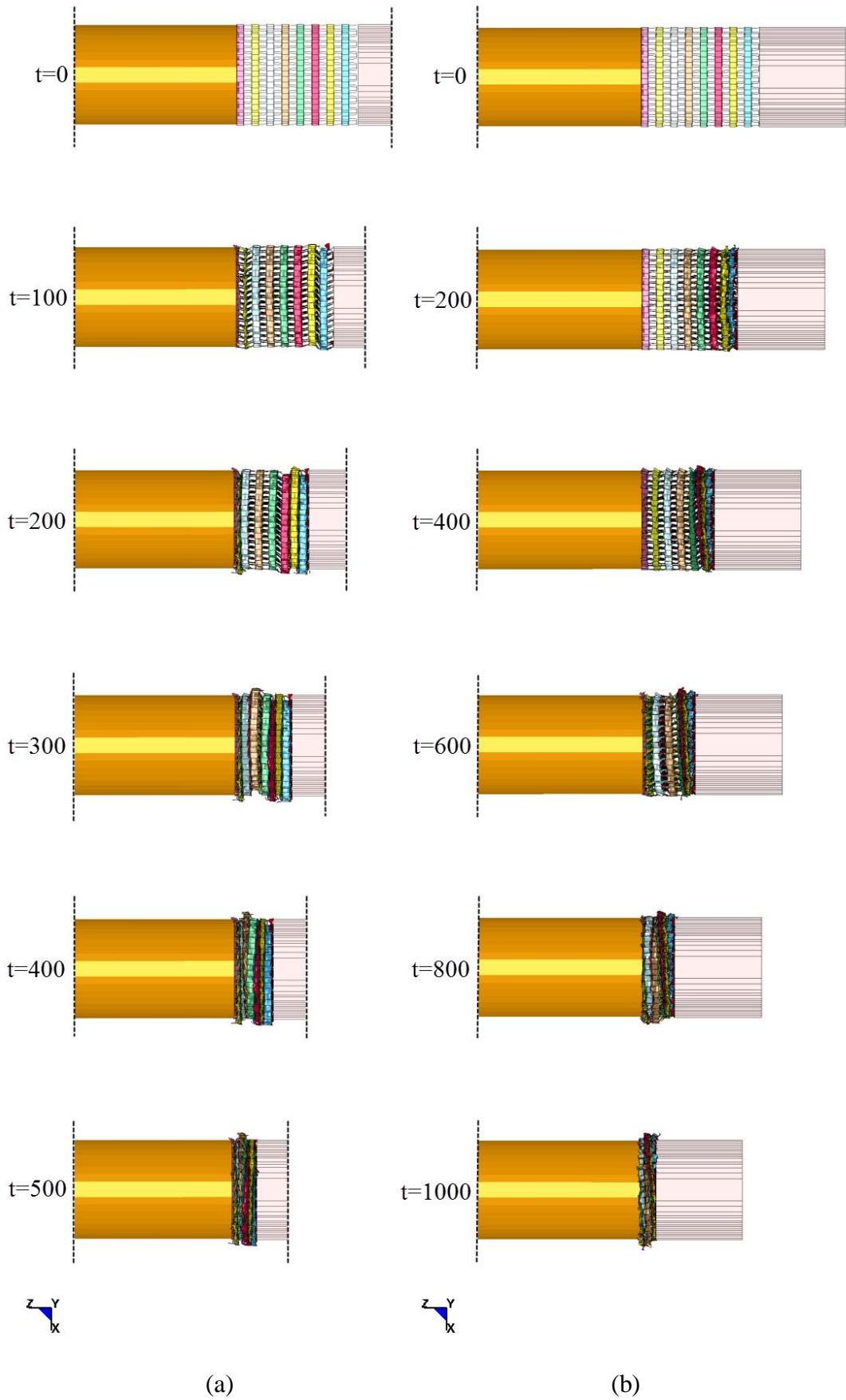


Figure 8.16. The numerical simulation deformation sequence of corrugated projectile subjected to stationary impact at (a) 10 and (b) 50 m/s.

## CHAPTER 9

### ANALYTIC MODELS OF IMPACT TESTS

#### 9.1. Rigid Perfectly Plastic Locking Shock Model

The pressure developed as a result of shock deformation in the r-p-p-l model depends on the crushing stress or plateau stress ( $\sigma_p$ ) and densification strain ( $\varepsilon_D$ ) as indicated in Eqn. 5.5. These two parameters, crushing stress and densification strain, have to be initially determined in order to apply the r-p-p-l model to the investigated corrugated structure. The crushing stress is determined from the stress-strain curves at a quasi-static strain rate. The experimental quasi-static stress-strain and mean stress-strain curves of four different tests at the same quasi-static strain rate ( $10^{-1} \text{ s}^{-1}$ ) are shown in Figure 9.1(a). In the same figure, the energy absorption efficiency-strain curves of the tests based on experimental and mean stresses are also shown for comparison. The average crushing and mean stresses are determined 0.7 MPa (0.64-0.76 MPa) and 0.46 MPa, respectively (Figure 9.1(b)). The densification strain of the investigated corrugated structure is calculated using three different methods. In the first method, a tangent line is drawn to the rising part of the stress-strain curves in the densification region and the intercept of this line with stress or mean stress is taken as the densification strain [115]. The densification strain by this method is found 0.74 (Figure 9.1(b)). The second method is based on the energy absorption efficiency [114]. The energy absorption efficiency is,

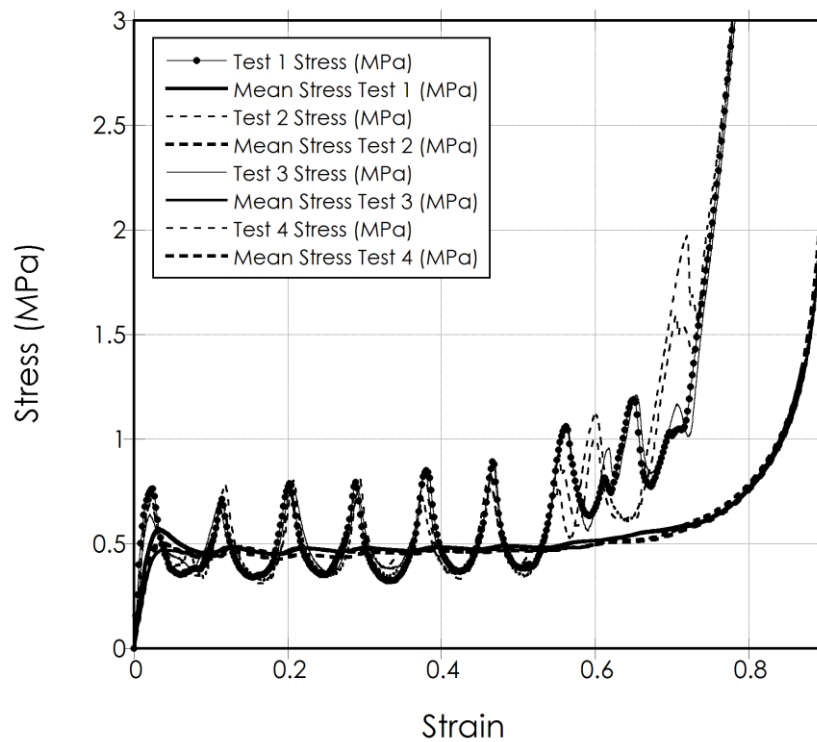
$$EE(\varepsilon) = \frac{\int_0^{\varepsilon_f} \sigma(\varepsilon) d\varepsilon}{\sigma(\varepsilon)} \quad (9.1)$$

where  $\varepsilon_f$  is the final strain attained in the test sample, which is larger than the densification strain. The maximum in the EE-strain curve is defined as the densification strain,  $\varepsilon_{EE_{\max}} = \varepsilon_D$  [114]. The densification strain calculated based on the energy absorption efficiency using the experimental and mean stresses are sequentially 0.5 and

0.74 (Figure 9.1(b)). The use of mean stress in the calculation of energy absorption essentially gives the same densification strain as the intercept method. The perfect and imperfect simulation mean stress-strain curves also give very similar energy absorption efficiency-strain responses with the experimental stress-strain curves. Both intercept and energy absorption efficiency methods give the densification strain of 0.74 (Figure 9.1(b)). Throughout the analytic calculations, the densification strains of 0.50 and 0.74 determined by the intercept and energy methods were implemented to the direct impact test results and the results were compared.

At the impact velocities above the subcritical velocities, the densification strain is also calculated numerically by tracking the individual corrugate layer strains. Figures 9.2(a) and (b) show the numerical variations of the layer velocity and layer strain as function of time for the sample tested at 105 m/s. The proximal end layer of the sample (impact end) is numbered as layer 16 and the distal end as layer 1 as shown in the inset of Figure 9.2(a). Sequentially, the velocities are measured from layer 1 to layer 16. It is noted in the same figure that the distal end layer has the longest duration of velocity, while the proximal end layer the lowest duration as the distal end deforms at the latest stage while the proximal end at the earliest stage of the impact. The velocity profiles of the first three layers are noted to be very much similar, showing slight differences between each other, while the velocity profiles of the following layers show distinct differences between each other as seen in Figure 9.2(a). The final strain attained in layer 1 shown in Figure 9.2(b) is the lowest one (0.06), while it gradually increases to 0.72 in layer 7. The final layer strain values; however, almost saturate at about 0.77 after layer 7. The final simulation and experimentally deformed cross-sectional views of the tested sample are shown at the top of Figure 9.2(b). When the impact velocity increases to 140 m/s, the durations of the velocities are shortened (Figure 9.3(a)) and the first layer strain increases to 0.29; the strain values saturate at about 0.81 after layer 6, Figure 9.3(b). When the velocity increases to 200 m/s, the durations of the velocities are further shortened (Figure 9.4(a)) and the first layer strain increases to 0.63; the layer strains saturate at a strain of 0.9 after layer 3 (Figure 9.4(b)). Except the first layer, all layers are fully compacted at 200 m/s as seen in the numerical and experimental deformed pictures of the sample in Figure 9.4(b). The variations of the nominal strain with time is also shown in Figure 9.2(b) for 105 m/s, in Figure 9.3(b) for 140 m/s and in Figure 9.4(b) for 200 m/s. The final nominal strain is lower than the layer densification strain at 105 and 140 m/s, while it reaches the layer densification strain at 200 m/s. This also

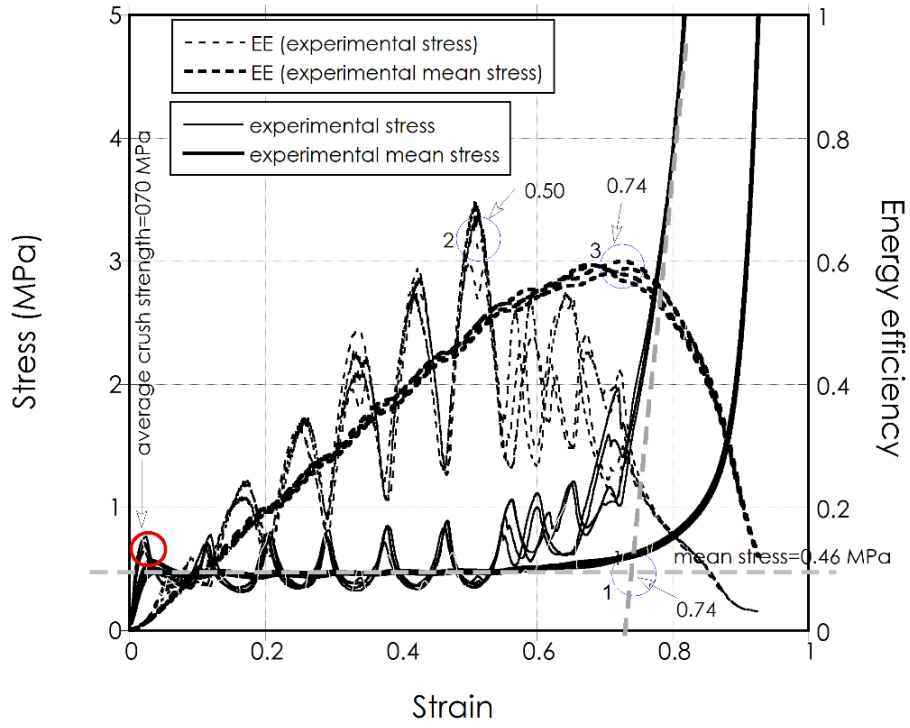
proves the fully compaction of the corrugated projectile at 200 m/s. The numerical and experimental final deformed cross-sections of the tested samples show well correspondence between each other at all velocities. Although, the initiation and progression of the layer strains are sequential, the first 3-4 layers are noted to be compacted to a final strain below the densification strain at 105 m/s (Figure 9.2(b)). These first 3-4 layers are partially deformed during the course of the impact. At 140 m/s, only the first layer is crushed under the densification strain both experimentally and numerically (Figure 9.3(b)), while all layers are nearly compacted until about the densification strain at 200 m/s (Figure 9.4(b)).



(a)

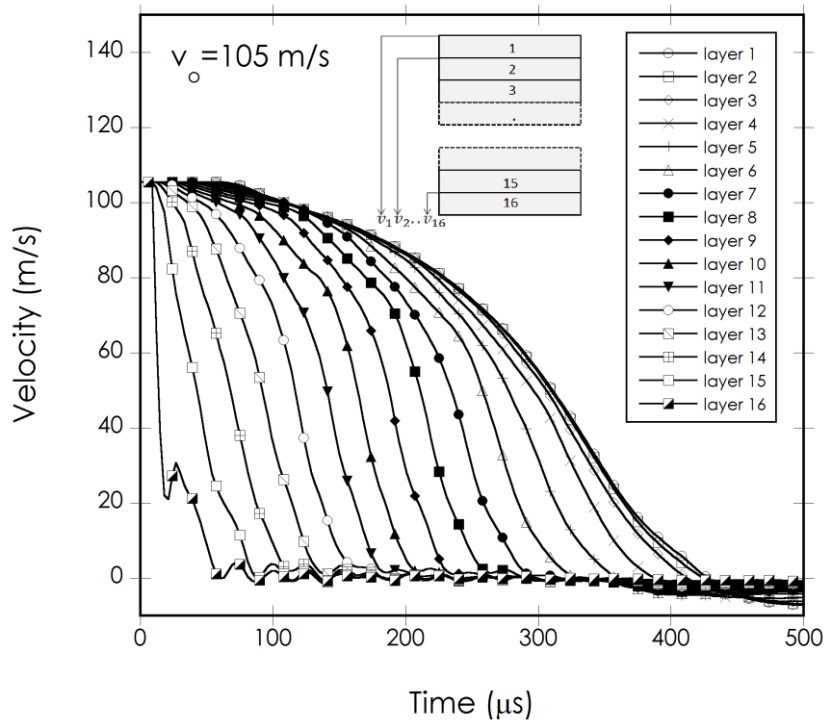
Figure 9.1. (a) experimental stress-strain and mean stress-strain curves and (b) energy efficiency-strain curves at  $10^{-1} \text{ s}^{-1}$ .

(cont. on next page)



(b)

Figure 9.1. (cont.)



(a)

Figure 9.2. (a) velocity and (b) layer strain vs. time curves of direct impact test at 105 m/s.

(cont. on next page)

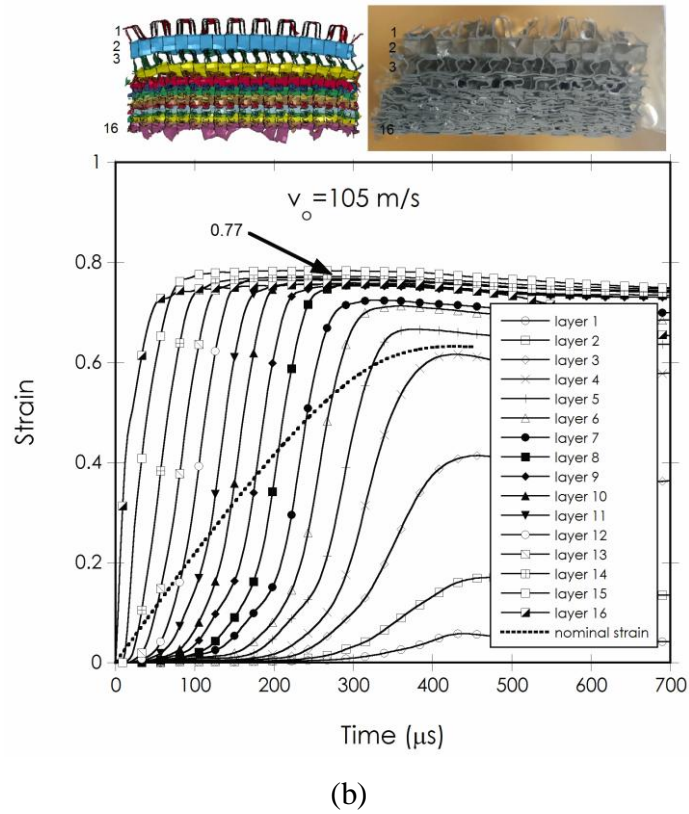


Figure 9.2. (cont.)

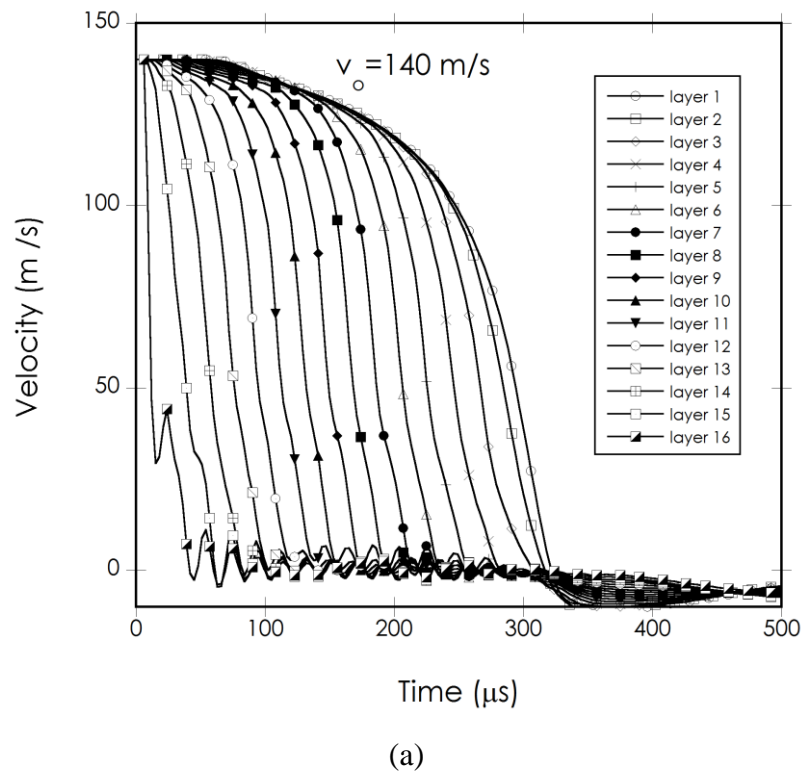
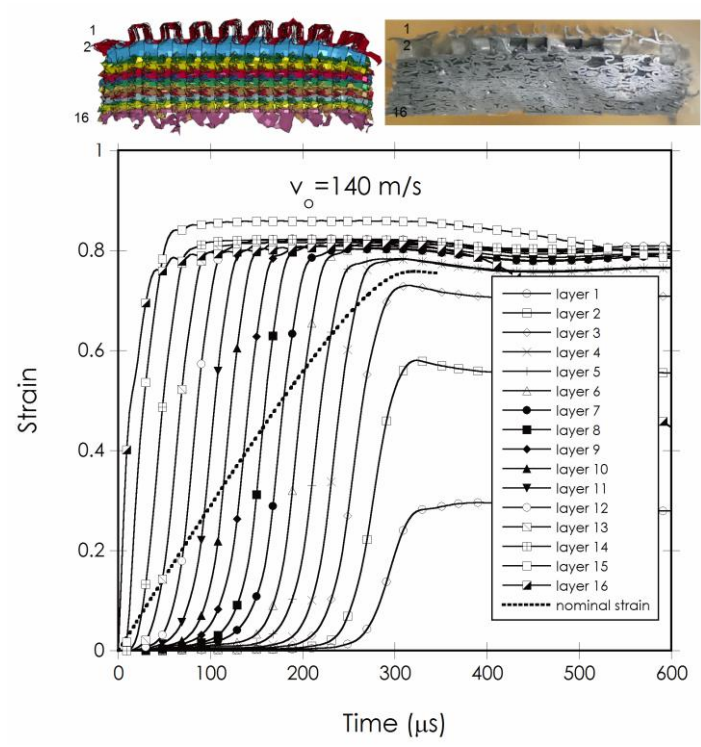


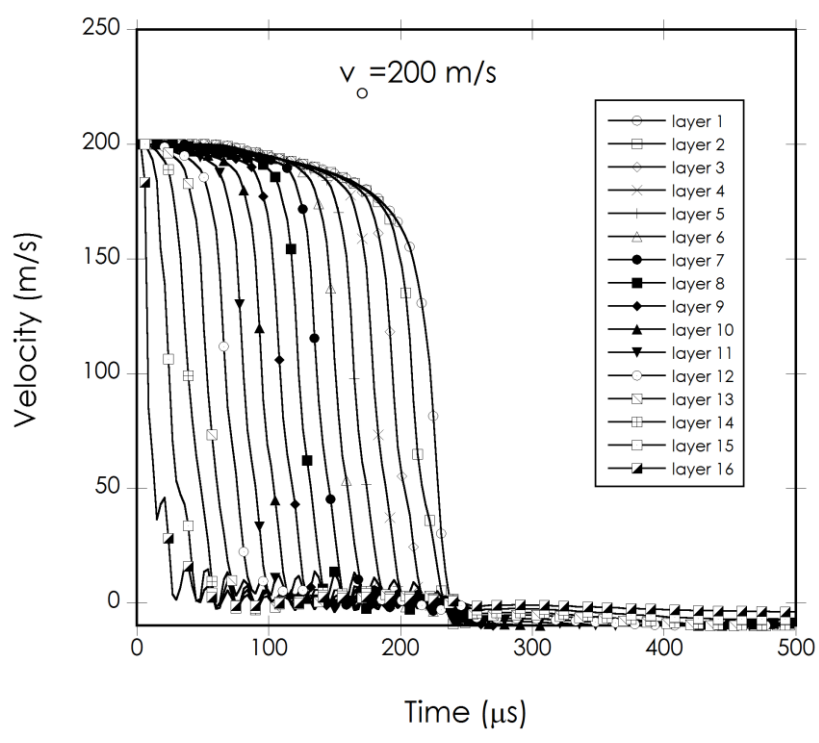
Figure 9.3. (a) velocity and (b) layer strain vs. time curves of direct impact test at 140 m/s.

(cont.on next page)



(b)

Figure 9.3. (cont.)



(a)

Figure 9.4. (a) velocity and (b) layer strain vs. time curves of direct impact test at 200 m/s.

(cont. on next page)

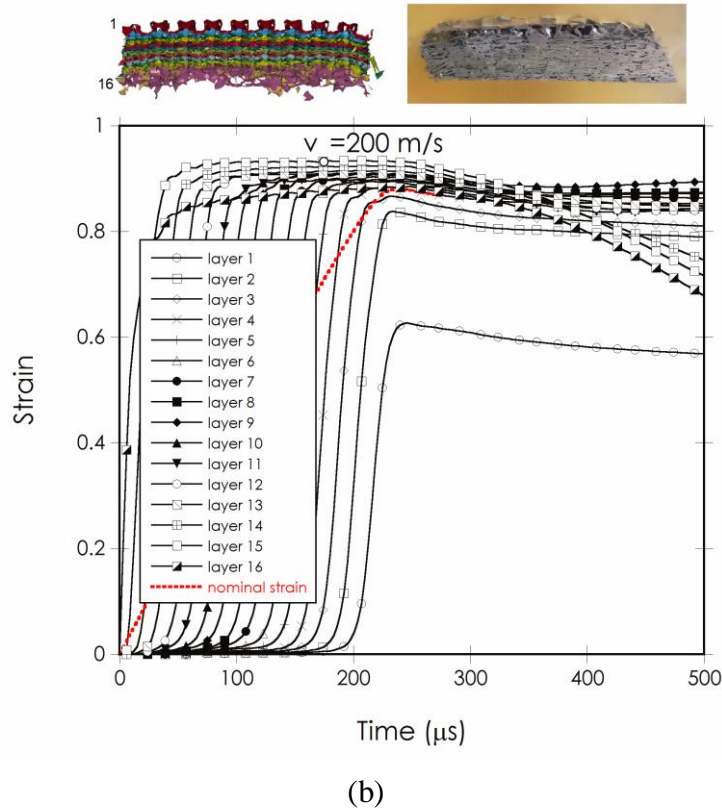


Figure 9.4. (cont.)

The layer compaction profile becomes completely different when the impact velocity is near or below the subcritical velocities. The strain-time profile at 50 m/s is mostly diffusive although, an intense deformation of the layers occurs near the proximal end (Figure 9.5(a)). The deformation profile is not sequential; layers deformed to a larger and lower extend together at a given deformation time. This diffusive nature of the strain or deformation becomes more pronounced following the last three layers of the intense deformation region at the proximal end. The diffusive nature of the strain is somewhat reduced when the velocity increases to 75 m/s (Figure 9.5(b)). At this velocity, the shock deformation nature is seen in the last 5 layers at the proximal end and the strain gradually becomes diffusive in the following layers. The impact deformation at this velocity reflects a transition stage from non-sequential and diffusive quasi-static to sequential and concentrated shock deformation.

The r-p-p-l model over estimates the pressure values of both the experiments and simulations, particularly at 200 m/s, when  $\epsilon_d=0.5$  and  $\sigma_p=0.7$  MPa (Figure 9.6). The use of experimental mean stress value of 0.46 MPa also predicts higher pressure values than the experiments and simulations at 200 m/s. When  $\epsilon_d=0.5$  and  $\sigma_p=0.7$  MPa, the r-p-p-l model gives similar pressure-time profiles with experiments at 105 and 140 m/s,

while a relatively shorter pressure duration is found at 200 m/s (Figure 9.6). Better predictions of experimental and simulation pressure-time profiles are reached with the r-p-p-l model by employing the numerically determined densification strain for each velocity (Figure 9.7(a) and (b)). The prediction of velocity-time and pressure-nominal strain profiles with the r-p-p-l model using the numerically determined densification strains are compared with those of simulations and the r-p-p-l prediction using  $\epsilon_d=0.74$  and  $\sigma_p=0.7$  MPa, sequentially in Figure 9.8(a) and (b). Although the use of numerically determined densification strain results in slightly longer velocity duration than simulation at 200 m/s (Figure 9.8(a)), it gives similar pressure-nominal strain profile with those of simulations at all velocities (Figure 9.8(b)). In the following figures, Figures 9.9(a)-(c), the numerically determined densification strain r-p-p-l model bar pressure-nominal strain and proximal end pressure-nominal strain curves are compared with the simulation bar pressure-nominal strain and proximal end pressure-nominal strain curves at 105, 140 and 200 m/s, respectively. Again, the r-p-p-l model shows well accordance with both the bar and proximal end pressures at all velocities.

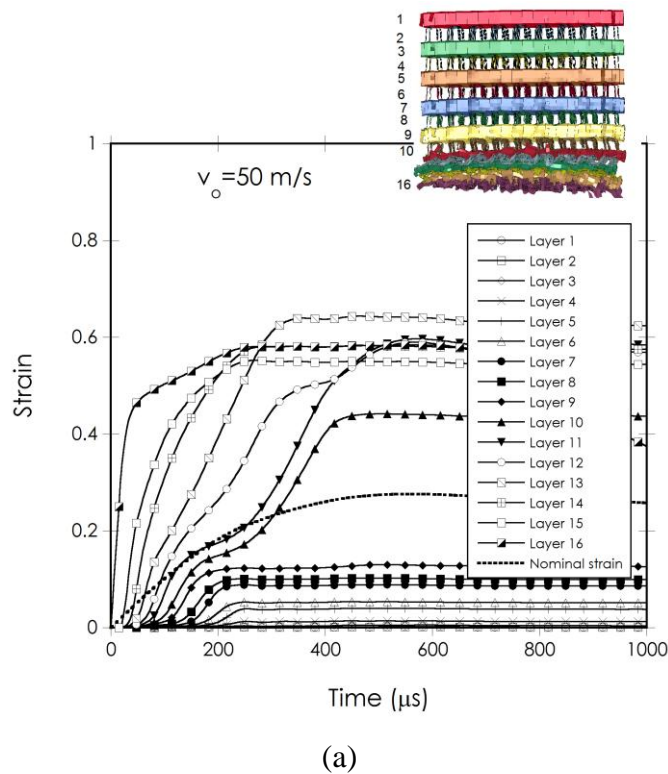
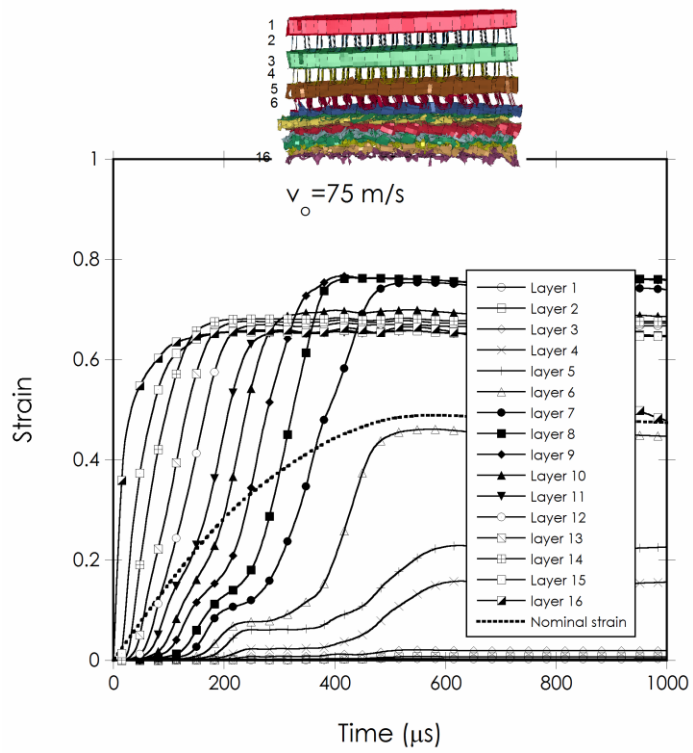


Figure 9.5. Layer strain vs. time curves of direct impact test at (a) 50 and (b) 75 m/s.

(cont. on next page)



(b)

Figure 9.5. (cont.)

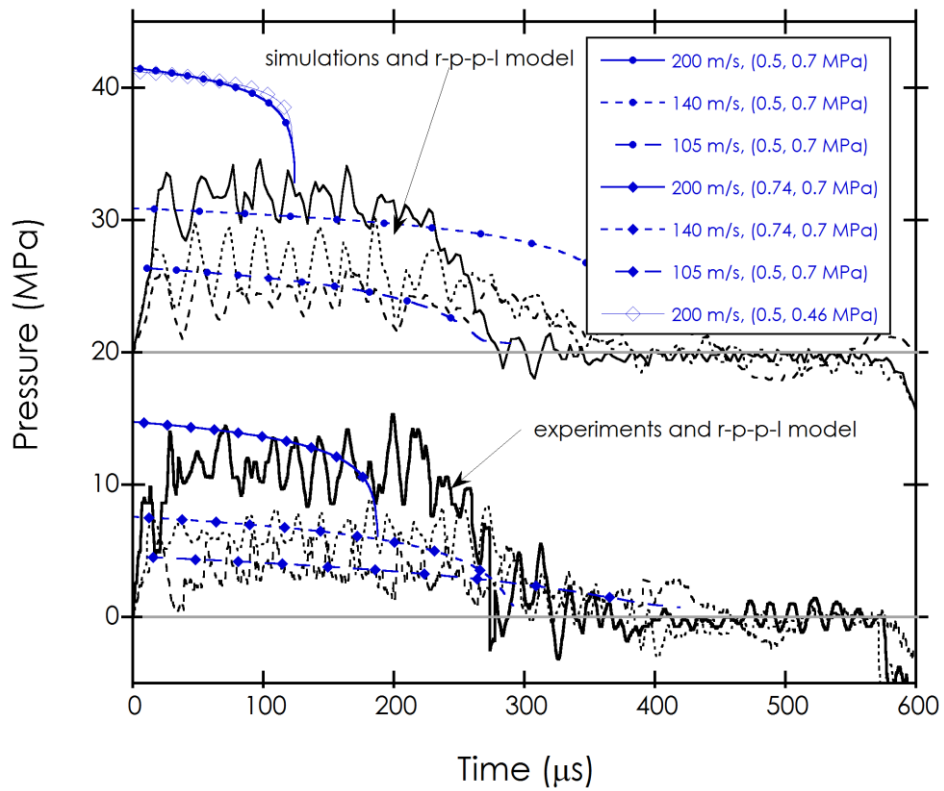
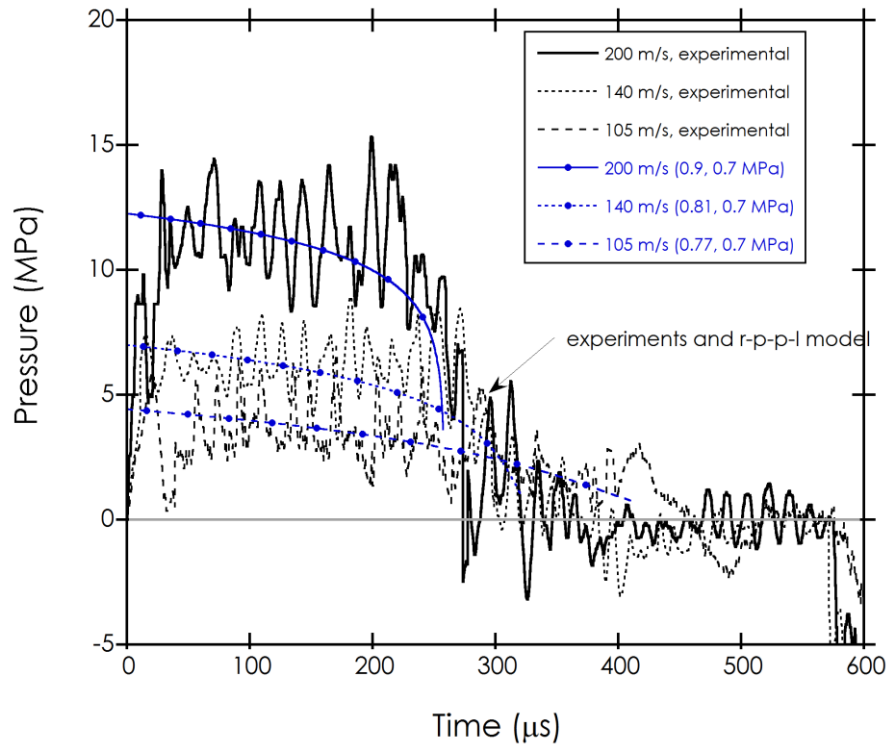
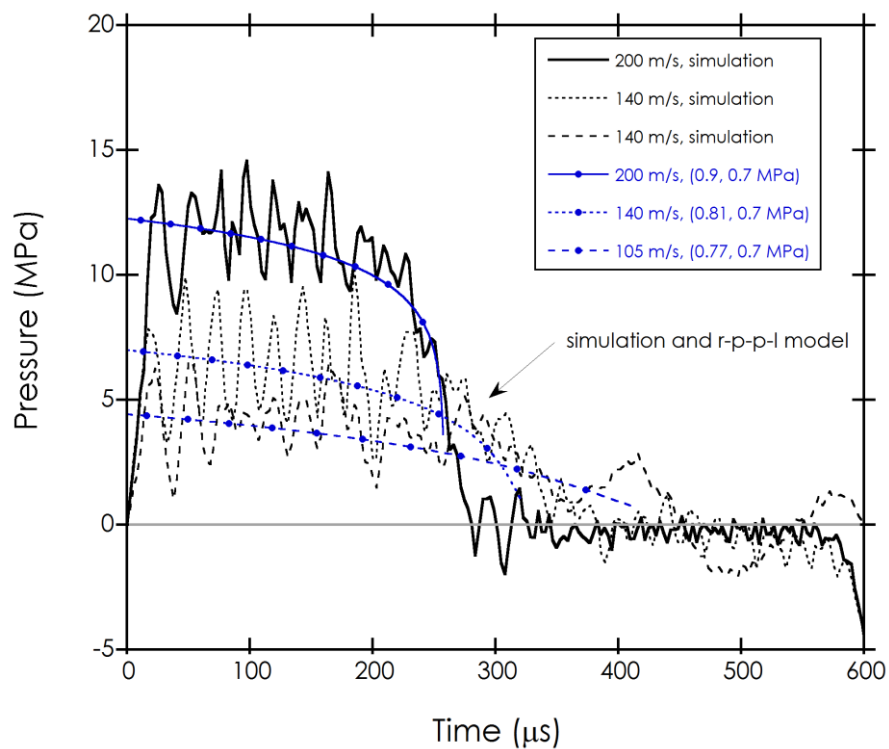


Figure 9.6. Experimental, simulation and the r-p-p-l model predicted bar pressure-time curves.

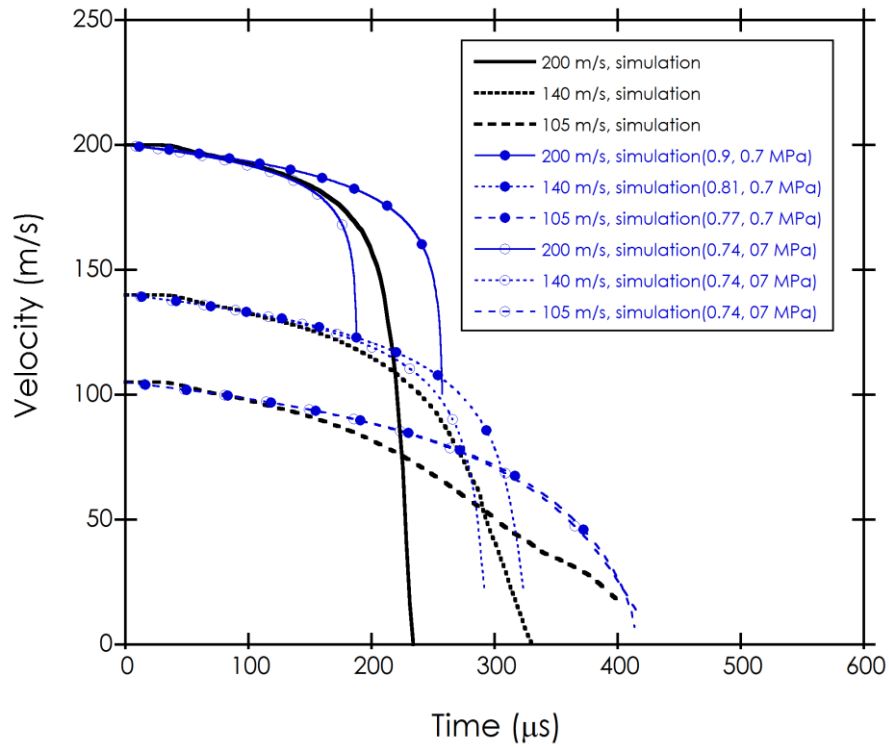


(a)

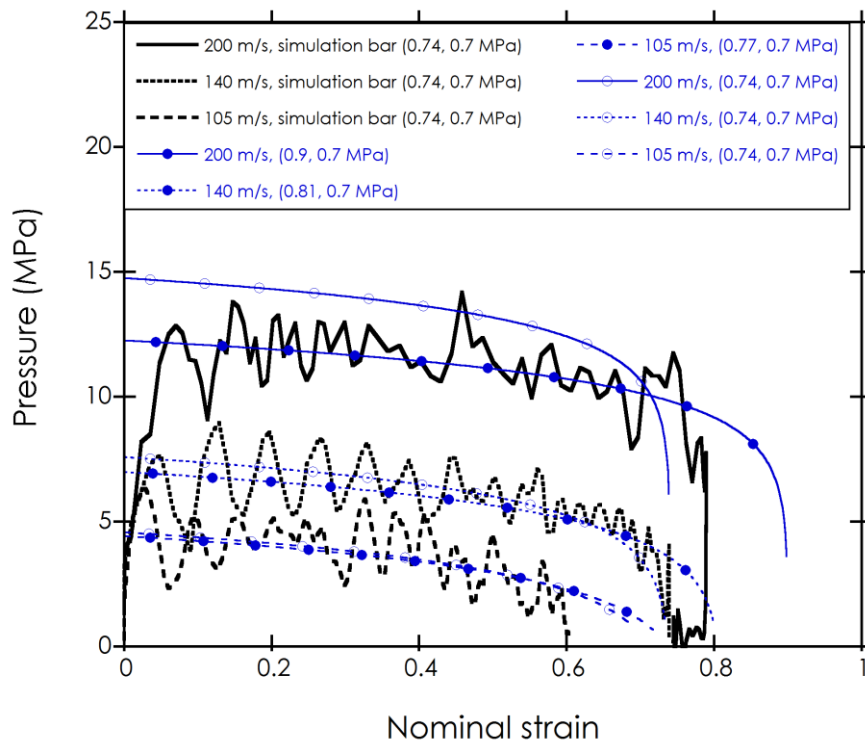


(b)

Figure 9.7. The comparison of the numerically determined densification strain r-p-p-l model pressure-time curves with those of (a) experiment and (b) simulation.

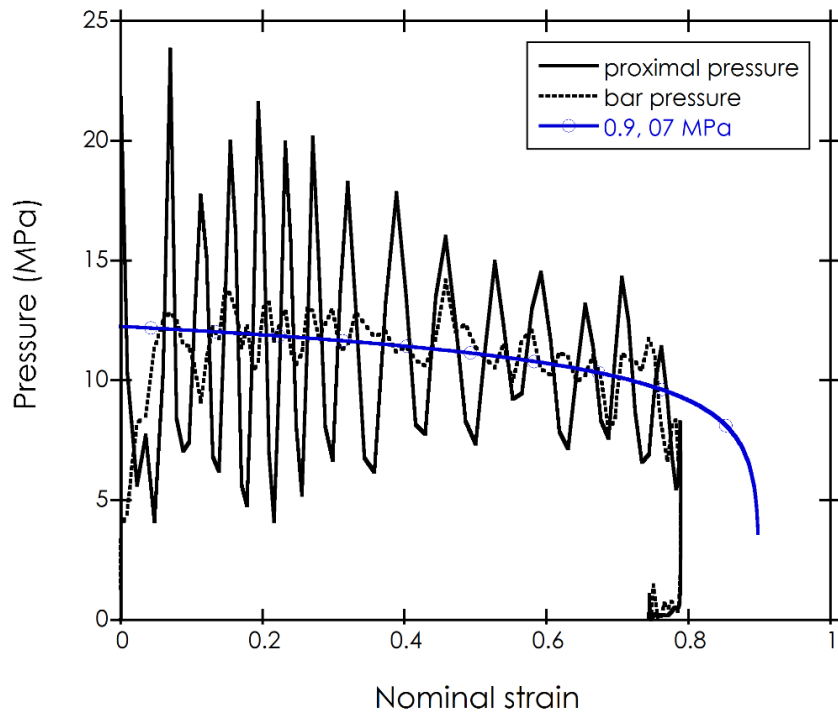


(a)

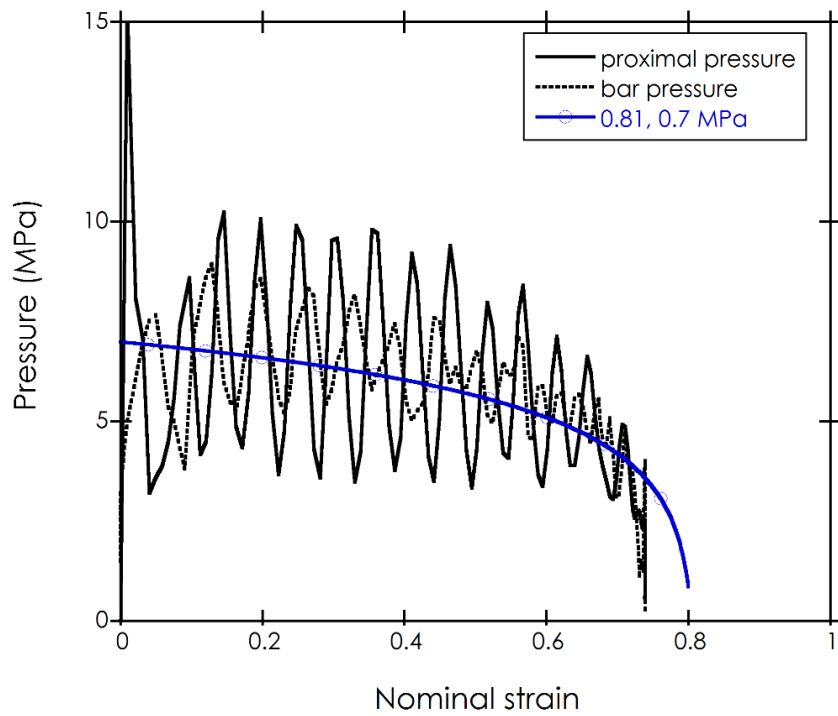


(b)

Figure 9.8. The comparison of the numerically and experimentally determined densification strain r-p-p-l model (a) velocity-time and (b) bar pressure-nominal strain curves with those of simulation.



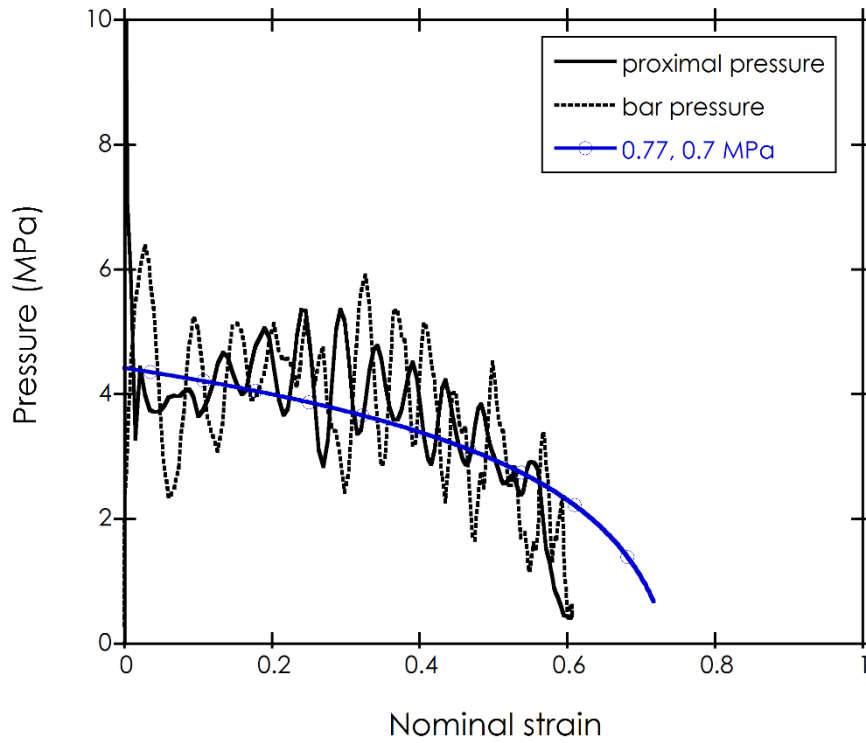
(a)



(b)

Figure 9.9. The comparison of the numerically determined densification strain r-p-p-l model pressure-nominal strain curves with the simulation bar and proximal pressure-nominal strain curves at (a) 105, (b) 140 and (c) 200 m/s.

(cont. on next page)



(c)

Figure 9.9. (cont.)

The r-p-p-l model is fitted with the simulation and experimental peak and mean/plateau pressures. The peak pressure is determined from the first peak, if it is the highest, if not then it is determined from the second or third peak pressures whichever is the highest (Figures 9.10(a-f)). The mean pressure corresponding to the plateau pressure is calculated by integrating the stress with time after the peak pressure and then dividing the integration with stress. Few of the calculated mean pressures are presented in Figure 9.10(a) for simulation and experimental impact tests. The densification strain predicted using the simulation layer strains are drawn as function of impact velocity in Figure 9.11(a). The simulation densification layer strains at 50 and 75 m/s were determined from the final attained strains in the first several layers. The densification strain in Figure 9.11(a) is fitted with a linear and power law relation to the impact velocity. The experimental and simulation peak and mean pressure values at different impact velocities are shown in Figure 9.10(b). Both experimental and simulation peak pressure values are seen in the same figure greater than mean pressure values. The variation of the r-p-p-l model pressure values of  $\varepsilon_d=0.5$  and  $\varepsilon_d=0.74$  with the impact velocity are also shown in Figure 9.11(b). The experimental and simulation peak pressure values are only well matched with r-p-p-l model of  $\varepsilon_d=0.5$  at 105 and 140 m/s velocities; at higher

velocities the model predicts higher peak pressure values than the experiments and simulations and at lower velocities it predicts lower peak pressure values. It is found that the experimental and simulation peak stress values are well fitted with a linear relation with impact velocity, while mean pressure values are well fitted with the numerical densification strain r-p-p-l model as shown in Figure 9.11(c).

The r-p-p-l model predicts the peak and mean pressure of 4.6 MPa and the loading duration of 421  $\mu$ s at 105 m/s. These values are sequentially 6.225 MPa, 4.135 MPa and 453  $\mu$ s experimentally and 4.44 MPa, 4.2 MPa and 450  $\mu$ s numerically. Well matching between the r-p-p-l model peak pressure values and simulation and experimental mean pressure values. The small discrepancies may arise from several reasons. In the r-p-p-l model, the projectile is assumed perfectly plastic; hence the elastic deformation of the projectile is neglected. This may cause mismatch in the loading duration and velocity time profile.

The arrest distance ( $u_f$ ) in the r-p-p-l model is

$$u_f = \varepsilon_d L_o \left[ 1 - e^{\left( \frac{-v_0^2 \rho_o}{2 \sigma_p \varepsilon_d} \right)} \right] \quad (9.2)$$

The arrest distance vary between 0 and  $\varepsilon_d L_o$ . Note that inserting fully compacted case,  $u_f = \varepsilon_d L_o$ , into Eqn. 9.2 results infinite time. This shows that during the impact the shock wave generated is arrested before it reaches to the end of the sample. The arrest time ( $\tau$ ) is estimated as,

$$\tau = \frac{u_f}{v_0} \quad (9.3)$$

and

$$\tau = \frac{\varepsilon_d L_o}{v_0} \quad (9.4)$$

The experimental, numerical and r-p-p-l model arrest time final thicknesses of corrugated projectiles are shown in Figure 9.12(a) as function of projectile velocity. In the same figure the simulation and experimental final deformed pictures of the

projectiles are also shown for comparison. The r-p-p-l model nearly predicts the simulation and experimental arrest times at 140 and 200 m/s, while it predicts lower arrest times below the subcritical velocities. The r-p-p-l model however results in lower final lengths than simulation and experiments. In the experiment and simulation the densification strain is varied within the individual layers, while the variations of the densification strain in the layers are ignored in the r-p-p-l mode. The reduced nature of densification strain in subsequent layers in the test results in longer final lengths than the r-p-p-l model in which a constant densification strain is determined from the first several layers at the proximal end. The r-p-p-l model final lengths are sequentially 15, 10 and 4.1 mm for 105, 140 and 200 m/s. These values are 18, 13.3 and 6.4 mm and 17.2, 12.3 and 8.8 for the simulations and experiments, respectively. A perfect final thickness matching are found between the simulation and experiments in the projectiles with face sheets (Figure 9.12(b)). The simulation and experimental final thickness are sequentially 16.3, 16.1, 11.5 mm and 11.3, 9 and 8.6 mm for 105, 140 and 200 m/s.

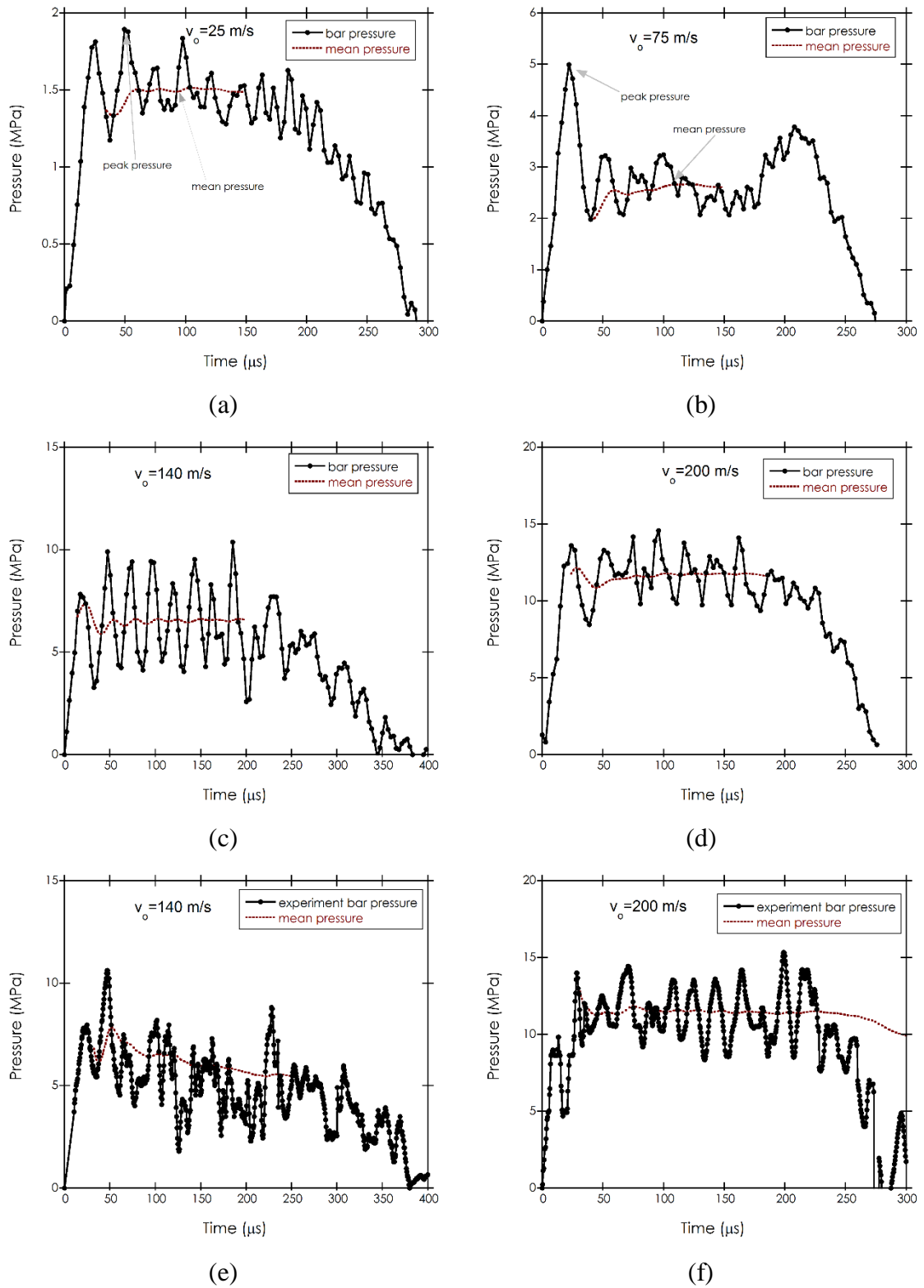


Figure 9.10. Bar pressure vs. time and mean pressure curves of numerical simulations (a) 25, (b) 75, (c) 140 and (d) 200 m/s and experiments of (e) 140 and (f) 200 m/s.

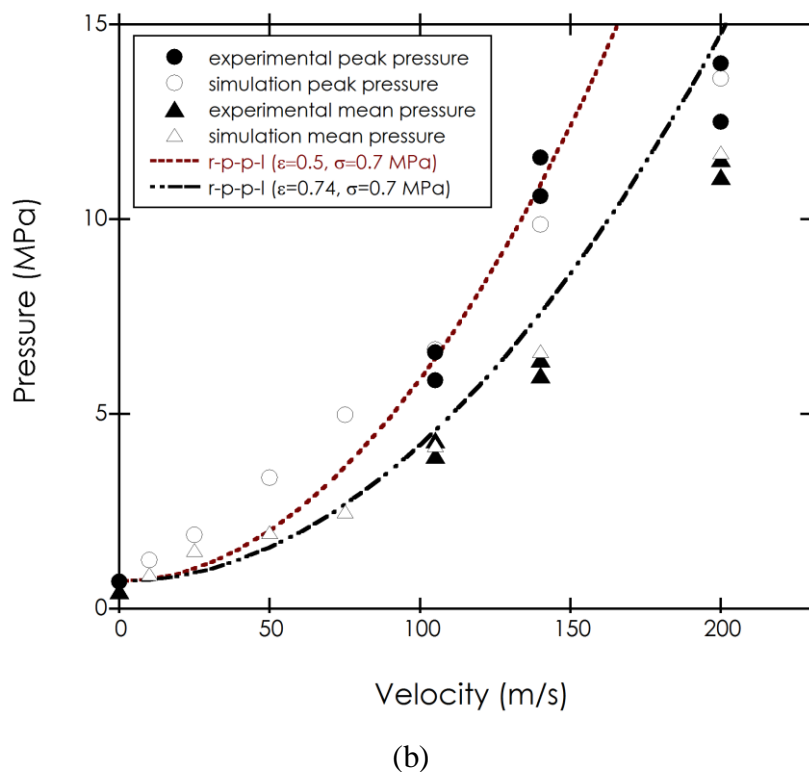
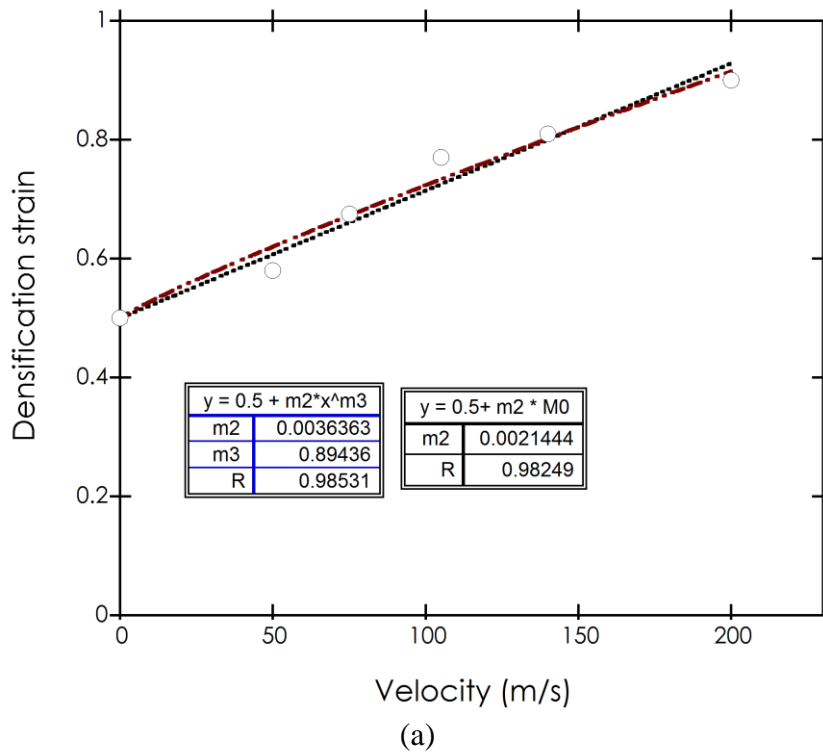
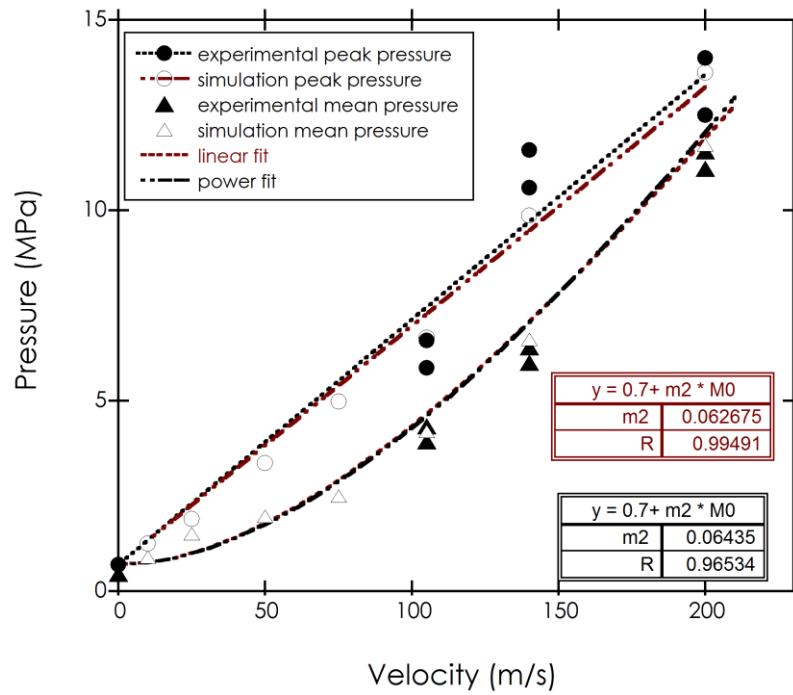


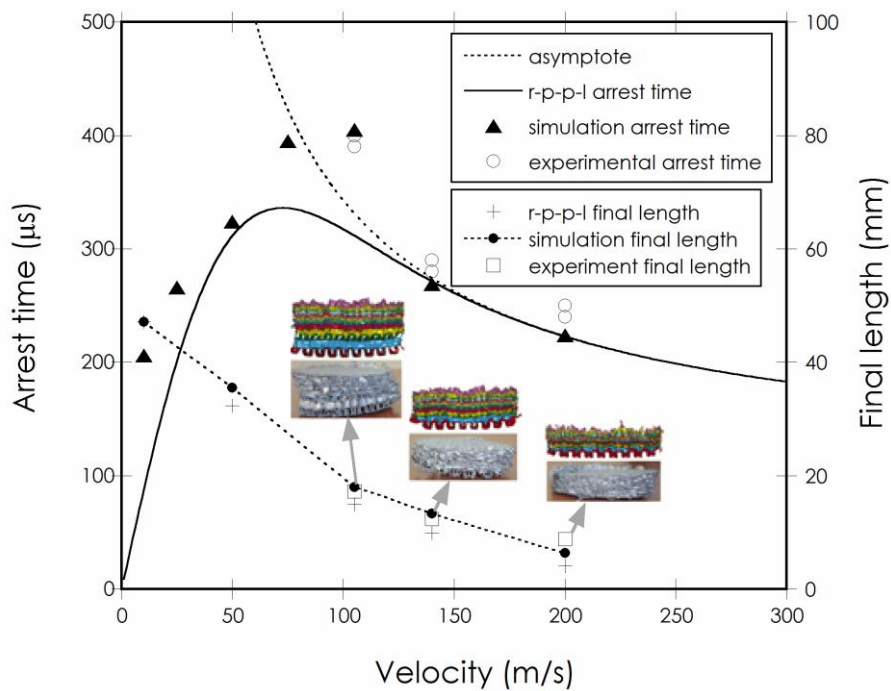
Figure 9.11. (a) Linear and power relation fit of numerical densification strain with velocity (b) simulation and experimental peak and mean pressure vs velocity and r-p-p-l model peak and mean pressure variation with velocity and (c) fitting simulation and peak pressures with r-p-p-l model of numerical densification strain.

(cont. on next page)



(c)

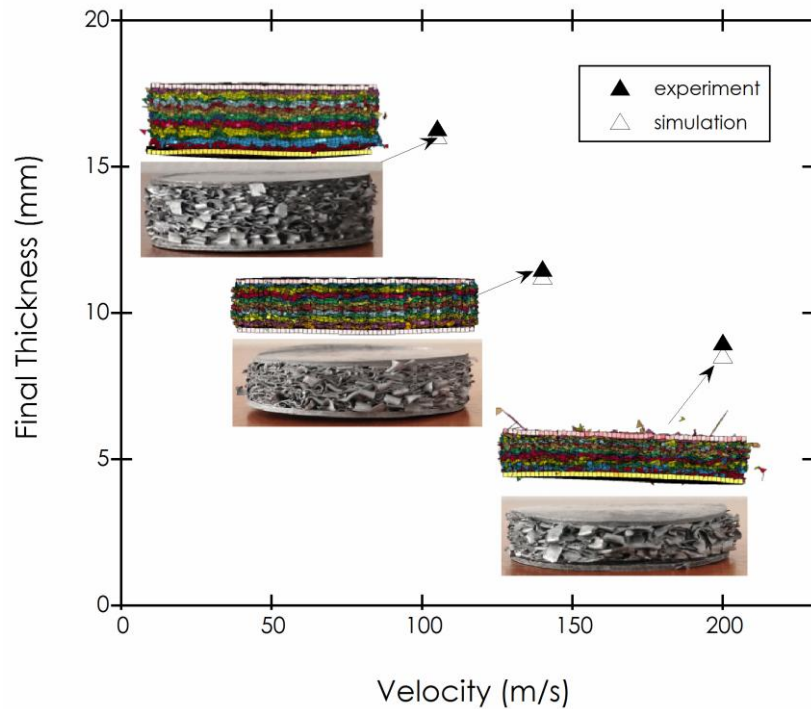
Figure 9.11. (cont.)



(a)

Figure 9.12. (a) The experimental, numerical and r-p-p-l model arrest time and experimental and simulation final thickness of the corrugated projectile without face sheet and (b) experimental and simulation final thickness of the corrugated projectile with face sheet.

(cont. on next page)



(b)

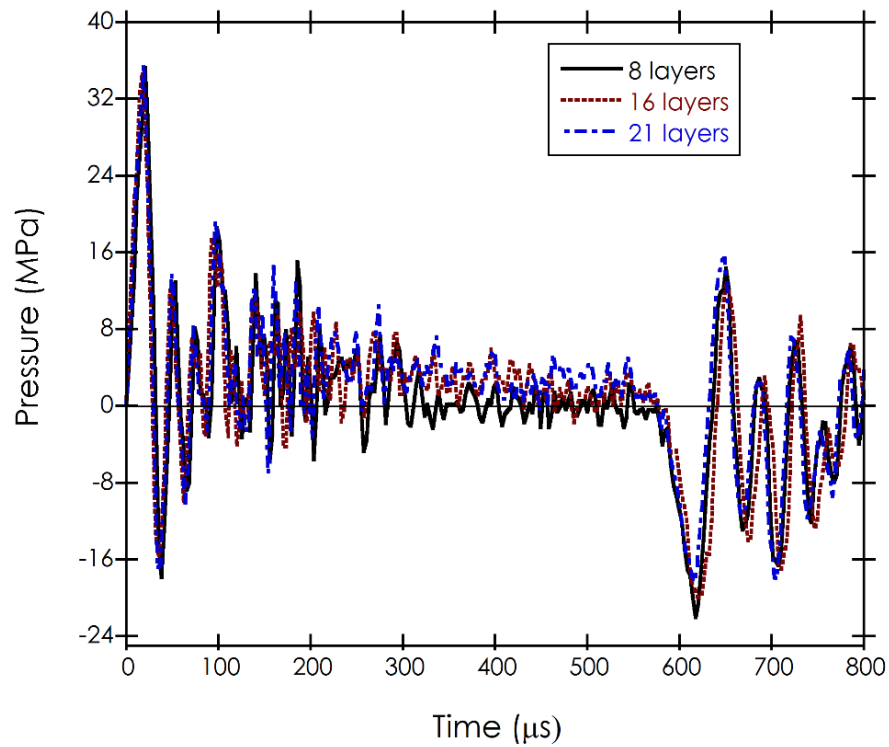
Figure 9.12. (cont.)

## 9.2. Effects of Number of Fin Layers

Figures 9.13(a-b) show the effect of the number of fin layers on the pressure-time profile of the corrugated projectile with and without face sheet (1 mm thick) at 105 m/s. As is seen in the same figure the number of layers changes the total loading duration without any change in the pressure profile (Figure 9.13(a)). The peak pressures for all projectiles with face sheets are almost the same, 35 MPa, but the total loading durations are  $\sim 325$ , 486 and 580  $\mu\text{s}$  for 8, 16 and 21 layers, respectively. The pressure response of the projectiles without face sheet is also the same for 8, 16 and 21 layers, 6.22 MPa, as shown in Figure 9.13(b), while the total pressure durations are 262, 450 and 580  $\mu\text{s}$  for 8 layers, 16 layers and 21 layers, respectively.

The difference of the loading durations is attributed to the initial length of the projectile in Eqns. 9.2 and 9.3, as the initial length increases the arrest time increases. The effect of the thickness of the face sheet is shown in Figure 9.13(c) for without face sheet and 1 mm and 2 mm thick face sheets (16 layer projectile, 105 m/s)). Increasing the thickness of face sheet increases the initial peak pressure as shown in the same figure. The peak pressures increases from 6.22 MPa for no face sheet to 35 and 52 MPa

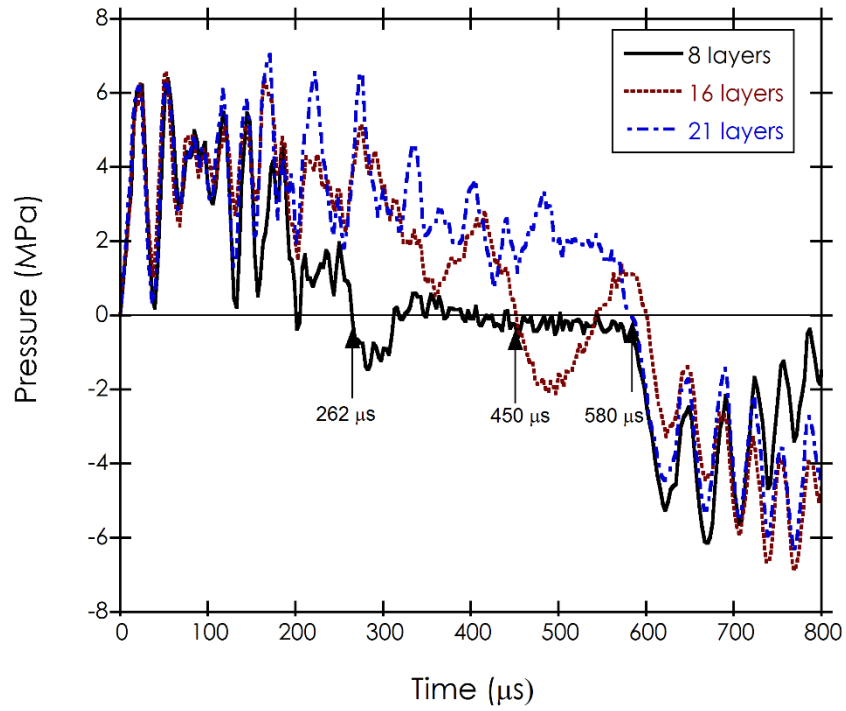
for 1 and 2mm thick face sheets, respectively. The increase in the pressure developed with the thickness of the face sheet is partly due to the increase in the mass of the projectile according to the Eqn. 5.7. The total durations of the projectiles also changes with the thickness of the projectile for the investigated impact velocity, 484 and 565  $\mu\text{s}$  for 1 and 2 mm thick face sheet, respectively.



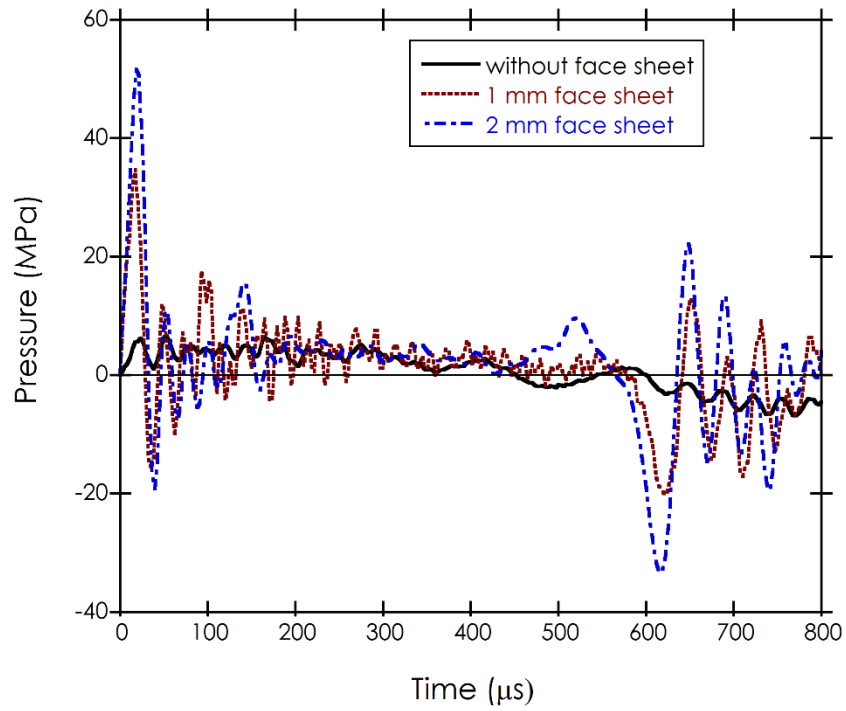
(a)

Figure 9.13. Effect of number of fin layers on the pressure (a) 1 mm thick face sheets, (b) without face sheets and (c) the effect of face sheet thickness on the pressure.

(cont. on next page)



(b)

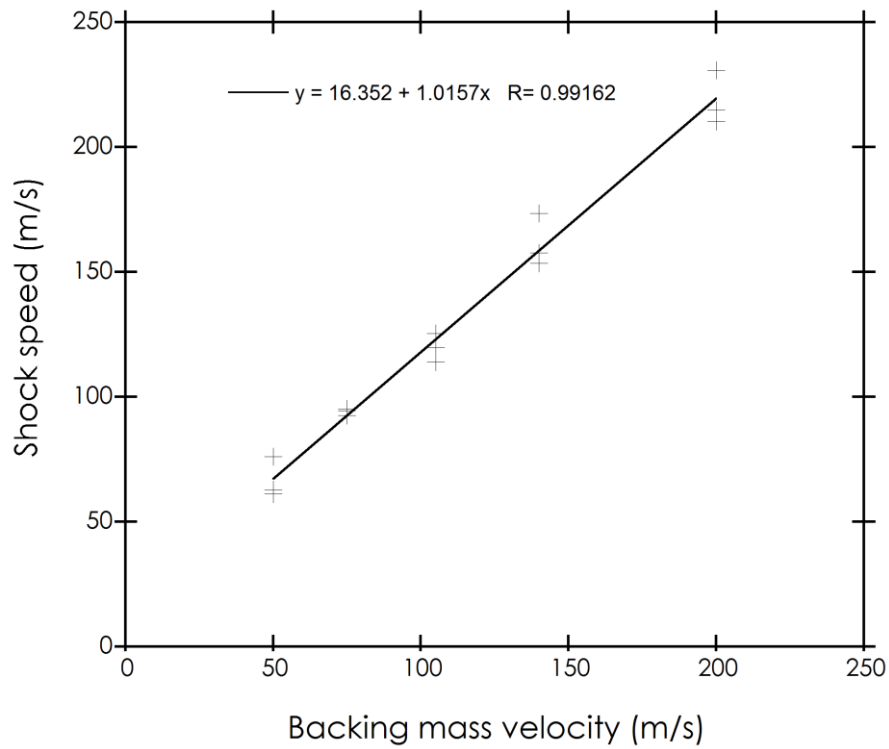


(c)

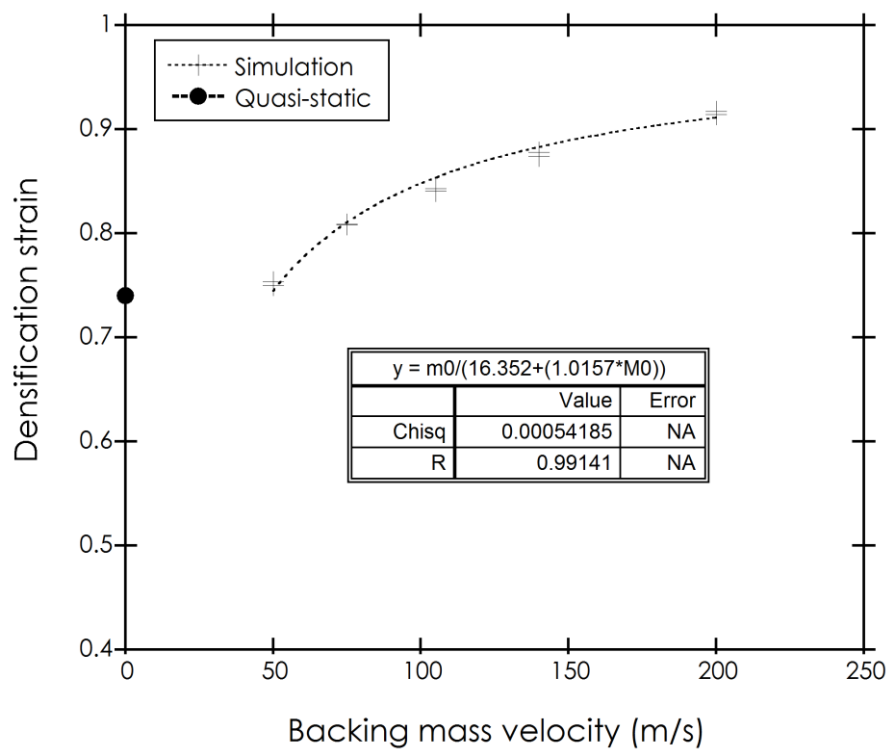
Figure 9.13. (cont.)

### 9.3. Hugoniot Jump Equations; tests with backing mass and stationary impact

The variation of the Hugoniot shock speed with backing mass velocity is shown in Figure 9.14(a). The graph data are generated from the measurements collected from the direct impact simulations without backing mass, direct impact simulations with backing mass and stationary impact simulations. The shock speed in the corrugated projectiles is calculated from crushing displacement of the undeformed fin region with respect to time. A linear fit in accord with Eqn. 5.15 results  $A=16.352$  m/s and  $B=1.0157$  ( $R=0.991$ ). A similar trend of  $V_b - \dot{s}$  relation was also found studies on a previous study on polyurethane and aluminum foams [116, 126]. Hugoniot strain generated according to Eqn. 5.16 is shown in Figure 9.14(b) as dotted lines. The Hugoniot strain shows well matching with the numerical densification strain determined by intercept method using pressure-nominal graphs at different impact velocities. Figure 9.14(b) also proved that the densification strain increased with the increasing velocity and this behavior showed a contrast with the assumption used in rigid perfectly plastic locking material model.



(a)

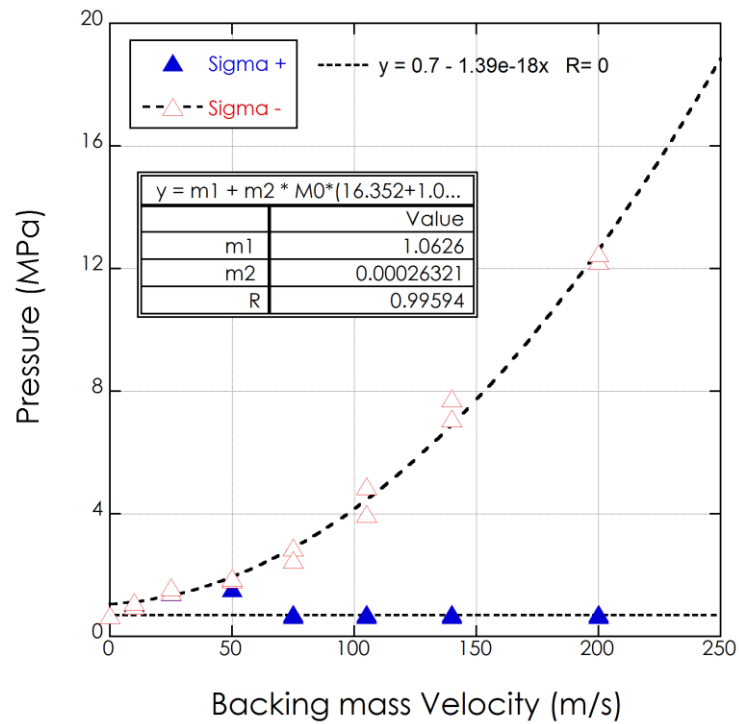


(b)

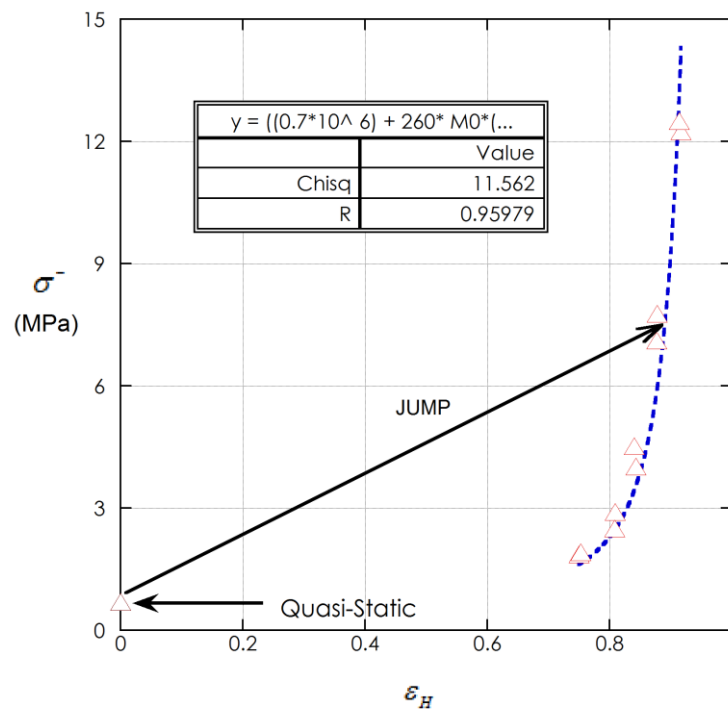
Figure 9.14. (a) Hugoniot shock speed vs. backing mass velocity and fitting and (b) variation of the densification strain with backing mass.

Equation 5.16 can be used to generate the stress-backing mass velocity (impact velocity) relationship. The stress behind the shock (at proximal end,  $\sigma^-$ ) and ahead the shock (distal end,  $\sigma^+$ ) are shown as function of velocity in Figure 9.15(a) together with the simulation stresses. The proximal end responses for both direct and stationary impact simulations display a quadratic increase with increasing impact velocity. However, the distal end responses below the critical impact velocity are higher than the quasi-static responses. On the other hand, above the critical impact velocities, the distal end is under the effect of elastic wave since the response remains constant up to densification region. The analytical fit satisfies a good agreement with both direct and stationary impact numerical simulations. A straight line can be constructed between the initial and final states of the compression wave if the Hugoniot jump conditions are satisfied for the entire loading conditions. This straight line is called the Rayleigh line and the Rayleigh line for 140 m/s is shown in Figure 9.15(b). The slope of the Rayleigh line can also be used to evaluate the shock speed. The Eqn. 5.18 is plotted as dashed line in the same figure. It was found that the stress and strain measurement from direct and stationary numerical simulations satisfies well agreement with the Hugoniot shock equation above the critical impact velocities. The analytically calculated pressure-time responses of the corrugated structure with a backing mass and using numerically calculated densification and Hugoniot strains obtained from fits are drawn for 105, 140 and 200 m/s sequentially in Figures 9.16(a-c). The r-p-p-l model using numerically determined densification and Hugoniot strains are able to catch the average pressure response of the numeric simulations. At 105 and 140 m/s, the r-p-p-l model with numerically determined densification strain results in higher pressure, while at 200 m/s very much similar pressure with the r-p-p-l model with the Hugoniot strains. The discrepancies between the analytical models and the simulation may be due to lateral inertia of the strut-like elements that is opposed and delayed the onset of the primary deformation mode of bending. In the analytical model, the material is assumed to yield at a constant yield stress and the inertia effects are neglected. The analytic and numerical velocity-time response of corrugated projectiles with a backing mass are shown in Figure 9.17 for three impact velocities. The analytical model only predict the solution up to the arrest time compared with the numerical simulation. This discrepancy occurs due to the projectile mass and backing mass ratio. When the backing mass is higher than the mass of the projectile, mass the ratio becomes smaller than 1 and the

velocity reduction curve becomes linear. However, when this ratio is higher than 1, the velocity reduction curve becomes parabolic [7].

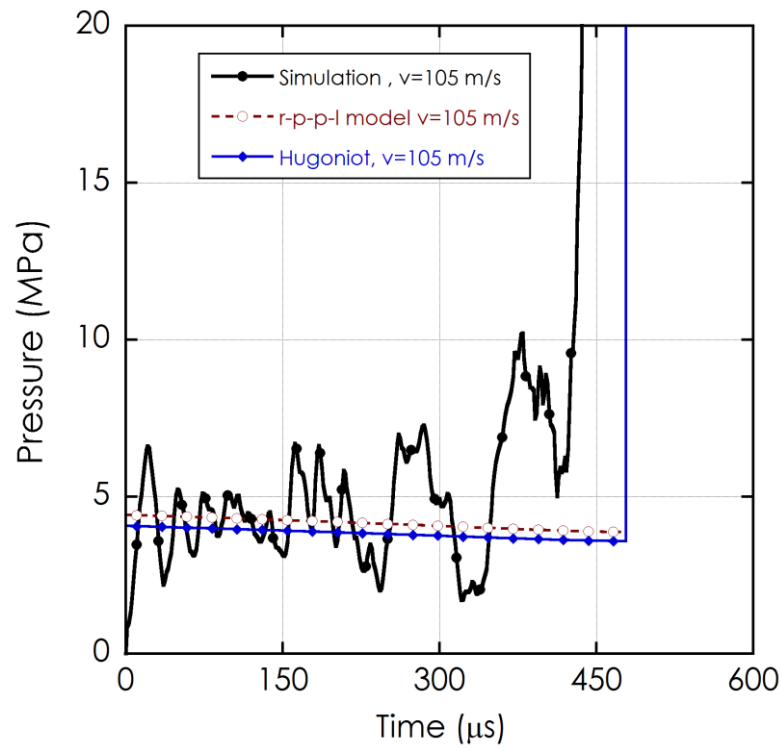


(a)

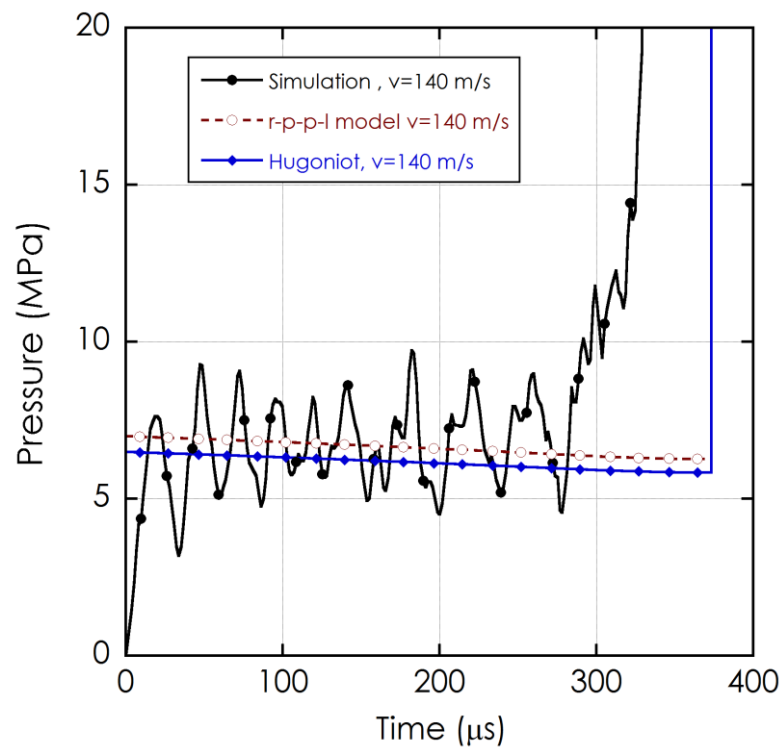


(b)

Figure 9.15. (a) Hugoniot stress-backing mass velocity and (b) Hugoniot stress-strain plot and Rayleigh line for 140 m/s impact velocity.



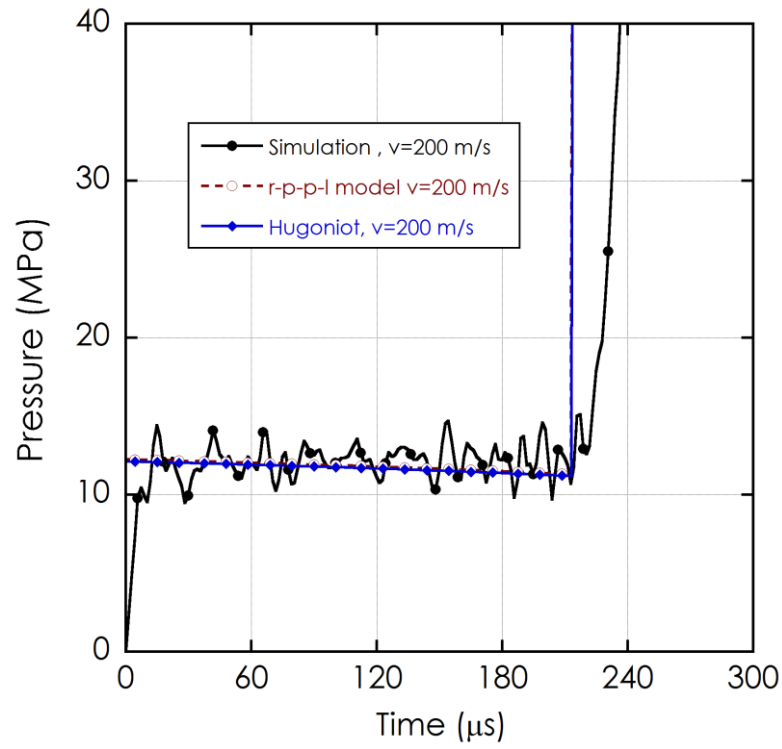
(a)



(b)

Figure 9.16. Numeric and analytic pressure-time response impact with a backing mass at (a) 105, (b) 140 and (c) 200 m/s.

(cont.on next page)



(c)

Figure 9.16. (cont.)

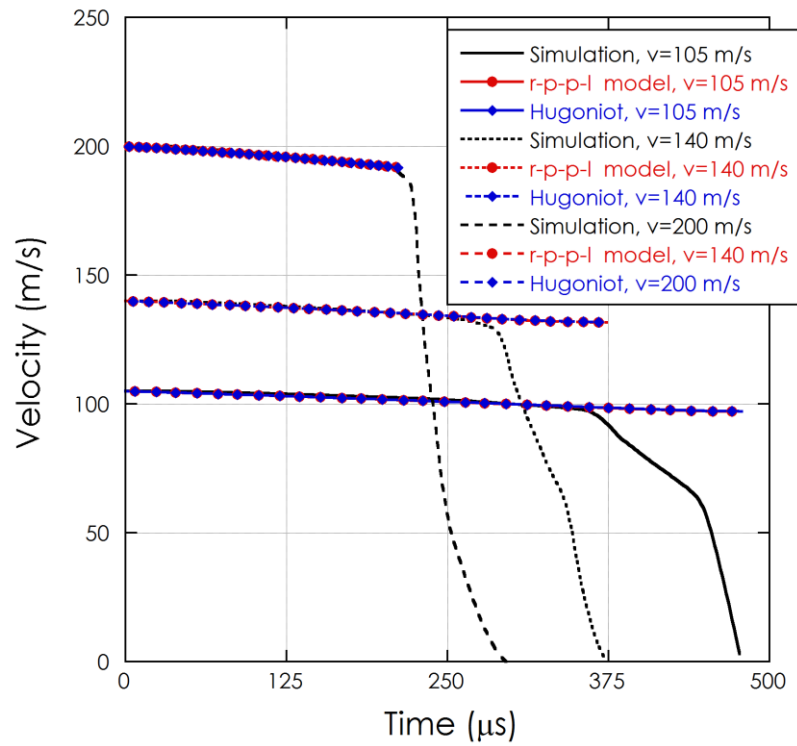


Figure 9.17. Numeric and analytic residual velocities of corrugated projectiles with backing mass.

## CHAPTER 10

### IMPACT TESTS ON CLAMPED COMPOSITE PLATES AND SANDWICH STRUCTURES

#### 10.1. Experimental, Numerical and Analytical Solutions of Blast-Like Loading of Composite Plates and Sandwich Structures

The clamped monolithic and sandwich plates were loaded using corrugated structures with and without face sheets as projectile. The impacts were tried to be as possible as close to the center of the clamped plate. The deformation was recorded using a high speed camera. The midspan deflections of the samples were measured by taking the specimen holder back surface as reference. The experiments were compared with the numerical models to validate the numerical model results. The numerical simulations were implemented to determine the mid-span deflections of plates and sandwiches above and below the critical impact velocities. Conwep blast simulations were performed on the composite plates and sandwich structures to compare the mid-span deflections with corrugated projectile loaded plates and sandwiches. In the analytical section, the approximate circumscribing and inscribing yield criteria were applied to the plates and sandwich structures to obtain the upper and lower bounds of the maximum deflections. Finally, comparative studies were carried out to investigate the performances of square monolithic plates and square sandwich plates with the same mass per unit area.

#### 10.2. Impact Tests Using Corrugated Core Sandwich as Projectile

High speed camera records of the projectile impact tests of the monolithic 2-, 5- and 8-mm thick composite plates with different thicknesses are shown for the initial stage of projectile contact (1), projectile contact (2) and final stage of the projectile contact (3) in Figures 10.1 (a-c), respectively. In all test, a spark flash is observed in the initial contact of the projectile with the plate (Figures 10.1(a-c)). This spark is due to the friction between the projectile and plates which produces heat. It is also noted that at the

same velocity the deformation of the projectile intensifies as the thickness of the plate increases and the corrugated projectile fully densifies when 8 mm-thick plate is tested (Figure 10.1(c)). The backward displacement of the plates decreases with increasing plate thickness. Furthermore, the deformation zone (delamination zone) becomes smaller as the thickness of the plate increases. The experimentally measured maximum back face deflections of the composite plates and the impact parameters for projectiles with and without face sheets are tabulated in Tables 10.1 and 10.2, respectively. As the initial momentum of the projectiles with face sheet is noted to be higher, hence, a higher deflection of the composite is measured in these tests.

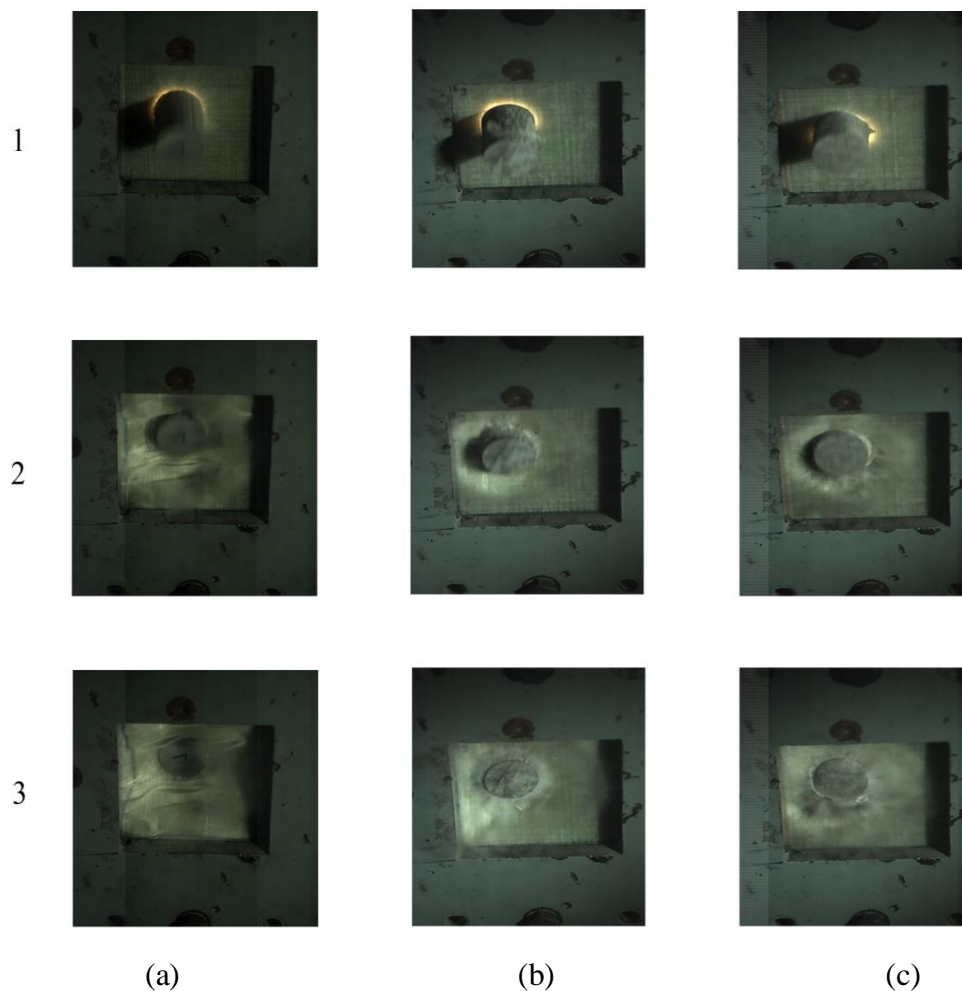


Figure 10.1. High speed camera record of the monolithic composite plates loaded with corrugated projectiles; (a) 2, (b) 5 and (c) 8 mm-thick.

Table 10.1. The parameters of the projectile (with face sheets) impact of composite plates.

<b>Projectile with Face Sheets</b>						
<b>Specimen</b>	<b>Type</b>	<b>Initial Momentum (kNsm<sup>-2</sup>)</b>	<b>Projectile Density (kg/m<sup>3</sup>)</b>	<b>Projectile Length (mm)</b>	<b>Impact Velocity (m/s)</b>	<b>Maximum Deflection (mm)</b>
2 mm	Plate	3.55	320	50	222	45
2 mm	Plate	3.69	320	50	231	48
5 mm	Plate	3.14	320	50	196.27	19
5 mm	Plate	3.54	320	50	221.85	21.5
8 mm	Plate	3.15	320	50	197.24	8.5
8 mm	Plate	3.56	320	50	222.23	12.4

Table 10.2. The parameters of the projectile (without face sheets) impact of composite plates.

<b>Projectile without Face Sheets</b>						
<b>Specimen</b>	<b>Type</b>	<b>Initial Momentum (kNsm<sup>-2</sup>)</b>	<b>Projectile Density (kg/m<sup>3</sup>)</b>	<b>Projectile Length (mm)</b>	<b>Impact Velocity (m/s)</b>	<b>Maximum Deflection (mm)</b>
2 mm	Plate	2.56	260	48	205.34	31
2 mm	Plate	2.85	260	48	228.31	34
5 mm	Plate	2.50	260	48	200.40	12.5
5 mm	Plate	2.78	260	48	222.97	14.9
8 mm	Plate	2.49	260	48	200.20	6.2
8 mm	Plate	2.87	260	48	229.62	9.8

High speed camera records of the projectile impact tests of sandwich plates with single and 3-layer corrugated core are shown for the initial stage of projectile contact (1), projectile contact (2) and final stage of the projectile contact (3) in Figures 10.2 (a-b), respectively. The core crushing of the projectile and impulse transfer from the projectile to the sandwich structure is seen at the instant of the projectile contact (2). At this moment, the front face sheet of the sandwich gains an acceleration with the kinetic energy transfer and this acceleration motion causes the crushing of the big fin corrugated core layers. Until the velocity of the projectile gets rest, the loading of the

sandwich structure continues and the faces sheets show maximum back and front face displacements as seen in 3 of Figure 10.2.

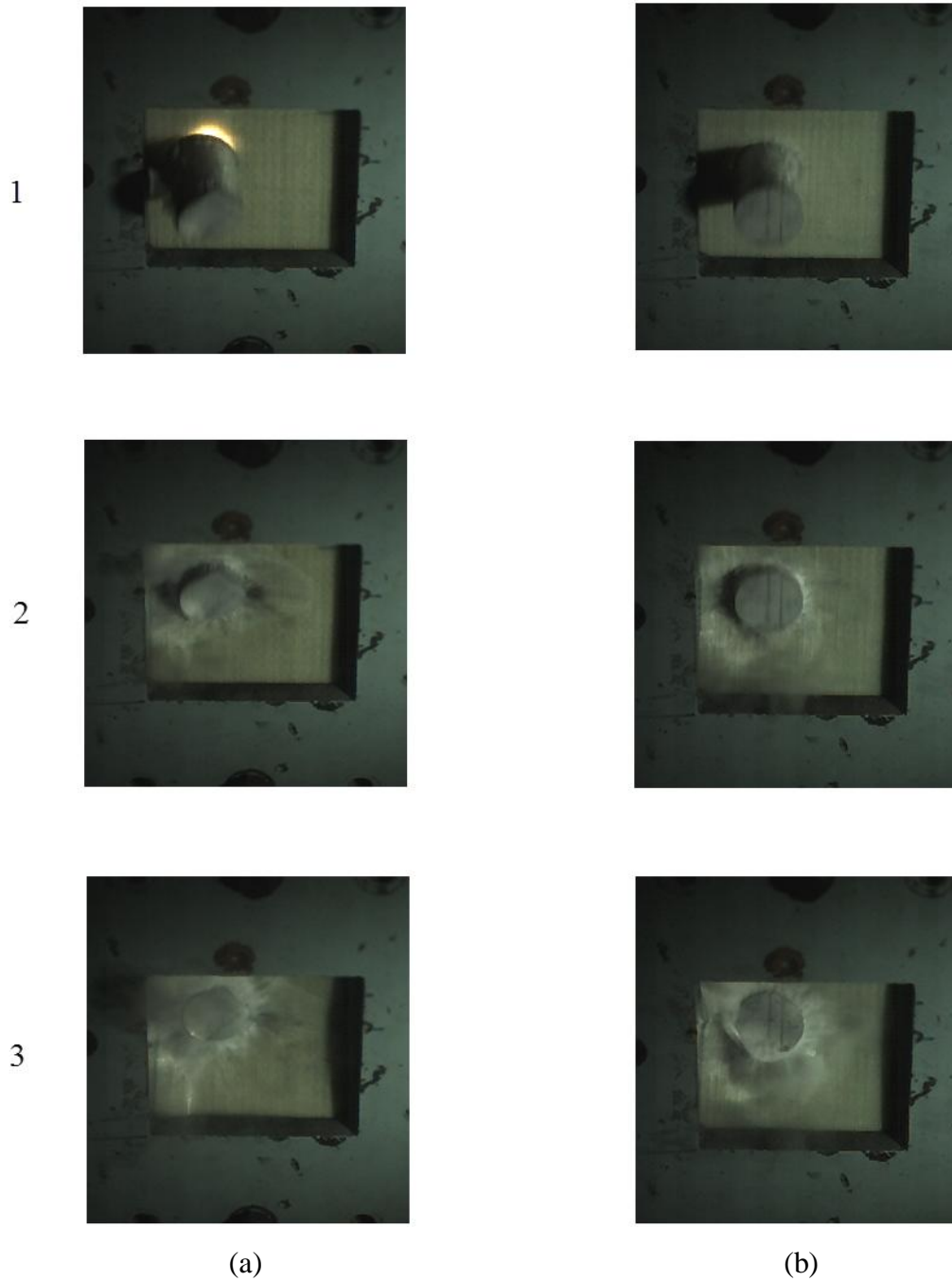


Figure 10.2. Projectile impact loading of sandwich structures with: (a) single layer corrugated core and (b) 3-layer corrugated cores.

The pictures of the sandwich structures after the impact loading are shown in Figures 10.3(a-c) shown sequentially for single layer core, 3-layer core and single and 3-layer core together. Both single and 3-layer core sandwiches are loaded with the same projectile impact velocity of 197.53 m/s. The post-test examination of the specimen show that when the clamping is removed the front and back face sheet return approximately to their original shape. However, significant core crushing is seen for the single layer sandwich structure ( $\sim 0.81$  strain) in Figure 10.3(a). It is also concluded that following the core crushing, the core is pushed through the front face sheet by the stored kinetic energy in the back face sheet during the energy release stage. The final corrugated core crushing of 3-layer corrugated core sandwich is less than the single layer sandwich ( $\sim 0.69$  strain) as seen in Figure 10.3(b). The amount of imported impulse to the back face sheet in 3-layer sandwich is less than that in the single layer sandwich (Figure 10.3(c)). In 3-layer corrugate core sandwich the extent of core crushing and back face sheet displacement is reduced comparatively. The deformation of the impact zone in sandwich plates could not be examined as the cores are damaged during cutting process. The back face sheet displacement of the sandwich structures could not also be measured due to the clamping and after the test the structures are returned to its original shape.

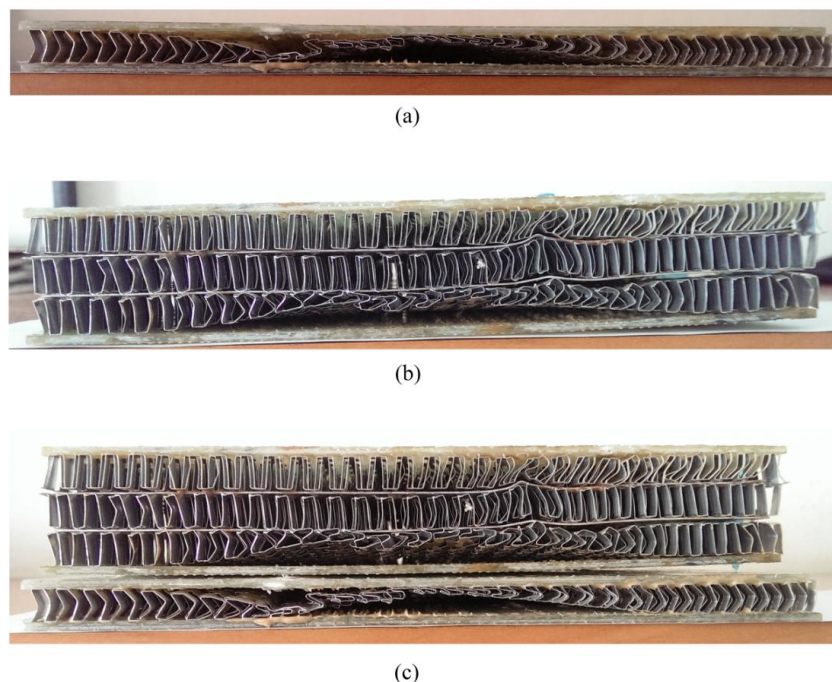


Figure 10.3. The pictures of the sandwich structures after impact test: (a) single layer core, (b) 3-layer core and (c) single and 3-layer core together.

### 10.3. Blast-Like Loading of Plates and Sandwich Structures

The experimental and numerical delamination deformation pictures of composite plates of 2, 5 and 8 mm-thick are shown sequentially in Figures 10.4(a-f). The delamination area was approximately calculated by drawing rectangles covering the delamination zones. In 2 mm thick composite plates, the experimental delamination area (Figure 10.4(a)) is 26505 mm<sup>2</sup> and in the numerical delamination zone area (Figure 10.4(b)) is 26243 mm<sup>2</sup>. The discrepancy is ~1%. In 5 mm-thick composite plates, the experimental delamination area (Figure 10.4(c)) is 22436 mm<sup>2</sup> and the numerical delamination area (Figure 10.4(d)) is 21880 mm<sup>2</sup> and the discrepancy is ~2.48%. In 8 mm-thick composite plates, the experimental delamination area (Figure 10.4(e)) is 21390 mm<sup>2</sup> and in the numerical delamination area (Figure 10.4(f)) is 20727 mm<sup>2</sup> and the discrepancy is ~3.1%. The experimental and numerical maximum displacement values of the composite plates loaded with and without face sheets are listed in Tables 10.3 and 10.4, respectively. The impact location on the composite plate in the numerical models are set to be the same with the experiments at the same impact velocity. The displacement measurements are directly taken using a ruler from the composite plates before they are removed from specimen holder so the precision of the measurement may be low. However, it is seen that the numerical displacement values are in good agreement with the experimental values with a maximum error of 17.45%.

The experimental and numerical delamination deformation pictures of single layer sandwich plate are shown in Figures 10.5(a-c). The front face delamination is seen for both experimentally and numerically tested sandwich Figure 10.5(a). The experimental delamination area (Figure 10.5(a)) is 18200 mm<sup>2</sup> and the numerical delamination area (Figure 10.5(a)) is 19044 mm<sup>2</sup>. The discrepancy between experiment and simulation is ~4.64%. The delamination zone in the back face sheet in sandwich is smaller than the delamination zone in the front face as shown in Figure 10.5(b). The corrugated core is crushed experimentally and numerically up to 0.81 and 0.79 strain levels with a discrepancy of ~2.47% (Figure 10.5(c)). The maximum displacement value is 9.58 mm at the impact region. The experimental and numerical front face delamination deformation of 3-layer core sandwich is shown in Figure 10.6(a). The experimental and numerical delamination area is 16380 mm<sup>2</sup> and 17526 mm<sup>2</sup>, respectively, with a discrepancy of ~6.99%. There is no back face sheet delamination in

experimentally and numerically tested 3-layer core sandwiches (Figure 10.6(b)). The corrugated core is crushed experimentally and numerically up to 0.69 strain and 0.76 strain levels with a discrepancy of ~11.1% (Figure 10.6(c)). The maximum displacement value is 8.84 mm at the impact region.

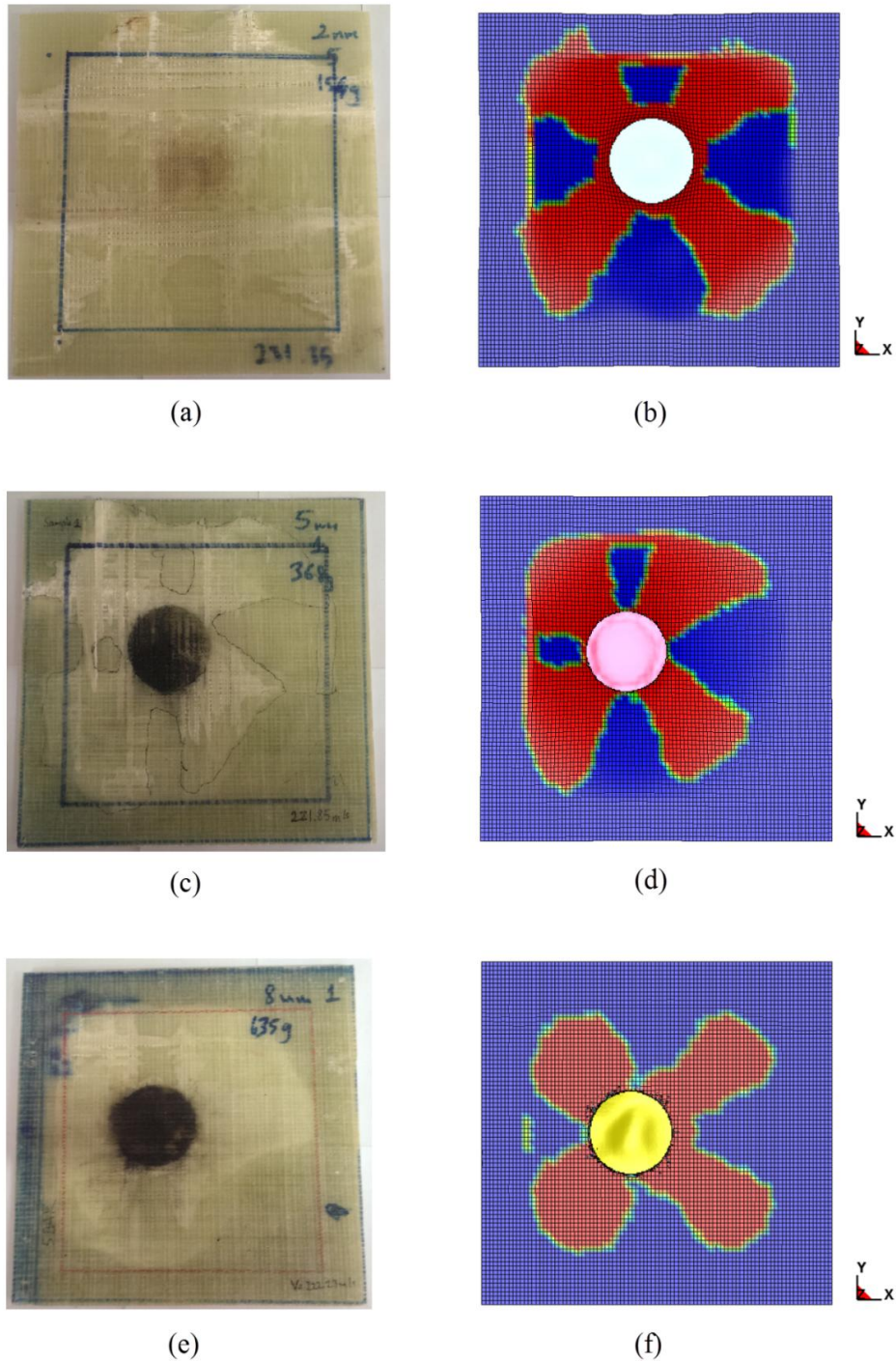


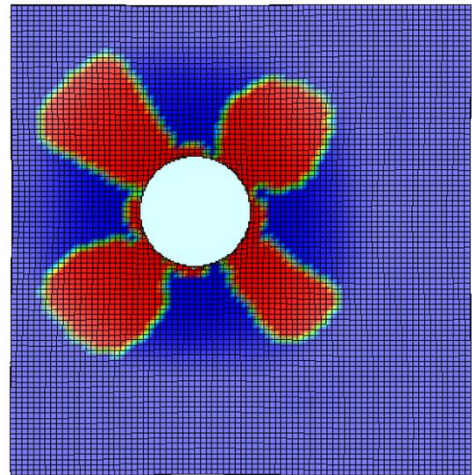
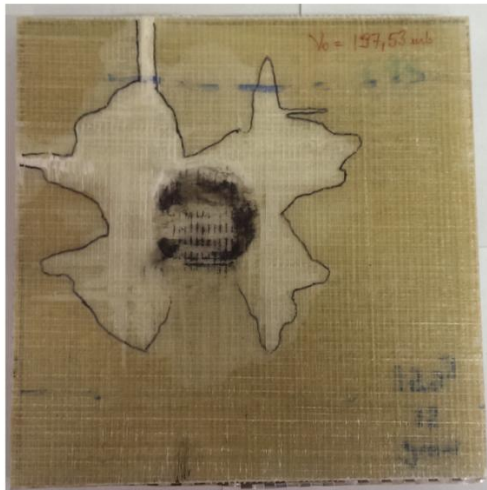
Figure 10.4. Delamination zones: (a) 2 mm experimental, (b) 2 mm numerical, (c) 5 mm experimental, (d) 5 mm numerical, (e) 8 mm experimental and (f) 8 mm numerical.

Table 10.3. Numerical and experimental back face sheet displacements of the composite plates.

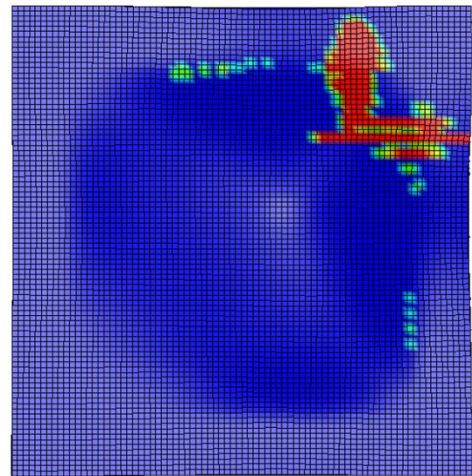
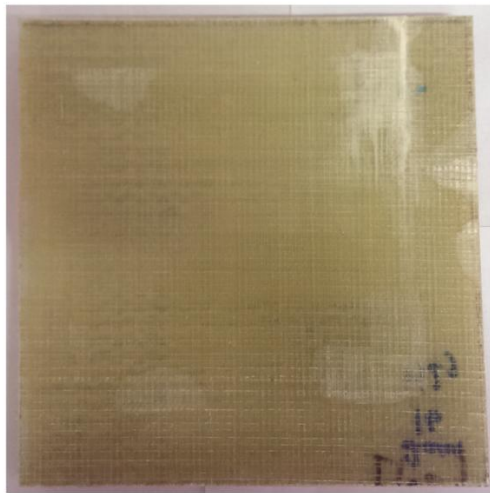
<b>Projectile with Face Sheets</b>					
<b>Specimen</b>	<b>Type</b>	<b>Impact Velocity (m/s)</b>	<b>Experimental Deflection (mm)</b>	<b>Numerical Deflection (mm)</b>	<b>Error (%)</b>
2 mm	Plate	222	45	46.34	2.97
2 mm	Plate	231	48	51.84	8
5 mm	Plate	196.27	19	17.18	9.58
5 mm	Plate	221.85	21.5	21.29	0.98
8 mm	Plate	197.24	8.5	8.63	1.47
8 mm	Plate	222.23	12.4	11.82	4.68

Table 10.4. Numerical and experimental back face sheet displacements of composite plates.

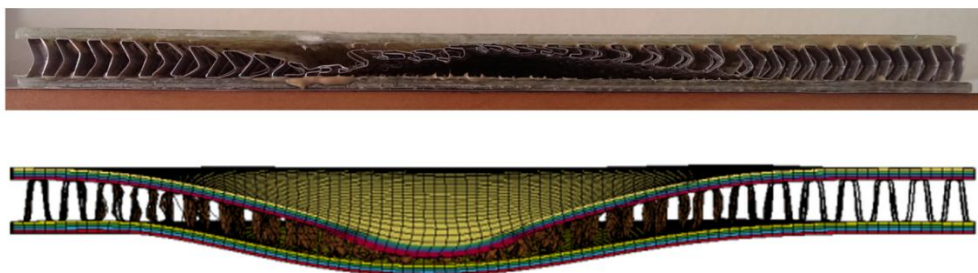
<b>Projectile without Face Sheets</b>					
<b>Specimen</b>	<b>Type</b>	<b>Impact Velocity (m/s)</b>	<b>Experimental Deflection (mm)</b>	<b>Numerical Deflection (mm)</b>	<b>Error (%)</b>
2 mm	Plate	222	31	31.99	3.19
2 mm	Plate	231	34	35.71	5.04
5 mm	Plate	196.27	12.5	11.90	4.77
5 mm	Plate	221.85	14.9	12.30	17.45
8 mm	Plate	197.24	6.2	5.72	7.73
8 mm	Plate	222.23	9.8	8.25	15.73



(a)

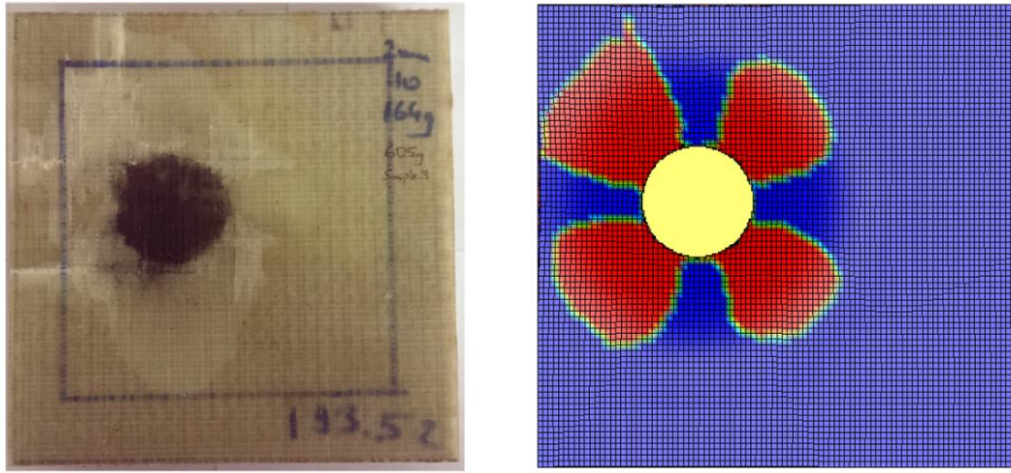


(b)

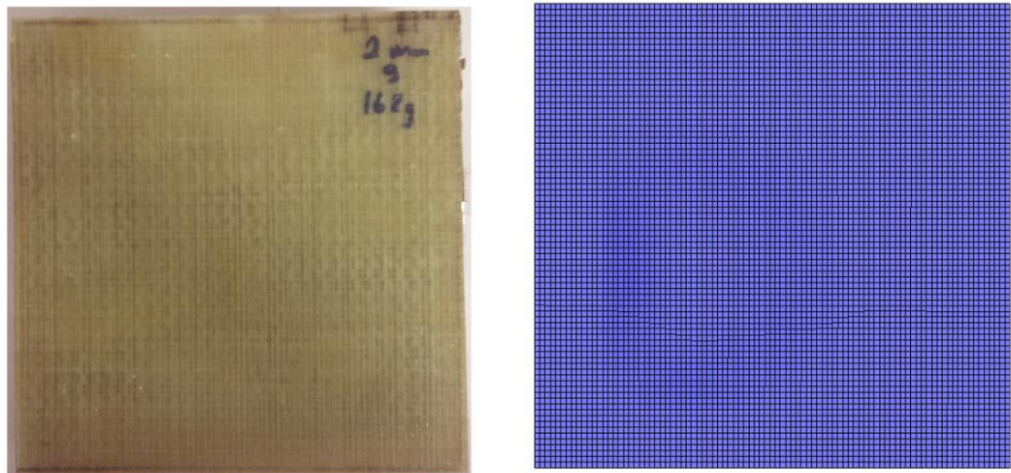


(c)

Figure 10.5. Delamination regions in: (a) front face, (b) back face of the sandwich structure and (c) crushed corrugated cores.



(a)



(b)



(c)

Figure 10.6. Delamination regions in 3 layers core sandwich: (a) front face, (b) back face of the sandwich structure and (c) crushed corrugated cores.

The composite plates and sandwich structures were also loaded from the midspan of the targets in order to compare with the analytical solutions since the analytical solutions are based on the midspan loading. All the targets were subjected to corrugated projectiles with and without face sheets at the impact velocities of 25, 50, 75, 100, 150 and 200 m/s. The maximum displacement values were used to compare the response of the structures. Furthermore, equivalent blast loading with Conwep option was used to compare the displacement values with the corrugated projectiles. The equivalent TNT mass with a 0.5 m stand-off distance was calculated for each of the impact velocities by considering the crushing stress of the projectiles obtained from the SHPB numerical simulations run at the same impact velocities. The numerical models of targets loaded with corrugated projectiles from the midspan are shown in Figures 10.7(a-c).

The maximum back face displacement of composite plates and sandwich structures loaded with corrugated projectiles with face sheet is shown in Figures 10.8. As is expected 2 mm-thick composite has the highest displacements at all impact velocities. On the other side, 5 mm-thick composite plate and its mass equivalent single layer corrugated core sandwich structure has very much the same displacements up to 50 m/s impact velocity. For example, 5 mm-thick composite plate has 2.4886 mm midspan deflection and the 1 layer corrugated core sandwich structure has 2.7630 mm displacement at 25 m/s impact velocity. At higher impact velocities, the sandwich structure performs better than the composite plate in terms of deflection. At 200 m/s impact velocity, the sandwich structure has 45.93% lower back face displacement than the composite counterpart. Similarly, 8 mm thick composite plate and its mass equivalent 3-layer corrugated core sandwich structure have similar responses up to 100 m/s impact velocity. At the impact velocities higher than 100 m/s, the sandwich structure performs better than the composite plate. At 200 m/s impact velocity the sandwich structure has 37.92% lower back face displacement than composite counterpart. The maximum back face displacement of composite plates and sandwich structures loaded with corrugated projectiles without face sheet is shown in Figures 10.9. The displacement values of without face sheet tests are comparably lower as lower impulse generated. Again, composite has similar displacement with the corrugated core sandwich structure up to certain velocity; thereafter, the sandwich structure show lower displacements than the composite plates. The single and 3-layer core sandwich

structures have 40.52% and 38.98% lower back face displacement than composite counterpart at 200 m/s, respectively.

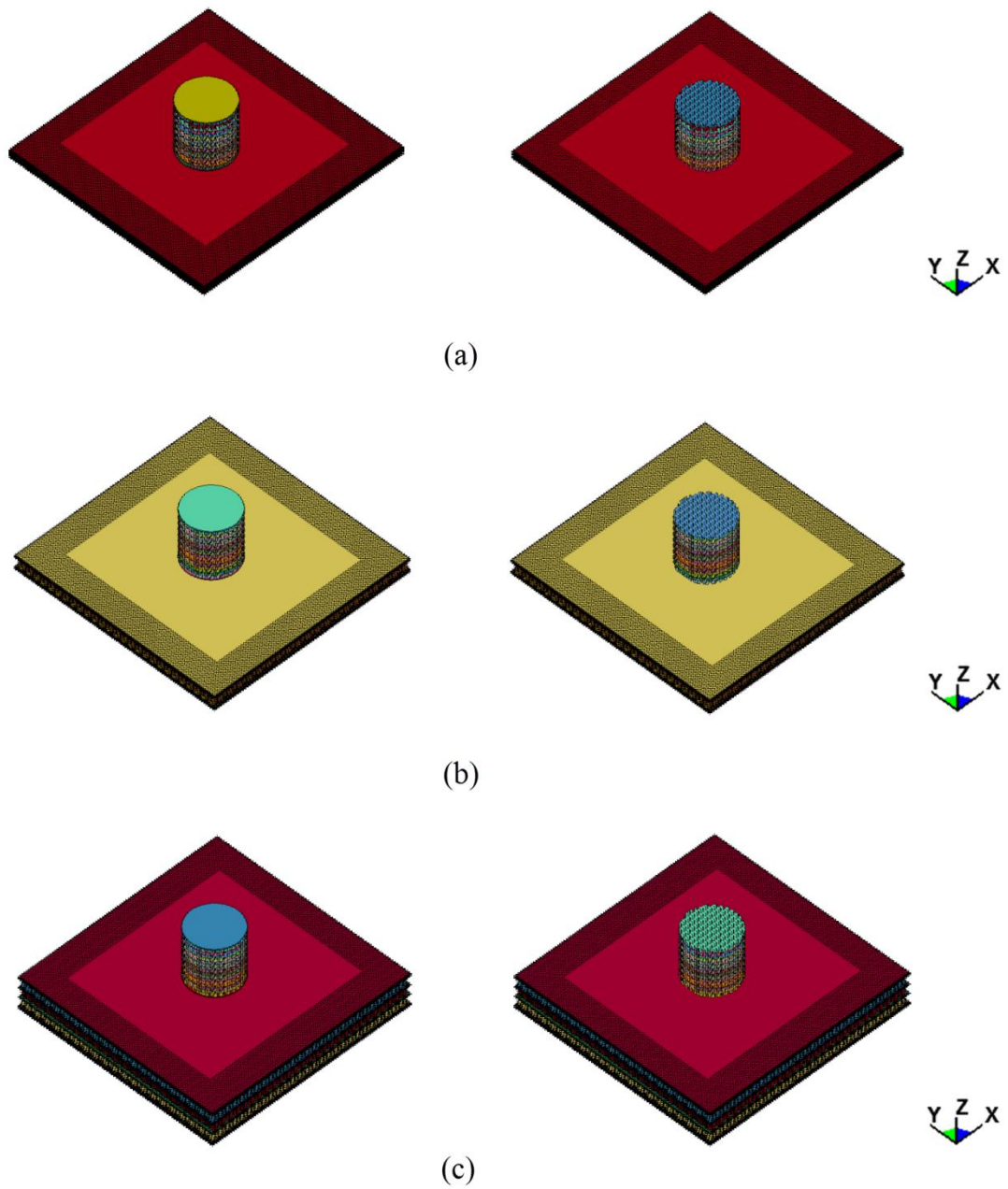


Figure 10.7. The numerical models of clamped: (a) composite plates, (b) single layer corrugated core sandwich and (c) 3-layer corrugated core sandwich structure.

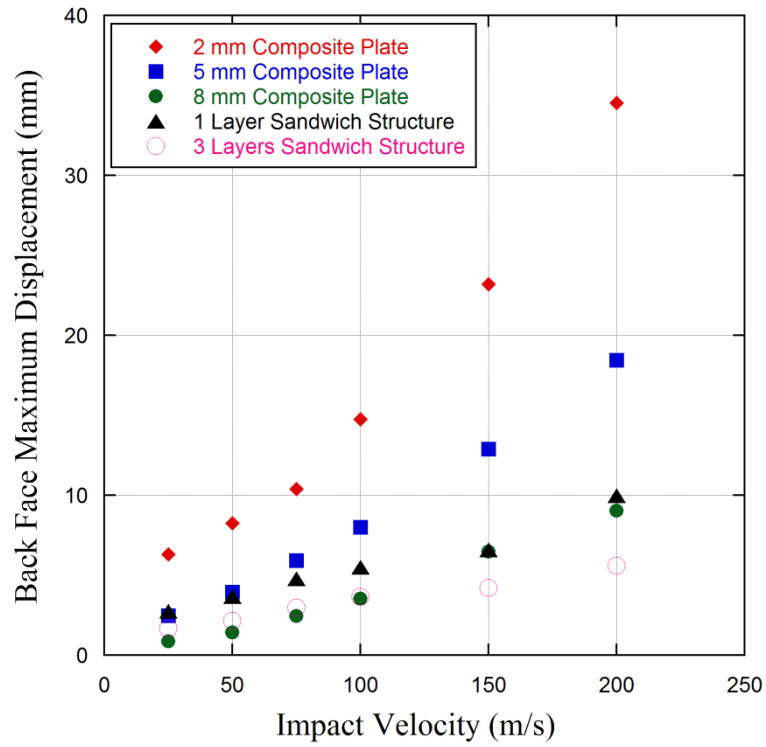


Figure 10.8. Back face maximum displacement values of composite plates and sandwich structures loaded with corrugated structures having face sheets.

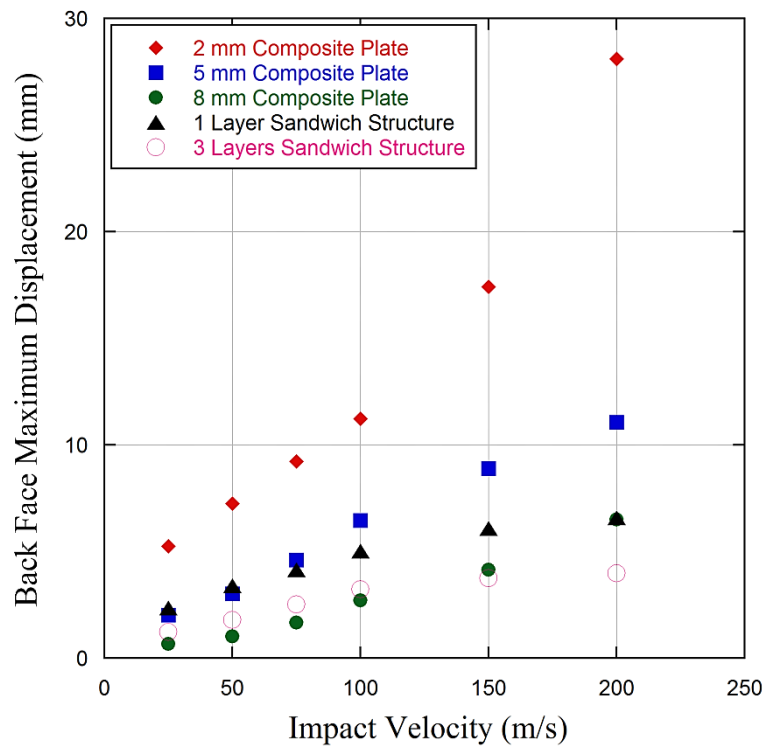


Figure 10.9. Back face maximum displacement values of composite plates and sandwich structures loaded with corrugated structures having no face sheets.

The TNT mass with a stand-off distance 0.5 m was calculated based on the projectile impact tests and simulations. In the calculations, the simulation results of impact velocities 25, 50, 75, 100, 150 and 200 m/s were used. The obtained average crushing stresses for these impact velocities were; 0.8, 1.36, 2.18, 4.21, 8.64 and 12.86 MPa, respectively. These crushing stress values were assumed to be the maximum blast pressures in the Conwep simulations and the TNT masses were found to be 0.02, 0.035, 0.06, 0.105, 0.235 and 0.4 kg for corresponding impact velocities. The TNT mass-impact velocity graph is shown in Figure 10.10. A parabolic fit shown in the same graphs gives the TNT mass-velocity relation with a high accuracy for the impact velocities up to 200 m/s. The displacement values of 2, 5 and 8 mm thick composite plates subjected to projectile impact with and without face sheets and blast simulations with Conwep are shown all together in Figure 10.11. In the same figure, it is seen that the projectiles with face sheets show a better agreement with blast simulations with respect to projectiles without face sheets. The face sheets in the simulation behave like an interface and distribute the crushing stress of the core layers to the targets. The displacements of sandwich structures with single layer and 3-layer corrugated cores subjected to projectiles with and without face sheets and Conwep blast simulations are shown in Figure 10.12. Two types of Conwep blast simulations are implemented in this figure. First, the same amount of TNT is used in the plate blast simulations, but this over estimates the displacements. In modified Conwep blast simulations, the crushing stress of the projectile is obtained from the projectile impact on sandwich structure simulations and it is noticed that the crushing stress decreases with respect to plate impact simulations. The TNT mass is calculated according to simulation results and new TNT amounts are shown in Figure 10.13. The maximum discrepancy between the projectile impact and Conwep simulations is reduced to 17.1% and 8.09% by modifying the TNT masses for single layer and 3-layer corrugated core sandwich structures, respectively. It is also noted that the projectiles without face sheets impose lower displacements compared to the projectiles with face sheet due to the lower kinetic energy. The projectile impact and Conwep blast simulation deformation pictures of 8 mm composite plate and single layer and 3-layer corrugated core sandwich structures at 100 m/s are shown in Figure 10.14. The projectile impact simulations show good agreements with the Conwep blast simulations. In projectile test, the pressure effecting zone on the 8-mm thick plate is smaller than that of the Conwep simulations because the entire face of the plate is selected as the target in Conwep simulations. This discrepancy

changes the deformation profile of the back face of the plate while the maximum displacement values are still very close to each other. The same discrepancy can also be seen in sandwich structures.

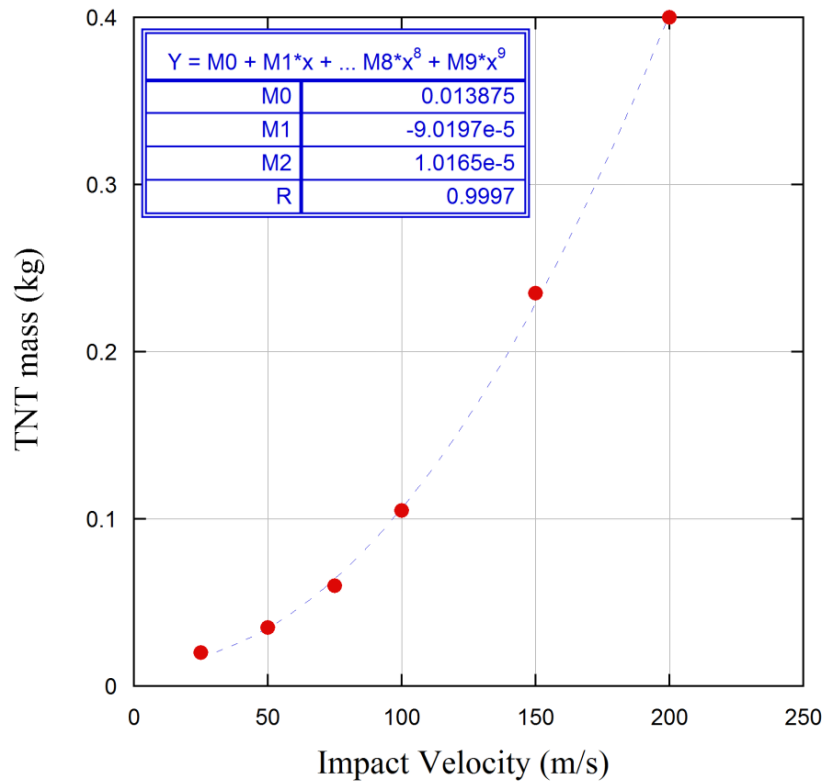


Figure 10.10. Projectile impact velocity vs. TNT mass.

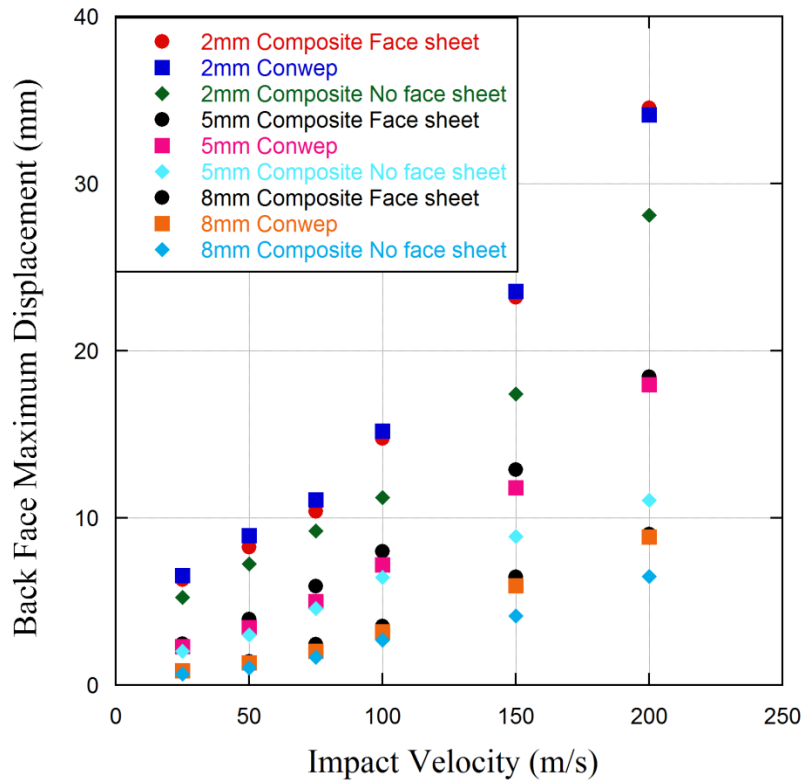


Figure 10.11. Back face displacement of composite plates loaded by projectiles and Conwep blast loading.

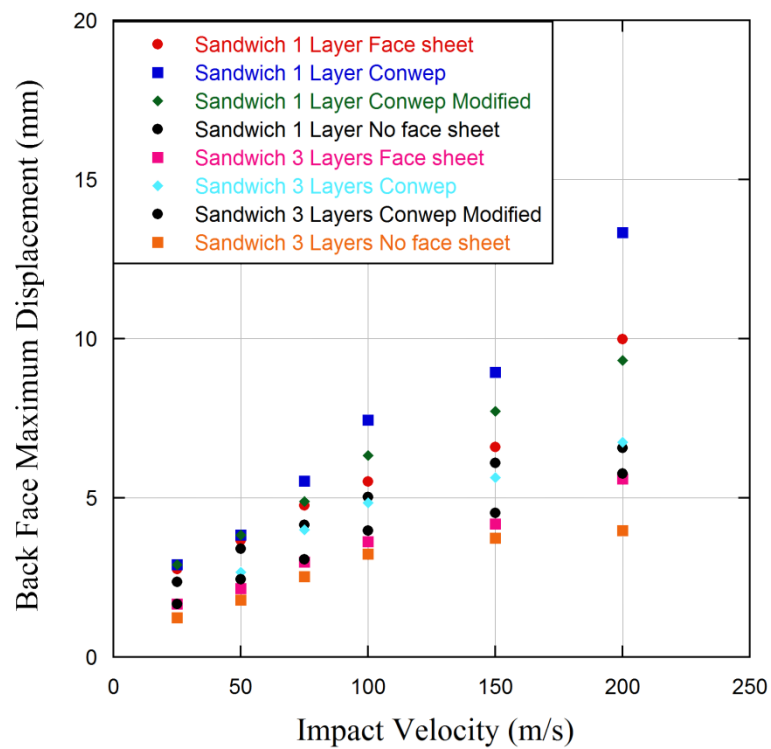


Figure 10.12. Back face displacement of sandwich structures loaded by projectiles and Conwep blast loading.

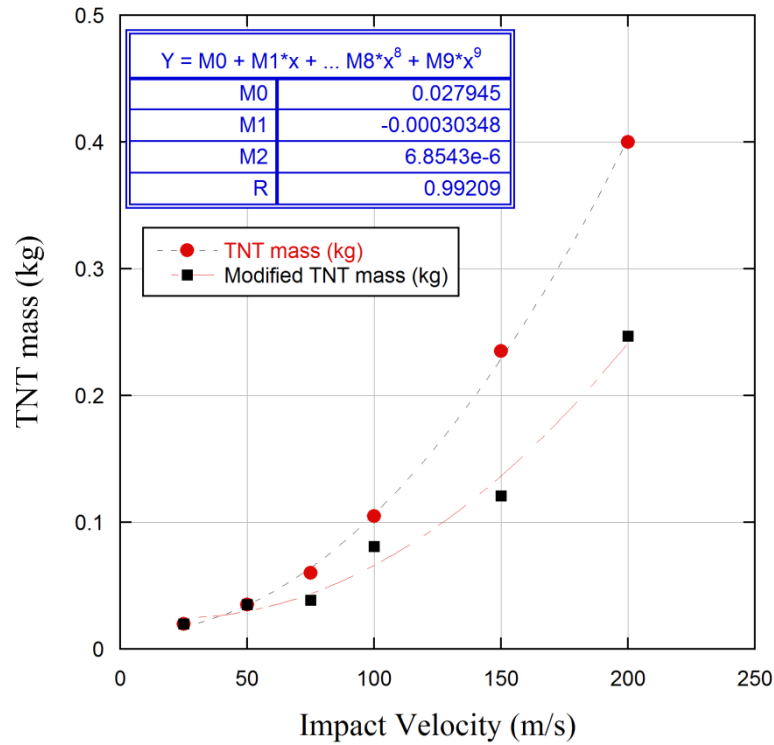


Figure 10.13. Projectile impact velocity vs. corresponding TNT mass for sandwich structures.

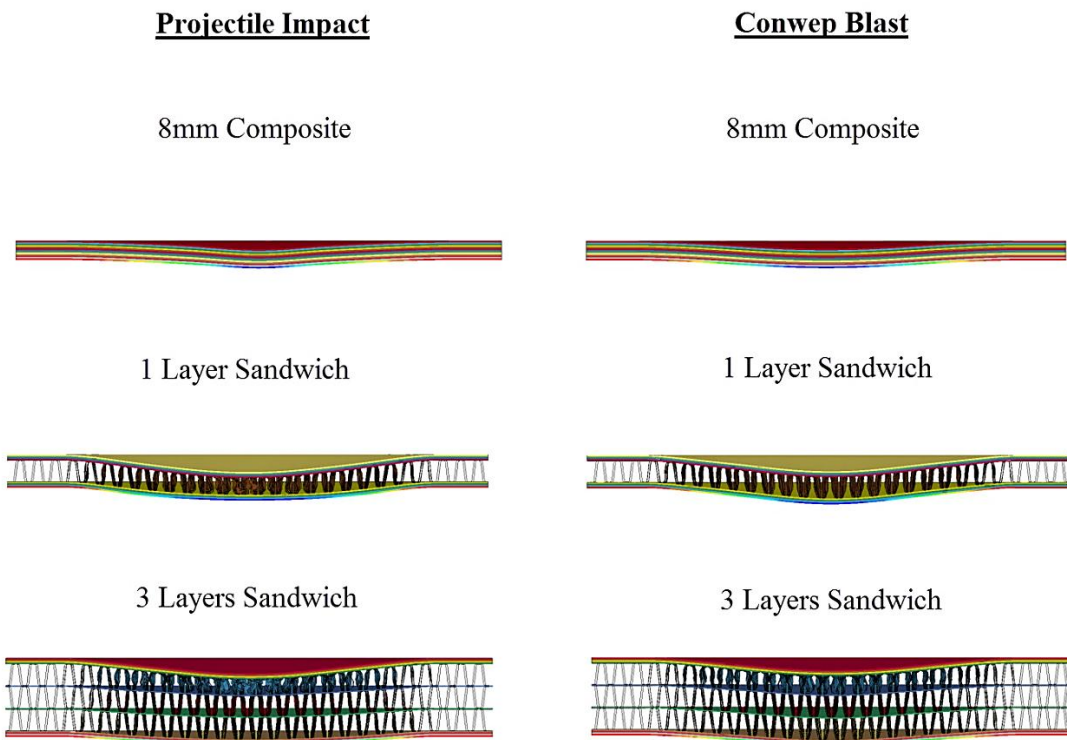


Figure 10.14. Deformation of plates and sandwich structures loaded by projectiles at 100 m/s and its equivalent TNT blast simulations.

## 10.4. Analytical Studies of Blast-Like Loaded Plates and Sandwich Structures

The mid-span maximum deflections of the plates and sandwich structures (equal mass) were calculated analytically in order to determine the upper and lower bound limits of deflections. The parameters used in the calculations are listed in Table 10.5. One dimensional wave theory is assumed and the core is treated as a rigid, ideally plastic solid with nominal crush strength up to a nominal densification strain in the calculations. The calculations were conducted in the impact velocity range of 25-200 m/s including the projectiles with and without face sheets. The upper and lower bound displacements of the composite plates loaded using the corrugated structures with and without face sheets are shown in Figures 10.15 and 10.16, respectively. In the same figures, the simulation displacements are also shown for comparison. The analytical displacement of 2, 5 and 8 mm thick composite plates loaded by projectiles with face sheets show well agreements with the simulation displacements (Figure 10.15). The simulation displacements are very close to the lower bound regions. However, the discrepancy between analytical and numerical displacements for the composite plates loaded by projectiles without face sheets increases, especially for 8 mm thick composite plate (Figure 10.16). This discrepancy is related to the deformation types of the corrugated projectiles. At the same impact velocities, the back face sheet behaves like an attached mass and causes more cores crushing with respect the projectile without face sheet. Moreover, at lower impact velocities, the number of crushed layers is fewer than the projectiles with face sheets, so the resultant displacement values become smaller than the displacement values of projectiles with face sheets. The discrepancy between the analytical and simulation displacements is found higher in sandwich plates as depicted in Figures 10.17 and 10.18. One of the main reasons of the discrepancy is that the analytical model assumes the core as a single unit but the sandwich structure in this study is composed of corrugated layers and interlayer sheets. The analytical model also neglects the elastic deformations. At low impact velocities, the impulsive loading conditions cannot be satisfied exactly in the simulations and the corrugated core deforms only in the elastic region and small amount of bending is observed up to 75 m/s for single layer sandwich and 100 m/s for 3-layer sandwich core. At velocities lower than 100 m/s the core moves with the face sheets of the sandwich with little crushing; therefore, the back face simulation deflections are higher than those of the analytical

model. When the core crush starts at higher velocities, the analytical model overestimates the deflection values as it neglects the strain hardening and strain rate sensitivity. Moreover, the model predicts the deformation at the contact area and underestimated the momentum transfer away from the loading patch. Although the analytical model for sandwich structures cannot give the exact displacement values, it can be used to predict displacements in pre-designing. Furthermore, the analytical model may have accurate results for single unit cores such as aluminum foams, honeycombs and balsa wood instead of layer of the cores using interlayer sheets.

Table 10.5. Material properties of composite plates and sandwich structures.

<b>Properties</b>	<b>Symbol</b>	<b>Value</b>
Span of beam	$2L$	150 mm
Loading segment	$2a$	48 mm
Thickness of monolithic plates	$H$	2-5-8 mm
Thickness of sandwich face sheet	$h$	2 mm
Failure strength of face sheets	$\sigma_f$	412 MPa
Density of face sheet	$\rho_f$	1850 kg/m <sup>3</sup>
Thickness of corrugated core	$h_c$	9-27 mm
Density of corrugated core	$\rho_c$	320 kg/m <sup>3</sup>
Compressive strength of big fin corrugated core	$\sigma_c$	0.4 MPa
Longitudinal tensile strength of corrugated core [98]	$\sigma_l$	0.012 MPa
Densification strain of corrugated core	$\varepsilon_d$	0.74

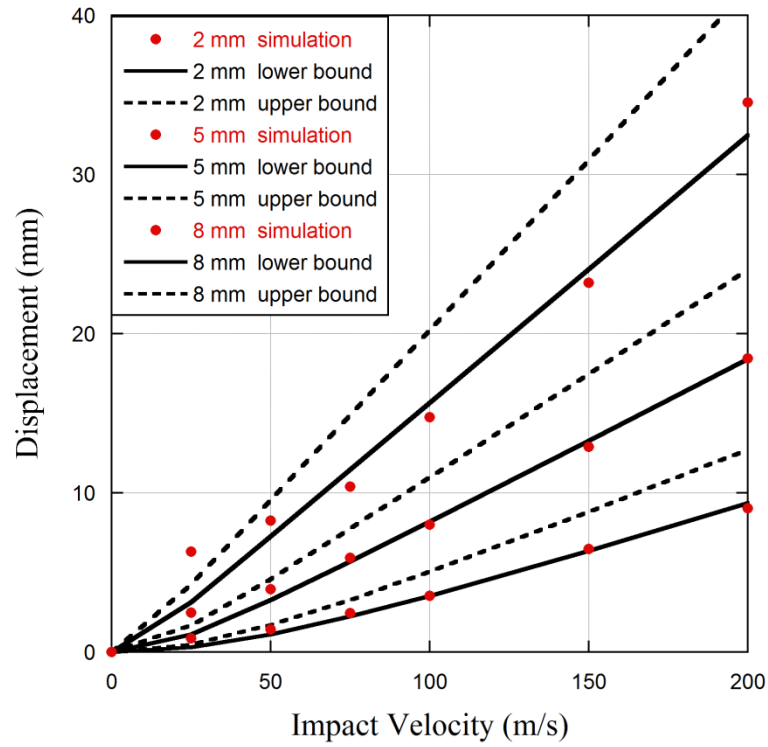


Figure 10.15. Analytical and numerical displacements of the composite plates loaded by projectiles with face sheets.

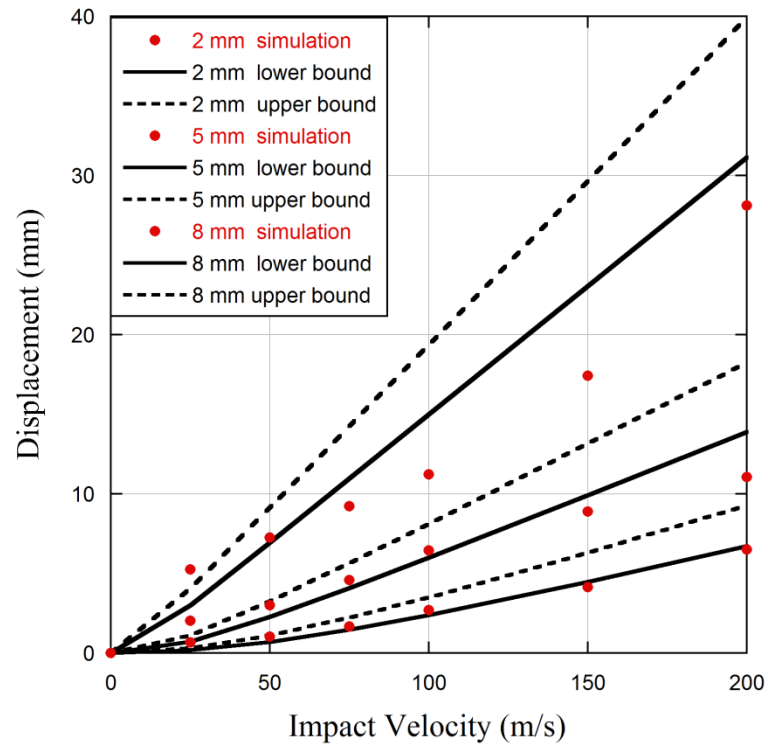


Figure 10.16. Analytical and numerical displacements of composite plates loaded by projectiles without face sheets.

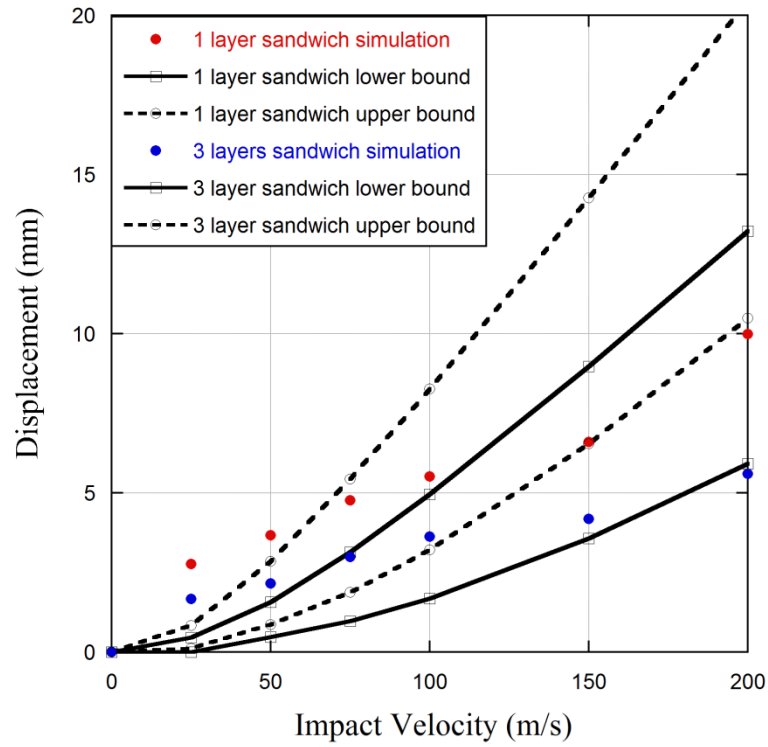


Figure 10.17. Analytical and numerical displacements of sandwich structures loaded by projectiles with face sheets.

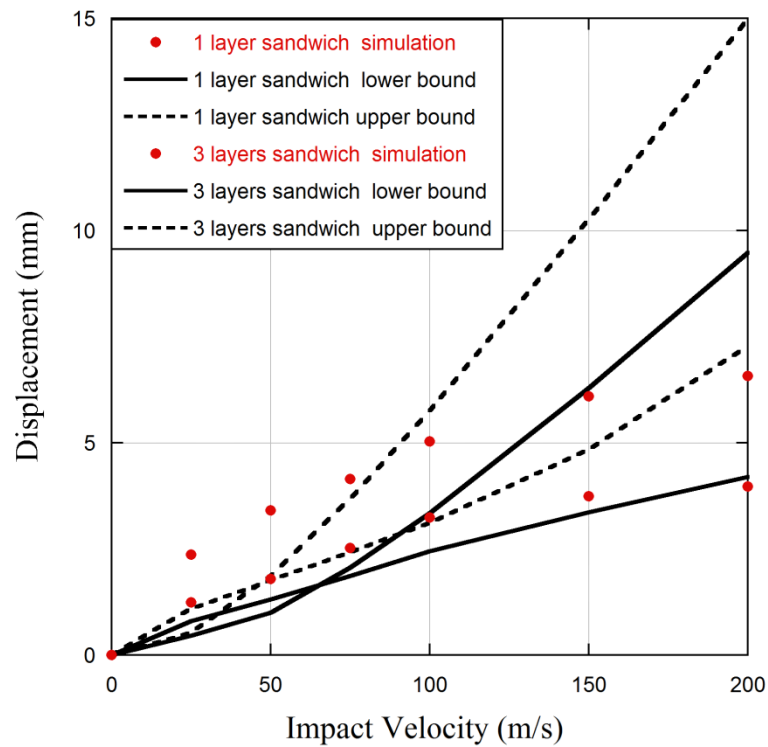


Figure 10.18. Analytical and numerical displacements of sandwich structures loaded by projectiles without face sheets.

## CHAPTER 11

### CONCLUSION

A non-explosive blast-like testing method was developed to simulate the explosive blast tests in laboratory without using explosives. In the non-explosive blast tests and simulations, E-glass/polyester composite plates and big fin corrugated core composite sandwich structures were used as targets and loaded by 1050 H14 aluminum trapezoidal small fin corrugated core sandwich projectiles. The mechanical characterization of E-glass/polyester composite was conducted in accordance with the LS-DYNA MAT\_162 material model. The corrugated core sandwich structures were impact tested using a Split Hopkinson Pressure Bar. The tests were simulated in LS-DYNA. Furthermore, the non-explosive blast-like tests of composite plates and sandwich structures were performed with a gas gun test system by launching corrugated projectiles at high velocities and the tests were numerically modeled. Finally, the experimental results and numerical results were compared with the Conwep blast simulations to validate the non-explosive blast-like testing method.

The experimental and numerical studies on the composite material were carried out to obtain the optimized MAT\_162 material model parameters. The tensile tests were conducted on both in-plane directions. The average tensile strength of the composite was found to be 400 MPa and the failure strain 0.022. The composite showed fiber fracture in warp direction and fiber pull-out in weft direction and delamination between the adjacent layers. The strain rate dependency of the composite was investigated through compression testing in all principle directions. Both elastic modulus and failure strength increased as the strain rate increased. The composite exhibited ductile failure and the failure strain increased with increasing strain rate in in-plane direction, as opposite to the through thickness direction. The specimens failed by fiber buckling and splitting in both quasi-static and dynamic in-plane compression tests while the deformation was found more severe at high strain rate tests. The deformation was matrix dominant through thickness direction and the samples showed shear type failure at an angle of 42° to the loading axis.

The numerical results showed that the resultant mechanical properties of the composite depended on the mesh size. The values of  $m$  parameters were determined by iterations and  $m_1=m_2=4$  gave the best predictions for the tension test and  $m_1=m_2=0.5$  for compression test simulations. The value of  $m_3$  was determined 0.5. The value of  $m_4$  parameter was determined through quasi-static shear test simulations and found to be -0.15. Low velocity impact tests and simulations were performed to determine OMGMX value. The results showed that OMGMX value decreased as the predicted peak load and the duration of the unloading decreased. An OMGMX value of 0.999 showed close agreements with the experiments. The values of EEXP, E\_LIMT and friction coefficients were determined based on the residual velocity of the projectile in the projectile impact tests. The EEXP and E\_LIMT increased as the back face deflection of the plates increased and the residual velocity of the projectile decreased. The best agreement with the experiments was shown when EEXP and E\_LIMT=4. The optimized MAT\_162 material model parameters were determined by both quasi-static and high strain rate tests and the parameters can be used in all static, impact, blast and strain rate sensitive loading conditions.

The quasi-static crushing of the corrugated layers started from the weakest layer and the layers crushed non-sequentially. This mechanism continued until the densification of the corrugated projectiles. The quasi-static deformation mechanism at quasi-static strain was well simulated by inducing imperfections in the perfect model geometry. The fin wall buckling applied on 6<sup>th</sup> and 12<sup>th</sup> layers and a coarse mesh size showed the stress values comparable with the experimental stress values. It was also shown that the quasi-static simulations were more imperfection sensitive than the mesh size. While, no imperfection sensitivity was detected in high strain rate tests.

In the direct impact test of the corrugated projectile, the shock wave formation and propagation started above ~50 m/s. A planar shock wave propagated from the impact side to the free side. The existence of plastic shock waves in corrugated sandwich structures revealed that the energy dissipated within a shock front significantly exceeded the quasi-static energy absorption within the corrugated projectile and this energy absorption increased with increasing impact velocity. The face sheets in the projectiles increased the initial contact pressure and the number of crushed cores due to the backing mass effect of back face sheet. The thickness of the face sheets also effected the initial contact pressure, increasing the thickness of the face sheets increased the initial contact pressure. Increasing the number of corrugated layers

increased the loading time but did not change the initial contact pressure and crushing stress. The analytical model based on the r-p-p-l material model gave inaccurate predictions of the pressure developed using a constant densification strain obtained from the quasi-static compression tests. However, it was shown that the densification strain increased with the increasing impact velocity and when this variation was applied, the analytical model showed better agreements with the experimental and numerical pressure values.

In the impact simulations with backing masses, the behavior of the corrugated projectile started to change from non-progressive to progressive or shock loading above 50 m/s. At lower velocities, the shock wave was weak and only some layers showed planar deformation and the rest of the fin layers created local bending zones similar to quasi-static behavior. However, different from the quasi-static response the material showed higher yield and plateau stresses with the enhancement of inertia for the 1 m/s impact velocity. For the velocity range of 10-50 m/s, a mixed shock and non-shock behavior was obvious. The proximal end responses for this range increased for low strain values and the distal ends had stress values close to the yield limit for low strains showing a very weak shock behavior. The Hugoniot shock equations were applied to corrugated sandwich projectiles and well agreements with the numerical results were found.

The plates and sandwich structures were loaded by corrugated sandwich projectiles with and without face sheets at different impact velocities both experimentally and numerically. The projectiles with face sheets showed better agreements with the Conwep blast simulation displacements. Although the projectiles without face sheets underestimated the Conwep displacements, they can still be used to simulate the blast like loading of structures. The analytical solutions also showed well agreements with the numerical simulations but discrepancies were seen for the sandwich structures.

This thesis showed that the corrugated core sandwich structures can generate shock loading as in the explosive blast tests and can be used to produce shock loads in laboratory scale experiments. As future work, different unit fin and sandwich geometries can be investigated to generate planar shock waves. Furthermore, the localized effect of corrugated sandwich structures can be enlarged to global effects by using multiple projectiles attached on rigid surface and this application may be used on blast-like loading of large size plates and sandwich structures.

## REFERENCES

- [1] Internet. (15.09.2015). *A Cougar mine-resistant ambush protected vehicle (MRAP) blast testing*. Available: <http://www.peocscss.army.mil/PMMRAP.html>
- [2] M. R. Amini, J. B. Isaacs, and S. Nemat-Nasser, "Experimental investigation of response of monolithic and bilayer plates to impulsive loads," *International Journal of Impact Engineering*, vol. 37, pp. 82-89, 2010.
- [3] R. J. D'Mello, S. Guntupalli, L. R. Hansen, and A. M. Waas, *Dynamic axial crush response of circular cell honeycombs* vol. 468, 2012.
- [4] A. G. Hanssen, L. Enstock, and M. Langseth, "Close-range blast loading of aluminium foam panels," *International Journal of Impact Engineering*, vol. 27, pp. 593-618, 2002.
- [5] P. Huson, R. J. Asaro, L. Stewart, and G. A. Hegemier, "Non-explosive methods for simulating blast loading of structures with complex geometries," *International Journal of Impact Engineering*, vol. 38, pp. 546-557, 2011.
- [6] J. LeBlanc, A. Shukla, C. Rousseau, and A. Bogdanovich, "Shock loading of three-dimensional woven composite materials," *Composite Structures*, vol. 79, pp. 344-355, 2007.
- [7] D. D. Radford, V. S. Deshpande, and N. A. Fleck, "The use of metal foam projectiles to simulate shock loading on a structure," *International Journal of Impact Engineering*, vol. 31, pp. 1152-1171, 2005.
- [8] D. V. Reneer, R. D. Hisel, J. M. Hoffman, R. J. Kryscio, B. T. Lusk, and J. W. Geddes, "A Multi-Mode Shock Tube for Investigation of Blast-Induced Traumatic Brain Injury," *Journal of Neurotrauma*, vol. 28, pp. 95-104, 2011.
- [9] T. Rodriguez-Nikl, G. A. Hegemier, and F. Seible, "Blast Simulator Testing of Structures: Methodology and Validation," *Shock and Vibration*, vol. 18, 2011.
- [10] H. A. Bethe, "On the Theory of Shock Waves for an Arbitrary Equation of State," in *Classic Papers in Shock Compression Science*, J. Johnson and R. Chéret, Eds., ed: Springer New York, 1998, pp. 421-495.
- [11] E. J. Barbero, *Introduction to Composite Materials Design*, Second Edition ed.: CRC Press, 2011.

- [12] K. K. Chawla, *Composite Materials: Science and Engineering*, Third Edition ed.: Springer, 1998.
- [13] D. D. L. Chung, *Composite Materials: Science and Applications*, Second Edition ed.: Springer, 2010.
- [14] T. W. C. D. Hull, *An Introduction to Composite Materials* Second Edition ed.: Cambridge University Press, 1996.
- [15] J. N. Reddy, *Mechanics of Laminated Composite Plates and Shells Theory and Analysis*, Second Edition ed., 2003.
- [16] F. C. Campbell, *Structural Composite Materials*, First Edition ed.: ASM International, 2010.
- [17] J. D. Muzzy and A. O. Kays, "Thermoplastic vs. thermosetting structural composites," *Polymer Composites*, vol. 5, pp. 169-172, 1984.
- [18] P. K. Mallick, *Fiber-Reinforced Composites: Materials, Manufacturing, and Design*, Third ed.: CRC Press, 2007.
- [19] S. K. Mazumdar, *COMPOSITES MANUFACTURING Materials, Product, and Process Engineering*, First ed. Florida: CRC Press, 2002.
- [20] R. A. Chaudhuri, "Prediction of the Compressive Strength of Thick-Section Advanced Composite Laminates," *Journal of Composite Materials*, vol. 25, pp. 1244-1276, 1991.
- [21] D. F. Adams, R.B. Pipes, and L. A. Carlsson, *Experimental Characterization of Advanced Composite Materials*, Forth ed. Boca Raton: CRC Press, 2014.
- [22] C. H. J. Davies, E. B. Hawbolt, I. V. Samarasekera, and J. K. Brimacombe, "Constitutive behaviour of composites of AA6061 and alumina," *Journal of Materials Processing Technology*, vol. 70, pp. 244-251, 1997.
- [23] T. S. Gates and C. T. Sun, "Elastic/Viscoplastic Constitutive Model for Fiber Reinforced Thermoplastic Composites," *AIAA Journal*, vol. 29, pp. 457-463, 1991.
- [24] H. T. Hahn and S. W. Tsai, "Nonlinear Elastic Behavior of Unidirectional Composite Laminae," *Journal of Composite Materials*, vol. 7, pp. 102-118, 1973.

- [25] J. Harding and L. Dong, "Effect of strain rate on the interlaminar shear strength of carbon-fiber-reinforced laminates," *Composites Science and Technology*, vol. 51, pp. 347-358, 1994.
- [26] B. Song, W. Chen, and T. Weerasooriya, "Quasi-Static and Dynamic Compressive Behaviors of a S-2 Glass/SC15 Composite," *Journal of Composite Materials*, vol. 37, pp. 1723-1743, 2003.
- [27] T. E. Tay, H. G. Ang, and V. P. W. Shim, "An empirical strain rate-dependent constitutive relationship for glass-fibre reinforced epoxy and pure epoxy," *Composite Structures*, vol. 33, pp. 201-210, 1995.
- [28] S. V. Thiruppukuzhi and C. T. Sun, "Models for the strain-rate-dependent behavior of polymer composites," *Composites Science and Technology*, vol. 61, pp. 1-12, 2001.
- [29] T. Yokozeki, T. Ogasawara, and T. Ishikawa, "Nonlinear behavior and compressive strength of unidirectional and multidirectional carbon fiber composite laminates," *Composites Part A: Applied Science and Manufacturing*, vol. 37, pp. 2069-2079, 2006.
- [30] K. J. Yoon and C. T. Sun, "Characterization of Elastic-Viscoplastic Properties of an AS4/PEEK Thermoplastic Composite," *Journal of Composite Materials*, vol. 25, pp. 1277-1296, 1991.
- [31] H. Kolsky, "An Investigation of the Mechanical Properties of Materials at very High Rates of Loading," *Proceedings of the Physical Society. Section B*, vol. 62, p. 676, 1949.
- [32] W. W. Chen and B. Song, *Split Hopkinson (Kolsky) Bar Design, Testing and Applications*, First ed. New York: Springer, 2011.
- [33] E. Woldesenbet and J. R. Vinson, "Specimen Geometry Effects on High-Strain-Rate Testing of Graphite/Epoxy Composites," *AIAA Journal*, vol. 37, pp. 1102-1106, 1999.
- [34] G. A. Kumar P, Agarwal B.D., "Dynamic Compressive Behaviour of Unidirectional GFRF for Various Fibre Orientations," *Materials Letters*, vol. 4, pp. 111-116, 1986.
- [35] A. Gilat, R. K. Goldberg, and G. D. Roberts, "Experimental study of strain-rate-dependent behavior of carbon/epoxy composite," *Composites Science and Technology*, vol. 62, pp. 1469-1476, 2002.

- [36] M. Guden, U. Yildirim, and I. W. Hall, "Effect of strain rate on the compression behavior of a woven glass fiber/SC-15 composite," *Polymer Testing*, vol. 23, pp. 719-725, 9// 2004.
- [37] F L Matthews, G A O Davies, D Hitchings, and C. Soutis, *Finite element modelling of composite materials and structures*. Boca Raton: CRC Press, 2003.
- [38] F.-K. Chang and K.-Y. Chang, "A Progressive Damage Model for Laminated Composites Containing Stress Concentrations," *Journal of Composite Materials*, vol. 21, pp. 834-855, September 1, 1987 1987.
- [39] H. M. Elsanadedy, T. H. Almusallam, S. H. Alsayed, and Y. A. Al-Salloum, "Flexural strengthening of RC beams using textile reinforced mortar – Experimental and numerical study," *Composite Structures*, vol. 97, pp. 40-55, 3// 2013.
- [40] P. Feraboli, F. Deleo, B. Wade, M. Rassaian, M. Higgins, A. Byar, *et al.*, "Predictive modeling of an energy-absorbing sandwich structural concept using the building block approach," *Composites Part A: Applied Science and Manufacturing*, vol. 41, pp. 774-786, 6// 2010.
- [41] P. Feraboli, B. Wade, F. Deleo, M. Rassaian, M. Higgins, and A. Byar, "LS-DYNA MAT54 modeling of the axial crushing of a composite tape sinusoidal specimen," *Composites Part A: Applied Science and Manufacturing*, vol. 42, pp. 1809-1825, 11// 2011.
- [42] H. Ghasemnejad, V. R. Soroush, P. J. Mason, and B. Weager, "To improve impact damage response of single and multi-delaminated FRP composites using natural Flax yarn," *Materials & Design*, vol. 36, pp. 865-873, 4// 2012.
- [43] M. Guida and F. Marulo, "Partial Modeling of Aircraft Fuselage During an Emergency Crash Landing," *Procedia Engineering*, vol. 88, pp. 26-33, 2014.
- [44] A. G. Mamalis, D. E. Manolakos, M. B. Ioannidis, P. K. Kostazos, and D. P. Papapostolou, "Axial collapse of hybrid square sandwich composite tubular components with corrugated core: numerical modelling," *Composite Structures*, vol. 58, pp. 571-582, 2002.
- [45] A. Manes, L. M. Bresciani, and M. Giglio, "Ballistic Performance of Multi-layered Fabric Composite Plates Impacted by Different 7.62 mm Calibre Projectiles," *Procedia Engineering*, vol. 88, pp. 208-215, 2014.

- [46] A. Mosallam, H. M. Elsanadedy, T. H. Almusallam, Y. A. Al-Salloum, and S. H. Alsayed, "Structural evaluation of reinforced concrete beams strengthened with innovative bolted/bonded advanced frp composites sandwich panels," *Composite Structures*, vol. 124, pp. 421-440, 2015.
- [47] J. Obradovic, S. Boria, and G. Belingardi, "Lightweight design and crash analysis of composite frontal impact energy absorbing structures," *Composite Structures*, vol. 94, pp. 423-430, 2012.
- [48] H. Zarei, M. Kröger, and H. Albertsen, "An experimental and numerical crashworthiness investigation of thermoplastic composite crash boxes," *Composite Structures*, vol. 85, pp. 245-257, 2008.
- [49] A. Matzenmiller, J. Lubliner, and R. L. Taylor, "A constitutive model for anisotropic damage in fiber-composites," *Mechanics of Materials*, vol. 20, pp. 125-152, 1995.
- [50] Z. Fawaz, W. Zheng, and K. Behdinan, "Numerical simulation of normal and oblique ballistic impact on ceramic composite armours," *Composite Structures*, vol. 63, pp. 387-395, 2004.
- [51] J. LeBlanc and A. Shukla, "Dynamic response and damage evolution in composite materials subjected to underwater explosive loading: An experimental and computational study," *Composite Structures*, vol. 92, pp. 2421-2430, 2010.
- [52] J. LeBlanc and A. Shukla, "Dynamic response of curved composite panels to underwater explosive loading: Experimental and computational comparisons," *Composite Structures*, vol. 93, pp. 3072-3081, 2011.
- [53] C. Menna, D. Asprone, G. Caprino, V. Lopresto, and A. Prota, "Numerical simulation of impact tests on GFRP composite laminates," *International Journal of Impact Engineering*, vol. 38, pp. 677-685, 2011.
- [54] H. Mou, T. Zou, Z. Feng, and J. Ren, "Crashworthiness Simulation Research of Fuselage Section with Composite Skin," *Procedia Engineering*, vol. 80, pp. 59-65, 2014.
- [55] X. Xiao, M. E. Botkin, and N. L. Johnson, "Axial crush simulation of braided carbon tubes using MAT58 in LS-DYNA," *Thin-Walled Structures*, vol. 47, pp. 740-749, 2009.
- [56] Z. Hashin, "Failure Criteria for Unidirectional Fiber Composites," *Journal of Applied Mechanics*, vol. 47, pp. 329-334, 1980.

- [57] J. R. Xiao, B. A. Gama, and J. W. Gillespie Jr, "Progressive damage and delamination in plain weave S-2 glass/SC-15 composites under quasi-static punch-shear loading," *Composite Structures*, vol. 78, pp. 182-196, 2007.
- [58] L. Maio, E. Monaco, F. Ricci, and L. Lecce, "Simulation of low velocity impact on composite laminates with progressive failure analysis," *Composite Structures*, vol. 103, pp. 75-85, 2013.
- [59] L. J. Deka, S. D. Bartus, and U. K. Vaidya, "Multi-site impact response of S2-glass/epoxy composite laminates," *Composites Science and Technology*, vol. 69, pp. 725-735, 2009.
- [60] J. B. Jordan, C. J. Naito, and B. Z. Haque, "Progressive damage modeling of plain weave E-glass/phenolic composites," *Composites Part B: Engineering*, vol. 61, pp. 315-323, 2014.
- [61] C.-F. Yen, "A ballistic material model for continuous-fiber reinforced composites," *International Journal of Impact Engineering*, vol. 46, pp. 11-22, 2012.
- [62] A. Tasdemirci, A. Kara, A. K. Turan, G. Tunusoglu, M. Guden, and I. W. Hall, "Experimental and Numerical Investigation of High Strain Rate Mechanical Behavior of a [0/45/90/ - 45] Quadriaxial E-Glass/Polyester Composite," *Procedia Engineering*, vol. 10, pp. 3068-3073, 2011.
- [63] E. Andrews, W. Sanders, and L. J. Gibson, "Compressive and tensile behaviour of aluminum foams," *Materials Science and Engineering: A*, vol. 270, pp. 113-124, 1999.
- [64] M. F. Ashby, A. G. Evans, N. A. Fleck, L. J. Gibson, J. W. Hutchinson, and H. N. G. Wadley, "Chapter 4 - Properties of metal foams," in *Metal Foams*, M. F. Ashby, A. G. Evans, N. A. Fleck, L. J. Gibson, J. W. Hutchinson, and H. N. G. Wadley, Eds., ed Burlington: Butterworth-Heinemann, 2000, pp. 40-54.
- [65] G. J. Davies and S. Zhen, "Metallic foams: their production, properties and applications," *Journal of Materials Science*, vol. 18, pp. 1899-1911, 1983.
- [66] I. W. Hall, M. Guden, and C. J. Yu, "Crushing of aluminum closed cell foams: density and strain rate effects," *Scripta Materialia*, vol. 43, pp. 515-521, 2000.
- [67] C. J. Yu, H. H. Eifert, J. Banhart, and J. Baumeister, "Metal foaming by a powder metallurgy method: Production, properties and applications," *Material Research Innovations*, vol. 2, pp. 181-188, 1998.

- [68] E. Wu and W.-S. Jiang, "Axial crush of metallic honeycombs," *International Journal of Impact Engineering*, vol. 19, pp. 439-456, 1997.
- [69] L. Aktay, A. F. Johnson, and B.-H. Kröplin, "Numerical modelling of honeycomb core crush behaviour," *Engineering Fracture Mechanics*, vol. 75, pp. 2616-2630, 2008.
- [70] J. Kee Paik, A. K. Thayamballi, and G. Sung Kim, "The strength characteristics of aluminum honeycomb sandwich panels," *Thin-Walled Structures*, vol. 35, pp. 205-231, 1999.
- [71] C. C. Foo, G. B. Chai, and L. K. Seah, "Mechanical properties of Nomex material and Nomex honeycomb structure," *Composite Structures*, vol. 80, pp. 588-594, 2007.
- [72] G. Bartolozzi, M. Pierini, U. Orrenius, and N. Baldanzini, "An equivalent material formulation for sinusoidal corrugated cores of structural sandwich panels," *Composite Structures*, vol. 100, pp. 173-185, 2013.
- [73] S. Hou, C. Shu, S. Zhao, T. Liu, X. Han, and Q. Li, "Experimental and numerical studies on multi-layered corrugated sandwich panels under crushing loading," *Composite Structures*, vol. 126, pp. 371-385, 2015.
- [74] S. Hou, S. Zhao, L. Ren, X. Han, and Q. Li, "Crashworthiness optimization of corrugated sandwich panels," *Materials & Design*, vol. 51, pp. 1071-1084, 2013.
- [75] J. J. Rimoli, B. Talamini, J. J. Wetzel, K. P. Dharmasena, R. Radovitzky, and H. N. G. Wadley, "Wet-sand impulse loading of metallic plates and corrugated core sandwich panels," *International Journal of Impact Engineering*, vol. 38, pp. 837-848, 2011.
- [76] H. N. G. Wadley, K. P. Dharmasena, M. R. O'Masta, and J. J. Wetzel, "Impact response of aluminum corrugated core sandwich panels," *International Journal of Impact Engineering*, vol. 62, pp. 114-128, 2013.
- [77] L. L. Yan, B. Yu, B. Han, C. Q. Chen, Q. C. Zhang, and T. J. Lu, "Compressive strength and energy absorption of sandwich panels with aluminum foam-filled corrugated cores," *Composites Science and Technology*, vol. 86, pp. 142-148, 2013.
- [78] V. Rubino, V. S. Deshpande, and N. A. Fleck, "The three-point bending of Y-frame and corrugated core sandwich beams," *International Journal of Mechanical Sciences*, vol. 52, pp. 485-494, 2010.

- [79] L. St-Pierre, V. S. Deshpande, and N. A. Fleck, "The low velocity impact response of sandwich beams with a corrugated core or a Y-frame core," *International Journal of Mechanical Sciences*, vol. 91, pp. 71-80, 2015.
- [80] M. W. Joosten, S. Dutton, D. Kelly, and R. Thomson, "Experimental and numerical investigation of the crushing response of an open section composite energy absorbing element," *Composite Structures*, vol. 93, pp. 682-689, 2011.
- [81] T. Yokozeki, S.-i. Takeda, T. Ogasawara, and T. Ishikawa, "Mechanical properties of corrugated composites for candidate materials of flexible wing structures," *Composites Part A: Applied Science and Manufacturing*, vol. 37, pp. 1578-1586, 2006.
- [82] Y. S. Tian and T. J. Lu, "Optimal design of compression corrugated panels," *Thin-Walled Structures*, vol. 43, pp. 477-498, 2005.
- [83] J. Xiong, A. Vaziri, L. Ma, J. Papadopoulos, and L. Wu, "Compression and impact testing of two-layer composite pyramidal-core sandwich panels," *Composite Structures*, vol. 94, pp. 793-801, 2012.
- [84] F. Côté, V. S. Deshpande, N. A. Fleck, and A. G. Evans, "The compressive and shear responses of corrugated and diamond lattice materials," *International Journal of Solids and Structures*, vol. 43, pp. 6220-6242, 2006.
- [85] C. Kılıçaslan, M. Güden, İ. K. Odacı, and A. Taşdemirci, "Experimental and numerical studies on the quasi-static and dynamic crushing responses of multi-layer trapezoidal aluminum corrugated sandwiches," *Thin-Walled Structures*, vol. 78, pp. 70-78, 2014.
- [86] M. R. M. Rejab and W. J. Cantwell, "The mechanical behaviour of corrugated-core sandwich panels," *Composites Part B: Engineering*, vol. 47, pp. 267-277, 2013.
- [87] F. Jin, H. Chen, L. Zhao, H. Fan, C. Cai, and N. Kuang, "Failure mechanisms of sandwich composites with orthotropic integrated woven corrugated cores: Experiments," *Composite Structures*, vol. 98, pp. 53-58, 2013.
- [88] L. L. Yan, B. Han, B. Yu, C. Q. Chen, Q. C. Zhang, and T. J. Lu, "Three-point bending of sandwich beams with aluminum foam-filled corrugated cores," *Materials & Design*, vol. 60, pp. 510-519, 2014.
- [89] T. Ngo, P. Mendis, A. Gupta, and J. Ramsay, "Blast Loading and Blast Effects on Structures – An Overview," *Electronic Journal of Structural Engineering*, vol. 7, pp. 76-91, 2007.

- [90] A. S. Fallah, K. Micallef, G. S. Langdon, W. C. Lee, P. T. Curtis, and L. A. Louca, "Dynamic response of Dyneema® HB26 plates to localised blast loading," *International Journal of Impact Engineering*, vol. 73, pp. 91-100, 2014.
- [91] G. S. Langdon, W. J. Cantwell, and G. N. Nurick, "The blast response of novel thermoplastic-based fibre-metal laminates – some preliminary results and observations," *Composites Science and Technology*, vol. 65, pp. 861-872, 2005.
- [92] T. F. Henchie, S. Chung Kim Yuen, G. N. Nurick, N. Ranwaha, and V. H. Balden, "The response of circular plates to repeated uniform blast loads: An experimental and numerical study," *International Journal of Impact Engineering*, vol. 74, pp. 36-45, 2014.
- [93] M. D. Theobald, G. S. Langdon, G. N. Nurick, S. Pillay, A. Heyns, and R. P. Merrett, "Large inelastic response of unbonded metallic foam and honeycomb core sandwich panels to blast loading," *Composite Structures*, vol. 92, pp. 2465-2475, 2010.
- [94] P. Zhang, Y. Cheng, J. Liu, C. Wang, H. Hou, and Y. Li, "Experimental and numerical investigations on laser-welded corrugated-core sandwich panels subjected to air blast loading," *Marine Structures*, vol. 40, pp. 225-246, 2015.
- [95] H. N. G. Wadley, T. Børvik, L. Olovsson, J. J. Wetzel, K. P. Dharmasena, O. S. Hopperstad, *et al.*, "Deformation and fracture of impulsively loaded sandwich panels," *Journal of the Mechanics and Physics of Solids*, vol. 61, pp. 674-699, 2013.
- [96] M. Yazici, J. Wright, D. Bertin, and A. Shukla, "Experimental and numerical study of foam filled corrugated core steel sandwich structures subjected to blast loading," *Composite Structures*, vol. 110, pp. 98-109, 2014.
- [97] L. Zhang, R. Hebert, J. T. Wright, A. Shukla, and J.-H. Kim, "Dynamic response of corrugated sandwich steel plates with graded cores," *International Journal of Impact Engineering*, vol. 65, pp. 185-194, 2014.
- [98] M. R. Amini, A. V. Amirkhizi, and S. Nemat-Nasser, "Numerical modeling of response of monolithic and bilayer plates to impulsive loads," *International Journal of Impact Engineering*, vol. 37, pp. 90-102, 2010.
- [99] D. D. Radford, N. A. Fleck, and V. S. Deshpande, "The response of clamped sandwich beams subjected to shock loading," *International Journal of Impact Engineering*, vol. 32, pp. 968-987, 2006.

- [100] A. Chen, H. Kim, R. J. Asaro, and J. Bezares, "Non-explosive simulated blast loading of balsa core sandwich composite beams," *Composite Structures*, vol. 93, pp. 2768-2784, 2011.
- [101] D. Whisler and H. Kim, "A non-explosive test method for generating wide area dynamic blast-type pressure pulse loading on armored panels," *International Journal of Impact Engineering*, vol. 68, pp. 28-40, 2014.
- [102] ASTM D3518 / D3518M-94, Standard Test Method for In-Plane Shear Response of Polymer Matrix Composite Materials by Tensile Test of a  $\pm 45^\circ$  Laminate, ASTM International, West Conshohocken, PA, 2001, [www.astm.org](http://www.astm.org) [Online].
- [103] ASTM D3410 / D3410M-03(2008), Standard Test Method for Compressive Properties of Polymer Matrix Composite Materials with Unsupported Gage Section by Shear Loading, ASTM International, West Conshohocken, PA, 2008, [www.astm.org](http://www.astm.org) [Online].
- [104] ASTM D790-10, Standard Test Methods for Flexural Properties of Unreinforced and Reinforced Plastics and Electrical Insulating Materials, ASTM International, West Conshohocken, PA, 2010, [www.astm.org](http://www.astm.org) [Online].
- [105] ASTM D6415 / D6415M-06a(2013), Standard Test Method for Measuring the Curved Beam Strength of a Fiber-Reinforced Polymer-Matrix Composite, ASTM International, West Conshohocken, PA, 2013, [www.astm.org](http://www.astm.org) [Online].
- [106] S. Abrate, "Impact Dynamics," in *Impact Engineering of Composite Structures*. vol. 526, S. Abrate, Ed., ed: Springer Vienna, 2011, pp. 71-96.
- [107] İ. K. Odacı, C. Kılıçaslan, A. Taşdemirci, and M. Güden, "Projectile impact testing of glass fiber-reinforced composite and layered corrugated aluminium and aluminium foam core sandwich panels: a comparative study," *International Journal of Crashworthiness*, vol. 17, pp. 508-518, 2012.
- [108] ASTM E8M-04, Standard Test Methods for Tension Testing of Metallic Materials [Metric] (Withdrawn 2008), ASTM International, West Conshohocken, PA, 2008, [www.astm.org](http://www.astm.org) [Online].
- [109] C. Kılıçaslan, M. Güden, İ. K. Odacı, and A. Taşdemirci, "The impact responses and the finite element modeling of layered trapezoidal corrugated aluminum core and aluminum sheet interlayer sandwich structures," *Materials & Design*, vol. 46, pp. 121-133, 2013.

- [110] W. Johnson and A. G. Mamalis, "A survey of some physical defects arising in metal working processes," in *17th International MTDR Conference*, London, UK, 1977, pp. 607-621.
- [111] R. Gümrük and S. Karadeniz, "A numerical study of the influence of bump type triggers on the axial crushing of top hat thin-walled sections," *Thin-Walled Structures*, vol. 46, pp. 1094-1106, 2008.
- [112] S. P. Santosa, T. Wierzbicki, A. G. Hanssen, and M. Langseth, "Experimental and numerical studies of foam-filled sections," *International Journal of Impact Engineering*, vol. 24, pp. 509-534, 2000.
- [113] Guoxing Lu and T. Yu, *Energy Absorption of Structures and Materials*. England: Woodhead Publishing, 2003.
- [114] P. J. Tan, S. R. Reid, J. J. Harrigan, Z. Zou, and S. Li, "Dynamic compressive strength properties of aluminium foams. Part II—'shock' theory and comparison with experimental data and numerical models," *Journal of the Mechanics and Physics of Solids*, vol. 53, pp. 2206-2230, 2005.
- [115] S. R. Reid and C. Peng, "Dynamic uniaxial crushing of wood," *International Journal of Impact Engineering*, vol. 19, pp. 531-570, 1997.
- [116] A. T. Barnes, K. Ravi-Chandar, S. Kyriakides, and S. Gaitanaros, "Dynamic crushing of aluminum foams: Part I – Experiments," *International Journal of Solids and Structures*, vol. 51, pp. 1631-1645, 2014.
- [117] "Plane Longitudinal Shocks," in *Fundamentals of Shock Wave Propagation in Solids*, ed: Springer Berlin Heidelberg, 2008, pp. 37-62.
- [118] N. Jones, *Structural Impact*. Cambridge: Cambridge University Press, 1989.
- [119] X. Qiu, V. S. Deshpande, and N. A. Fleck, "Impulsive loading of clamped monolithic and sandwich beams over a central patch," *Journal of the Mechanics and Physics of Solids*, vol. 53, pp. 1015-1046, 2005.
- [120] J. B. Martin and P. S. Symonds, "Mode Approximations for Impulsively-Loaded Rigid-Plastic Structures," *Journal of the Engineering Mechanics Division*, vol. 92, pp. 43-66, 1966.
- [121] N. A. Fleck and V. S. Deshpande, "The Resistance of Clamped Sandwich Beams to Shock Loading," *Journal of Applied Mechanics*, vol. 71, pp. 386-401, 2004.

- [122] Q. H. Qin and T. J. Wang, "A theoretical analysis of the dynamic response of metallic sandwich beam under impulsive loading," *European Journal of Mechanics - A/Solids*, vol. 28, pp. 1014-1025, 2009.
- [123] Z. Xue and J. W. Hutchinson, "A comparative study of impulse-resistant metal sandwich plates," *International Journal of Impact Engineering*, vol. 30, pp. 1283-1305, 2004.
- [124] V. Papadopoulos and P. Iglésis, "The effect of non-uniformity of axial loading on the buckling behaviour of shells with random imperfections," *International Journal of Solids and Structures*, vol. 44, pp. 6299-6317, 2007.
- [125] D. Karagiozova, G. S. Langdon, and G. N. Nurick, "Propagation of compaction waves in metal foams exhibiting strain hardening," *International Journal of Solids and Structures*, vol. 49, pp. 2763-2777, 2012.
- [126] E. Zaretsky, Z. Asaf, E. Ran, and F. Aizik, "Impact response of high density flexible polyurethane foam," *International Journal of Impact Engineering*, vol. 39, pp. 1-7, 2012.

# VITA

İsmet Kutlay ODACI was born in Odunpazarı/Eskişehir/TURKEY in August 15, 1986. After graduation from Mechanical Engineering department of Izmir Institute of Technology, he carried on his M.Sc. and Ph.D. studies as research assistant in Dynamic Testing and Modeling Laboratory in the same institute.

## Education

- **Ph.D.** in English, 2011, Mechanical Engineering, İzmir Institute of Technology.
- **M.Sc.** in English, 2009, Mechanical Engineering, İzmir Institute of Technology.
- **B.Sc.** in English, 2004, Mechanical Engineering, İzmir Institute of Technology.

## Publications

- İ. K. Odacı, C. Kılıçaslan, A. Taşdemirci, and M. Güden, "Projectile impact testing of glass fiber-reinforced composite and layered corrugated aluminium and aluminium foam core sandwich panels: a comparative study," International Journal of Crashworthiness, vol. 17, pp. 508-518, 2012/10/01 2012.
- C. Kılıçaslan, M. Güden, İ. K. Odacı, and A. Taşdemirci, "The impact responses and the finite element modeling of layered trapezoidal corrugated aluminum core and aluminum sheet interlayer sandwich structures," Materials & Design, vol. 46, pp. 121-133, 4//2013.
- C. Kılıçaslan, İ. K. Odacı, M. Güden A. Taşdemirci, "Experimental testing and full and homogenized numerical models of the low velocity and dynamic deformation of the trapezoidal aluminum corrugated core sandwich", Strain (2014) 50, 236-249, DOI: 10.1111/str.12085, 2014.
- C. Kılıçaslan, M. Güden, İ. K. Odacı, A. Taşdemirci, "Experimental and numerical studies on the quasi-static and dynamic crushing responses of multi-layer trapezoidal aluminum corrugated sandwiches", Journal of Thin-Walled Structures, vol.78, pp.70-78, 2014.